

# Double-sided Fresnel zone plates as high performance optics in X-ray microscopy

**Inauguraldissertation**

ZUR

Erlangung der Würde eines Doktors der Philosophie

vorgelegt der

Philosophisch-Naturwissenschaftlichen Fakultät  
der Universität Basel

VON

Istvan Mohacsi

von Budapest, Ungarn

Basel, 2015

Original document stored on the publication server of the University of Basel  
[edoc.unibas.ch](http://edoc.unibas.ch)



This work is licenced under the agreement  
Attribution Non-Commercial No Derivatives 3.0 Switzerland (CC BY-NC-ND 3.0 CH).

The complete text may be reviewed here:  
[creativecommons.org/licenses/by-nc-nd/3.0/ch/deed.en](http://creativecommons.org/licenses/by-nc-nd/3.0/ch/deed.en)

Genehmigt von der Philosophisch-Naturwissenschaftlichen Fakultät

auf Antrag von

Prof. F. Nolting

Prof. C. Schroer.

Basel, den 23.06.2015

---

Prof. Dr. Jörg Schibler

*“The flourishing of thoughts is particularly stimulated by the diversity of ideologies and the clash of opinions.”*

Marx György



# *Abstract*

X-ray microscopy describes a range of analytical techniques, specialized for the characterization of organic and inorganic samples using high energy photons. It takes advantage of the high penetration depth, high resolution and chemical sensitivity of X-rays and allows for the study of extended samples in their native environment without extensive sample preparation. Many of these experimental methods employ diffractive X-ray optics, like Fresnel zone plate lenses to obtain high spatial resolution or the better utilization of the incoming flux. Since improving the efficiency of zone plates can increase the throughput, quality and resolution of measurements, there is a constant demand for high efficiency and high resolution X-ray optics.

Stacking is an established concept for extending the capabilities of zone plate optics. By stacking two zone plates in each other's optical near field, they act as a single zone plate with combined optical transmission profile, that would be infeasible to make as a single optical element. Yet the existing implementations of stacking suffer from issues regarding complexity and stability.

This work presents the development of an alternative solution to conventional zone plate stacking, that circumvents most of its drawbacks. By patterning two zone plates on the front and back sides of a membrane, double-sided zone plates can deliver the advantages of stacked zone plates as inherently monolithic, single-chip optical elements.

Double-sided blazed zone plates with two complementary binary zone plates on the two sides of the membrane were produced to provide an effective four level transmission profile. This allowed to bypass the fundamental limitations of binary zone plates by providing up to 54.7% diffraction efficiency at 6.2 keV while having 200 nm smallest half-pitch and a reasonable working distance.

For high resolution zone plates, structure height is the main limiting factor. Therefore by patterning two identical zone plates on the two sides of the membrane, one can double the effective structure height. This provided us with a significant gain in focusing efficiency at high photon energies, as we have successfully measured 9.9% focusing efficiency at 9 keV with 30 nm smallest half-pitch, while preserving diffraction limited optical performance.

Stacking two complementary zone plates for multiplying their spatial frequencies opens the possibility for ultra-high resolution zone plate optics. We have successfully produced and tested interlaced zone plate optics down to 7 nm smallest half-pitch while still maintaining practical aperture sizes.

This thesis is a comprehensive summary of the work performed for the fabrication and characterization of the high performance zone plates representing each concept and provides possible examples for their future use.



# *Acknowledgements*

First and foremost, I wish to express my gratitude to my advisor, Frithjof Nolting for his valuable advices and guidance during my progress, to my counsellor Christian David for his orientation, assistance, encouragement and helpful remarks and to Jens Gobrecht for his support during my work performed at the Laboratory for Micro- and Nanotechnology. I am equally grateful for Andrea Somogyi and Cameron Kewish from Synchrotron SOLEIL for the initiation of this collaboration and for their invaluable help during the presented measurements and I also thank you for the financial support provided by the Nanoscopium beamline of Synchrotron SOLEIL.

I am indebted to my colleagues at the Laboratory for Micro- and Nanotechnology who's help made the presented achievements possible. I would like to say a special thanks to Petri Karvinen, Ismo Vartiainen, Jeroen Bosgra, Mikako Makita and Vitaliy Guzenko for the inspiration and the fruitful discussions. This thesis would not have been possible without the help of Anja Weber, Eugen Deckardt, Thomas Neiger, Jana Lehmann, Bianca Haas and the rest of the technical staff, who introduced me to the instrumentation and took care of the infrastructure. I am also grateful to the rest of my colleagues who supported me through this venture.

I am also grateful to Ana Diaz and Manuel Guizar-Sicairos for all the measurements and discussion at the cSAXS beamline, that not only yield the backbone of this thesis but also provided a deeper understanding of the observed phenomena. I would also like to say thank you to Alke Meents and Karolina Stachnik from the P11 beamline of PETRA III, to Pascal Mercère at the Metrologie beamline of Synchrotron SOLEIL and to Ian McNulty and Robert Winarski at the 26-ID beamline of APS for their help during the presented measurements. I also give due credit to Raymond Leung and Michael Feser for pointing my attention towards new directions. I am also thankful for the engineers working at the aforementioned beamlines and to Elisabeth Müller from the Paul Scherrer Institute as well as to Elina Färm and Mikko Ritala at the University of Helsinki. My gratitude also extends to a large number of lecturers, who shared their expertise on conferences or seminar talks providing an overview of the related fields.

I also express my gratitude for my family for their continuous support and for my friends who remained in touch despite being scattered across whole Europe. At last but not least, I also send my gratitude to all who directly or indirectly contributed to the presented work.





# The scope of this thesis

This work was created as a collaboration between the Paul Scherrer Institute and the Nanoscopium beamline of Synchrotron SOLEIL for the development of efficient Fresnel zone plate optics for the hard X-ray range. The Nanoscopium beamline[1] is the first extended beamline of SOLEIL with up to 155 metre sample distance from the undulator-source and 70 m from the secondary source to improve spatial coherence. The Nanoscopium beamline houses three end stations, working in the 5-20 keV range. The first end-station is dedicated to coherent diffractive imaging, requiring moderate spot size but very high efficiency and aperture size together with a reasonably compact focal distance. The second and third end-stations of the beamline specialize in scanning X-ray spectro-microscopy measurements requiring a small focal spot of 30 nm while collecting as much as possible photons especially towards higher photon energies.

Therefore starting from the idea of zone plate stacking, after initial investigation the presented double-sided stacking turned out to be a viable concept for both high resolution and high efficiency zone plate optics for the targeted energy range. The development and characterization of these optics represent the key message of this thesis.

The related nanofabrication work was performed by the author of this thesis at the clean room facilities of the Paul Scherrer Institute's Laboratory for Micro- and Nanotechnology. Testing of the fabricated optics was performed mainly at the Metrologie and Nanoscopium beamlines of Synchrotron SOLEIL and at the cSAXS beamline of the Swiss Light Source. Additional measurements were carried out at the P11 beamline of PETRA III and at the 26-ID beamline of the Advanced Photon Source.

Due to the fabrication and characterization being separated in both time and space, this thesis is organized in two main blocks: the first three chapters describe the theoretical background, methodology and relevant literature. The fourth chapter briefly discusses experiments performed with the mechanical stacking of zone plates. The fifth, sixth and seventh chapters describe the characterization of double-sided zone plates. Specifically, the fifth chapter discusses double-sided blazed zone plate optics with moderate spot sizes and very high focusing efficiency as appealing focusing optics for the coherent diffractive imaging end-station. The sixth chapter describes high resolution double-sided zone plate optics for the nanoprobe end-station. The seventh chapter is aimed to extend current resolution capabilities of zone plate optics into the sub-10 nm range with the use of double-sided interlacing. Finally, the eighth chapter summarizes the presented achievements and provides an outlook for future work. The appendix chapters discuss topics that are related to the body of the thesis and provide a valuable addition, but would require additional investigations for more detail.



# Contents

<b>Abstract</b>	<b>v</b>
<b>Acknowledgements</b>	<b>vii</b>
<b>The scope of this thesis</b>	<b>ix</b>
<b>Abbreviations</b>	<b>xv</b>
<b>1 Historical background</b>	<b>1</b>
1.1 The beginnings of X-ray science . . . . .	1
1.2 The first half of the 20 <sup>th</sup> century . . . . .	3
1.3 Early years of synchrotron radiation . . . . .	4
1.4 Present day storage rings . . . . .	7
1.5 Future X-ray sources . . . . .	7
1.6 Nanofocusing X-ray optics . . . . .	9
<b>2 Methods and theory</b>	<b>13</b>
2.1 Interactions between X-rays and matter . . . . .	13
2.1.1 Classical theory of dielectrics . . . . .	14
2.2 Fresnel zone plates . . . . .	17
2.2.1 Ideal lens . . . . .	17
2.2.2 Resolution of ideal lenses . . . . .	19
2.2.3 Fresnel zone plates as ideal lens . . . . .	20
2.2.4 The resolution of Fresnel zone plates . . . . .	21
2.2.5 Fresnel zone plates in the X-ray range . . . . .	22
2.2.6 Fabrication of Fresnel zone plates . . . . .	27
2.2.6.1 High resolution zone plates . . . . .	27
2.2.6.2 Multilevel zone plates . . . . .	27
2.2.7 The stacking of zone plates . . . . .	28
2.2.8 Beyond the planar approximation . . . . .	30
2.2.9 Other diffractive optical elements . . . . .	30
2.3 Simulation of diffractive optics . . . . .	31
2.4 Imaging with X-rays . . . . .	34
2.4.1 Full-field X-ray microscopy . . . . .	35
2.4.2 Scanning probe X-ray microscopy . . . . .	36
2.4.3 Coherent diffractive imaging . . . . .	38

---

2.4.4	Ptychography . . . . .	39
2.4.4.1	Reconstruction algorithms in ptychography . . . . .	40
2.4.4.2	Difference-map algorithm . . . . .	40
2.4.4.3	Ptychographic iterative engine . . . . .	41
2.4.4.4	Maximum likelihood method . . . . .	43
2.4.4.5	Experimental setup . . . . .	43
2.4.4.6	Ptychographic characterization of X-ray optics . . . . .	44
2.5	Measurement considerations . . . . .	44
2.5.1	Shot noise and its effect on image resolution . . . . .	45
2.5.2	Limitation of radiation damage . . . . .	47
<b>3</b>	<b>Nanofabrication and numerical methods</b>	<b>49</b>
3.1	Electron beam lithography . . . . .	49
3.1.1	Basics of electron beam lithography . . . . .	50
3.1.1.1	Electron beam lithography at LMN . . . . .	51
3.1.2	Direct patterning of high aspect ratio nanostructures . . . . .	52
3.2	Reactive-ion etching . . . . .	55
3.3	Electroplating . . . . .	55
3.3.1	The basics of electroplating . . . . .	55
3.3.2	Electroplating on the nanoscale at LMN . . . . .	56
3.4	Atomic layer deposition . . . . .	58
3.4.1	Conformal deposition of Iridium . . . . .	60
3.5	Critical point drying . . . . .	62
3.6	Electroplated zone plates in PMMA resist . . . . .	62
3.7	High resolution zone plates in HSQ resist . . . . .	65
3.8	Simulations . . . . .	68
<b>4</b>	<b>The mechanical stacking of blazed zone plates</b>	<b>71</b>
4.1	Design considerations . . . . .	71
4.2	Sample fabrication and characterization . . . . .	72
4.3	Early measurements . . . . .	74
4.3.1	Efficiency measurements . . . . .	74
4.3.2	Spatially resolved measurements . . . . .	76
4.4	Final measurements . . . . .	78
4.4.1	4-level blazed zone plate stacks . . . . .	79
4.4.2	6-level blazed zone plate stacks . . . . .	80
4.5	Conclusions . . . . .	82
<b>5</b>	<b>Double-sided blazed zone plates</b>	<b>85</b>
5.1	Motivation and design consideration . . . . .	85
5.2	Sample fabrication . . . . .	86
5.3	Efficiency measurements . . . . .	89
5.4	Detailed characterization . . . . .	91
5.5	Conclusions . . . . .	95
<b>6</b>	<b>Line-doubled double-sided zone plates</b>	<b>97</b>
6.1	Background and motivation . . . . .	97
6.2	Sample fabrication . . . . .	98

---

6.3	Efficiency measurements . . . . .	99
6.4	Ptychographic characterization and STXM imaging . . . . .	102
6.5	Conclusions . . . . .	104
<b>7</b>	<b>The interlaced stacking of zone plates</b>	<b>107</b>
7.1	Motivation . . . . .	107
7.2	Sample fabrication . . . . .	108
7.2.1	Alignment issues . . . . .	109
7.3	Efficiency measurements and pre-selection . . . . .	109
7.3.1	15 nm outermost zone FZPs . . . . .	110
7.3.2	7 nm outermost zone FZPs . . . . .	110
7.4	Ptychography with interlaced zone plates . . . . .	111
7.5	Imaging experiments . . . . .	114
7.5.1	STXM with sub-10 nm zone plate . . . . .	114
7.5.2	Full-field X-ray microscopy with 15 nm zone plates . . . . .	115
7.6	Conclusion . . . . .	116
<b>8</b>	<b>Summary and conclusion</b>	<b>117</b>
<b>A</b>	<b>Generalized update procedure in ptychographic reconstructions</b>	<b>121</b>
<b>B</b>	<b>Alignment tolerance of stacked zone plates</b>	<b>127</b>
	<b>Bibliography</b>	<b>131</b>
	Curriculum vitae	



# Abbreviations

<b>FZP</b>	Fresnel Zone Plate
<b>CRL</b>	Compound Refractive Lens
<b>MLL</b>	Multilayer Laue Lens
<b>KB mirror</b>	Kirkpatrick-Baez mirror
<b>OSA</b>	Order Selecting Aperture
<b>Si</b>	Silicon
<b>Cr</b>	Chromium
<b>Ni</b>	Nickel
<b>Au</b>	Gold
<b>Ir</b>	Iridium
<b>PMMA</b>	Poly(Methyl MethAcrylate)
<b>HSQ</b>	Hydrogen SilsesQuioxane
<b>MIBK</b>	Methyl IsoButyl Ketone
<b>IPA</b>	Isopropyl Alcohol
<b>STXM</b>	Scanning Transmission X-ray Microscopy
<b>SEM</b>	Scanning Electron Microscopy
<b>TEM</b>	Transmission Electron Microscopy
<b>FIB</b>	Focused Ion Beam
<b>CCD</b>	Charge-Coupled Device
<b>CMOS</b>	Active pixel sensor
<b>VUV</b>	Visual-Ultraviolet energy range
<b>EUV</b>	Extreme Ultraviolet energy range
<b>keV</b>	Kiloelectron Volt
<b>CVD</b>	Chemical Vapour Deposition
<b>NA</b>	Numerical Aperture





# Chapter 1

## Historical background

Present achievements of X-ray science were preceded by more than a century of continuous progress[2–4]. Therefore, despite the rapid developments over the past two decades, this chapter is meant to give due credit to the pioneers of X-ray science. The historical concept not only tells the story of X-ray imaging, but also gives an overview on actual trends, as well as an outlook towards future progress.

### 1.1 The beginnings of X-ray science

Fuelled by the ever growing demands of the society, the pre-world war era was a time of rapid technological and scientific development on the European and American continent. With the theoretical background provided by James Clerk Maxwell’s work[5], the study of the electromagnetic phenomena became a dynamic field of scientific development. Gas discharge tubes, developed by Heinrich Geissler were the earliest devices to exhibit exotic electric phenomena in low pressure gasses, showing luminescence that is now commonly employed in lighting tubes. By improving the vacuum in glow discharge tubes, the emitted radiation concentrated in the vicinity of the cathode, granting their name: ”cathode-rays”[6]. Several scientists investigated unexplained phenomena surrounding cathode ray tubes[7] but their early studies were of limited scale due to low-throughput photographic plates.

The first large-scale study on cathode-rays was done by Wilhelm Conrad Röntgen in 1895 at the University of Würzburg. Unlike his predecessors he used a fluorescent screen made of barium platinocyanide instead of photographic plates. The quick feedback greatly increased the speed and throughput of his experiments allowing him to conduct the first throughout study on cathode rays. His initial observations revealed that the invisible radiation caused fluorescence on the scintillator screen even when a black cardboard blocked all optical light emanating from the tube. Further studies

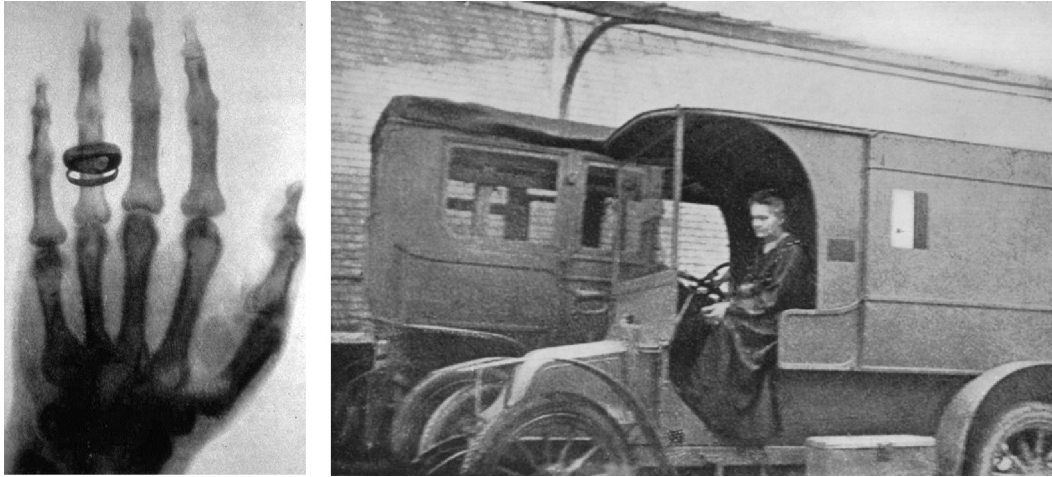


FIGURE 1.1: Left: The famous photograph from the hand of Albert von Kölliker, from Röntgen's original work[8]. Right: Marie Curie in a French military X-ray vehicle[4, 9].

revealed that it can not be focused or diffracted by conventional optics and can pass through optically thick objects such as books and even the human body, with attenuation specific to the materials. Due to the unusual phenomena, he called the new radiation X-rays. The reports of his initial studies were presented to the president of the Würzburg physical and medical society, under the title "On A New Kind Of Rays" (Über eine neue Art von Strahlen)[8]. This report included the radiograph from the hand of his colleague, Albert von Kölliker, that became the first published medical radiograph and is widely considered as the start of X-ray science (see Figure 1.1).

The discovery of X-rays generated a large public interest in the phenomena that lead to the rapid development of X-ray imaging both for entertainment and for science. In 1912, Max von Laue reported the successful diffraction of X-rays, which proved that X-rays belong to electromagnetic radiation[10]. One year later in 1913 William Lawrence Bragg and William Henry Bragg published their essay[11] about the diffraction of X-rays from crystalline materials (see Figure 1.3) founding X-ray crystallography. In the same year, Pierre Goby recorded the first X-ray contact micro-radiograms by placing various objects on a high resolution photographic plate[12] and magnifying the developed image (see Fig. 1.3). The outbreak of World War I led to a slow-down in fundamental developments in X-ray science, but highlighted their medical applications thanks to the work of Marie Curie (see Figure 1.1).

The history of X-ray science strongly correlated with the development in available X-ray sources. The first man made X-ray sources were the Crookes tubes, consisting of an anode and a cathode in a partially evacuated glass tube (see Figure 1.2). When high voltage is applied between the electrodes, free electrons are accelerated towards the anode, ionizing the residual gas in the tube, creating an avalanche of electrons. If the acceleration voltage and the pressure was in the right range, some electrons were energetic enough to generate X-rays through bremsstrahlung (breaking radiation) or by

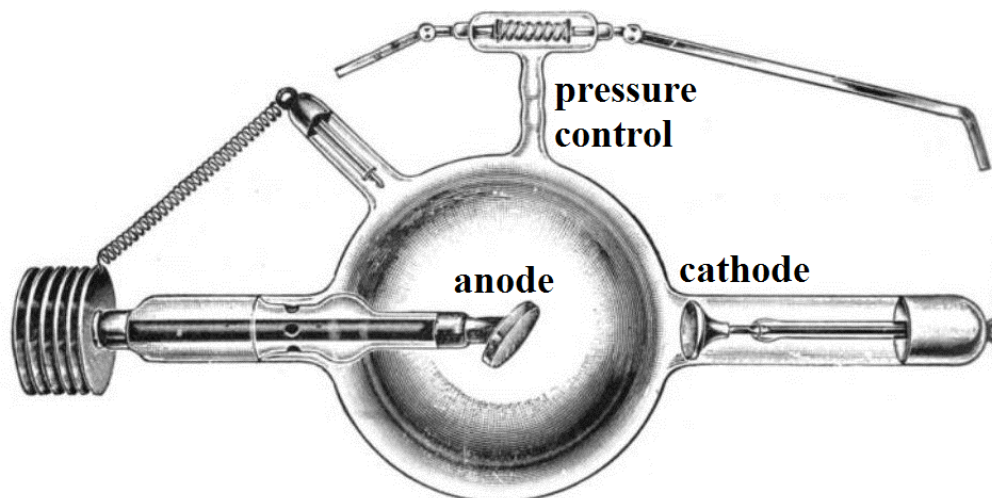


FIGURE 1.2: Illustration of a Crookes tube X-ray source from the early 1900s with automatic pressure regulator against the ageing of the tube. The platinum target is tilted by  $45^\circ$  to maximize output. (from G. W. C. Kaye: X rays: an introduction to the study of Röntgen rays, 1914).

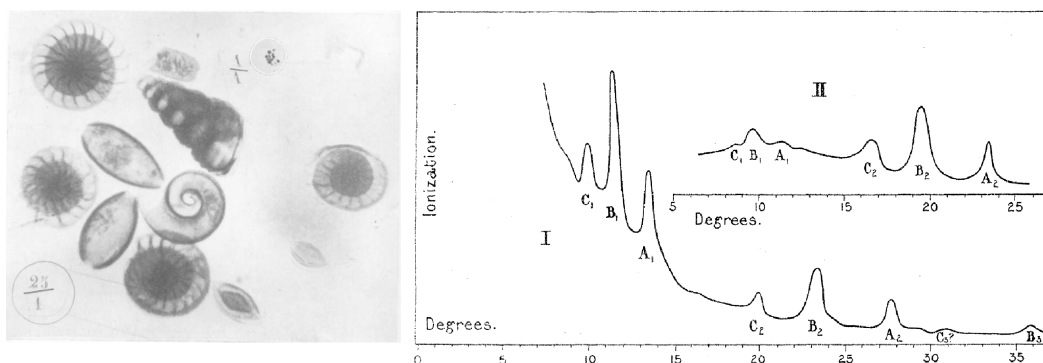


FIGURE 1.3: Left: Early micro-radiograph, showing the inside structure of foraminifera shells, the image was magnified from a  $5.5 \times 5.5 \text{ mm}^2$  area [12]. Right: reflection from (100) and (111) face of rock salt as a function of angle [11]. The diffraction peaks correspond to well-defined distances within a crystalline lattice, allowing the reconstruction of the structure from its X-ray diffraction patterns.

exciting the core electrons of atoms (characteristic X-rays) when hitting the anode. As Crookes tubes relied on ionization of the residual gas as an electron source, they were sensitive to pressure variations and subject to ageing. Therefore, despite their invaluable role in the early years of X-ray science, the growing interest towards X-rays required dedicated sources for their production.

## 1.2 The first half of the 20<sup>th</sup> century

The ancestor of today's modern X-ray tubes was built in 1913 by William D. Coolidge [13]. It employed a heated tungsten filament electron source, allowing it to work under higher vacuum. The thermal electron source separated the extraction voltage from the

current of the tube and granting higher tunability of the emitted flux and X-ray spectra. Full-body medical imaging required high-flux sources and went towards higher power, while electrostatic lenses were developed to produce high brightness microfocused X-ray sources for higher resolution micro- and nanoimaging. Both high flux and microfocused X-ray tubes expressed high thermal load on the anode, with the damage threshold eventually limiting their brightness to  $\sim 1 \text{ kW/mm}^2$ . In order to prevent the electron beam from melting the anode, Coolidge developed the rotating anode X-ray tube to distribute the generated heat over a larger, continuously refreshing area[14]. Rotating anode X-ray tubes were commercialized in 1929 providing two orders of magnitude increase in brightness, but their descendants still represent the standard technology in medical and laboratory equipment up to date.

The 1930's was also an important period because of pioneering work on electron microscopy[15]. In 1928 the Technological University of Berlin launched a project to improve cathode-ray oscilloscopes. Thanks to the work of Max Knoll, Ernst Ruska and Bodo von Borries, the project outgrew its original scope and by 1931, led to the development of the transmission electron microscope[16]. Transferring his expertise on electron optics, Knoll used an electron beam scanner for characterizing of extended samples[17]. Manfred von Ardenne recognized the potential of scanning samples with a fine electron beam for magnification thus developing the scanning electron microscope[18].

By the time of the 1950s, both scanning and transmission electron microscopes have undergone a rapid development. High contrast, sub-100 nm resolution micrographs like on Figure 1.4 could be acquired, albeit these studies were limited to surface information or required very thin, conductive specimens. X-ray "macroscopy" at this time was limited by the lack of X-ray optical elements. While magnified images could be obtained using a "pinhole" camera, the decrease in flux led to very limited practical applications. The first true X-ray microscope that employed optical elements was built by Paul Kirkpatrick and Albert V. Baez [19] in 1948. By grazing incidence mirrors they could provide a  $29\times$  magnified image of a test grid using an X-ray tube based setup.

### 1.3 Early years of synchrotron radiation

The theoretical background of synchrotron radiation reaches back to the time of Thomson's discovery of the electron in 1897. Early studies made by Larmor and Lienard[22] showed that charged particles on a circular orbit should continuously lose some of their energy, but the nature of this energy loss was unknown at the time. After the discovery of Einstein's special theory of relativity Schott extended their studies to the relativistic case and in 1912 he published his summary on the energy loss mechanisms of relativistic charged particles [23]. However, due to the lack of experimental verification, his studies were quickly forgotten by the scientific community.



FIGURE 1.4: By the time of world war II, electron microscopy was already a developed technique as shown in on some example images. Left: Electrolytically generated oxide imprint of etched aluminium in TEM [20]. Right: Iron oxide particles from iron-pentacarbonyl in SEM [21].

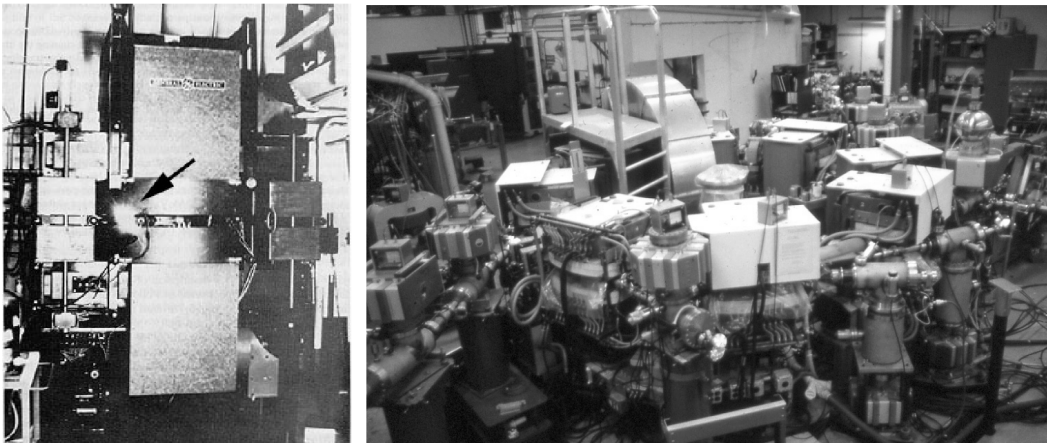


FIGURE 1.5: Left: Synchrotron light as seen through the window of Pollock’s 70 MeV synchrotron. (source: <http://xdb.lbl.gov>) Right: Tantalus I, the first dedicated synchrotron multi-user light source for the 10 – 100 nm range (from SRC homepage).

With the development of the first cyclic particle accelerators, known as betatrons in 1940, the energy loss mechanism of circulating charged particles regained interest. Synchrotron radiation was first observed in 1947 at General Electric’s 70 MeV synchrotron. Unlike previous accelerators, this synchrotron included a peaking hole into the chamber to monitor possible arcing. Much to the observing technician, Floyd Haber’s surprise, he saw the emission of intense bluish light from the synchrotron (see Figure 1.5.). The subsequent investigations of Pollock and Langmuir linked the spectra of the radiation to the accelerator energy, verifying that the phenomena was indeed the predicted synchrotron radiation[24].

After the initial discovery of synchrotron radiation as a by-product of particle accelerators, upcoming accelerators were designed to make use of the emitted synchrotron

radiation. The increasing accelerator energies shifted the peak of the radiation towards higher energies and the 6-GeV Deutsches Elektronen-Synchrotron (DESY) was the first accelerator in 1964 to allow for measurements in the hard X-ray range, providing X-rays down to 0.1 nm wavelength. Although the first generation of synchrotrons were not dedicated light sources, they allowed early measurements and instrumentation development in the UV, soft X-ray and hard X-ray range opening the path towards dedicated storage rings. The 240 MeV Tantalus I storage ring built in 1968[25] was the first dedicated multi-user synchrotron light source that housed 10 beamlines to conduct simultaneous measurements in the soft X-ray range (see Fig. 1.5).

Around the time of the first dedicated synchrotrons, both scanning and transmission electron microscopy was already a well established technique for nanoscale imaging. While diffraction patterns with sub-atomic spatial frequencies could be routinely recorded, real space resolution required considerable efforts to reach the sub-10 nanometre range. To reduce the mismatch between Fourier space and real space imaging, several iterative algorithms have been developed[26, 27] to solve the phase problem and improve real-space images with the recorded diffraction patterns. However, with the maturing of electron microscopy, its limitations became evident regarding extensive sample preparation and penetration depth.

Meanwhile, with increasing brightness and availability of synchrotron sources, scientists adapted existing schemes from visual light and electron microscopy to the X-ray range. Following Albert V. Baez's recommendations[28] and Janos Kirz's pioneering work [29], Fresnel zone plates were recognized as the X-ray counterparts of optical or magnetic lenses. Soon after his suggestion, the group of Günter Schmahl developed the first full-field X-ray microscope[30] as the X-ray analogue of an optical microscope. Their microscope employed a condenser zone plate for illumination and an objective zone plate for image formation to project a magnified image of biological specimens onto a photographic plate (see Figure 1.6). A few years later, the group of Janos Kirz [31, 32] demonstrated the scanning transmission X-ray microscope as the X-ray analogue of scanning electron microscopes (see Figure 1.6). The first generations of holographic zone plates[33, 34] were later replaced by electron beam patterned lenses [35, 36] allowing X-ray microscopy to clearly overtake the resolution of visible light microscopy.

The increasing demand for synchrotron radiation facilities prompted the construction of numerous dedicated lightsources, including redesigning existing particle accelerators from particle physics to provide higher beam currents and increased brightness and stability for user experiments.

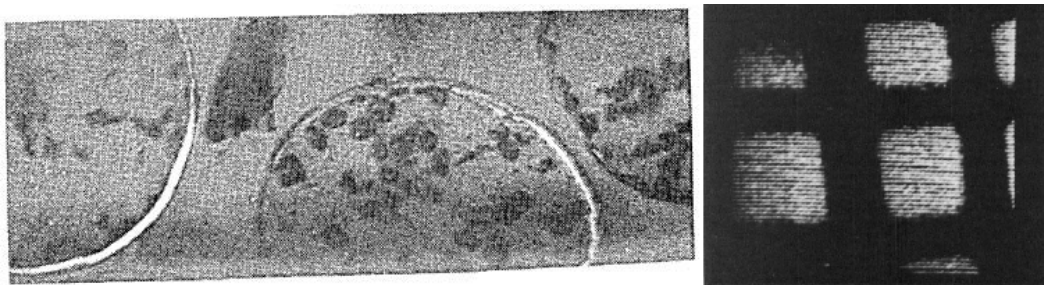


FIGURE 1.6: The discovery of Fresnel zone plate lenses gave new momentum to X-ray microscopy. This development allowed the successfully demonstration of full field (left) and scanning transmission X-ray microscopy (right). (source [30] and [31])

## 1.4 Present day storage rings

Present day "third generation" synchrotron lightsources were designed to provide increased brightness, spatial coherence and better time resolution to the user community. Availability and stability of the X-ray beam greatly improved, also due to the incorporation of modern beam diagnostic devices around the electron storage ring. The majority of bending magnet sources were replaced by insertion devices (undulators or wigglers), increasing the brightness and providing better spatial and temporal coherence for imaging. Photographic plates were replaced by electronic detectors [37], allowing fast feedback, data collection and visualization and advances in digital data processing paved the way for X-ray tomography, showing the superiority of X-rays over electrons for volumetric imaging. After the start of the third millennium, the increase in computing power and the development of numerical methods led to the rapid expansion of lensless imaging techniques[38]. Using iterative phase retrieval, the resolution was no longer limited by the X-ray lenses, allowing X-ray microscopy to catch up to the resolution of electron microscopy[39] even in 3D tomographic imaging[40].

However the biggest achievement of third generation synchrotron lightsources is that they opened up X-ray science for a wide user community. Being an established, "user-friendly" technology, they were no longer considered risky mega-projects of rich countries. Fuelled by the construction of new facilities, the increased availability led to practical applications and many collaborations between academia and industry.

## 1.5 Future X-ray sources

The guideline of the past century of X-ray science was the development of brighter X-ray sources; however present day lightsources have reached the point, where there is no single "yellow brick road" representing the only path for development. With the increasing diversity and specialization in different fields of X-ray science, the framework of existing large scale facilities can no longer satisfy all specialized user demands. Future

X-ray sources will probably serve certain focus groups, rather than enforcing a "one size fits all" strategy. Therefore, while some overlap and competition will always exist, the branching and specialization of X-ray science is unavoidable in the near future.

Large synchrotron facilities represent today's well established and dominating technology in X-ray science, each housing several beamlines specialized to serve the needs of a targeted user community. They not only provide the tools for measurement, but also valuable services in the analysis and interpretation of the acquired experimental data. Although synchrotrons have been around for nearly half a century, they are still subjected to constant improvement. Following the progress in accelerator physics, most synchrotron light sources periodically undergo massive refurbishments, improving their capacity, brightness and coherence or reducing operation costs. Emerging technologies, like multi-bend achromats[41] and narrow gap undulators represent the next step of progress, offering increased brightness and coherence to upcoming synchrotron sources. These technologies will be first implemented in the Max IV synchrotron (Lund, Sweden) followed by the foreseeable updates of the existing facilities around the world[42].

Following the guideline of the past century, the next candidate for a large step forward in terms of brightness, coherence and temporal resolution are X-ray free electron lasers (XFELs). XFELs provide 8-10 orders of magnitude higher peak brightness than 3<sup>rd</sup> generation synchrotron sources, together with femtosecond scale time resolution and highly coherent X-ray beam. The goal was to outrun radiation damage, enabling the imaging of single nanoparticles and macromolecules before their destruction[43]. The first generation of XFELs are already operational in the soft (FLASH, Fermi) and hard (LCLS, SACLA) X-ray range, with several facilities being under construction around the world, including the SwissFEL at the Paul Scherrer Institute in Switzerland. XFELs are large and expensive experimental facilities providing destructive intensity and far superior time resolution than existing synchrotron sources. However present facilities offer very limited multi-user capability, high overbooking and their intensity limits their use to time resolved and single-shot "diffract-and-destroy" experiments[43]. Therefore, they are not expected to be direct competitors of present day synchrotron facilities, but more aimed towards protein crystallography and ultrafast dynamics.

One of the biggest drawback of current large scale facilities is their 6-12 months schedule, that makes accessing beamtime a long and uncertain procedure. Therefore besides increased brightness coherence and time resolution, increasing the availability of X-ray sources is also a strong driving force. While X-ray tubes represent today's standard and affordable laboratory sources, the brightness of conventional X-ray tubes is often insufficient, prompting the rapid development of next generation compact X-ray sources. Recent developments like liquid metal jet X-ray tubes[44], plasma based soft X-ray sources[45] and compact synchrotrons[46] all aim to provide sufficient brightness to bring X-ray analytical techniques from the beamlines to the laboratory. With sufficient



brightness, existing high-end commercial products can provide lab based micro-CT and even high resolution X-ray microscopy setups for those willing to pay for it. Even if a measurement takes a hundred times longer in the laboratory than at a synchrotron, the increased availability and fast feedback can be a decisive advantage.

## 1.6 Nanofocusing X-ray optics

Following the historical context, the development of the first optical elements for the X-ray range initiated the rapid development of X-ray microscopy. The right optical elements allowed the adoption of well-established optical schemes from visible light and electron microscopy. However their development took nearly 80 years for a reason since X-ray optics need completely different principles than the ones used with electron or visible light imaging.

In this range of the electromagnetic spectrum, the refractive index of all materials is very close to unity. Furthermore, as the relative phase shifts are comparable to the absorption terms, traditional thick optical lenses are no option. Similarly to visible light, the focusing of hard X-rays can be done with reflective, refractive or diffractive optics, but their practical implementation requires custom designs. Regardless of the energy range, the basic laws of optics remain unchanged, most importantly, that the wavelength and the numerical aperture (NA) determines the resolution and together with the aperture size it also sets the working distance.

Historically, the first focusing optics for X-rays were developed by Kirkpatrick and Baez, using the total reflection of X-rays from grazing incidence mirrors[19] as illustrated on Figure 1.7.a. With well-established surface polishing technologies, KB mirrors provide the backbone of beamline optics as high efficiency, large aperture and fundamentally achromatic optical elements. Compact KB mirror systems offer over 70% focusing efficiency, with spot sizes approaching the 10 nm range[47]. Yet they have some severe drawbacks being difficult to use, off-axis optical elements and unsuitable for image formation as objectives. They require separate mirrors for high quality horizontal and vertical focusing, as high quality 2D focusing mirrors are still a work in progress. Since the total reflection angle in the X-ray range is very shallow, large aperture sizes require large and bulky mirrors. Due to their large area, they are difficult to make and small imperfections on the mirror surface contribute to parasitic small angle scattering in the vicinity of the focal spot.

While the design of a thick optical lens is generally not practical in the X-ray range, it is possible to produce efficient refractive lenses from light materials like lithium, beryllium or aluminium[49]. While a single refractive X-ray lens seen on Figure 1.7.c has a small numerical aperture and thus a very long focal length, the focal length can

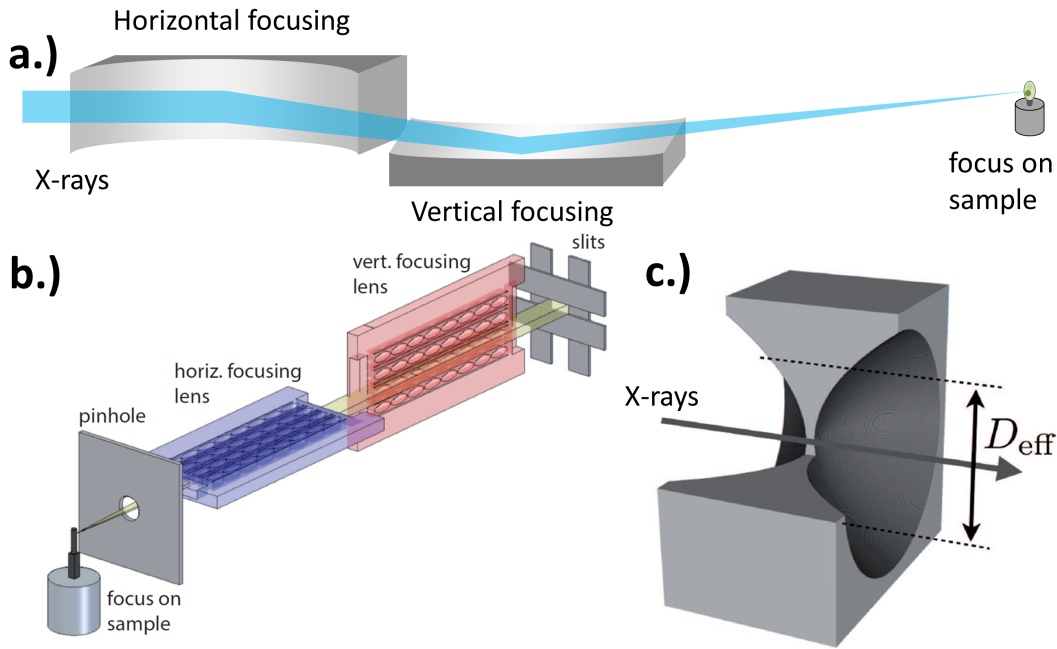


FIGURE 1.7: a.) KB mirror systems are reflective X-ray optics, providing wavelength independent focal distance. b.) Optical setup with nanofocusing compound refractive lenses, showing two sets of nanofabricated lenses for horizontal and vertical focusing (from [48]). c.) An individual 2D focusing refractive lens with the effective diameter limited by the absorption in the thick lens material (from [48]).

be mitigated into the reasonable range by stacking several lenses. The efficiency of such compound refractive lenses (CRLs) can be close to 100% and their negligible absorption allows them to focus free electron laser beams. However optical aberrations are hard to prevent during the fabrication procedure and the inhomogeneities in the lens material produce parasitic small angle scattering, resulting in a dirty and smeared out focal spot.

Planar refractive lenses work on similar optical schemes as CRLs by patterning a large number of subsequent refractive lenses on the same substrate[50] as seen on Figure 1.7.b. Using well-established fabrication methods for silicon, germanium or diamond patterning[51–54], the shape and curvature of the patterns can be optimized[55] to minimize absorption and provide an aberration free focus. Yet their aperture size is limited by the etching depth, falling typically in the 100 micron range for sub-100 nm focal spots[48]. While lenses can be made larger by the micromachining[56, 57] of the substrates, pushing the aperture size shifts resolution from the nano- to the micrometre range. Similar to KB-mirrors, they only provide one dimensional nanofocusing, requiring separate, matched lenses for horizontal and vertical focusing. Planar refractive lens retain their focusing abilities towards very high X-ray energies[58], but they suffer from absorption losses in the soft X-ray and multi-keV energy range.

Fresnel zone plate lenses[59] are compact, easy to use, on-axis diffractive optical elements with customizable aperture size, resolution and focusing properties. As will be

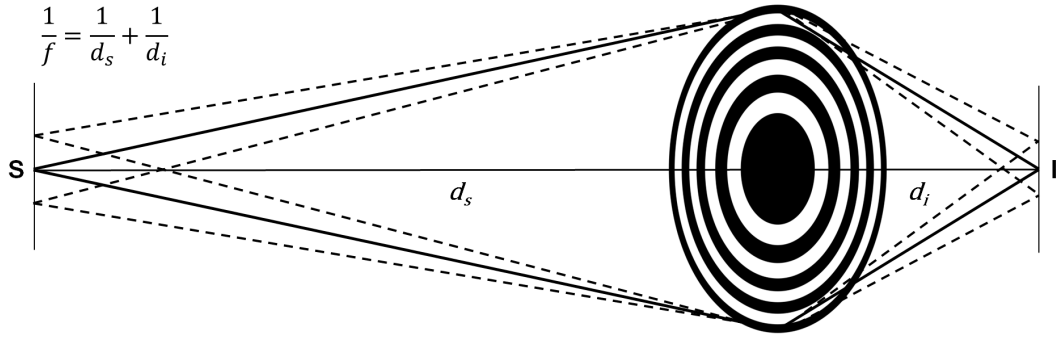


FIGURE 1.8: Fresnel zone plate lenses are compact, on-axis optical elements with the shape of a circular grating with radially decreasing pitch. They are stigmatic optical elements, as they image the contents of their sample plane into their image plane.

described in the next chapter, they originate from refractive lenses by minimizing absorption in the bulk of the lens material. They have the appearance of a concentric grating with radially decreasing pitch (see Figure 1.8). Their focusing efficiency is generally determined by the height and their resolution is determined by the smallest half-pitch of their structures. As the fabrication of Fresnel zone plates requires the production of high aspect ratio nanostructures, they require a compromise between resolution and efficiency. Efficiency of zone plates becomes particularly problematic at high photon energies, while they are better suited for the soft X-ray and multi keV range. Despite their relatively low efficiency, the popularity of Fresnel zone plates lies in their simple use and high spot quality, capable of providing diffraction limited optical performance in an on-axis setup.

Multilayer Laue-lenses[60] represent a borderline case of linear Fresnel zone plates. The alternating deposition of multilayers with different refractive index materials according to the zone plate-law offers unlimited aspect ratios and atomic-scale half-pitches using a relatively simple fabrication method. However the practical fabrication of multilayer Laue-lenses suffers from issues arising from surface roughness, grain size and error propagation in the subsequent layers. Due to their virtually unlimited aspect ratios, MLLs provide excellent efficiency, especially at high photon energies, but their practical use is hindered by their complexity. It requires a total of four aligned multilayer Laue-lenses to achieve complete 2 dimensional focusing, with a minimum of two required to achieve a point focus[61]. Nevertheless, due to the potential of extremely thin layers, multilayer Laue-lenses have been demonstrated with sub-20 nm resolution[61, 62] even for high photon energies.

As described in the preceding paragraphs, there are several appealing concepts for the nanofocusing of X-rays, each having advantages and drawbacks. With the image-forming contrast mechanisms for organic and many inorganic materials peak in the soft X-ray (0.2-2.4 keV), tender X-ray (2-5 keV) and multi-keV energy range (5-12 keV), these ranges have practical interest for high resolution imaging experiments. In these

---

ranges Fresnel zone plates are widespread optical elements. Hence their behaviour in the multi-keV range is discussed in detail in the following sections of this thesis.

## Chapter 2

# Methods and theory

In general terms, microscopy is the science of imaging objects below the millimetre range. It also belongs to the few scientific techniques that can generate significant public interest by providing easy to comprehend and visually impressive images. However, the scientific interpretation of the images requires one to know the mechanism of image formation. Knowing the optical setup and the possibilities and limitations of a technique allows to determine its suitability for a given purpose and to obtain quantitative information from the obtained dataset. Therefore, this chapter is aimed describing the theoretical background of X-ray interactions with matter, the behaviour of diffractive X-ray optics and some basic X-ray microscopic techniques.

### 2.1 Interactions between X-rays and matter

Maxwell's equations[5] represent the foundation of classical electrodynamics. Their free space solution is a wave equation, that describes the propagation of electromagnetic waves in vacuum or dielectric media. Their simple plain wave solution of the electric field  $\vec{E}$  has the form:

$$\vec{E}(\vec{r}, t) = \vec{E}_0 e^{i(\vec{k}\vec{r} - \omega t)} \quad (2.1)$$

where  $k = 2\pi/\lambda$  is the wave vector, and  $\omega$  is the angular frequency of the propagating wave. The interaction between the electromagnetic wave and a medium can be implemented in this equation as an change in phase velocity  $c$  by a factor of  $n = \frac{c}{c_0} = \frac{c}{\omega} k$ , this factor is called the refractive index. The Beer-Lambert law states that the attenuation of electromagnetic waves obeys a similar exponential law, allowing it to be included in the refractive index as a complex term:  $n = \alpha + i\beta$ . Here the real part stands for the phase shift and the imaginary part stands for the absorption in the material. Hence transforming the one dimensional solution of equation 2.1 into:

$$E(z, t) = E_0 e^{i(nkz - \omega t)} = E_0 e^{i((\alpha + i\beta)kz - \omega t)} = E_0 e^{-\beta kz} e^{i\alpha kz} e^{-i\omega t} \quad (2.2)$$

This separates the terms responsible for time dependence, phase evolution and the attenuation, while satisfying the Beer-Lambert law as  $I(z) \sim |E(z)|^2 = I_0 e^{-\frac{4\pi\beta z}{\lambda}}$ . Since the complex refractive indices of materials in the X-ray range are slightly smaller than unity, the refractive index is often written as  $n = 1 - \delta + i\beta$ . Substituting this into equation 2.2, one obtains a separate term responsible for the propagation within the medium:

$$E(z, t) = E_0 e^{ikz} e^{-i\delta kz} e^{-\beta kz} e^{-i\omega t} = E_0 e^{in_r kz} e^{i(kz - \omega t)} \quad (2.3)$$

This results in the commonly accepted terminology of working with the  $n_r = -\delta + i\beta$  relative refractive index in the X-ray range. Typical values of  $\delta$  and  $\beta$  in the 4-10 keV "multi-keV" range are on the order of  $10^{-5}$  even for the densest materials and can be orders of magnitudes smaller for lighter elements. Unlike in visible light optics, the  $\delta$  phase and  $\beta$  absorption terms are usually comparable to each other, resulting in non-negligible absorption. The refractive index shows direct correlation with the electron density of the materials and is largely unaffected by the presence of chemical bonds. Generally both the phase shift and the absorption terms decrease with increasing photon energy. However, the presence of absorption edges in the multi-keV range complicates the otherwise predictable behaviour. Therefore, while the complex refractive index allows us to use a simplified picture similar to visible light optics, the better understanding of the optical properties requires a more detailed explanation.

### 2.1.1 Classical theory of dielectrics

Using the more detailed model for the classical theory of dielectric materials, one may assume that the medium is composed of tiny oscillating elemental dipoles (as described in detail in [63]). Then the interaction between electromagnetic radiation and matter can be regarded as an external perturbing potential to this existing system. When the electromagnetic wave travels through the medium, the electric field polarizes its atoms and their bound electrons, leading to the  $\vec{D} = \epsilon_0 \epsilon_r \vec{E}$  electric displacement as:

$$\vec{D} = \epsilon_0 \vec{E} + \vec{P} \quad (2.4)$$

The  $\vec{P}$  polarization density can be written as the sum of all elemental dipoles per each electron of each atom per unit volume, giving:

$$\vec{P} = \sum_a n_a p_a = \sum_a n_a \sum_{i=0}^{Z_a} p_{a,i} \quad (2.5)$$

One can assume, that for sufficiently low intensities, the  $\vec{P}$  polarization density is directly proportional to the inducing  $\vec{E}$  electric field:

$$\vec{P} = \epsilon_0 \chi \vec{E}. \quad (2.6)$$

Here,  $\chi = \frac{\vec{P}}{\epsilon_0 \vec{E}}$  is the dielectric susceptibility, transforming equation 2.4 into:

$$\vec{D} = \epsilon_0 \epsilon_r \vec{E} = \epsilon_0 (1 + \chi) \vec{E}. \quad (2.7)$$

The refractive index is the square root of the dielectric susceptibility:  $n = \sqrt{\epsilon_r} = \sqrt{1 + \chi}$ . In the ground state, each  $i$  electron of every  $a$  atom is a harmonic oscillator, that circulates around its nucleus with its corresponding  $\omega_0$  natural angular frequency and  $\gamma$  damping corresponding to the individual atomic or molecular energy levels:

$$\ddot{\vec{r}}_i + \gamma \dot{\vec{r}}_i + \omega_{0,i}^2 \vec{r}_i = 0 \quad (2.8)$$

This harmonic oscillator is perturbed by the  $E = E_0 e^{i\omega t}$  electric field of the incoming electromagnetic radiation, acting as an external force on the system. Therefore, the differential equation for forced oscillation becomes:

$$\ddot{\vec{r}}_i + \gamma \dot{\vec{r}}_i + \omega_{0,i}^2 \vec{r}_i = \frac{e \vec{E}_0}{m_e} e^{i\omega t} \quad (2.9)$$

The solution of this differential equation has the form of:

$$\vec{r}_i(t) = \frac{e \vec{E}_0}{m_e} \frac{e^{i\omega t}}{\omega_{0,i}^2 - \omega^2 + i\gamma\omega} \quad (2.10)$$

As an accelerating charge, the perturbed electron emits electromagnetic radiation. According to the Larmor formula, the emitted transverse electric field in  $\Theta$  angle from the acceleration direction is:

$$E_{\perp} = \frac{e \sin \Theta}{rc^2} \ddot{\vec{r}}_i(t) \quad (2.11)$$

Where  $\Theta = \pi/2$  in case of forward scattering. From this, the amplitude of the emitted radiation from the bound electron in a unit distance is:

$$A_i = \frac{e^2 E_0}{m_e c^2} \frac{\omega^2}{\omega_{0,i}^2 - \omega^2 + i\gamma\omega} \sin \Theta \quad (2.12)$$

The scattering amplitude from a free electron can be obtained by substituting the unbound electron as  $\omega_0 = 0$  and  $q = 0$ :

$$A_{free} = -\frac{e^2 E_0}{m_e c^2} \sin \Theta \quad (2.13)$$

The ratio of the scattering amplitudes gives us the  $f_i$  dipole scattering factor from the bound electron:

$$f_i = \frac{A_i}{A_{free}} = \frac{\omega^2}{\omega^2 - \omega_{0,i}^2 - i\gamma\omega} \quad (2.14)$$

This is a very important expression, which shows that the dipole scattering factor is independent from the direction of the scattering. It is also visible that the dipole scattering factor has an inherent wavelength dependence and is dominated by its imaginary part, when  $\omega(0, i) \sim \omega$ . Therefore we can separate the real and imaginary parts by denoting  $f = f' + if''$ , where:

$$f'_i = \frac{\omega^2(\omega^2 - \omega_{0,i}^2)}{(\omega_{0,i}^2 - \omega^2)^2 + \gamma^2\omega^2} \quad f''_i = \frac{\gamma\omega^3}{(\omega^2 - \omega_{0,i}^2)^2 + \gamma^2\omega^2} \quad (2.15)$$

The dipole scattering factor can also be expressed as a function of energy, using the  $E = \hbar\omega$  relationship, hence:

$$f_i = \frac{E^2}{E^2 - E_{0,i}^2 - i\gamma\hbar E} \quad (2.16)$$

If the energy of the electromagnetic radiation is far beyond the energy of the dipole ( $E \gg E_0$ ), the dipole scattering factor converges towards unity:  $f_i \simeq 1$ . This explains the weak chemical contrast in the X-ray range, as the incident photon energies are far above the energy of chemical bounds. As the energy range of X-rays corresponds to the deeper electron shells, the  $f_a = \sum_i^{Z_a} f_i$  atomic scattering factor is determined by elemental composition. The element-specific contrast changes drastically between below and after a resonance edge  $E_{0,i}$ , allowing element specific measurements. Moreover the exact fine-structure of the resonance edge contains information about the chemical state of the studied element.

From equation 2.10, the polarizability of atomic dipoles takes the form of:

$$\vec{p}_a = e \sum_i^{Z_a} \vec{r}_i = \vec{E}_0 \frac{e}{m_e \omega^2} f_a = \vec{E}_0 \frac{e\hbar^2}{m_e E^2} f_a \quad (2.17)$$

Therefore the total polarization density can be obtained by summing up all dipoles in a unit volume:

$$\vec{P} = \sum_a n_a p_a = \vec{E}_0 \frac{e^2}{m_e E^2} \sum_a n_a f_a \quad (2.18)$$

According to equation 2.6, the dielectric susceptibility of the medium is:

$$\chi = \frac{e^2 \hbar^2}{\epsilon_0 m_e E^2} \sum_a n_a f_a = n^2 - 1 \quad (2.19)$$

As the complex amplitude of the dielectric susceptibility is very small in the X-ray range, the refractive index can be expanded into its Taylor series, as:

$$n = \sqrt{1 + \chi} \simeq 1 + \frac{\chi}{2} = 1 - \frac{e^2 \hbar^2}{2\epsilon_0 m_e E^2} \sum_a n_a f_a(E) \quad (2.20)$$



Far away from the absorption edges, the above expression for the refractive index can be further simplified as:

$$n = 1 - \delta \simeq 1 - \frac{e^2 \hbar^2}{2\epsilon_0 m_e E^2} \sum_a n_a Z_a \quad (2.21)$$

This means, that the refractive index is higher for dense, high-Z materials like gold, iridium or tungsten, while it is low for light, low-Z elements like lithium, aluminium or silicon. It is also visible, that the refractive index decreases with the square of the increasing photon energy and that due to the above mentioned reasons, it is insensitive regarding the chemical composition (with the exception of the vicinity of absorption edges). But most importantly, the refractive index of materials in the hard X-ray range is directly related to their electron density.

## 2.2 Fresnel zone plates

Diffraction X-ray optics like Fresnel zone plates [59] are commonly used from the extreme UV to the hard X-ray range. Due to their compact dimensions, they can fill their role as a focusing device for micro- and nanoprobe experiments, as well as to work as objective lens for full-field X-ray microscopes. Due to their versatility, they have undergone a significant development in the past four decades, since their initial suggestion for X-ray nanofocusing[29]. This section is aimed to derive their relevant optical properties from their relationship with simple optical lenses and briefly describe issues related to their fabrication and applications.

### 2.2.1 Ideal lens

The focusing properties of a thin lens can be described as a phase shifter that images the wavefront in its object plane into its image plane. When using a point source in the object plane, its image will be another point in the image plane; this requires that the lens must provide the necessary phase shift to the incoming radiation of the point source to constructively interfere in the image plane (see Figure 2.1.). If the object is at  $d_s$  distance from the lens, its image is formed at a distance  $d_i$ , where  $d_s$  and  $d_i$  is connected to the  $f$  focal distance of the lens by the lens maker's equation:

$$\frac{1}{f} = \frac{1}{d_s} + \frac{1}{d_i} \quad (2.22)$$

The emitted radiation will arrive in the lens plane with its phase shifted according to its path length from the source to the lens. Thus at  $r$  distance from its optical axis, the

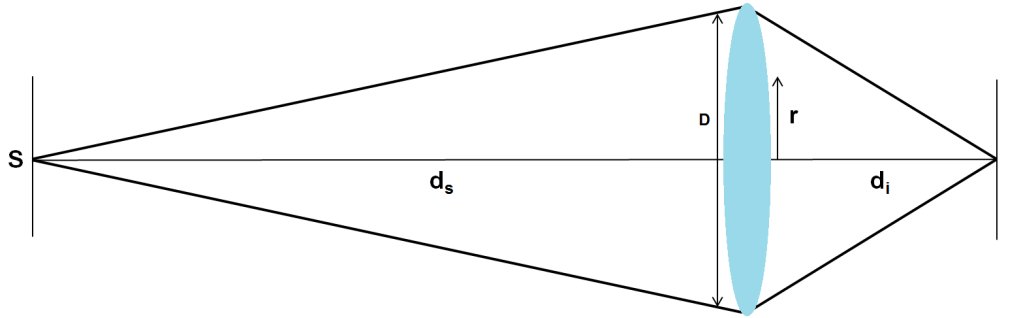


FIGURE 2.1: Working scheme of a thin ideal lens. The lens provides the required phase shift to the wavefront of the source to image it into its image plane.

phase of the incoming wavefront will be:

$$\phi_{inc}(r) = -\frac{2\pi}{\lambda} \left( \sqrt{d_s^2 + r^2} - d_s \right) = -\frac{2\pi}{\lambda} \left( d_s \sqrt{1 + \frac{r^2}{d_s^2}} - d_s \right) \quad (2.23)$$

In order to focus a wavefield into the focal spot, the focused radiation must arrive in the same phase to provide constructive interference in the focal spot. Therefore, the wavefront exiting the lens plane, must compensate for the geometric path length difference:

$$\phi_{out}(r) = \frac{2\pi}{\lambda} \left( d_i - \sqrt{d_i^2 + r^2} \right) = \frac{2\pi}{\lambda} \left( d_i - d_i \sqrt{1 + \frac{r^2}{d_i^2}} \right) \quad (2.24)$$

The phase difference between the incoming and outgoing wavefront is provided by the lens. Hence, the  $\Delta\phi(r) = \phi_{out}(r) - \phi_{inc}(r)$  phase shift of an ideal lens is:

$$\Delta\phi(r) = \frac{2\pi}{\lambda} \left( \frac{r^2}{2} \left( \frac{1}{d_s} + \frac{1}{d_i} \right) - \frac{r^4}{8} \left( \frac{1}{d_s^3} + \frac{1}{d_i^3} \right) + \frac{r^6}{16} \left( \frac{1}{d_s^5} + \frac{1}{d_i^5} \right) - \dots \right) \quad (2.25)$$

Using the lens maker's equation, the leading term can be separated from the higher order corrections, giving:

$$\Delta\phi(r) = \frac{2\pi r^2}{2f\lambda} + \frac{2\pi}{\lambda} \left( -\frac{r^4}{8} \left( \frac{1}{d_o^3} + \frac{1}{d_i^3} \right) + \frac{r^6}{16} \left( \frac{1}{d_o^5} + \frac{1}{d_i^5} \right) - \dots \right) \quad (2.26)$$

The leading term predicts a quadratic phase shift profile, while the lens radius  $R$  is relatively small ( $R \ll f$ ), originating the term: parabolic lens. Typical geometries at synchrotron light sources have the source placed very far away ( $d_o \gg f$ ), allowing the assumption of  $\frac{1}{d_o} \simeq 0$ ,  $f = d_i$ , and  $\phi_{inc}(r) = const$ . According to equation 2.24., this simplifies the lens profile into:

$$\Delta\phi(r) = \frac{2\pi}{\lambda} \left( \sqrt{f^2 + r^2} - f \right) = \frac{2\pi}{\lambda} \left( \frac{r^2}{2f} - \frac{r^4}{8f^3} + \frac{r^6}{16f^5} - \dots \right) \quad (2.27)$$

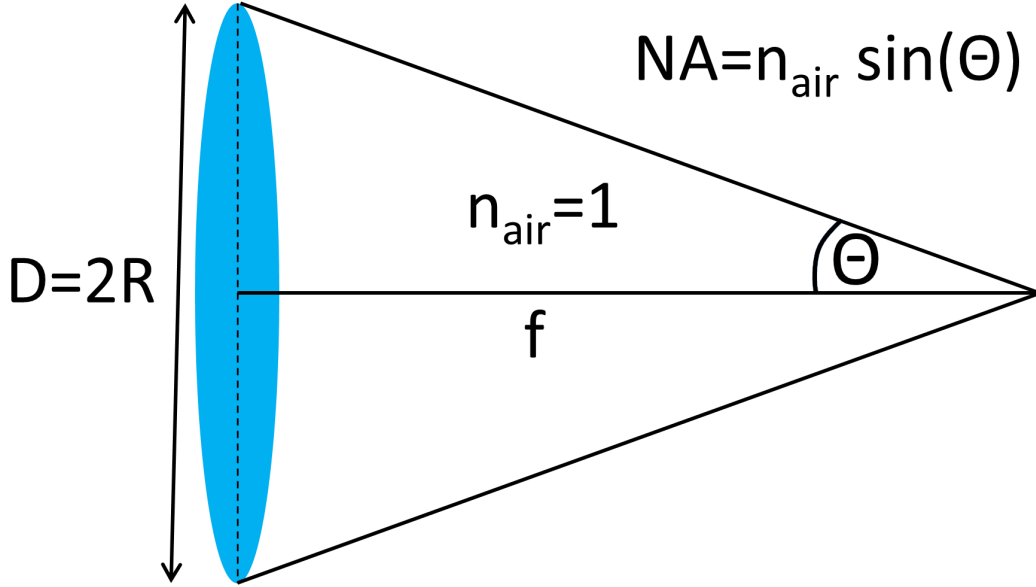


FIGURE 2.2: The resolution of an ideal lens is determined by the angle of incidence of the focused beam and the refractive index of the transmitting medium. The refractive index of air or vacuum is very close to unity and only becomes significant under special conditions.

### 2.2.2 Resolution of ideal lenses

In microscopy, the resolving power of an optical system is determined by the dimensionless number called numerical aperture (NA). The numerical aperture of a lens in the X-ray range can be obtained from the ratio of its focal length and radius, i.e. from its incidence angle  $\Theta$ , as illustrated in Figure 2.2:

$$NA = n \sin \Theta = \frac{R}{\sqrt{f^2 + R^2}} \simeq \frac{D}{2f} \quad (2.28)$$

The latter approximation is valid for small numerical apertures, that are common in the hard X-ray range.

The Rayleigh criterion was originally developed for telescopes and uses the Airy-pattern-like point spread function to determine the resolution of an optical system. It considers two point sources resolved, when the second source coincides with the first minima of the first source, corresponding to a 26.3% dip between the two peaks. The Rayleigh resolution limit of a microscope with numerical aperture  $NA$  is given as:

$$dr = \frac{1.22\lambda}{2NA} \simeq 1.22 \frac{\lambda f}{D} \quad (2.29)$$

While the Rayleigh resolution is a good starting point, one can easily deal with modulations smaller than 26.3%, allowing us to resolve even finer details. However, while the resolution determines the optical performance in the transverse direction, in the longitudinal direction it is limited by the depth of field (DoF). As the lens maker's equation

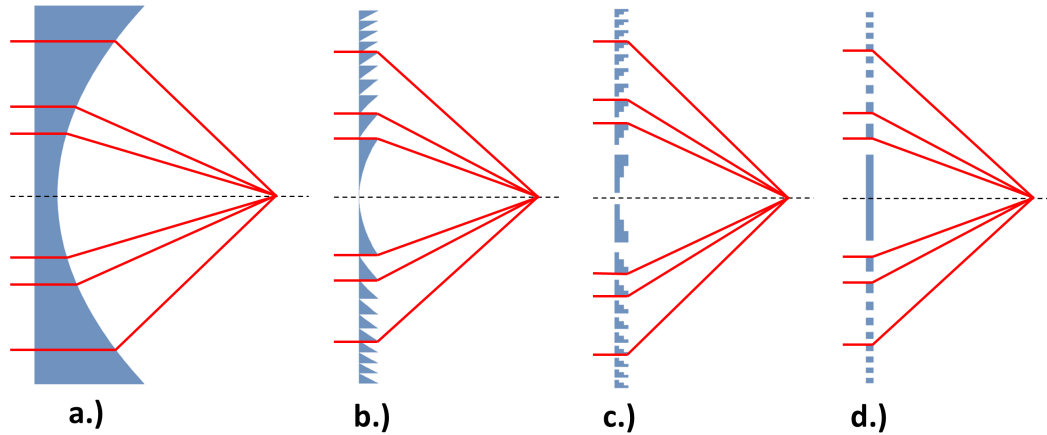


FIGURE 2.3: Towards lighter and more transparent lenses. By leaving out the bulk of the lens material while retaining the curvature the resultant Fresnel lens (b.) will retain the optical properties of the ideal lens (a.) using only a fraction of the lens material. Yet, since the blazed profile of the Fresnel lens is hard to produce with nanoscale structures, it can be approximated with a discrete number of steps (c.) with the binary zone plate being the most basic approximation (d.).

(Eq. 2.22) couples the distance of the detector plane to the sample plane, a deviation from this geometry results in degradation of the image quality. The tolerance range, where the degradation in image quality is considered to be negligible is the depth of field of an optical system:

$$DoF = \frac{\lambda n}{NA^2} \quad (2.30)$$

### 2.2.3 Fresnel zone plates as ideal lens

The ideal lens described in eq. 2.27 works fine in optical microscopy, where strongly phase shifting but transparent materials (such as glass) are available. However in the X-ray range, the refractive index of materials is slightly smaller than unity, requiring inverse lens profiles and the phase shift of materials is comparable to their absorption term. The latter leads to severe absorption losses for all but the lightest materials and inherently limits the effective aperture size.

Fortunately, the problem of thick lens material was already solved two hundred years ago in the optical range. Lighthouses were essential navigational guides in the early 19<sup>th</sup> century. Improving their brightness and fuel efficiency required the better utilization of their emitted light. Traditional bulk glass lenses with the required large apertures and short focal lengths were very large and extremely heavy. Augustin-Jean Fresnel realized that only the curvature of the lens participates in the focusing. This allowed him to separate the lens into several thin segments, while leaving out the bulk of the lens material to reduce its weight[64] (see Fig 2.3.b).

The same scheme can be adopted to X-rays, as the  $\phi$  phase of the electromagnetic radiation is not an absolute value, but is redundant according to  $2\pi$ . The above described

phase shift profile  $\Delta\phi(r)$  of an ideal lens can be wrapped modulo  $2\pi$  without any changes to the focusing properties:

$$\Delta\phi(r) = \frac{2\pi}{\lambda} \left( \sqrt{f^2 + r^2} - f \right) \text{ mod } \pi \quad (2.31)$$

As seen on Figure 2.3.c, this results in a sawtooth like phaseshift function between 0 and  $2\pi$  phase shift, eliminating absorption losses within the bulk lens material. The phaseshift of the lens jumps to zero, when it becomes a multiple of  $2\pi$ . Therefore the outer radius  $r_n$  of the  $n^{\text{th}}$  zone always corresponds to:

$$\Delta\phi(r) = \frac{2\pi}{\lambda} \left( \sqrt{f^2 + r_n^2} - f \right) = 2n\pi \quad (2.32)$$

This equation can be easily rewritten into the zone plate equation:

$$r_n^2 = 2n\lambda f + n^2\lambda^2 \quad (2.33)$$

This equation is the principal construction rule of Fresnel zone plates, determining the outer radius of the  $n^{\text{th}}$  ring of a zone plate with  $f$  focal length and  $\lambda$  photon energy. In case of X-ray Fresnel zone plates, the wavelength of electromagnetic radiation is so small, that the quadratic term becomes negligible, allowing the approximation  $r_n = \sqrt{2n\lambda f}$ . This predicts that the radius increases with the square-root of the zone number, while the pitch  $d_n$  of the zones decreases towards the zone plate edge as:

$$d_n = r_n - r_{n-1} = \sqrt{2n\lambda f} - \sqrt{2(n-1)\lambda f} = \sqrt{2n\lambda f} \left( 1 - \sqrt{1 - \frac{1}{n}} \right) \quad (2.34)$$

The total number of rings in a zone plate with  $D$  diameter is  $N = \frac{D^2}{8\lambda f}$  and its smallest pitch is  $d_N \simeq \frac{4\lambda f}{D}$ . For large zone numbers the change in pitch becomes small, allowing to locally approximate Fresnel zone plates as diffraction gratings. The diffraction angle from a grating with  $d_n$  pitch can be calculated from Bragg's law:

$$\lambda = 2d_n \sin \Theta \simeq 2\Delta d_N \frac{D}{2f} \quad (2.35)$$

By reordering this equation, we observe, that the  $f \simeq \frac{D\Delta d_N}{2\lambda}$  focal length of the zone plate is inversely proportional to the illuminating wavelength. This means that Fresnel zone plates are inherently chromatic optical elements.

#### 2.2.4 The resolution of Fresnel zone plates

The resolution of a zone plate can then be calculated from its numerical aperture  $NA \simeq \frac{D}{2f} = \frac{\lambda}{2d_N}$ , pointing out, that the resolution of Fresnel zone plates is on the order of their smallest half pitch  $d_N = \frac{\Delta r_N}{2}$ . Using the Rayleigh criterion as a benchmark, their

resolution can be expressed as:

$$dr = \frac{1.22\lambda}{2NA} = \frac{1.22\lambda 2f}{D} = 0.61\Delta r_N = 1.22d_N \quad (2.36)$$

It is visible, that the resolution is independent of the wavelength or the aperture size, in fact it is coupled to their smallest feature size. Therefore high resolution zone plate lenses require the fabrication of high resolution structures. Their working distance needs to be tailored via their diameter, resolution and the applied wavelength.

Similar to their resolution, their depth of field can be also expressed with their smallest zone width as:

$$DoF = \pm \frac{\lambda n}{2NA^2} = \pm \frac{2d_N^2}{\lambda} \quad (2.37)$$

This is identical for the Fraunhofer distance, the characteristic distance of the near-field. Hence the depth of field decreases quadratically with increasing resolution and increases towards the shorter wavelengths.

### 2.2.5 Fresnel zone plates in the X-ray range

Fresnel zone plates with no absorption and the ideal "sawtooth profile" are direct equivalents of thin optical lenses, focusing 100% of the incoming intensity into the focal spot. However, when one aims to take advantage of the resolution provided by X-rays, the smallest structures of the zone plate must match their intended resolution (Eq. 2.36). In practice, the fabrication of quasi-triangular structures with the required aspect ratios is unfeasible on the nano scale with existing methods. Most known nanofabrication processes are planar processes in terms that they pattern one layer at a time. Therefore, Fresnel zone plates in the X-ray range must approximate the ideal wrapped parabolic profile using a discrete number of steps.

The behaviour of zone plate lenses in the X-ray range was first described by Janos Kirz[29]. According to equation 2.34, the decrease of the pitch converges towards zero for large zone numbers, making Fresnel zone plates locally very similar to a periodic grating. A periodic grating diffracts the incoming light into discrete diffraction orders of both positive and negative orders. Hence Fresnel zone plates have several discrete diffraction orders, including focusing positive, the defocusing negative and the directly transmitted 0<sup>th</sup> orders. Therefore, Fresnel zone plates have a series of focal spots corresponding to each positive diffraction order in the fractional distances from the zone plate:

$$f_m = \frac{f_1}{m} \quad (2.38)$$

As the higher diffraction orders correspond to higher diffraction angles, they provide higher numerical aperture and hence resolution in their corresponding focal spot[65].

However the trade-of of using high order zone plates for imaging is focusing efficiency, i.e. the fraction of the illuminating intensity that is focused in the relevant diffraction order. The scattering amplitude of the  $m^{\text{th}}$  diffraction order equals to the amplitude of the corresponding Fourier component in the grating's  $T(\Theta)$  complex transmittance function:

$$A_m = A_0 \frac{1}{2\pi} \int_0^{2\pi} e^{ikT(\Theta)} e^{im\Theta} d\Theta = A_0 \frac{1}{2\pi} \int_0^{2\pi} e^{ikn_{\text{grat}}h(\Theta)} e^{im\Theta} d\Theta \quad (2.39)$$

Here,  $n_{\text{grat}}$  is the complex refractive index and  $h(\Theta)$  is the height profile of the grating material. As the intensity is the squared absolute value of the amplitude. From solving the above integral, we can see, that the efficiency of higher diffraction orders will be penalized by a  $\frac{1}{m^2}$  scaling term for rectangular zone profiles, meaning a quick degradation of efficiency towards higher orders. Changing the zone profile also alters the ratio of the diffraction orders, allowing one to tailor them to his specific needs.

Binary zone plates with rectangular profiles represent the most basic approximation of the blazed lens profile, as their fabrication only requires a single production step. Each period of the zone plate consist of a structure with  $T_{\text{phase}} = kh\delta$  phase shift and  $T_{\text{trans}} = kh\beta$  transmission. The fill factor, i.e. the fraction of the period covered by the phase shifting structure is also often called the duty cycle (DC). According to equation 2.39, the diffraction efficiency of a partially absorbing zone plate with  $\eta = \beta/\delta$  opacity in the  $m^{\text{th}}$  order is given by:

$$\frac{I_m}{I_0} = \frac{1}{m^2\pi^2} \sin^2(m\pi DC) (1 + e^{-2\eta\Phi} - 2e^{-\eta\Phi} \cos(m\Phi)) \quad (2.40)$$

As illustrated on Figure 2.4, the efficiency scales quadratically for small inaccuracies in phase shift and duty cycle, giving it a significant tolerance for fabrication uncertainties. A line to space ratio of 0.5 provides the best diffraction efficiency in the 1<sup>st</sup> order, in this case, the efficiency of even diffraction orders becomes zero. The efficiency of the zone plate also depends on the opacity of the material and favours the low absorption case ( $\eta \sim 0$ ) as seen on figure 2.5. In a phase zone plate, the focusing efficiency increases quadratically with small phase shifts and saturates when the phase shift of the zone plate corresponds to  $\pi$ . The optimal structure height seen on Figure 2.4 lies in the micron range in the multi-keV X-ray range, therefore the fabrication of efficient high resolution X-ray optics requires the production of high aspect ratio metallic nanostructures. Binary zone plates have symmetric positive and negative diffraction orders, thus 50% of the diffracted intensity is scattered into the defocusing negative orders. With additional light scattered into higher diffraction orders, the diffraction efficiency of binary zone plate with rectangular profile is fundamentally limited up to  $\frac{1}{\pi^2} \simeq 0.4053$ .

In order to improve the focusing efficiency of Fresnel zone plates beyond the fundamental limitations of binary zone plates, one must provide a better approximation

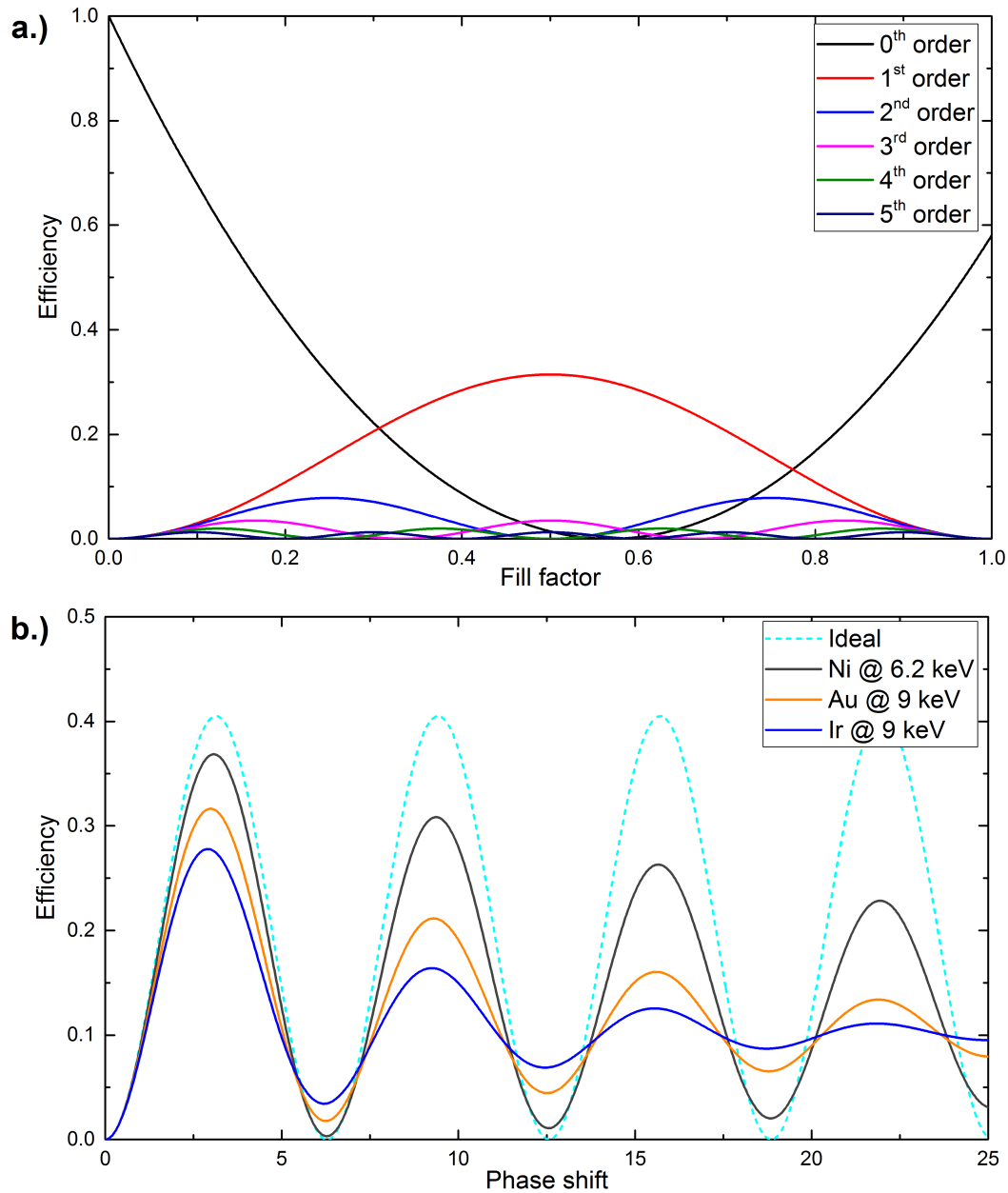


FIGURE 2.4: Calculated efficiency of ideal binary Fresnel zone plates with a rectangular zone profile in the most prominent diffraction orders. The efficiency in the first order is tolerant to small inaccuracies in the fill factor (a.), while the intensity of higher orders depends a lot on small variations during the fabrication process. The focusing efficiency of the primary diffraction order as a function of phase shift (b.). For small phase shift, the efficiency increases quadratically but it peaks around the height corresponding to  $\sim \pi$  phase shift. Higher orders reach their maximum at the exact same height as the first order.



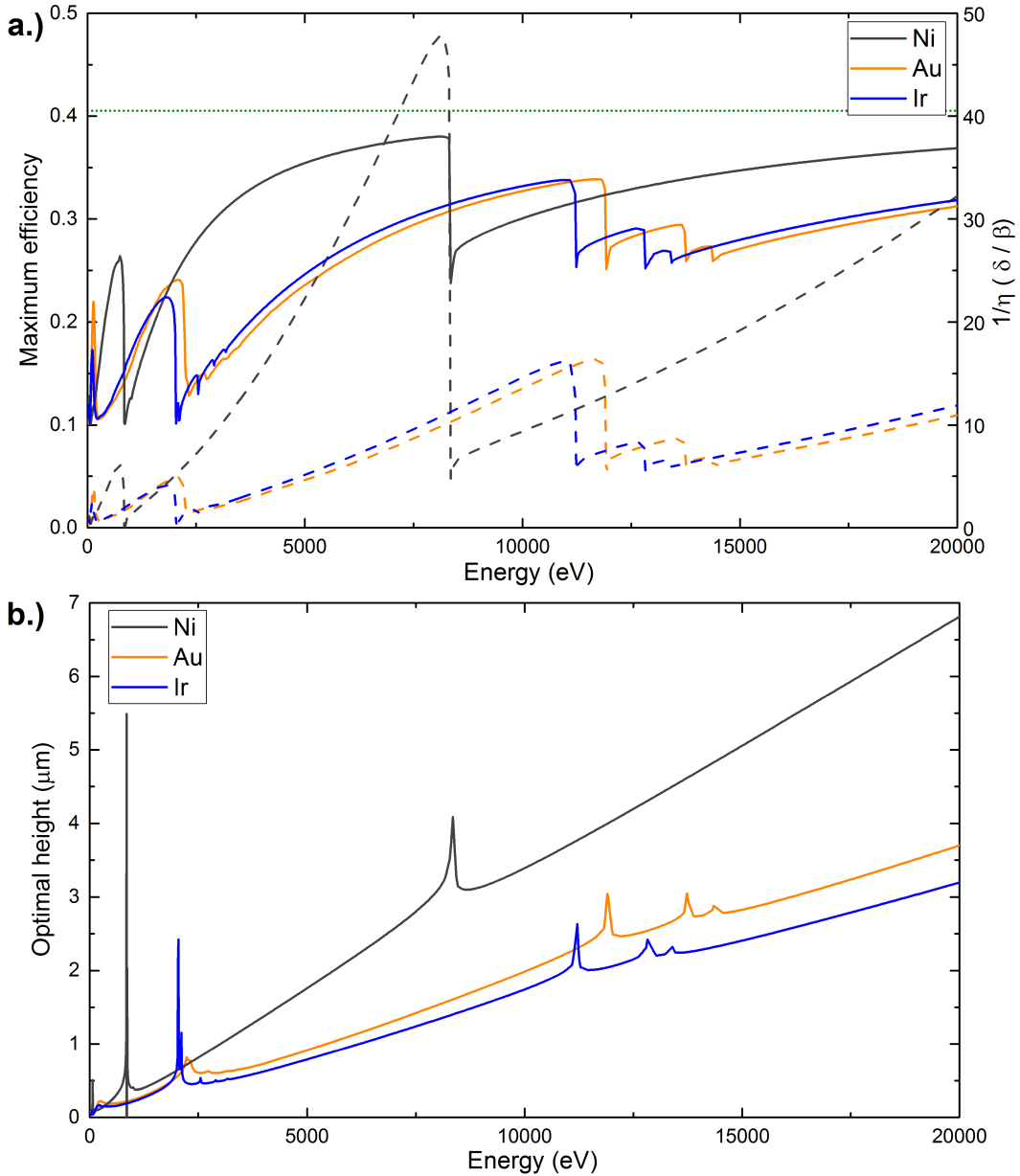


FIGURE 2.5: Calculated maximal efficiency (solid line) and transparency (dashed line) (a.) and the corresponding optimal structure height (b.) binary Fresnel zone plates with a rectangular zone profile. Absorption zone plates are limited to 10% efficiency but increasing transparency can improve the fundamental limit up to a factor of four. The absorption edges of the zone plate material reduce the transparency at particular energies, moving away from the absorption edges increases transparency and hence the possible efficiency. Apart from narrow variations at the resonant energies, the required optimal structure height increases linearly with the photon energy. Denser materials require shallower structures, while materials with different electron configuration benefit from the distinct placement of the resonance energies.

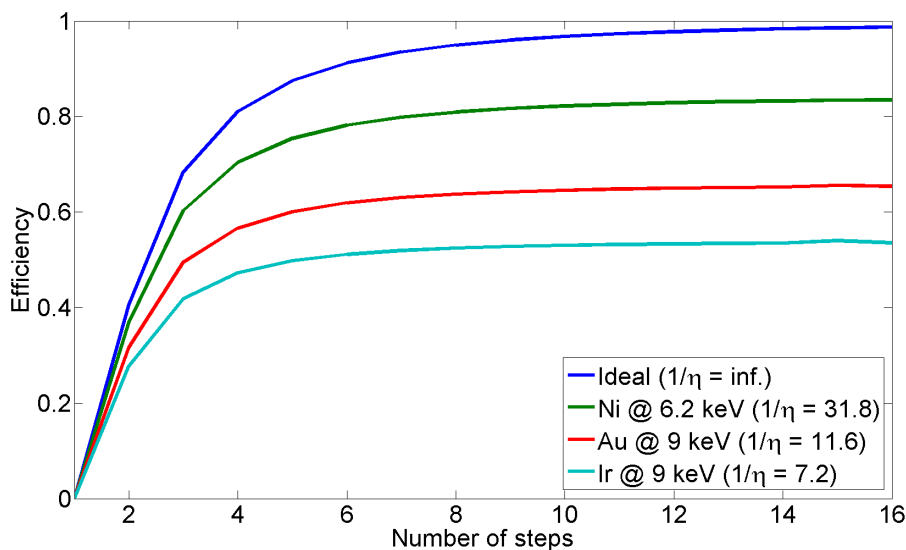


FIGURE 2.6: Fundamental efficiency limit of optimized multilevel Fresnel zone plates as a function of the number of steps. Going beyond the two-level "binary" approximation can provide massive benefits. However for large step numbers, the gain of additional levels becomes marginal.

of the blazed lens profile. Multilevel "blazed" structures break the symmetry of the focusing positive and the parasitic negative orders, hence can direct more light into the focusing positive diffraction orders. Absorption in the lens material requires the optimization of the zone profiles as described in [66]. Yet even with optimized profiles, higher absorption losses in the thicker lens material can greatly reduce the benefits of multilevel zone plates as seen in Figure 2.6. Phase shifting zone plates can clearly benefit more from the multilevel profile by directing more light in the primary focus. However while adding more steps to the optical transmittance profile will always increase the fundamental limit in zone plate efficiency, the incremental benefit of additional steps becomes marginal at large step numbers while fabrication complexity continues to increase with the number of steps.

When taking into account the dependence of the efficiency on the required structure height (from Figures 2.5 and 2.4) and of the resolution and working distance on the smallest zone width (from Equations 2.36 and 2.35) it becomes evident, that the production of high resolution, high efficiency or easy to use Fresnel zone plates requires the production of high aspect ratio nanostructures.

**The focusing efficiency of conventional binary Fresnel zone plate lenses in the hard X-ray range is limited. High resolution zoneplates suffer from the achievable aspect ratios, while their lower resolution counterparts are limited by the fundamental limitations of binary zone plates. Therefore, the efficiency of Fresnel zone plates can be improved either by the increasing structure height or by the patterning of multilevel structures.**

### 2.2.6 Fabrication of Fresnel zone plates

Since the initial proposal of using zone plates for X-ray focusing [29], Fresnel zone plates have been popular X-ray optics in the EUV and X-ray range and have undergone significant development in the past decades. The earliest Fresnel zone plates for X-ray nanofocusing were patterned by optical holography into a polymer photoresist layer[30, 33, 34], however this fabrication method fundamentally limited their achievable resolution. Shortly afterwards, electron beam lithography (EBL) opened new frontiers in the fabrication of high resolution zone plates[35, 67].

#### 2.2.6.1 High resolution zone plates

Thanks to the introduction of electron beam lithography for zone plate patterning, as early as 1992, already 30 nm resolution was demonstrated in the soft X-ray range[36, 68] using plasma based pattern transfer procedures. But the transition towards higher energies demanded a drastic increase in structure heights adding the patterning of high aspect ratio nanostructures to the focus of zone plate fabrication for the multi-keV and hard X-ray range. High energy electron beam writing tools greatly simplified the zone plate fabrication process, allowing the direct writing of zone plates to improve their resolution[69, 70] or efficiency[71]. Since the patterned resist templates had to be transferred into heavy metals, gold or nickel electroplating became popular methods for pattern transfer[70, 72].

As electroplating of very small, high aspect ratio structures becomes increasingly challenging, zone doubling, i.e. pattern transfer via the conformal metal coating of a high aspect ratio template was developed as a dedicated procedure for the fabrication of ultra high resolution of zone plates[73, 74]. Other methods employed reactive ion etching as pattern transfer procedure for producing zone plates on tungsten [75, 76] or tantalum[77] coated substrates.

As direct electron beam writing based methods quickly filled their headroom for improvement, indirect patterning fabrication methods have also gained considerable attention. The conformal coating of wires can provide impressive numbers[78] and severe aberrations in the sub-10 micron (annular) aperture range. Emerging advanced etching techniques, like metal assisted deep chemical etching [79] also have great potential for high efficiency X-ray optics in the hard X-ray range. However no information is available on their actual optical performance.

#### 2.2.6.2 Multilevel zone plates

While the resolution of Fresnel zone plates has been subjected to constant developments, certain applications do not require extreme resolution, but they would profit

from high focusing efficiency. KB mirrors are widespread instruments for high efficiency focusing. However, due to their large size, difficulty of alignment and tighter stability requirements, they are difficult to integrate in a flexible experimental setup. With the improving fabrication possibilities of Fresnel zone plates, the fundamental limitations by the parasitic orders of binary zone plates became a major limiting factor in focusing efficiency. Therefore multilevel zone plates were developed to produce a better approximation to the ideal blazed profile and free zone plates from their fundamental limitations (see Figure 2.6).

The first multilevel zone plates in the X-ray range were demonstrated by the group of Enzo Di Fabrizio [71], by fabricating three levels on top of each other to produce four-level zone plates. Having 1 micron smallest half pitch, these zone plates were able to achieve 55% diffraction efficiency, which is clearly beyond the capabilities of binary zone plates. Inspired by these results, linear Fresnel zone plate plates up to 65% efficiency have been later demonstrated using the plasma etching of silicon[80]. Similarly to e-beam written structures, multilayer deposition on rotating wires have also demonstrated over 50% focusing efficiency in the hard X-ray to the gamma range (20-200 keV) with essentially unlimited aspect ratios[81–83]. But their low optical quality due to surface roughness and their limited aperture size have so far prevented their wider adoption.

The lack of high efficiency blazed zone plates with smallest half pitch below 500 nm clearly shows the difficulties that arise when reducing structure size. The fabrication of several overlaid layers requires high overlay accuracy and fabrication errors in the underlying layers propagate through the upcoming levels. This puts an extra emphasis on process reliability instead of pushing the limits of nanofabrication. In the soft X-ray range, where required structure heights are lower the benefits of multilevel zone plates are negated by the high absorption losses within the zone plate material.

### 2.2.7 The stacking of zone plates

Lithography has its own limits and one can spend endless efforts for pushing them. Various approaches are known for the production of dense high aspect ratio nanostructures, required for zone plate fabrication. However, eventually they all face the compromise between resolution and efficiency. Hence instead of pushing the limits of nanofabrication methods, the stacking of zone plates aims to improve their performance while staying within the possibilities of existing nanofabrication methods. If we stack two separate zone plates in each other's near field –within a fraction of the  $d_F = dr_N^2/\lambda$  Fraunhofer-distance[84]– they will act as a single zone plate with combined optical transmission

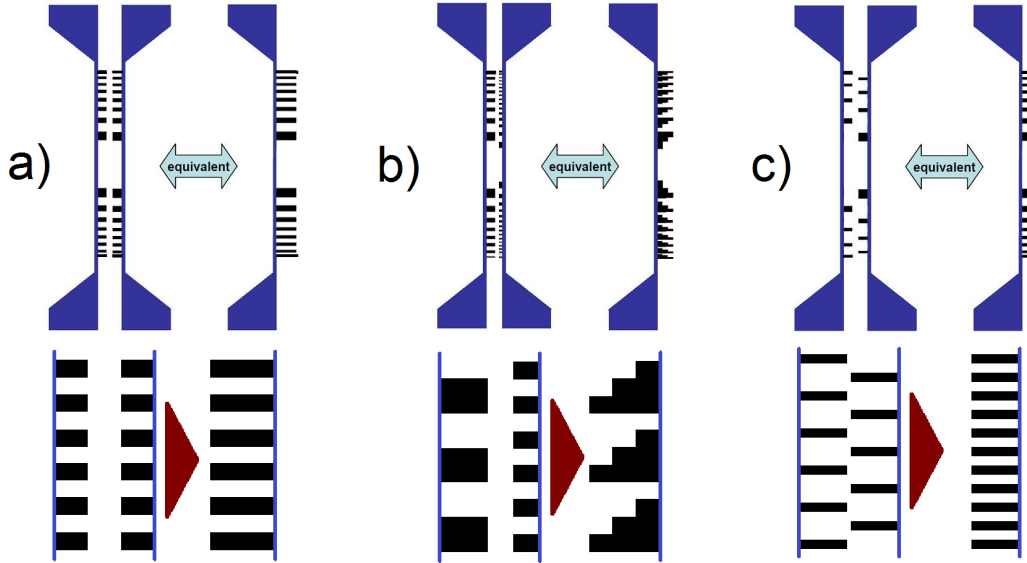


FIGURE 2.7: The zone plate stacking schemes as described in the literature: a.) Stacking two identical zone plates to increase structure height. b.) Stacking a coarse zone plate with  $\pi$  phase shift and a fine zone plate with  $\pi/2$  phase shift to create an effective blazed profile. c.) The interlaced stacking of zone plates to double the line density of high resolution zone plates.

profile[85]. The two zone plates are patterned individually, using the established fabrication methods for binary zone plates. Amongst the various combinations so far only three methods could prove their practical use:

- Stacking of identical zone plates: By stacking two identical binary zone plates, one can add up the effective structure height of the zones. According to Figure 2.5.b, doubled structure height can provide up to a factor of four gain in efficiency, especially in the case of high resolution zone plates or at high photon energies[85]. (Figure 2.7.a)
- Blazed stacking of zone plates: By stacking two complementary binary zone plates, a "coarse" zone plate with  $\pi$  phase shift and a double density "fine" zone plate with  $\pi/2$  phase shift, one can obtain an effective four level blazed transmission profile. This offers to surpass the fundamental limit of binary zone plates without the actual patterning of multilevel structures[86]. (Figure 2.7.b)
- Interlaced stacking of zone plates: Unlike the previous stacking schemes, that employ stacking to increase efficiency, the aim of the interlaced stacking of zone plates is to improve their resolution. By stacking two complementary, deliberately shifted zone plates in each other's optical near-field one can double their effective line density. This enables to provide increased resolution while patterning only relatively coarse, easy to make structures[87, 88]. (Figure 2.7.c)

The major challenge in zone plate stacking lies in maintaining the proper alignment of the stack. As both calculations[89] and simulations (seen in Appendix B) show that the required alignment accuracy between the two zone plates in the stack is approximately 1/3 of the smallest zone width, which can be in the sub-10 nm range for high resolution zone plates. In early experiments of zone plate stacking, the precise alignment of the two zone plates required the use of a complex mechanical setup for alignment. Such a setup greatly complicates the use of stacked Fresnel zone plates and compromise their stability due to thermal or non-thermal drifts, making them difficult to use. Yet, the massive performance gains of stacking prompted several groups[75, 90] to permanently glue together stacks of Fresnel zone plates, to provide their benefits in a permanently fixed, monolithic setup. In order to achieve sufficient alignment accuracy, the zone plates were aligned and glued while verifying their alignment within an X-ray beam. However, the release of stress and chemical or structural changes in the glue can lead to a small but non-negligible shift between the two zone plates both during and even after the gluing process, compromising their long term stability. Nevertheless, despite its obvious issues the stacking of zone plates became a commercialized technique due to its benefits at high photon energies.

### 2.2.8 Beyond the planar approximation

While the above discussion represents an accurate description of most zone plates working in the hard X-ray range, it is often insufficient for the description of diffractive optics at lower energies. The planar diffraction theory seen in Eq. 2.39 assumes that optical elements can be described with their optical transfer profile, that can be easily calculated from their structure height. If the wavefront is subjected to noticeable changes by diffraction already within the diffracting structures, the above approximation becomes invalid. In other words, if the thickness of the zone plate becomes comparable to its Fraunhofer distance  $d_F = 2dr_N^2/\lambda$ , its exact description will require taking volumetric effects into account. This is particularly noticeable in zone plate stacking, as determining an upper limit on stacking distance[84] and ultra-high resolution zone plates working in the soft X-ray range requiring tilted zones for optimal performance [65, 91–93]. Due to the shorter wavelength, near-field effects are generally negligible in the hard X-ray range, yet Chapter 7 will discuss an exceptional case.

### 2.2.9 Other diffractive optical elements

While Fresnel zone plates and diffraction gratings are the most widely used diffractive optical elements, diffractive optics are not limited to a single layout. Electron beam lithography allows the patterning of arbitrary patterns, enabling one to tailor their optical properties to specific purposes. These optical elements employ similar theoretical

and fabrication background as Fresnel zone plates and benefit from the developments in their fabrication. Some examples include:

- **Diffraction gratings:** Simple periodic or chirped gratings are widely used in optics in all energy range. They are in fact so versatile, that their discussion goes beyond the scope of a single paragraph.
- **Beamshapers:** Beamshapers are commonly used condenser optics to provide a uniformly illuminated area or structured illumination for full-field X-ray microscopy. They consist of periodic segments, where the period of each segment is determined by the zone plate equation (eq. 2.33) at its centre ( see Fig. 2.8). This results in an evenly illuminated focal area of equal size as the segments, providing a large and evenly illuminated field of view up to hundreds of microns[94].
- **Linear zone plates:** One dimensionally focusing Fresnel zone plates can be tailored for the coherence length of the beamline as well as to change their effective structure height by tilting[95].
- **Extended depth of field (eDOF) lenses:** Encoding certain aberrations within the lens profile can lead to an increase in the focal depth at the cost of contrast. The known point spread function of the aberrated lens can be later deconvolved to enhance image quality[96].
- **Twin spot zone plates:** Twin spot zone plates focus the incoming illumination in two focal spot in each other's close vicinity. This results in differential interference-based phase contrast in the offset direction in the recorded micrographs, increasing their sensitivity to low-contrast biological specimens[97, 98].
- **Spiral zone plates:** Twin spot zone plates provide phase contrast in one particular direction. Spiral zone plates extend the differential interference contrast to two directions, providing edge enhancement in the recorded micrographs[99, 100].

## 2.3 Simulation of diffractive optics

The past decade has been a vibrant scene in the IT industry. Available computational resources have been multiplied in the recent years, allowing higher computational performance in a present day desktop, than the world's fastest supercomputer 15 years ago<sup>1</sup>. While most other aspects of science became more expensive, computing performance became cheaper.

---

<sup>1</sup>The peak performance of the ASCI Red supercomputer equalled 2.38 TFLOPS in the year 2000, while in early 2015, the AMD FirePro S9150 professional GPU can provide 2.53 TFLOPS double precision performance and even consumer GPUs break 1 TFLOPS.

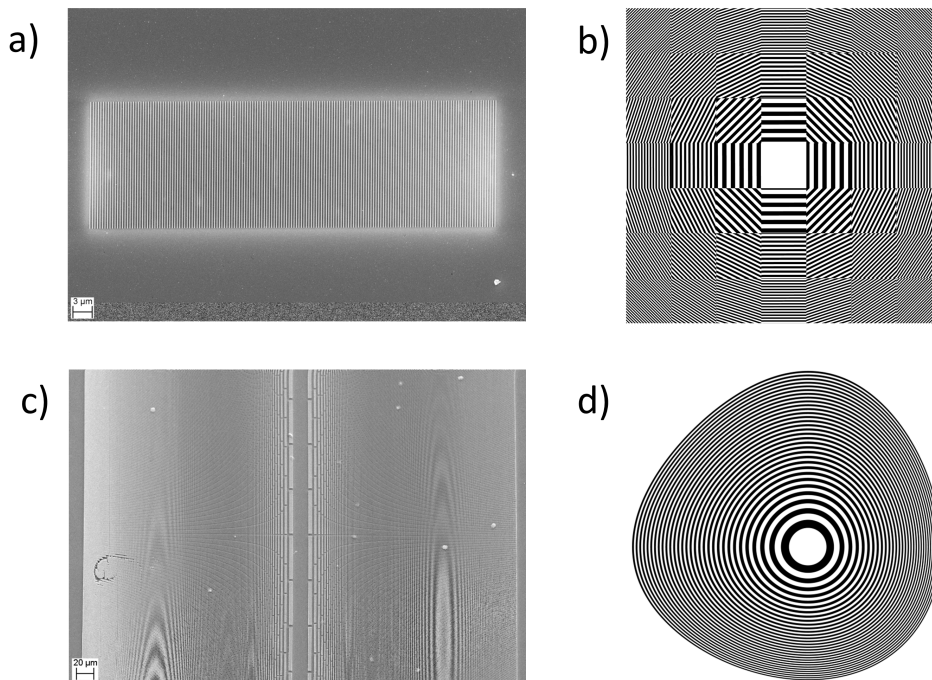


FIGURE 2.8: Examples of other diffractive optical elements, that employ similar conceptual and production background as Fresnel zone plates. a.) Diffraction gratings are amongst the most widespread optical elements. b.) Beamshapers to provide uniform illumination for full-field X-ray microscopy. c.) Linear zone plates that provide one dimensional focusing. d.) Extended depth of field lenses to combat depth of field limitations towards high resolutions.

Analytical description of nearly ideal Fresnel zone plates in the X-ray range has been available for over four decades[29], providing detailed understanding of their basic mechanisms. However for more exotic optical schemes[73, 74, 85, 94] analytical solution is practically impossible. In these cases, numerical methods can fill the gap and provide accurate description for more generalized cases. Simulating diffractive X-ray optics is available to model complex optical systems well before fabricating and testing them with X-rays. Simulations can provide both qualitative and quantitative description of an optical system as a function of a wide range of parameters.

Several methods have been described in the literature for the simulation of X-ray optics, with each method constrained by the possibilities of its age. The rigorous coupled wave method[85] has been successfully employed as the simple, one dimensional description of periodic diffraction gratings. It has been widely employed for the simulation of volumetric[88] and near-field effects in optically thick systems, including the effects of tilted zones[65, 91] and side wall roughness[101]. The available methods were soon extended by the Leontovich-Fock approximation of wave propagation to describe the propagation of arbitrary patterns [102, 103]. With the increase of available computing



power, the next generation of simulations were no longer restricted to approximations but were prepared to handle objects with radial symmetry by employing the Hankel transform[84]. This allowed more realistic modelling of near-field conditions of stacked Fresnel zone plates[84], consisting of structures with a broad spectrum of spatial frequencies. In the recent years, the two dimensional propagation of wavefields became a standard procedure, thanks to the spread of coherent imaging techniques. With the appearance of TFLOPS scale commercial accelerators, the available computing power made another jump. Thus with present day computational resources, the propagation of an arbitrary wavefield can be calculated according to methods detailed in the literature[104, 105].

Assuming that the light's propagation along the Z-axis any optical element can be described by its  $O_l(x, y) = A(x, y)e^{i\Phi(x, y)}$  planar optical transmittance profile perpendicular to this direction. The transmittance profile is a complex quantity, that represent both the absorption and the phase shift inflicted by the object on the illuminating wavefield. For example, the transmittance profile of a lens is its phase shift profile:

$$O(x, y) = e^{\frac{ik}{2f}(x^2+y^2)} \quad (2.41)$$

For a realistic material with  $n = \delta + i\beta$  refractive index and  $H_z(x, y)$  thickness along the propagation direction, the transmittance function becomes:

$$O(x, y) = e^{iknH_z(x, y)} = e^{-k\beta H_z(x, y)} e^{ik\delta H_z(x, y)} \quad (2.42)$$

This object transmittance function is illuminated by  $A_{in}(x, y)$  incoming complex wavefield, so that the resultant outgoing wavefield will be:

$$A_{out}(x, y) = A_{in}(x, y)O(x, y) \quad (2.43)$$

As the wavefield is sampled on a Cartesian grid, with  $\Delta x = \Delta y$  step size, this denotes the element-wise product of two complex arrays. Normally one layer corresponds to one optically thin optical element or plane of interest. Optically thick objects are described consisting of several layers by themselves. The propagation of light between two planes can be expressed in Fourier space using a propagator. One of the following two propagators can describe almost any experimental geometry:

- Fraunhofer propagator i.e. far-field diffraction can be expressed as a simple Fourier transform, transforming the initial real-space wavefield into its reciprocal space counterpart. However, the scale of the propagated diffraction pattern changes. Depending on the projection distance  $\Delta Z$  and the number of pixels  $N$ , the pixel size  $\Delta x$  will change according to:  $\Delta x_f = \frac{\lambda \Delta Z}{N \Delta x_i}$ . The latter makes it particularly well-suited for large propagation distances.

- Angular spectrum method: the angular spectrum method aims to express the  $\vec{k} = (k_x, k_y, k_z)$  wave vector in the propagation direction from its in-plane components as  $k_z = |k| \sqrt{1 - k_x^2/k^2 - k_y^2/k^2}$ . Therefore, the calculation of the angular spectrum proceeds as:

- Calculating the Fourier transform of the real space wavefield:

$$A(q_x, q_y)_i = \mathcal{F}(A(x, y)_i) \quad (2.44)$$

- Multiplying the reciprocal space wavefield with a propagator:

$$A(q_x, q_y)_f = A(q_x, q_y)_i e^{ikZ \sqrt{1 - \lambda^2 q_x^2 - \lambda^2 q_y^2}} \quad (2.45)$$

- Calculate the inverse Fourier transform to obtain the final, real space wavefield in the final plane:

$$A(x, y)_f = \mathcal{F}^{-\infty}(A(q_x, q_y)_f) \quad (2.46)$$

The angular spectrum propagator maintains the pixel size and is an exact solution of the Helmholtz equation. Therefore is better suited for the short-distance or near-field propagation where the propagated patterns are not influenced by the periodic boundary condition.

While the exact implementation of the models may vary, it must be noted that the accurate simulation of X-ray optics can be computationally expensive. The sufficiently high resolution sampling of large areas requires a considerable amount of memory, and the calculation of the Fourier transform scales extensively with the number of points. On the other hand, the Fast Fourier Transform (FFT)[106, 107] of large areas can be effectively segmented and calculated on parallel architectures such as GPUs.

## 2.4 Imaging with X-rays

Our brain has an obvious expertise in apprehending visual data, making micrographs a natural way of information input. Microscopy in the visible light range has particular sensitivity to colours induced by chemical bonds and valence electron configuration but has limited resolution or high complexity. Electron microscopy employs different interactions using electron density contrast for image formation and can provide ultimate resolution, but only from a very thin layer of the specimen. X-ray microscopy takes the middle ground by offering resolution between conventional optical and electron microscopy together with the possibility of using thick specimens and not limiting the sensitivity to particular structures. With several established microscopy techniques, X-ray metrology offers practical applications for sample characterization.

### 2.4.1 Full-field X-ray microscopy

The full-field X-ray microscope[30] is the direct X-ray analogue of the optical microscope, employing the same basic scheme as in visible light optics. Due to the relatively low efficiency of X-ray optics, the optical scheme is simplified to minimize the number of optical elements, leaving us with a minimalistic design as seen in Figure 2.9. The key part of the experimental setup is the objective lens, that produces a magnified real-space image of the sample plane in the detector plane. Using an additional condenser for illumination not only makes a better use of the illuminating flux by concentrating it to the studied area, but also increases the highest possible resolution. The ultimate resolution of full-field microscopes is limited by the numerical aperture of the optical system[108], i.e. the highest spatial frequencies that are captured by the objective lens:

$$dr = \frac{1.22\lambda}{(NA_{cond} + NA_{obj})} \quad (2.47)$$

In practice the actual resolution of full-field X-ray microscopes is more determined by the achieved contrast. Hence the exact optical transfer function of the system is more important, than its fundamental capabilities. The magnification of the full field microscope depends on its geometry and obeys the  $M = d_{img}/d_{sam}$  law. Here the image and sample planes are determined from the lens maker's equation (2.22) as:

$$\frac{1}{f_{obj}} = \frac{1}{d_{sam}} + \frac{1}{d_{img}} \quad (2.48)$$

The practical implementation of full-field X-ray microscopes generally employ a zone plate[30], capillary[109] or beamshaping[94] condenser. Most X-ray microscopy setups employ a zone plate as their objective lens. This brings us to the problem of efficiency: while the full beam of the condenser illuminates the sample, only a fraction of it actually contributes to the image formation. Without condenser, the 0<sup>th</sup> order of the zone plate directly hits the detector, drowning the relatively faint magnified image of the specimen. With the centre of the condenser blocked by a central stop, a clean-up pinhole can block the direct beam while transmitting the functional illumination. Matching the numerical aperture of the objective and the condenser can allow higher resolution[110] or a customized OTF for particular frequency ranges[111]. High resolution CCD or CMOS cameras are commonly employed as detectors, with their resolution and sensitivity to X-rays increased by scintillator screen and optical pre-magnification.

The basic contrast mechanism in full-field microscopy is absorption contrast, which is sufficient in the soft X-ray range or for high-Z materials in the hard X-ray range, but provides low contrast for organic materials in the hard X-ray range. However, similarly to optical microscopy, full-field X-ray microscopy can provide Zernike

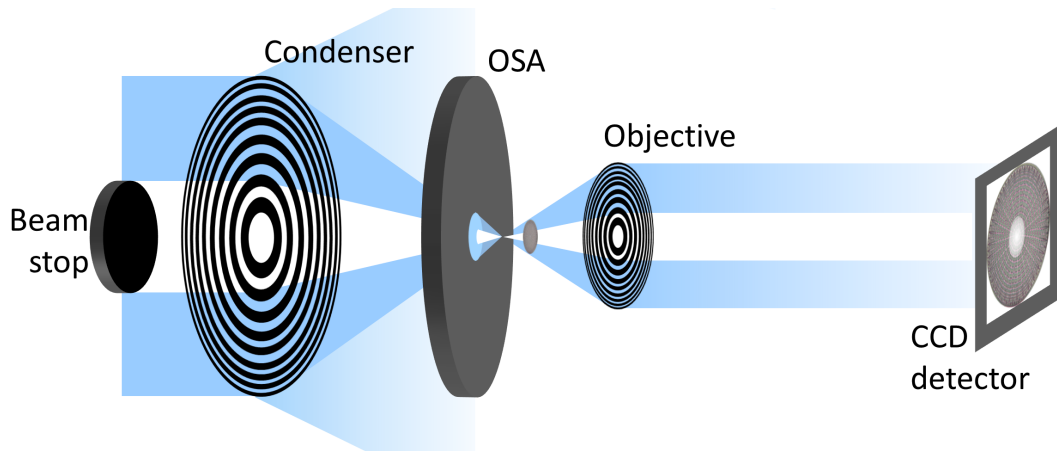


FIGURE 2.9: The basic experimental setup for full-field transmission X-ray microscopy. A condenser focuses the incoming radiation on the translucent specimen. The scattered intensity from the specimen is collected by the objective, that projects the magnified image of the specimen on the detector.

phase contrast by placing a phase shifter in the back focal plane of the objective[112–114].

Due to the image forming mechanism, full field microscopy probes the whole targeted area of the sample at the same time. Its high speed makes it particularly well-suited for tomography[115]. Due to issues regarding the depth of field, high resolution generally rules out large field of view, hence the optical setup must be fitted to the experimental requirements. For many applications, that do not need extreme resolution, parallel beam or cone beam micro-CTs can provide sufficient information even without the use of magnifying optics.

#### 2.4.2 Scanning probe X-ray microscopy

Scanning probe microscopy aims to provide spatially resolved images of a sample by raster scanning a confined probe on the specimen to locally test its properties. When it comes to imaging thick specimens, the large penetration depth of X-rays provide a decisive advantage by using a focused X-ray beam for the local probing of the specimen. Scanning X-ray microscopy employs the basic optical setup as seen on Figure 2.10, with one condenser focusing the incoming X-ray beam into a well confined, micro- to nanometre sized spot. Unlike in full field microscopy, the resolution of scanning probe microscopy has no fundamental limit and is only a matter of step size, stability, contrast and signal to noise ratio. The beam can be focused by KB mirrors, zone plates or refractive lenses. Depending on the experimental setup and especially on the detector, up-to three contrast mechanisms can be recorded simultaneously:

- Scanning transmission X-ray microscopy (STXM): Records the transmitted X-ray signal from the sample on a detector. Using a segmented detector, contrast

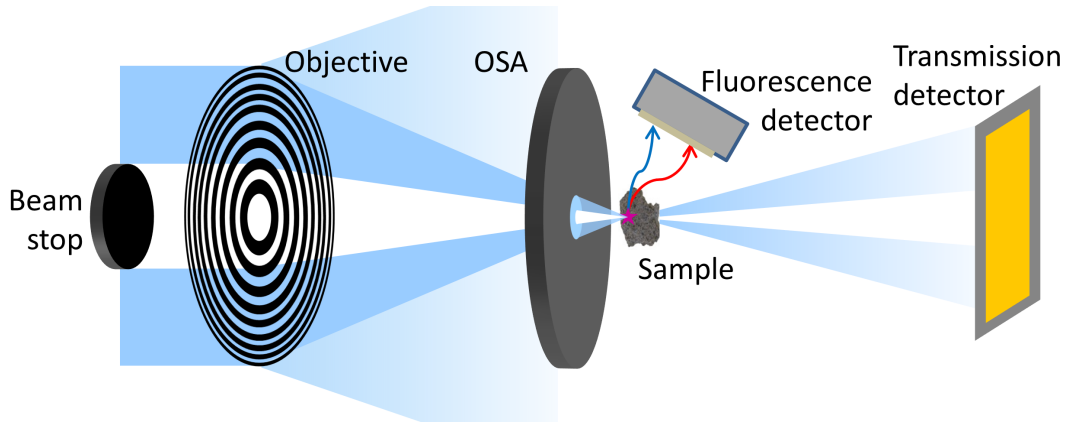


FIGURE 2.10: The basic experimental setup for scanning probe X-ray microscopy. A condenser focuses the incoming radiation into a tight spot on the specimen that is being scanned in the focal plane. Both the transmitted signal and the fluorescence signal can be collected. Even opaque specimens can be studied via X-ray fluorescence.

mechanisms include absorption contrast, differential phase contrast and dark-field signal[31, 116, 117].

- Scanning fluorescence microscopy: The localized probe excites the atoms of the sample that emit characteristic X-ray radiation. By measuring the emitted fluorescence with an energy dispersive detector, one can record a quantitative elemental composition map of the sample[118].
- Scanning small angle X-ray scattering: This further developed STXM concept records the far-field diffraction pattern of the sample on a pixel detector[119, 120]. Using the spatial filtering of the recorded diffraction patterns can reveal additional information about the size, distribution and orientation of particles or macromolecules within the sample. If the sample is placed out of focus of the illuminating optics, the diffraction pattern will also include a magnified hologram of the examined area.

The typical resolution of scanning X-ray microscopes depends upon application and ranges from microprobes to the 10 nanometre range. However high resolution generally rules out large field of view. Unlike in full-field microscopy, most scanning probe microscopy techniques measure only one point at a time. High-end scanning setups can measure hundreds of points per second. In comparison, a full-field X-ray microscope can record a  $4k \times 4k$  image within the same time. Fluorescence mapping can further constrain the scan speed by the intensity of the desired signal (i.e. trace element analysis). The recent years brought several breakthroughs in the interpretation of holograms, that offer the super-sampling of the traditional STXM signals, with the most promising candidate being ptychography.

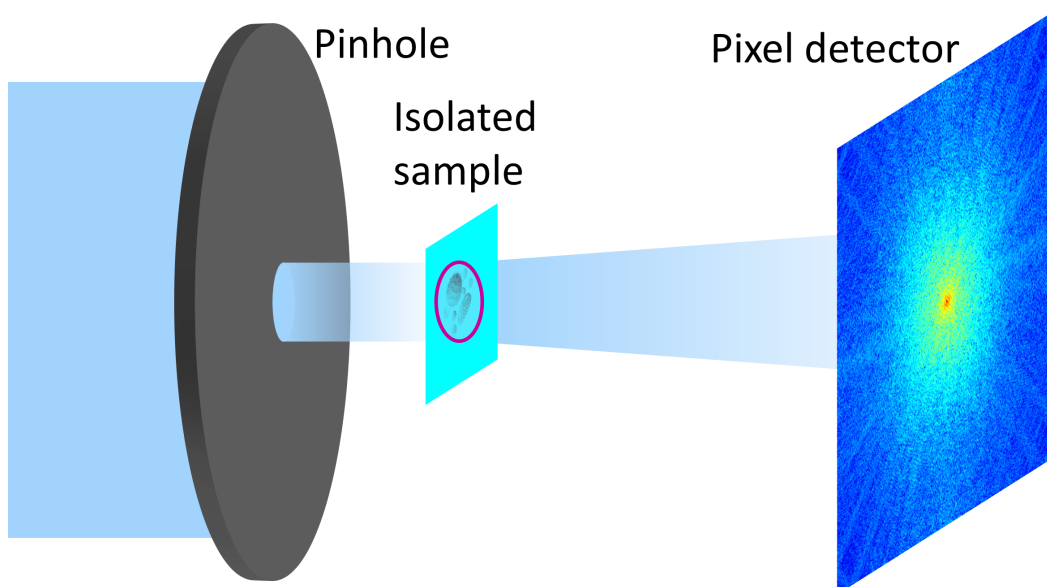


FIGURE 2.11: Experimental setup for coherent diffraction imaging. The sample is illuminated through a pinhole to provide a sharply-defined, confined illumination. The reconstructions can be then calculated from a single diffraction pattern.

### 2.4.3 Coherent diffractive imaging

Ever since the far-field approximation of the Kirchhoff-integral[121], it is widely known that recorded far-field diffraction patterns correspond to the Fourier transform of the originating wavefield. However with today's detectors, the phase of the electromagnetic wavefield is lost during the detection process, this is known as the phase problem. It prevents the straightforward recalculation of the sample-plane wavefront, yet if the lost phase is recovered, one can recalculate a high resolution image of the object. While the simplest solution to the phase problem is using an objective lens, it inherently limits the captured spatial frequencies and hence resolution beside having potentially low focusing efficiency as in the X-ray case.

The phase problem is a major challenge in X-ray science as diffraction patterns with spatial frequencies corresponding to a fraction of a nanometre can be easily recorded, while real-space imaging lags orders of magnitudes behind. While holography[122, 123] also offers a solution to the phase problem, it requires the help of a well-characterized reference illumination enforcing strong sample constraints.

The development of iterative phase retrieval algorithms[26, 27] provided scientists with powerful tools facilitating wavefield retrieval from a single far-field diffraction pattern. Starting from an initial guess, iterative algorithms alternate between the sample and detector plane while applying both real space and Fourier space constraints. The latter generally covers an opaque frame in the sample plane and the measured amplitudes in the detector plane according to the simplified figure of 2.12. Its introduction to X-ray microscopy[124] offered several key advantages over conventional optics

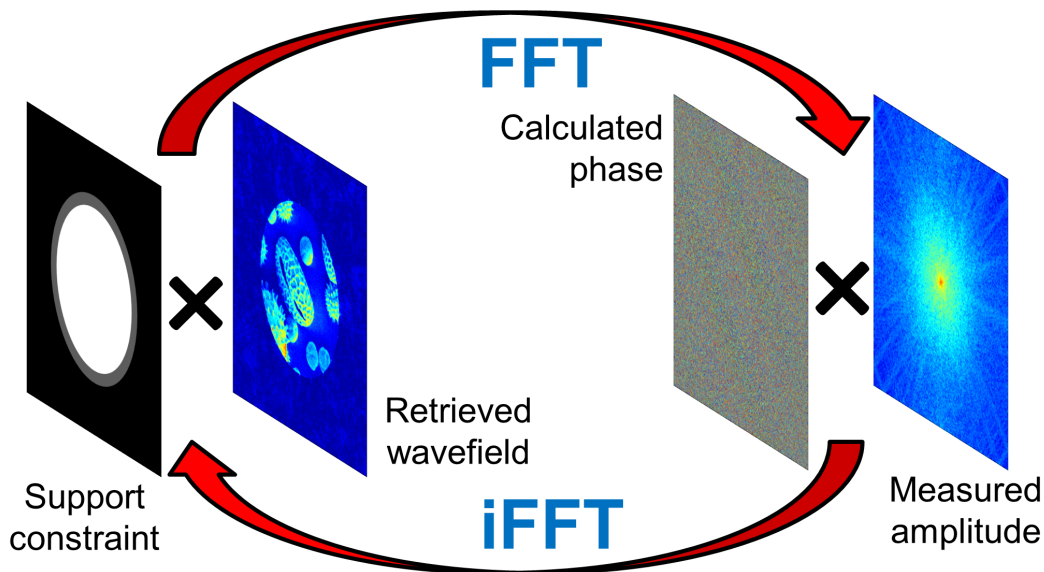


FIGURE 2.12: Reconstruction algorithms in coherent diffraction imaging alternate between real space and reciprocal space while enforcing constraints on both sides on the iterated wavefront.

based microscopy. This includes a resolution, that is not limited by optics, only by the scattering intensity into high spatial frequencies and quantitative phase contrast of the reconstructed samples. On the downside, CDI is limited in other terms, including sample size constraints, illumination function and ghost images[125].

Since its key weak points have been largely addressed by the "extended" CDI method called ptychography[126, 127] the importance of CDI is diminishing in the synchrotron community. However its ability to recover the sample from a single image made it an invaluable tool for free electron laser-based "diffract and destroy" measurements.

#### 2.4.4 Ptychography

Ptychography[126, 127] is a high resolution, phase sensitive, scanning coherent diffractive imaging method that uses multiple diffraction patterns from partially overlapping areas for the solution of the phase problem. It addresses CDI's issue of limited sample size by applying the overlap as an additional constraint to allow for the study of extended objects. The reconstruction recovers both the complex transmittance profile of the sample object as well as the illuminating wavefront (probe). Being a super-resolution lensless imaging method, its resolution is neither limited by the numerical aperture of an objective lens nor by the step size of the scan. Besides mechanical stability issues, it is only limited by the scattered flux to high  $q$ -values, making ptychography highly attractive for ultra-high resolution imaging. Planar resolutions below 10 nm[39] and 3D tomographic resolution down to 16 nm[40] have been demonstrated bringing the

resolution of X-ray microscopy close to the resolution of scanning electron microscopes<sup>2</sup> without putting strict fundamental constraints on the sample size.

Moreover, its unique ability to reconstruct the illuminating wavefield allows it to work with focused illumination and characterize the illumination function in addition to the sample transmission function. The later makes it an invaluable tool for the characterization of X-ray optics[39, 128–130].

#### 2.4.4.1 Reconstruction algorithms in ptychography

Ptychography was originally developed by Walter Hoppe[131] and further developed by John Rodenburg[132, 133]. They envisaged solving the phase problem in transmission electron microscopy by scanning the position of the illuminating beam. However, early mathematical formulations like Wigner-deconvolution provided marginal benefits to existing experimental schemes. The development of modern iterative algorithms led to the rapid progress of the previously marginal field into the spotlight of X-ray microscopy.

#### 2.4.4.2 Difference-map algorithm

The difference-map algorithm is a commonly used iterative method for optimization. While the exact formulation and general properties of the algorithm are described in the literature, its implementation for ptychography[127] can be summarized through the following steps:

- Data loading and preprocessing. Includes converting measured intensities into amplitudes, masking bad pixels and detector gaps.
- Initial guess for  $P$  probe and  $O$  object. While the object can start from a completely flat or random guess, the probe guess must be reasonably accurate regarding the wavefront curvature.
- The ptychographic iterative engine in its  $n^{th}$  iteration:
  - Generate the difference map for each  $\Psi$  view in the sample plane:
 
$$\Delta_j(q) = 2 * O^n(r - r_j) \times P^n(r) - \Psi_j^n(r)$$
  - Propagate the difference map to the detector plane:
 
$$\Delta_j(q) = \mathcal{F}(\Delta_j(r))$$
  - Update calculated amplitudes with measured amplitudes:
 
$$\Delta_j(q) = \sqrt{I_j(q)} \frac{\Delta_j(q)}{|\Delta_j(q)|}$$
  - Propagate the difference map back to the sample plane:
 
$$\Delta_j(r) = \mathcal{F}^{-1}(\Delta_j(q))$$

---

<sup>2</sup> The resolution is often confused by the virtually unlimited reconstruction pixel size.



- Update the views according to:

$$\Psi_j^{n+1}(r) = \Psi_j^n(r) + \Delta_j(r) - O^n(r - r_j) \times P^n(r)$$

- Once all views have been updated, iterate the object and probe guesses using the following update procedure a few times:

$$O^{n+1} = \frac{\sum_j P^{*(r+r_j)} \Psi_j(r)}{\sum_j |P^{*(r+r_j)}|^2}$$

$$P^{n+1} = \frac{\sum_j O^{*(r-r_j)} \Psi_j(r)}{\sum_j |O^{*(r-r_j)}|^2}$$

- Repeat the update procedure, as the error metric  $ERR = |O(r - r_j) \times P(r) - \Psi(r)|$  converges towards zero. The iteration should be stopped after a sufficiently good solution has been found or the iteration converges towards a non-physical solution.

The difference-map algorithm is one of the most robust and error-proof algorithms up to date. It is largely insensitive to the initial probe guess and has a large convergence radius. On the other hand, the convergence of the difference map-algorithm is slow and its numerical implementation suffers scalability issues on distributed computers and GPU based computing setups.

#### 2.4.4.3 Ptychographic iterative engine

While the difference map algorithm is a reliable algorithm for ptychographic phase retrieval, its slow convergence and poor scaling requires excessive computational resources. Better convergence can be achieved with the Ptychographic iterative engine (PIE)[134] or its derivative, the extended Ptychographic Iterative Engine (ePIE)[135]. The ePIE algorithm uses a different update procedure to facilitate easier memory management, better scalability and higher adaptability[136, 137]. However, the fast convergence also applies to non-physical solutions, resulting in a high sensitivity to the initial guess. Therefore ePIE must be supplied with a sufficiently good starting guess, either from pre-characterized probes or from the difference-map algorithm. The essential steps of ePIE go as follows:

- Data loading and preprocessing. Includes converting measured intensities into amplitudes, masking bad pixels and detector gaps.
- A few iterations with the difference map algorithm. The ePIE algorithm is sensitive to the starting conditions for the  $O$  object and especially for the  $P$  probe.
- The extended ptychographic iterative engine in its  $n^{th}$  iteration:

- Generate the exit wavefield for each  $\Psi$  view at the sample plane:

$$\Psi_j^n(r) = O^n(r - r_j) \times P^n(r)$$

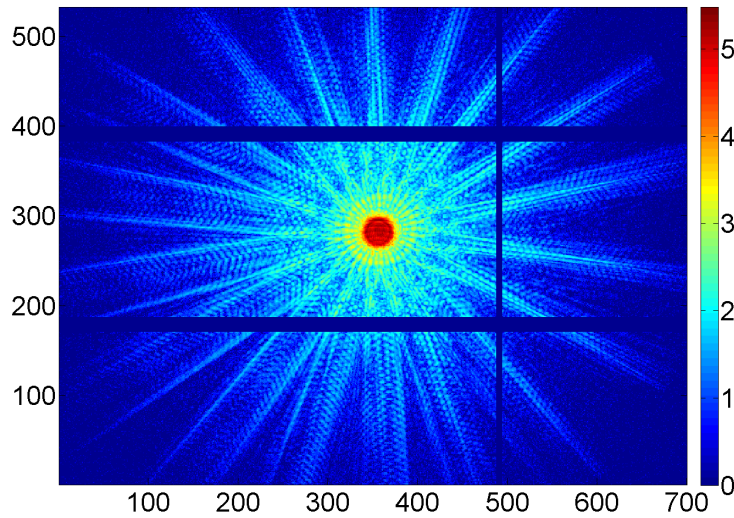


FIGURE 2.13: Diffraction pattern of a Siemens star test pattern on a single photon counting detector on a logarithmic scale. While the probe itself has over  $10^5$  counts/pixel, the high spatial frequencies have only a handful of counts in the individual pixels, illustrating the required dynamic range of the detector.

- Propagate the difference map to the detector plane:

$$\Delta_j(q) = \mathcal{F}(\Psi_j^n(r))$$

- Update calculated amplitudes with measured amplitudes:

$$\Psi_j^n(q) = \sqrt{I_j(q)} \frac{\Psi_j^n(q)}{|\Psi_j^n(q)|}$$

- Propagate the difference map back to the sample plane:

$$\Psi_j^n(r) = \mathcal{F}^{-1}(\Psi_j^n(q))$$

- Update the object and probe guesses using the following update procedure:

$$O^{n+1} = \alpha \frac{\sum_j P^*(r+r_j) \Psi_j(r)}{\max |P(r+r_j)|^2}$$

$$P^{n+1} = \beta \frac{\sum_j O^*(r-r_j) \Psi_j(r)}{\max |O(r-r_j)|^2}$$

- Repeat the update procedure, as the  $ERR = O(r - r_j) \times P(r) - \Psi(r)$  difference converges towards zero. The iteration should be stopped after a sufficiently good solution has been found.

As the processing of the individual views is independent, this algorithm achieves a high level of parallelism, making it suitable for GPU based compute nodes[138]. However, as a steepest descent method, it has issues with non-physical solutions when started with the wrong starting guess as well as it is susceptible to stalling, requiring moderation of the  $\alpha$  and  $\beta$  parameters.

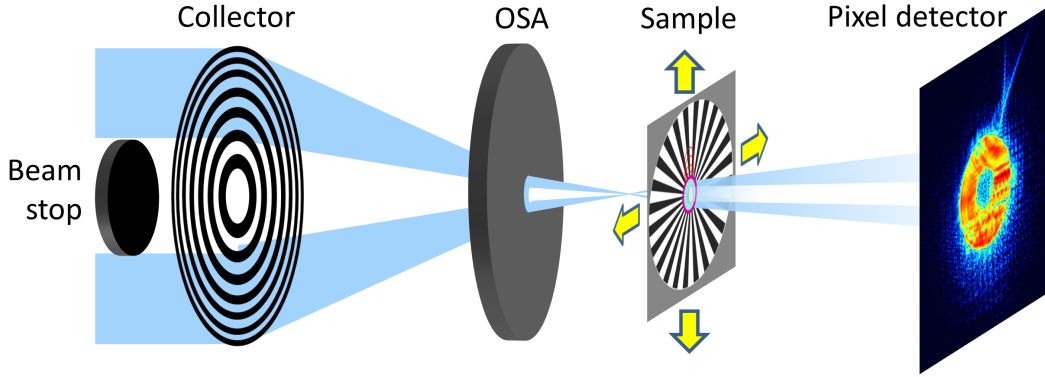


FIGURE 2.14: The basic experimental scheme for Ptychographic coherent diffractive imaging. The sample is illuminated by a Fresnel zone plate, with a clean-up aperture selecting the important first diffraction order. The sample is placed slightly after the focus and is raster scanned through the illuminating beam. The diffraction patterns of the sample are recorded in the far-field on a photon counting pixel detector (Figure based on [140]).

#### 2.4.4.4 Maximum likelihood method

As will be described in Section 3.5, the resolution of Ptychography is essentially limited by the sufficient sampling of high spatial frequencies. The Rose criterion for adequate sampling assumes a detail resolved, if at least 25 photons have contributed to its measurement. As seen on Figure 2.13, this is rarely satisfied for the highest spatial frequencies that correspond to the smallest details. Therefore, instead of calculating the best fit to the experimental data, the maximum-likelihood method calculates the solution that is the most likely to result in the measured diffraction patterns. Maximizing the likelihood equals the minimization of the negative log-likelihood function:

$$\mathcal{L} = - \sum_i \sum_q w_{j,q} \left\{ I_{j,q}^{meas} \log I_{j,q}^{cal} - I_{j,q}^{cal} - \log I_{j,q}^{meas} \right\} \quad (2.49)$$

The update procedure behind the maximum likelihood method is fundamentally different than the difference map or the ePIE algorithm and is discussed in detail in the literature[139]. However, similar to the ePIE algorithm, the maximum likelihood method requires a good initial guess for convergence.

#### 2.4.4.5 Experimental setup

Regarding the experimental setup (see Figure 2.14.), Ptychography requires coherent –or at least partly coherent[136]– illumination to resolve the speckles in the recorded diffraction patterns. The exact illumination function is flexible but it must be confined and a sufficiently good initial estimate must be fed to the reconstruction algorithm. Commonly used illuminations include pinholes, KB mirrors, zone plates and compound refractive lenses. Since the probe will be refined during the reconstruction, there is

no need for high optical quality. Using far-field diffraction, according to the Fraunhofer propagator the field of view of the individual projections is determined by the wavelength  $\lambda$ , detector distance  $Z_{det}$  and detector pixel size  $\Delta X_{det}$  as:

$$FoV = \frac{\lambda Z_{det}}{\Delta X_{det}} \quad (2.50)$$

Since the probe should cover less than half of this area, a clean-up aperture is usually applied to provide a clean wavefield at the sample plane. The sample is often placed slightly downstream of the focus to obtain a larger illumination, as each point of the sample must be measured with at least four different placement of the illuminating probe. Hence the maximal scan step size is half of the probe size. A regular scanning grid can result in severe artefacts[128], making random or non-periodic maps preferable. The scanning motors should be both fast and accurate to facilitate high-speed, high-resolution reconstructions. As the high spatial frequencies are often poorly sampled, low-noise detectors are essential for successful reconstructions. The optical, VUV, EUV and soft X-ray ranges must be contented with cooled CCD or CMOS cameras. While in the hard X-ray range, no-noise, high dynamic range single photon counting detectors are available for highest quality[141, 142].

#### 2.4.4.6 Ptychographic characterization of X-ray optics

Although ptychography is best known as a high resolution imaging method, its unique ability to recover both the object and the illuminating complex wavefield makes it a valuable tool for the characterization of X-ray optics[39, 128–130]. Using a high-contrast test sample, the recovered probe will be the combined wavefield of all beamline optics upstream of the sample. This wavefield can be propagated to any plane of the optical setup, allowing for the characterization of the focal spot or the aberrations of the illuminating optics. Therefore, the reconstructed point spread functions can even deconvolve scanning transmission X-ray microscopy images[143, 144] or show the source geometry of the beamline. However, it must be stated that ptychography can not pinpoint the source of the aberrations, just provides the resulting wavefront.

## 2.5 Measurement considerations

Information theory provides the essential mathematical background for data acquisition and analysis for experimental physics. Developed by the American physicist Claude E. Shannon, it aims to describe the limitations of signal processing[145]. Basically, it provides a mathematical background to separate real information from deceptive presentation, cherry-picked results, non-physical solutions and artefacts. Therefore it can potentially prevent the generation of exaggerated expectations in the user community

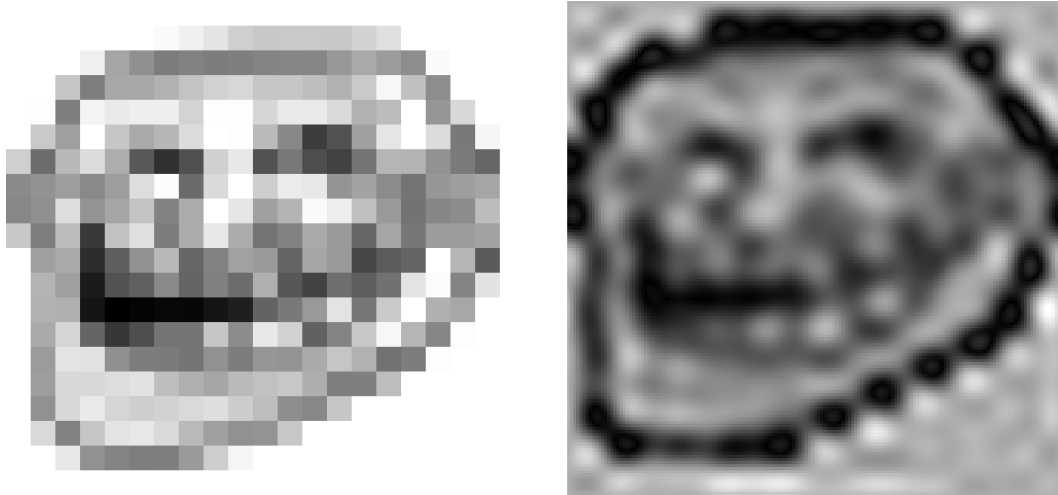


FIGURE 2.15: Upsampling as an example of data massage. The original image (left) of 20x20 pixels was upsampled by a factor of eight (right). Despite having more pixels and therefore a better visualization, the upsampled image does not contain more information than the original one. While scientific image processing is a powerful tool for visualization, it can also be used in a deceptive way.

as well as the spreading of claims arising from severe "data massage" (an example can be seen on Figure 2.15.). Therefore, this will discuss the fundamental capabilities and limitations of X-ray microscopy.

### 2.5.1 Shot noise and its effect on image resolution

Back in the golden age of classical physics, electromagnetic radiation could be described as an electric field with an arbitrary amplitude. However this illusion was dissipated by the discovery of the dual nature of light: electromagnetic radiation is transmitted through the elementary particles known as photons while it still retains its wave properties. The energy  $E = \hbar\omega$  transmitted by a single photon is on the order of kiloelectron volts in the X-ray range. From such high energy photons even a finite number can be detected, hence X-ray measurements can be performed even with a very small number of photons. In low flux measurements that contain only a few photons, statistical or Poisson-noise[146, 147] poses a fundamental barrier to the sensitivity[148–150].

Let us consider an incoming photon beam with an unknown flux  $F$ . The measurement of the individual photons occurs independently from each other with the average photon flux. Therefore given the finite measurement time window  $t$  and an unknown expected value  $\mu = Ft$ , the probability of measuring  $N$  photons is given by the Poisson distribution:

$$P(\mu, N) = \frac{\mu^N e^{-\mu}}{N!} \quad (2.51)$$

In practice, the real value of  $\mu$  is unknown and our best estimate is the measurement. However as the standard deviation of variables following the Poisson distribution equals

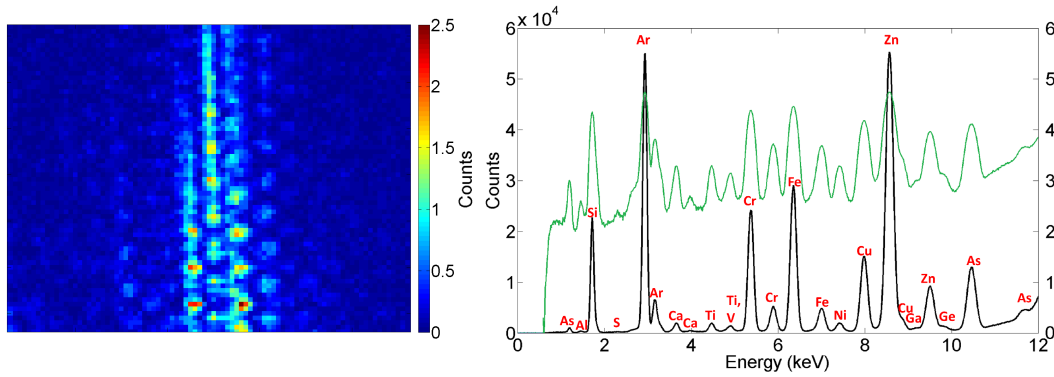


FIGURE 2.16: A subset of Figure 2.13 showing the discrete number of counts in the individual pixels. Well sampled peaks have no problem with visibility, but the badly sampled series die out in the noise. b.) X-ray fluorescence spectra of a paleo-geological rock-sample (from Andrea Somogyi). Besides the main components of the matrix, the identification of trace elements (Al, S, Ga, Ge) requires much better statistics.

to  $\sqrt{N}$ , the signal to noise ratio (SNR) of our measurement equals to:

$$SNR = \frac{N}{\sqrt{N}} = \sqrt{N} \quad (2.52)$$

This means that the information in low count measurements is unreliable and fine details can be lost due to insufficient statistics. Increasing the number of counts improves statistical significance giving a lower uncertainty on the observed features.

Poisson noise represents a visible limitation in coherent diffraction imaging, where noiseless photon counting detectors show the exact number of photons scattered into high spatial frequencies as seen on Figure 2.16. While the total scattered intensity might contain a considerable number of photons, poor statistics at high- $q$  values will eventually limit the resolution. Trace element analysis in scanning fluorescence microscopy also measures discrete number of counts in the individual channels that can be directly analysed for their statistical relevance. While less pronounced, due to the image forming mechanism, statistical variance is also present in full-field microscopy, albeit superimposed to other noise components in the instrumentation.

In order to calculate the dose required for the imaging of an isotropic,  $d \times d \times d$  sized voxel, a basic model is described in [148]. The transmitted amplitude coming from detail compared to its surroundings equals to  $T = e^{ikdn_d} - e^{ikdn_{bg}} = e^{ikdn_r}$ , where  $n_r$  is the relative refractive index of the detail compared to its surroundings. In respect to the unscattered wave, this results in  $A = A_0|1 - T| = A_0|1 - e^{ikdn_r}| \sim A_0ikdn_r$  scattered amplitude. As we measure the  $I_{scat} = |A|^2 d^2$  intensity scattered from the whole area of our structures, the scattering cross section can be obtained as:

$$\sigma_{scat} = \frac{I_{scat}}{I_0} = k^2 d^4 n_r^2 = \frac{E^2}{\hbar^2 c^2} d^4 n_r^2 \quad (2.53)$$

Since the scattering cross section scales with the fourth power of the feature size, this will translate into an inverse fourth power scaling for the required dose. As both the  $k$  wave-number and the  $n_r$  refractive index are related to the photon energy, by substituting equation 2.21, the scattering cross section becomes:

$$\sigma_{scat} = d^4 \frac{E^2}{\hbar^2 c^2} \frac{e^4 \hbar^4}{m_e^2 E^4} N_a^2 Z_a^2 = d^4 \frac{e^4 \hbar^2}{m_e^2 c^2 E^2} N_a^2 (\Delta Z)^2 \quad (2.54)$$

This approximation is only valid far from absorption edges. It shows, that the scattering cross section is actually determined by electron density contrast and decreases towards higher photon energies.

The scattering cross section means that from  $N_0$  incoming photons,  $P = \sigma_{scat} N_0$  contributes to imaging the detail. The Rose criterion[151] states that it requires a minimal SNR of 5 to distinguish a detail from noise with 100% certainty, meaning a minimum of  $N_0 = \frac{25}{\sigma_{scat}}$  incident photons over a unit area to adequately sample our details. The picture becomes more complicated in 3D tomographic reconstructions, where the images are reconstructed from several individual views. Nevertheless, according to the dose fractionation theorem[152], in the ideal case the same total dose would be required to distinguish our voxel as in the 2D case.

In summary, statistical noise is an existing limitation in X-ray microscopy, especially in high speed imaging, coherent diffraction imaging, fluorescence microscopy and lab based experimental setups. The sampling of finer details requires a massive increase in the flux, especially in the case of low-contrast specimens like biological samples.

### 2.5.2 Limitation of radiation damage

In the previous section, it was shown that X-ray microscopy requires a certain dose for sampling details up to a given resolution and contrast threshold, scaling with the fourth power of the decreasing feature size. However X-rays are considered ionizing radiation for a reason. The absorption of X-rays in the sample leads to the production of heat, the breaking of chemical bounds and the formation of ions and free radicals. These cause the deterioration of the measured specimens, as the aggressive chemistry attacks and blurs the fine details of the sample.

While the exact damage mechanism may vary, the radiation damage is related to the total deposited energy per unit mass, i.e. the radiation dose  $D$ . According to the Beer-Lambert law, the intensity of the X-ray beam is attenuated as  $I(x) = I_0 e^{-\mu x}$ , making the energy deposited per unit volume to be  $-\mu N_0 E$  and the energy deposited by unit mass to be:

$$D = \frac{\mu N_0 E}{\rho} = \frac{\mu P E}{\rho \sigma_{scat}} \simeq \frac{\mu P E}{\rho} \frac{m_e^2 c^2 E^2}{d^4 e^4 \hbar^2 N_a^2 \Delta Z^2} \quad (2.55)$$

and therefore the required number of photons for imaging:

$$N_0 = \frac{P}{\sigma_{scat}} = \frac{P\hbar^2 c^2}{E^2 d^4 n_r^2} \simeq \frac{m_e^2 c^2 E^2}{d^4 e^4 \hbar^2 N_a^2 \Delta Z^2} \quad (2.56)$$

The maximum tolerable dose  $D_{max}(d)$  represents the damage threshold, the maximum amount of radiation that the certain details of the sample can endure. According to numerical calculations[148, 150], for organic materials, due to the high contrast in the "water window" soft X-ray microscopy offers the most economic solution within bounds of radiation damage. However this energy range has its own drawbacks including extremely narrow depth of field, small penetration depth and the need of a vacuum setup. These concerns are less pronounced in the hard X-ray range but higher energies suffer from the lack of contrast, especially in organic materials.

Significant efforts have been done to increase the contrast or the radiation tolerance of biological specimens and resolve finer structures within the X-ray beam. Phase contrast imaging[112] is broadly employed to take advantage of the stronger phase shift terms of the refractive index. From the sample side, heavy metal staining is a well-known process for increasing the contrast and radiation resistance of organic specimens in electron and X-ray microscopy. However staining also alters the cell structure from its natural state. Freezing on the other hand aims to immobilize the aggressive by-products of radiation damage without destroying internal structure. By avoiding the migration of radiation by-products, the individual damage events can be contained at their origin until the end of the measurement.

It is important to note, that these methods can only reduce, but not completely avoid radiation damage. Therefore, despite the best efforts, radiation damage remains the ultimate resolution limit for X-ray microscopy. There are two known loopholes around this limitation, the first is to acquire an image of the sample before radiation damage can occur and the second one is to measure many similar samples[153]. The second scheme has been routinely employed in the field of protein crystallography, while the first has recently become possible with the extreme intensity and femtosecond time resolution of X-ray free electron lasers[43].



## Chapter 3

# Nanofabrication and numerical methods

As discussed in the previous chapters, the production of nanometre resolution diffractive X-ray optics is based on fabrication techniques on similar length scales. The X-ray optics group of the Laboratory of Micro- and Nanotechnology (LMN) at the Paul Scherrer Institut (PSI) has a long standing reputation for the production of high quality X-ray optics for the soft and hard X-ray range. This chapter is aimed to present the fundamentals of fabrication techniques and numerical methods that represent the base of the upcoming experimental part of this thesis.

### 3.1 Electron beam lithography

The term "lithography" originates from the printing process developed by Alois Senefelder in 1796 for the quick and cost-effective replication of texts and images using a limestone master template. In modern days, most nanofabrication techniques are based on the lithographic process by transferring a copy of a pre-defined pattern onto the surface of a substrate material. Following the persistent demand of the electronic industry for ever-shrinking feature sizes, a broad spectra of modern lithographic techniques have been described for the micro and nano-scale patterning of various substrates, meeting the demands of both industry and academia[154].

Electron beam lithography is a well-established method for the small volume production of structures from the multi-micron to the sub-10 nm range. It uses a focused beam of energetic electrons to write pre-defined patterns into suitable resists. As the movement of the electron beam can be controlled by a computer, electron beam lithography does not need a mask. This makes it an essential tool for photomask patterning in the electronic industry. Since most electron beam writer tools have a single writing

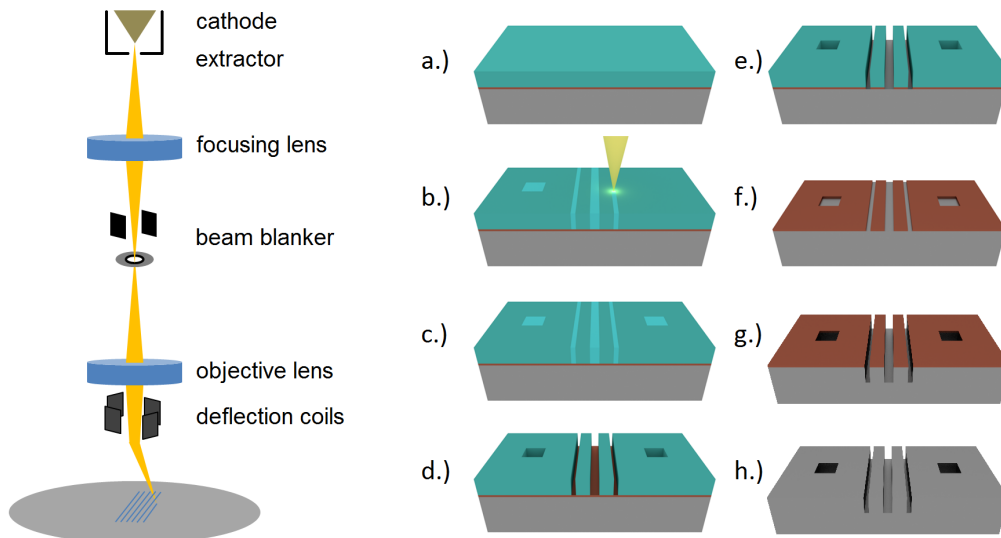


FIGURE 3.1: Left: A basic electron beam lithography tool involves a collimated electron source, a beam blanking unit, a focusing lens and deflection system. Right: An example patterning process starts from a.) resist coated substrate by b.) exposing the patterns into the resist. The c.) exposed resist is d.) selectively dissolved in developer and e.) the resist template is transferred to the hard mask. The f.) patterned mask is g.) transferred into the substrate allowing the h.) removal of the residual hard mask.

beam, the serial patterning makes electron beam lithography a relatively slow process. This limits it to academic purposes, process development, rapid prototyping and low volume production while keeping mass-production out of its reach.

### 3.1.1 Basics of electron beam lithography

Similar to many other lithography techniques, electron beam lithography relies on modifying selected areas of a resist layer. As seen on Figure 3.1, the resist layer is locally exposed by a beam of energetic electrons according to the pre-defined pattern. These resist areas have increased or decreased solubility in particular solvents called developers. For positive tone resists the exposed areas and for negative tone resists the unexposed areas can be selectively removed through development process. In order to reach adequate selectivity between the exposed and unexposed areas, the deposited energy by the beam –that can be adjusted by the exposure dose– must be fine-tuned for the choice of the resist material, post exposure treatment, developer chemistry and the developing conditions (duration, temperature, agitation e.g. by ultrasound). Finally the resist pattern is transferred onto the substrate by a series of etching and/or deposition steps. The available pattern transfer technologies can be separated to subtractive and additive processes, depending on whether the final structures are transferred into the substrate or added onto it.

Besides its flexibility due to digital pattern generation, e-beam lithography is also a high resolution patterning method, as sub-10 nm feature sizes can be patterned into

commercial high-resolution electron beam resists. While the spot size of the tool can be as small as a fraction of a nanometre, the actually achievable resolution is determined by the interaction between the electrons, the resist layer and the substrate[154]. Hence the deposited energy, seen on Figure 3.2 is determined as the resultant of the following three mayor contributors:

- Secondary electrons: As the electron beam enters the resist layer, it generates low-energy secondary electrons through a series of small angle scattering events. The secondary electrons have about 10 nm range and are responsible for the majority of the chemical changes induced by the electron beam. Since their range can be larger than the actual beam-size, their exposure leads to the effective blurring of the pattern. This makes the patterning of dense, high resolution patterns challenging. Sparse nanostructures are easier to pattern than dense ones, as larger distances between the patterns tolerate more blurring. Interfaces between low-Z resist and high-Z substrates are also a source of secondary electrons.
- Forward scattering: In case of a thick resist, the many small angle scattering events eventually lead to a widening of the primary electron beam towards the bottom of the resist layer, broadening the exposed patterns[154, 155]. This "trapezoidal" exposure cross-section seen on Figure 3.2 develops into an undercut in positive tone resist and into footing in negative tone resists. Forward scattering can be considerably confined into a shallow angle cone using higher electron energies.
- Backscattering: There is also a substantial contribution to the dose from electrons returned from the substrate itself. High angle scattering events completely change the trajectory of the incoming electrons, allowing backscattered electrons to pass through the resist layer a second time. Combined with the high penetration depth of high energy electrons in light substrates, this provides a smooth background of reduced contrast reaching up to tens of microns around the exposed structures.

#### 3.1.1.1 Electron beam lithography at LMN

Electron beam lithography at the Laboratory for Micro- and Nanotechnology (LMN) of the Paul Scherrer Institute (PSI) is based on a Vistec EBPG 5000+ ES electron beam writer seen on Figure 3.3. The 100 keV acceleration voltage of the tool provides a confined forward scattering cone and high penetration depth, facilitating the direct writing of nanostructures even in thick resist layers. The electron beam writer tool focuses the incoming electron beam into a small, Gaussian spot and uses magnetic beam deflection for patterning. The beam deflection is controlled in discrete steps by a two-stage, high-speed coil system, allowing up to 50 MHz stepping frequencies. The exposure dose can be freely changed across the pattern as long as the stepping frequency remains

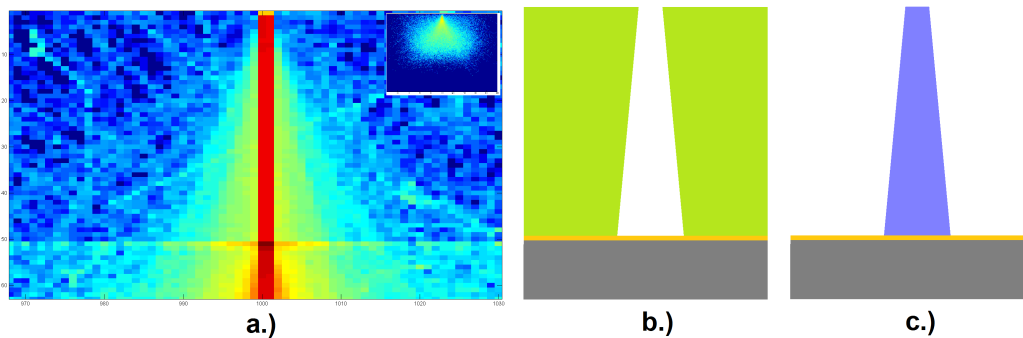


FIGURE 3.2: a.) Simulated energy distribution from a 100 keV electron beam on a 2500 nm thick PMMA and 5/20/5 nm thick Cr/Au/Cr layer coated silicon substrate[155]. Beam broadening due to forward scattering extends to several tens of nanometres towards the bottom of the resist layer. The exposed area is surrounded by a large area even background from backscattered electrons. The forward scattering leads to undercut b.) in positive tone and footing c.) in negative tone resists.

within range. Whenever the beam parameters are changed, the machine automatically re-calibrates the deflection system to the interferometer controlled stage. A single write field up to  $500 \times 500 \mu\text{m}^2$  can be exposed only with deflection without mechanical stage movement. Larger patterns are stitched together from several write fields with stage movement in between. Despite the calibration system's best efforts, there is a 30-50 nm stitching error between the write fields. The electron beam writer is also equipped to function in SEM mode and automatically locate and identify predefined exposure markers with high accuracy, using its built-in alignment procedures.

### 3.1.2 Direct patterning of high aspect ratio nanostructures

Beam broadening due to forward scattering limits low-energy electron beam lithography to the patterning of shallow resist layers. While several multi-step pattern transfer procedures exist for transferring low aspect ratio resist moulds into a high aspect ratio nanostructures within the substrate[75, 77, 79], yet increasing the number of process steps complicates process development and decreases its yield. High energy tools are more resistant to forward scattering by confining it into a narrow cone, facilitating the direct patterning of high aspect ratio features in thick resist layers. However, not all resists are suitable for high resolution and high aspect ratio patterning.

For zone plates requiring several micron high structures Poly(methyl methacrylate) (PMMA) is a popular electron beam resist (Figure 3.4). PMMA can provide several micron thick layers and even thicker layers can be achieved using multiple subsequent coating steps. PMMA is a polymer resist and chemically it is the same as common Plexiglass<sup>®</sup>. High energy electrons produce secondary electrons in the resist layer, that break up the long polymer chains of the resist into shorter segments. These short segments have higher solubility in solvents mixtures like MIBK:IPA or H<sub>2</sub>O:IPA[158]. As a

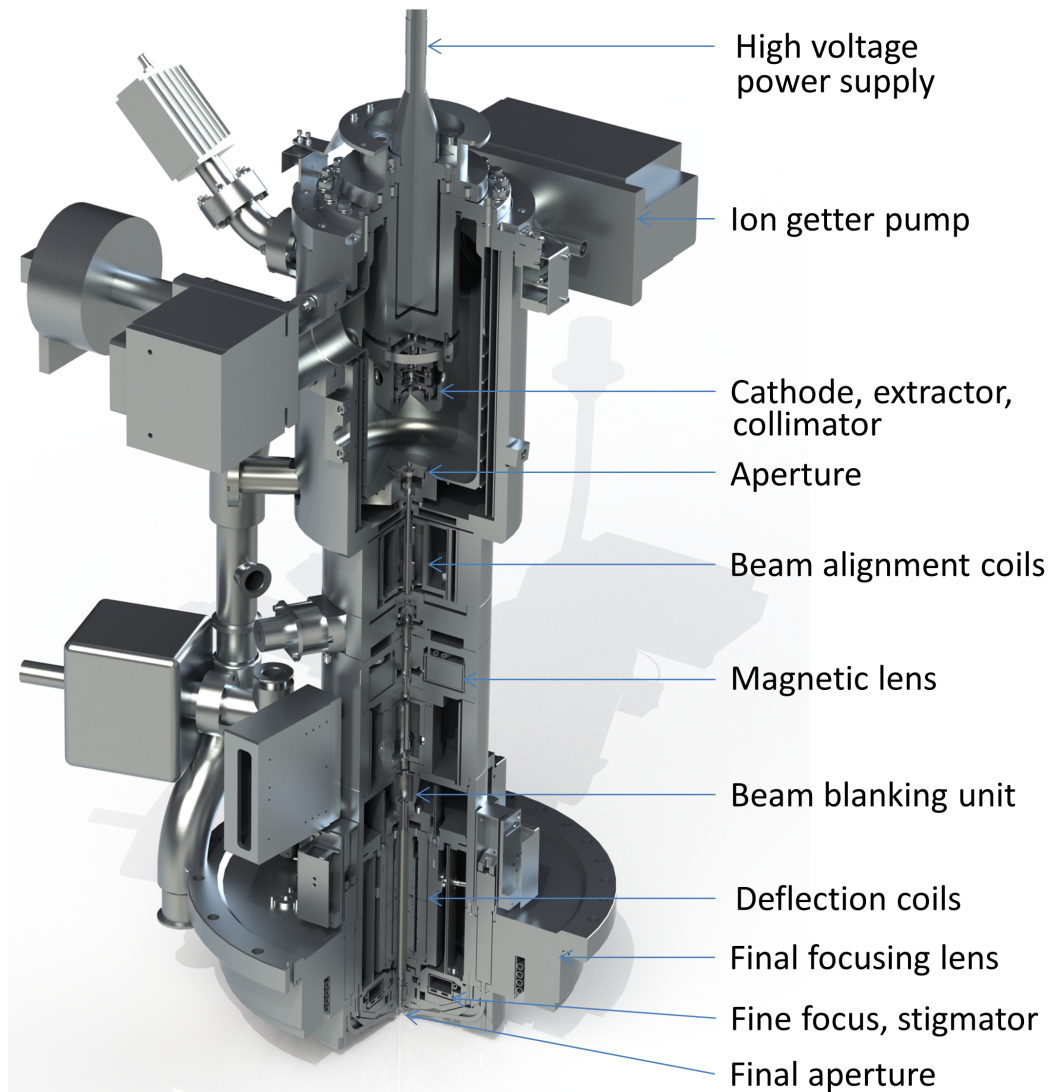


FIGURE 3.3: Rendered image of the Vistec EBPG 5000+ ES column at PSI. The advanced electron optics and the high-speed, two-stage coarse-fine deflection system allows the high-resolution patterning of write fields up to  $500 \times 500 \mu\text{m}^2$ . As a high-end dedicated writing tool, patterns are not limited to a single write field and their resolution can be adjusted independent from the write field size. (From Vistec Lithography Inc.)

higher exposure dose increases dissolution rate and the development speed drops inside narrow, high aspect ratio cavities, exposing smaller structures with higher dose allows uniform development speed. Secondary electrons in PMMA have a long free travel path and this results in severe undercut that can compromise the mould stability, especially in several micron thick resist layers. PMMA can be removed by a wide range of organic solvents or oxygen plasma ashing. Dense structures with  $\sim 100 \text{ nm}$  half-pitch can be realized with aspect ratios up to 20 with a reasonable yield. At smaller linewidth the contrast falls due to increased secondary electron exposure, eventually limiting achievable aspect ratios. Therefore PMMA is not the right choice for patterning ultra-high resolution nanostructures.

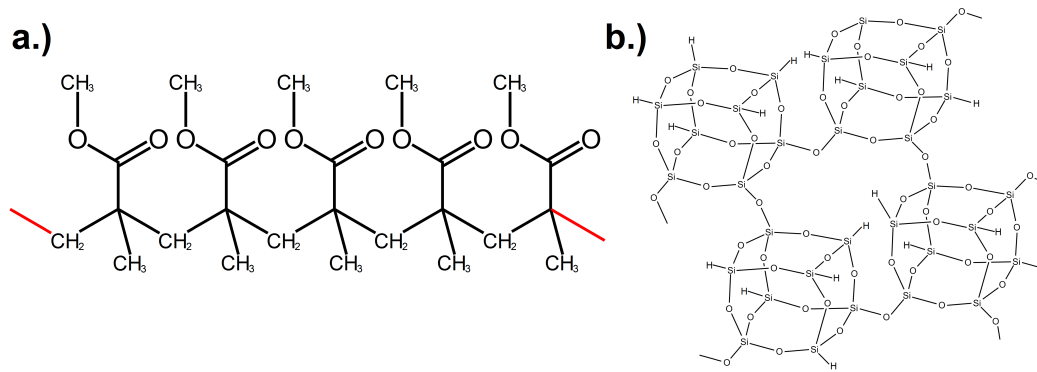


FIGURE 3.4: The basic structure of PMMA and HSQ electron beam resists[156, 157]. The exposure of PMMA breaks up the long polymer chain to shorter pieces. The exposure of HSQ leads to the release of hydrogen ligands, effectively closing the cage like structure.

For ultra-high resolution features, Poly(hydrogen silsesquioxane) (HSQ) is a widely used negative-tone resist[159]. HSQ is an inorganic, silicon based polymer of the hydrogen silsesquioxane monomer ( $H_8Si_8O_{16}$ ) (Figure 3.4). Energetic electrons or high energy photons crosslink the resist, making it very similar to porous, hydrogenated  $SiO_2$ . The unexposed areas can be dissolved by alkaline developers[160], while the exposed areas express an extreme chemical resistance similar to that of glass. Unlike PMMA, multiple coating steps of HSQ does not provide a reproducible thickness, thus the coating of thick HSQ layers relies on very low spin-speeds. As glass is an extremely stable compound, exposed structures are largely insensitive to development time. Thus aggressive development can dissolve all unexposed resist, leaving only the completely glassified HSQ behind. This allows the direct patterning of sub-10 nm resist structures[161, 162] with impressive aspect ratios[74]. The high selectivity reduces the significance of secondary electrons, thus the eventual resolution limit of HSQ for high aspect ratio nanostructures comes from beam forward scattering. Combined with secondary electrons coming from the substrate, resultant resist structures are generally supported by strong footing.

High aspect ratio resist layers are often strongly stressed, that can be released during the development. Therefore they require the placement of support structures to enhance the stability of the resist mould. Such support structures can be later seen on Figures 3.9 and 3.12. The detachment of the resist layer should be avoided by ensuring a good resist adhesion to the surface. Moreover, since the writing electron beam deposits considerable amounts of charge on the sample, it must be sufficiently conductive to prevent charging up to the distortion of the exposed patterns. Therefore insulating samples require a metallic surface layer while maintaining good adhesion properties. Once the ideal process parameters have been found, the fabrication of high aspect ratio resist nanostructures is a fairly straightforward process and is certainly simpler than the use of multi step pattern transfer procedures. However for the production of X-ray optics the exposed patterns must be transferred into metallic nanostructures.

## 3.2 Reactive-ion etching

Reactive ion etching covers a wide range of dry etching techniques commonly employed in micro- and nanofabrication. The general scheme employs a radio frequency generator to produce ionized, highly reactive radicals of the etching gas at gas pressures in the mTorr range. Due to a charge build-up between the plasma and the sample substrate, the ionized radicals are accelerated towards and react with the sample surface. The ionized nature of the radicals increases their chemical activity, allowing reactions with the surface that create volatile compounds that can be pumped out of the reaction chamber (see Figure 3.5.a). Increasing the acceleration bias of the ions increases their directionality that is welcome when processing high aspect ratio trenches as well as it adds a mechanical sputtering component to the chemical interaction. Using appropriate chemistry or high accelerating bias, almost any material can be etched or sputtered.

Restricting the discussion to the scope of this thesis, reactive ion etching is a well known method for the removal of chromium from exposed and developed mask blanks. Chromium can be etched with a mixture of chlorine and oxygen. The process first oxidises the surface chromium and forms volatile  $CrClO$  and  $CrCl_2O_2$  compounds that are flushed away with constant pumping[163]. The same procedure should be followed for removal of chromium from high aspect ratio trenches to facilitate electroplating that will be described in the next section.

## 3.3 Electroplating

Electroplating is a chemical process, that uses electric current to reduce metallic cations from their salty solution and deposit them as metallic layers on the cathode. By using an external power supply to drive reverse current through a galvanic cell, the dissolved metallic ions of the electrolyte will be deposited on the surface of a conductive cathode.

### 3.3.1 The basics of electroplating

The electrochemical potential (or Fermi level) of a neutral body expresses the work required to add or remove an electron to/from it. A closed electric circuit will aim for a constant potential across all of its components. Therefore, when two metallic electrodes made from different metals  $M_1^+$  and  $M_2^-$  are immersed in a conductive electrolyte solution, they will even out their potentials: by forming charged interfaces on the electrode-electrolyte boundaries, they will exchange electrons and metallic ions with the solution. When the potential difference is maintained by an external power supply, current will flow through the electrochemical cell depositing the metal  $D$  from the dissolved salt on the cathode. Thus if total charge  $Q$  has been transported through the

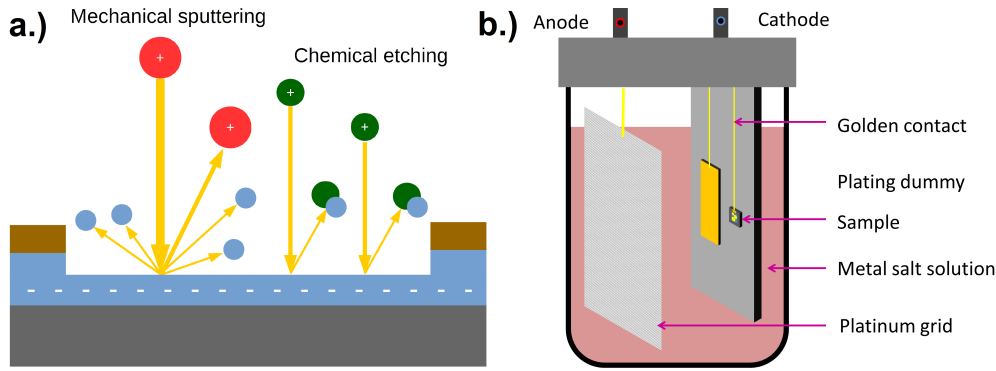


FIGURE 3.5: The two basic scheme of plasma etching involves either the mechanical bombardment of the substrate surface with energetic heavy ions or the generation of reactive radicals forming volatile compounds with the etched substrate (a.). Simplified drawing of the small-scale gold electroplating bath at LMN (b.). The cyanide bath does not dissolve platinum, making in an optimal choice as anode material. A large area reference electrode keeps the current density constant on the sample.

cell, where the ions of metal  $D$  are  $q$  times ionized ( $D^{q+}$ ), it requires  $n_D$  metallic ions to deposit the required charge to the cathode:

$$Q = It = n_D qe \quad (3.1)$$

If there are several competitive chemical processes the total charge is split between the different branches with efficiency  $\eta$  in the technically important process branch. The deposited mass of the metal is then given by  $m_D = \eta n_D M_D N_A$ , where  $M_D$  is the atomic mass of the deposited metal and  $N_A$  is Avogadro's constant. If the cathode has surface area  $A$  and the deposited metal  $D$  has density  $\rho_D$ , the deposition thickness is  $h = \frac{m_D}{A\rho}$  and hence the deposited thickness can be calculated as:

$$h = \eta \frac{It}{qDe} \frac{M_D N_A}{A\rho} \quad (3.2)$$

Electroplating itself is a highly isotropic process, that is widely employed in the industry for the cost-effective manufacturing of metallic surface coatings either for aesthetic (jewellery, shiny surfaces) or for protective (corrosion or wear resistance) reasons. As it requires a conductive substrate to function, a patterned insulating polymer mask will cause the growth of metallic structures.

### 3.3.2 Electroplating on the nanoscale at LMN

The nanoscale electroplating of high aspect ratio nanostructures is an established technology at the Laboratory for Micro- and Nanotechnology. Available electroplating baths are prepared for plating gold and nickel nanostructures for X-ray optics[72] using the bath seen on Figure 3.5. Section 1. already described the e-beam patterning of suitable



polymer moulds, but nano-scale electroplating faces complications, as high aspect ratio nanostructures act like capillaries:

- First of all, the deposition speed and deposition quality depends on the current density. With small, few millimetre sized chips the total area changes significantly between samples. In order to provide reproducible conditions, a large area plating dummy beside the sample should be employed to stabilize plating speed.
- If the surface tension of the electrolyte is high, residual airbubbles or gasbubbles from other reaction mechanisms can be trapped in the capillaries and prevent plating underneath. Surfactants and mechanical agitation before the plating can improve the uniformity.
- The transfer of ions within the electrolyte is performed via diffusion, that is significantly slower in confined spaces. If the plating rate is higher than the replenishment rate, the electroplating solution will become depleted in the narrow capillaries. This leads to structure size or geometry dependent plating rates. In order to provide a uniform plating height, mechanical cavitation, pulsed plating or high electrolyte concentrations should be employed.
- The adhesion of the wet, swollen resist layer can be much lower than that of a dry one. Either due to under-etching, swelling or capillary forces, the resist may become detached from the substrate leading to under-plating. A good adhesion is essential for electroplating.
- The plated structure sizes should be always significantly larger than the grain size. In other words the nucleation should be kept high during the whole plating process by tuning the plating rate, metal concentration and the pH of the solution.

For the work described in the following chapters, the nickel electroplating was performed using a commercial nickel-sulfamate based bath (LECTRO-NIC<sup>TM</sup> 10 03) in the recommended 52 – 62°C temperature range around 3.5 pH. The plating solution has low surface tension, good nucleation, is insensitive to composition and is a high efficiency process without noticeable gas formation. Yet its aggressive chemistry will dissolve already plated nanostructures and this effect is increased at low nickel content. Using pulsed plating helps to reduce the nucleation delay of the small structures, resulting in a uniform structure height and very fine grained depositions[164]. Due to the low material costs, troubleshooting involved the preparation of a new plating bath.

Similarly to the previous bath, gold electroplating was performed using a commercial potassium-gold-cyanide based bath (Autonexx). Due to better results, the bath was not operated at the recommended settings, instead a temperature of 35°C was used with a pH of 4.5, the gold concentration was around 4-6 mg/L and added surfactants

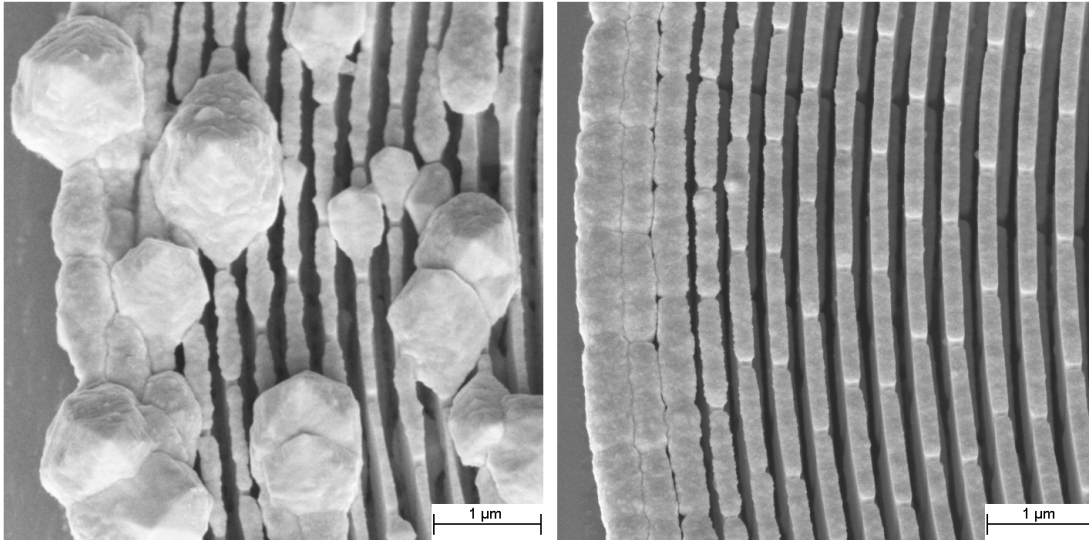


FIGURE 3.6: Gold Fresnel zone plates electroplated under nonoptimal (left) and optimal (right) plating conditions. The large, aggressively growing grains can distort the polymer mould as well as the resultant X-ray wavefront.

helped to reduce surface tension. Gold electroplating is a low efficiency process with inherent gas formation limiting current density. Nucleation is particularly sensitive to unclean plating base, as any residual chromium or resist inhibited structure growth. The gold bath had a more sensitive chemistry, as the deposition quality heavily depended on the status of the solution, leading to severe issues with nucleation, grain size and growth rate. Unfavourable chemistry led to the formation of large crystalline grains as seen on Figure 3.6. Both the growth direction and the growth speed of these crystallites were uncontrollable. They distorted the polymer mould and emerged far beyond zone plate's structures, leading to a distorted wavefront and poor optical performance as will be later seen on Figure 4.12.

### 3.4 Atomic layer deposition

Atomic layer deposition is a surface-catalysed, self-limiting sequential deposition process. Proposed already in 1952[165] and developed in the 1960's as "molecular layering"[166, 167], however it was the work of Tuomo Suntola[168] that led to its wider recognition and spread in industrial use. Today, atomic layer deposition can deposit a wide range of elements and their compounds[169], producing well-controlled, conformal coatings, even for exotic geometries[169].

Atomic layer deposition bears strong resemblance to chemical vapour deposition, using similar chemical processes between gas phase precursors. However unlike CVD, atomic layer deposition has only one precursor at a time within the reactor chamber, with the alternation of precursors being separated by pumping and flushing procedures.

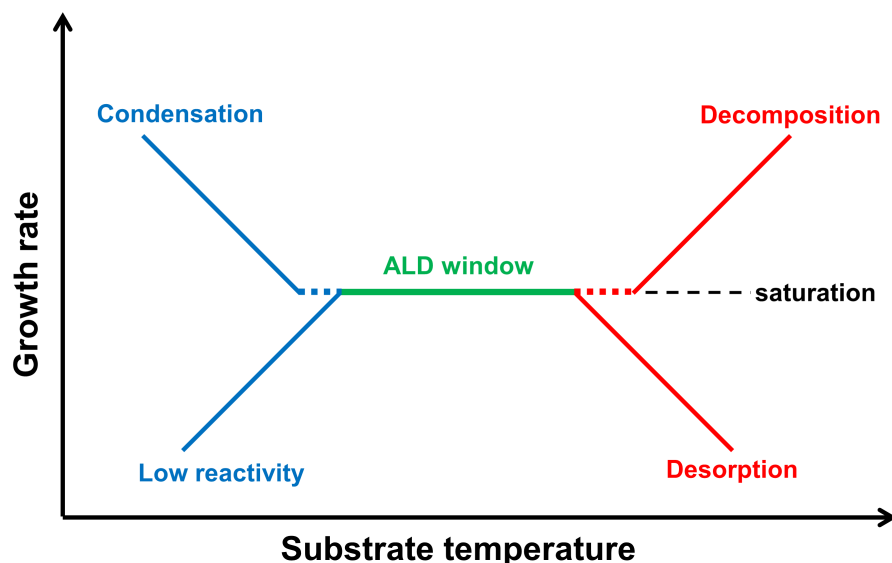


FIGURE 3.7: The term "ALD window" describes a particular temperature range corresponding to the growth of one monolayer per cycle. Outside this window, other processes lead to poor thickness and deposition quality control.

Once the first precursor is in the chamber, it forms a chemically bound monolayer on the sample's surface. After flushing the chamber, the second precursor is pumped into the reactor to react with the bound precursor on the sample's surface. As only a single monolayer is bound to the surface, atomic layer deposition inherently deposits one monolayer of the desired material in every cycle.

As with all deposition processes, there is a wide parameter space to optimize including choosing the right precursors, temperature and flow rate[169]. For oxides and other popular compounds several recipes are available, employing precursors aimed for different temperature, stability and toxicity requirements. However the deposition of heavy or noble metals is a niche application with more limited possibilities.

Thermal ALD depositions are often performed at elevated temperatures as it yields higher reactivity of the involved reagents. Yet too high temperature also facilitates the desorption of already bound atoms from the substrate surface and the spontaneous thermal decomposition of the precursors. Too low temperature on the other hand leads to insufficient reactivity, changes in deposited composition<sup>1</sup> and even precursor condensation on the sample's surface. The equilibrium of the surface processes leads to a constant, well controlled growth rate over a certain temperature range called the ALD window seen on Figure 3.7.

A well known workaround of the low reactivity of the precursors is plasma enhanced ALD[170]. Free radicals and excited molecules from a plasma source have much higher reactivity than thermally activated reactions. Therefore plasma enhanced ALD

<sup>1</sup>The rule of thumb for growing metal oxides is using the process for metals on a lower temperature.

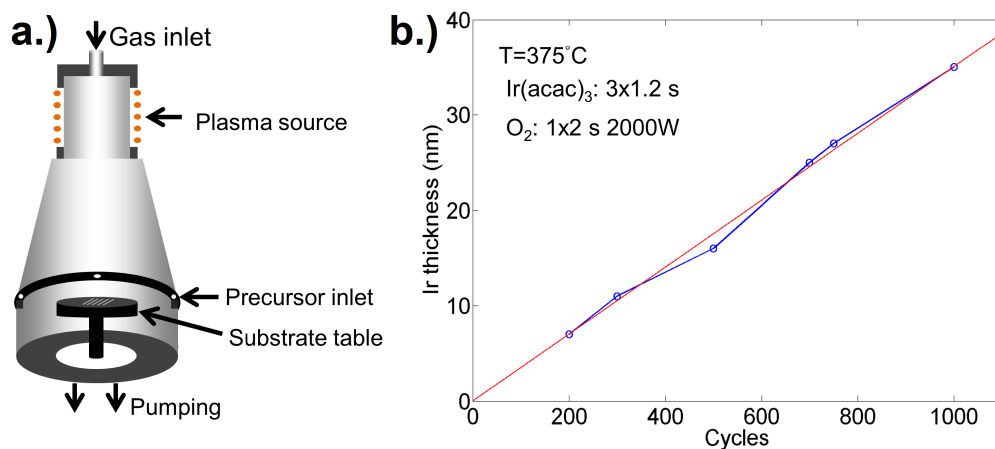


FIGURE 3.8: Left: Schematic drawing of the Picosun R200 PEALD tool at LMN. The precursors are pumped into the chamber through the precursor inlets while the chamber is constantly being pumped and flushed by argon from the gas inlet above the plasma source. Right: Experimentally measured iridium thickness as a function of the number of cycles using the plasma enhanced process. The linear fit corresponds to 0.35 Å/cycle growth speed with no nucleation delay.

has two main uses. The first is lowering the thermal barrier to allow temperature sensitive substrates. The second is facilitating reactions that are too difficult with purely thermal equipment. Yet, plasma enhanced ALD has a mayor drawback as it reduces the conformity and uniformity of the depositions, especially on high aspect ratio structures or porous samples.

Since both surface saturation and purging can take a considerable amount of time, ALD is generally considered as a slow process. Typical deposition speeds of easy-to-grow materials can exceed 100-300 nm/hour, but other materials may grow with a few nm/hour speed only. The throughput of ALD is also reduced by the so-called "nucleation delay" as the nucleation of the very first layer requires the chemical binding of the precursor to the substrate which can be a completely different mechanism than layer-to-layer growth. In case of sparse nucleation sites, a considerable number of cycles is spent on forming a closed layer, through the lateral growth of the crystallites, meanwhile the vertical growth of the crystallites results in increased roughness of the deposited film.

### 3.4.1 Conformal deposition of Iridium

The atomic layer deposition of iridium was developed at the University of Helsinki by the group of Mikko Ritala[171]. It employs iridium acetylacetonate ( $Ir(acac)_3$ ) as an iridium precursor and uses oxygen for stripping the iridium from the organic constituents as described in the literature[172]. In a brief summary, during the  $Ir(acac)_3$  pulse of the deposition process, precursor molecule is partially combusted and bound to the surface by reacting with a surface-bound but still active oxygen atom. During the following

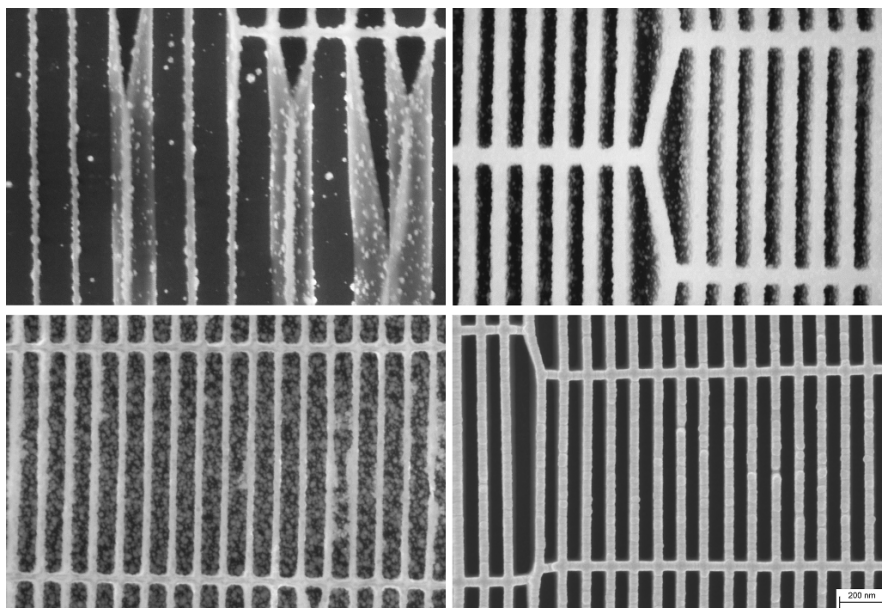


FIGURE 3.9: SEM images of iridium layers on HSQ nanostructures after 300 cycles, as deposited by thermal ALD at a.)  $350^{\circ}\text{C}$  b.)  $375^{\circ}\text{C}$  c.)  $390^{\circ}\text{C}$  and d.) as deposited at  $375^{\circ}\text{C}$  after the plasma activation of the surface. The higher temperature increases nucleation rate and plasma pre-treatment provides a massive boost by providing a closed layer at the same stage.

$\text{O}_2$  pulse, the rest of the organic ligands will be burnt away, resulting in an oxygen terminated layer of iridium atoms.

The Laboratory for Micro-and Nanotechnology operates a Picosun R200 plasma enhanced ALD tool with the schematic drawing seen on Figure 3.8. Since the deposition of metallic compounds is not a straightforward process, the cookbook recipe had to be adopted to the configuration. After consultations the University of Helsinki, process development started from a good initial guess based on literature values. Early test depositions of iridium had issues with poor nucleation rate, seen of Figure 3.9. This is commonly associated with noble metal deposition, as the passive surface oxide layer has a low affinity for reacting with the  $\text{Ir}(\text{acac})_3$  precursor. The nucleation could be greatly improved by starting the deposition process with a mild oxygen plasma treatment. Once initiating the nucleation and providing sufficient precursor for the reaction, the  $\text{Ir}(\text{acac})_3 + \text{O}_2$  process is a robust deposition process. The already nucleated layers were growing with the expected  $\sim 0.35$  nm/cycle growth rate seen on Figure 3.8. Deposited films were highly conformal even on high aspect ratio nanostructures and had sub-nanometre surface roughness.

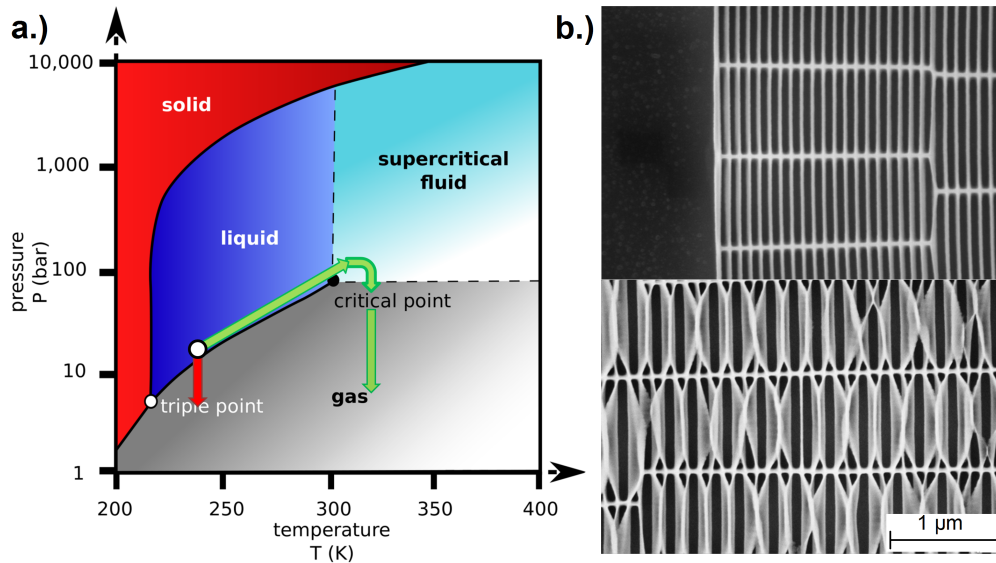


FIGURE 3.10: Phase diagram of  $CO_2$ , as a common intermediate medium for critical point drying (a.). Supercritical drying (green arrows) goes around the critical point, avoiding any phase boundaries as with conventional drying (red arrow)[173]. Zone plate structures dried with and without critical point drying (b.). Conventional drying led to the collapse of the zones due to surface tension.

### 3.5 Critical point drying

Supercritical drying is a controlled drying procedure that uses the continuity of state to preserve the structural integrity of delicate specimens. Sensitive biological specimens, micromechanical systems and high aspect ratio nanostructures would be destroyed by the capillary forces arising at the liquid-gas phase boundaries during conventional drying. Instead, critical point drying does not explicitly cross the liquid-gas boundary, but moves around it through the supercritical region. In this regime there is no difference between liquid and gas phase thus the samples move from liquid into gaseous environment without passing any phase boundary as seen on Figure 3.10. The critical point drying machine at LMN dries samples in isopropanol or acetone by exchanging the original solvent to liquid  $CO_2$  through a series of flushing steps and heating up the chamber to move it over the critical point. Once in the critical regime, the pressure is released slowly back to atmospheric pressure. Due to the high aspect ratio of high resolution e-beam written zone plate optics, critical point drying can be mandatory for preserving structure integrity as can be seen on Figure 3.10.

### 3.6 Electroplated zone plates in PMMA resist

The direct writing of a high aspect ratio PMMA mould and subsequent electroplating was originally developed by Sergey Gorelick at the Laboratory for Micro- and Nanotechnology and is described in the literature[72, 174] and the major steps illustrated

on Figure 3.11. It is a well-suited process for diffractive X-ray optics that do not require structures below 50 nm but rather aim for up to several micron structure height. This section describes the implementation of this nanofabrication process that was employed to achieve the goals of Chapter 4 and 5 of this thesis.

The fabrication process for zone plates starts with the substrates: 100-250 nm thick silicon-nitride membrane windows with a 1-2 mm silicon frame are well-suited substrates for zone plate fabrication for the hard X-ray range (Fig. 3.11.a). The membrane wafers were evaporated with 5 nm chromium, 20 nm gold and 5 nm chromium metal layers as an adhesion and conduction layer for electroplating (Fig. 3.11.b). The chromium layers produced by thermal evaporation under  $\sim 2 \times 10^{-5}$  mbar vacuum were better for resist adhesion compared to e-beam evaporated layers. Right before spin-coating the resist, the substrate was cleaned using high energy oxygen plasma etching to increase adhesion to the resist.

The resist was either 8% PMMA 950k in anisol or 4% PMMA 950k in etyllactate (Micro resist technology), depending whether thin or thick layers were required (Fig. 3.11.c). The resist was spin-coated on the samples with spin speeds above 2000 rpm to reduce edge bead. After spin coating, the chips were placed on a 175°C hotplate for solvent evaporation for at least 3 minutes. Thick layers were coated by repeating the coating and evaporation steps several times until the desired thickness has been reached. After the last coating step the samples were left on the 175°C hotplate for at least 15 minutes, followed by a slow cooling to room temperature to relieve the stress in the resist layer. Both the evaporation and the spin-coating could be done on larger chips, coating dozens of membranes at once, which increased the reproducibility of the upcoming process. The resist thickness was verified with optical interferometry. Layers up to  $\sim 1.5 \mu\text{m}$  could be removed from the hotplate without the cooling procedure, but thicker layers showed cracking when not cooled down properly.

The zone plate patterns were directly exposed into the PMMA resist layer by 100 keV electron beam lithography using LMN's Vistec EBPG 5000+ ES system (Fig. 3.11.d). For pattern exposure the membranes were mounted above holes on the e-beam writer's holder plate to reduce backscattering from the holder plates. Since the  $\text{Si}_3\text{N}_4$  is an insulator the chips were grounded by contacting a metal clamp to the plating base. The zone plate patterns were generated by the optimized code of Vitaliy Guzenko[175], which greatly reduces the overheads in the exposure time due to data fracturing and adds radial support structures to enhance mould stability. In case of the pattern was smaller than  $500 \times 500 \mu\text{m}^2$ , it was exposed in a single write field without field stitching. The pattern generator code allowed precise linewidth control through controlling the bias and the exposure dose of the lines. Using a constant bias and beam-current greatly simplified the parameter space by using a dose table to adjust the profile of the developed shapes. Typical base doses started from  $1300 \mu\text{C}/\text{cm}^2$  to  $2300 \mu\text{C}/\text{cm}^2$  using 2 nA beam-current,

depending on development conditions and –depending on the bias– increased by a factor of two to three for the smallest zone width.

SEM inspection was found to provide misleading results for exposure dose optimization. While SEM is a surface method, the cross section of the structures is heavily influenced by the undercut due to beam forward scattering. As will be seen later on Figure 5.4, in resist layers beyond  $\sim 1.5 \mu\text{m}$  thickness this results in a trapezoidal structure cross-section, hence SEM shows lower fill-factor. This can be pre-compensated by going for as low as possible exposure dose to avoid excessive undercut[176].

After exposure, the exposed membranes were developed in a 7:3 mixture of isopropanol and water (Fig. 3.11.e). Whenever using resist thickness beyond 1 micron, both the developer and the rinser was cooled down to  $2^\circ\text{C}$  for increased contrast[158]. This provided higher reproducibility and steeper side-walls, especially for structures beyond 2 micron height. The development time was fixed for a given PMMA thickness giving 7.5 minutes for the development of  $2.5 \mu\text{m}$  and 5 minutes for the development of  $1.5 \mu\text{m}$  thick resist layers. After development the samples were rinsed with cooled isopropanol and dried with nitrogen gas jet.

Since the chromium adhesion layer prevented electroplating, the developed trenches were cleaned both from residual organic materials and chromium using a  $\sim 40 - 60$  seconds long plasma etching procedure in a mixture of chlorine and oxygen (Fig. 3.11.f). As the etcher was not very anisotropic, under-etching had to be avoided as it led to adhesion problems during the following electroplating step. The prepared resist moulds were electroplated with either nickel or gold, using a support wafer as a constant reference area (Fig. 3.11.g). The current densities were adjusted for 100-200 nm/min plating rates. The plating could be stopped and resumed several times, allowing to use optical microscopy for thickness control: the plating was stopped when the structures started to over-plate. Optical microscopy was also the most important tool for quality control, as it reveals obvious problems regarding exposure dose, etching time, resist inhomogeneities, grain size and adhesion issues. Zone plates with a smooth profile could be used for nanofocusing without fundamental issues regarding optical performance, however their actual efficiency could be only evaluated within the X-ray beam as will be discussed in the following chapters. Finally, the residual resist was removed from the chips using acetone or oxygen plasma ashing with the latter being more gentle with low-dose structures (Fig. 3.11.h).

The advantages of using the direct patterning of PMMA nanostructures include the considerable structure heights reaching up to several microns. In the "golden middle" range, zone plates with 70-100 nm smallest zone width were patterned close to aspect ratios of 20. As electroplated zone plates represent a solid foundation, several processing steps can be produced in overlay for on-chip stacked[92] and multi-step[71] zone plates. Markers can be made together with the patterns, but the once used markers will be



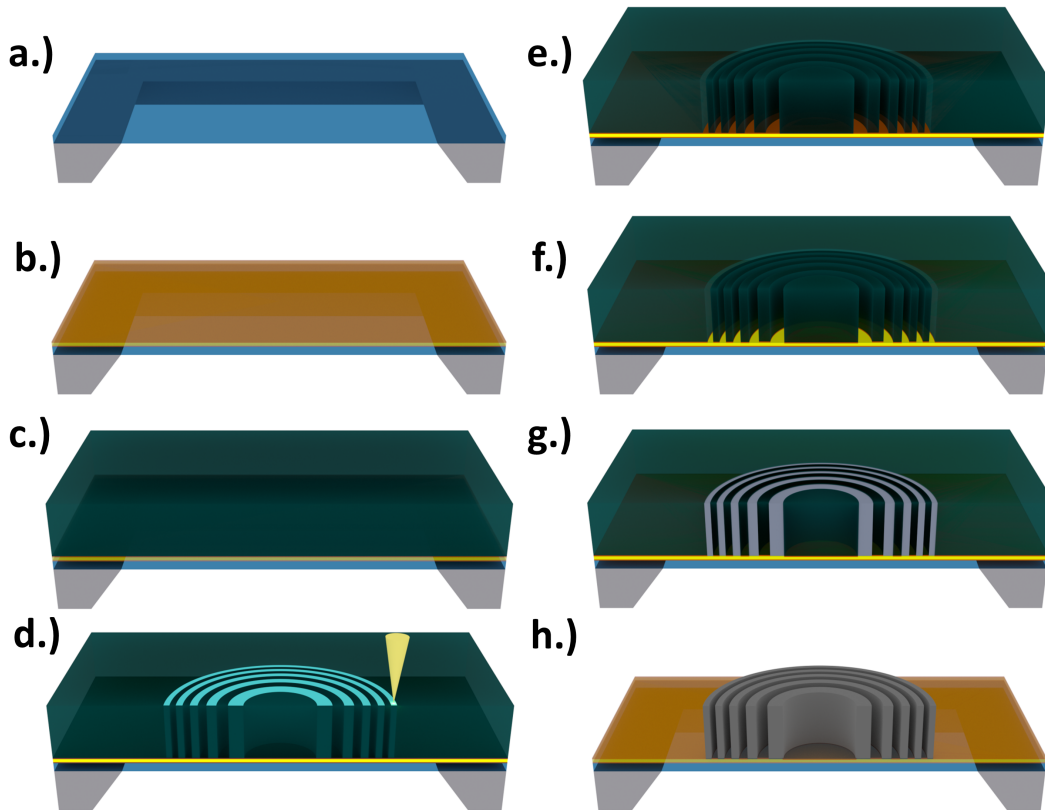


FIGURE 3.11: The mayor fabrication steps for the production of electroplated zone plates in PMMA resist. The empty  $Si_3N_4$  membrane (a.) is coated with a  $Cr/Au/Cr$  plating base (b.) and spin-coated with PMMA resist (c.). The zone plate patterns are directly exposed into the resist via e-beam lithography (d.) and the samples are developed in a mixture of  $IPA : H_2O$  (e.). The chromium layer is removed from the trenches using plasma etching (f.) and the mould is filled with electroplated nickel (g.). Finally the resist is removed by acetone or oxygen plasma (h.).

electroplated preventing their reuse in further processing steps as can be later seen on Figure 5.2. Electroplated zone plates also provide nearly optimal fill factor from the largest to the smallest zones corresponding to a smooth modulation transfer function in full-field microscopy.

### 3.7 High resolution zone plates in HSQ resist

The line-doubling of zone plates is a dedicated fabrication scheme for the production of high resolution zone plate optics. Originally developed by Konstantins Jefimovs[73] and further developed by Joan Vila-Comamala[74] it is used to produce high aspect ratio zone plate optics by patterning a high aspect ratio resist template and conformally coating it with heavy metal deposition. This section describes the implementation of this nanofabrication process for the production of high resolution zone plates discussed in Chapter 6 and 7 of this thesis.

The high resolution zone plates were also patterned on 100-250 nm thick silicon nitride windows (Fig. 3.13.a), that were coated by a chromium-gold-chromium metal layer for better conductivity and adhesion (Fig. 3.13.b). The latter is especially important as HSQ has poor adhesion on almost any metallic substrate and the exposed resist layer will shrink during the cross linking process, building up considerable amount of stress. Thermally evaporated chromium layers were better for resist adhesion than e-beam evaporated layers. Spin-coating of the resist layer was preceded by a short, high energy oxygen plasma sputtering to remove organic contaminations and increase surface roughness.

Commercial, undiluted FOX16 HSQ resist (Dow Corning) was used throughout this thesis. The resist was spin-coated on the sample substrate using the appropriate speeds (Fig. 3.13.c). HSQ resist can be coated on membranes with similar smoothness as PMMA, this requires the placement of a water droplet into the backside groove. This can provide homogeneous HSQ layers up to 1 micron thickness with a single coating step using 700 rpm spin speed. The chips were spin-coated for 1-1.5 minutes to evaporate most of the solvent from the resist layer.

Since HSQ has a very poor conductivity, special care was taken for grounding the conductive layers of the membranes during e-beam exposure. They were mounted above holes on the e-beam writer's holder for reduced backscattering from the titanium holder plates. Exposure patterns were generated by an optimized code for the efficient exposure of zone plate patterns in negative tone resist[175]. The addition of radial support structures increased the stability of the resist template and the ring-by-ring writing strategy minimized charging related issues (Fig. 3.13.d). Due to the narrow, high aspect ratio structures, the e-beam writer was set to a smaller aperture setting that increased its depth of field and reduced the spot size. Each batch of HSQ had its own required exposure dose in the range of  $6000 - 14000 \mu C/cm^2$ , that was slightly influenced by the 1-2 nA beam current and the beam step size. Due to the sharp threshold dose for crosslinking, the zone plates were exposed using a single dose value, that was sufficient to glassify the exposed resist.

The exposed chips were developed in a 1:3 mixture of a commercial *NaOH* and *NaCl* based developer (A351) and water (Fig. 3.13.e). Gas bubbles forming during development were removed by manual agitation. Once the trenches were fully developed after  $\sim 6 - 8$  minutes, the glassified resist structures bore great tolerance for additional development time up to a total of 12 minutes. After the development the samples were rinsed in a large bowl of water and placed in isopropanol. As fabricated nanostructures could approach aspect ratios of 40, capillary forces during conventional nitrogen-jet drying led to collapsing structures. Critical point drying (or supercritical drying) of the high aspect ratio structures ensured structure integrity by going around the supercritical region of the phase diagram as detailed in Section 3.5.

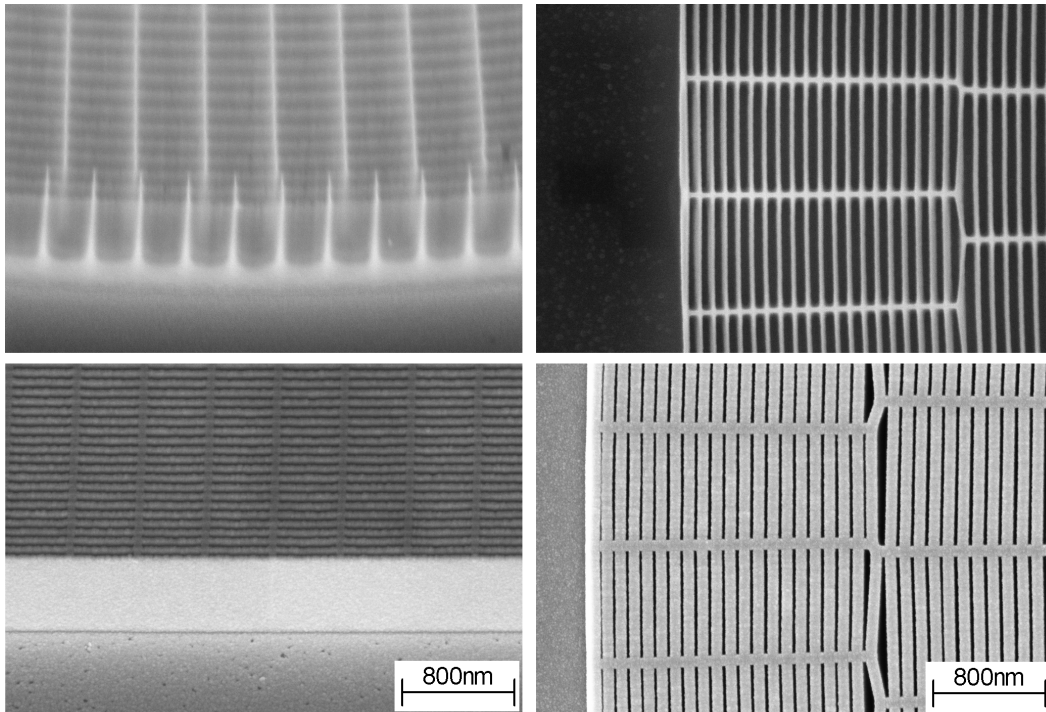


FIGURE 3.12: HSQ resist template before (up) and after (down) iridium coating. The uncoated HSQ template is patterned with 0.25 fill factor and is coated with iridium on both sidewalls, resulting in a final fill factor of 0.75.

The resist templates were subsequently coated with plasma-nucleated iridium, using atomic layer deposition (Fig. 3.13.f). As the deposited iridium layer has a uniform thickness, it must be adjusted to provide the best fill factor amongst the smaller zones while underfilling the largest central zones. However larger structures towards the centre can be fabricated with highly accurate profiles, whereas small errors in the resist profile become relatively more pronounced amongst the smallest zones. Incorrect fill factor not only alters the efficiency but also influences the zone placement on the sidewalls, directing more intensity into other diffraction orders. Hence fabrication inaccuracies amongst the smallest zones and the low fill factor amongst the centre both lead to a drop in efficiency in the mentioned regions.

The advantage of line-doubled zone plates is their high resolution combined with high efficiency. Line-doubled zone plates with 10 nm smallest zone width, as well as 20 nm zone plates with aspect ratios close to 30 have been demonstrated in the literature<sup>[74]</sup> providing optimal structure heights in the multi-keV range. The optimal smallest zone width range of HSQ template patterning is around 20 – 30 nm, where aspect ratios close to 30 can be reproducibly achieved in thick resist layers. For thicker layers beam forward scattering becomes a mayor challenge, while the secondary electron range limits the width of smaller structures. The fabrication of line-doubled zone plates is a relatively simple, high-yield process.

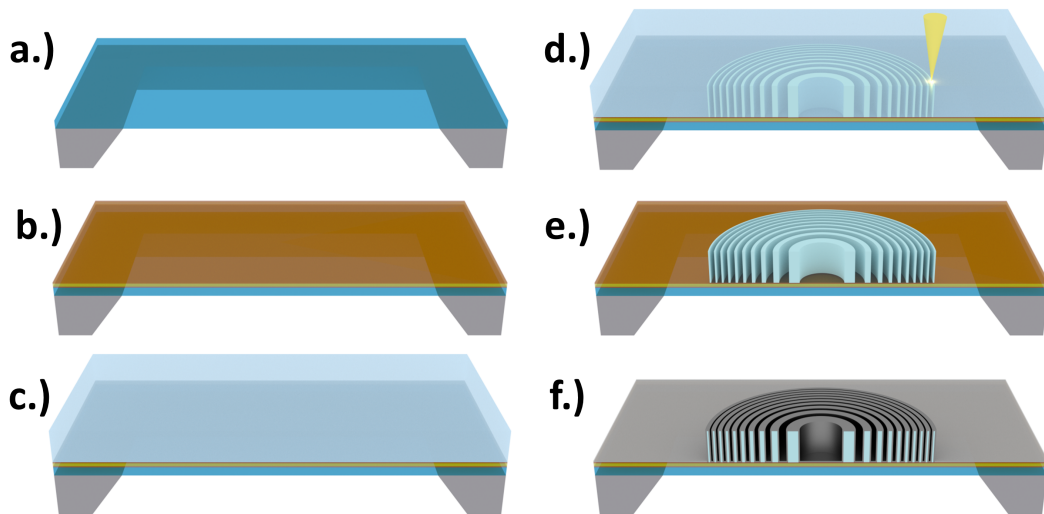


FIGURE 3.13: The mayor fabrication steps for the production of line-doubled zone plates in HSQ resist. The empty  $Si_3N_4$  membrane (a.) is coated with a  $Cr/Au/Cr$  conduction layer (b.) and spin-coated with HSQ resist (c.). The sparse template is directly exposed into the resist via e-beam lithography (d.) and the samples are developed in a salty solution and dried by critical point drying (e.). Finally the template is conformally coated with iridium using atomic layer deposition (f.).

A disadvantage of line doubled zone plates is their inherent high-pass spatial filtering, especially when used as an objective in full-field X-ray microscopy. This requires carefully matching the numerical aperture of the condenser to the objective and will be particularly problematic in Chapter 7.

### 3.8 Simulations

Several methods have been presented in the literature for the simulation of diffractive X-ray optics[84, 91, 102], yet prior methods were restricted to periodic boundary conditions[91] or radial symmetry[84] to reduce the required computational resources. Since many of the hereafter presented cases do not satisfy these criteria, they require a complete description of their optical behaviour.

Detailed description of the algorithms have been discussed in Chapter 2, as well as they can be found in the literature[105]. The base of the simulations is the representation of the wavefield. As seen on Figure 3.14, this is a large complex matrix that maps the amplitude and phase of the progressing electromagnetic radiation in the particular plane in 64 bit double precision for accurate representation. Its size can go up to several terapixels –limited by the available system memory– and it is the only large dataset in the code. Since most X-ray optics can be generated by their construction rules, the optical transmittance profile of optical elements (zone plates, beam shapers, pinholes) were dynamically generated according to Eq. 2.42 to conserve memory. The pixel size was chosen to adequately map the smallest structures of the simulated zone

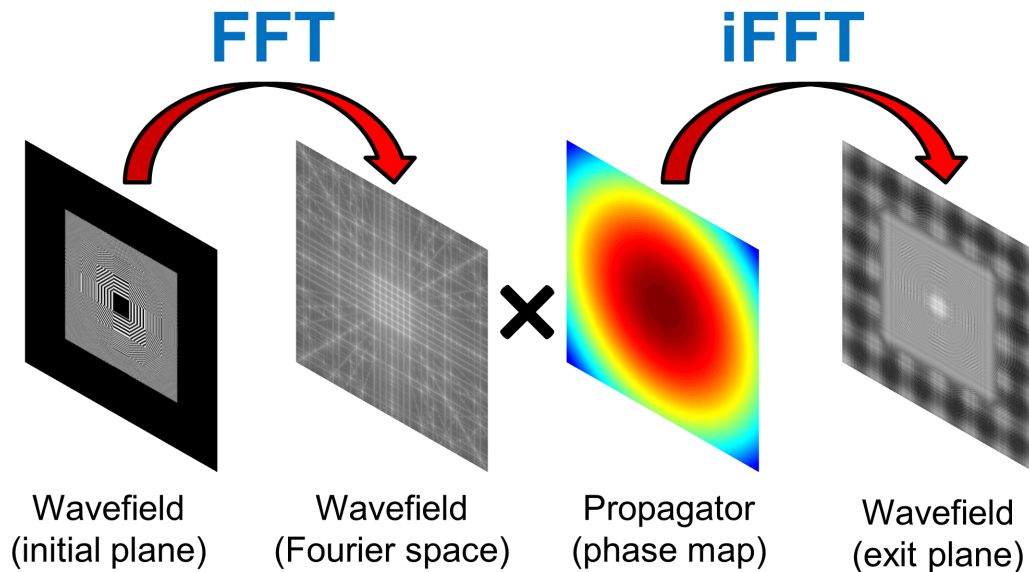


FIGURE 3.14: Schematic flowchart of two dimensional wavefield propagation. The initial wavefield is Fourier transformed and multiplied by the propagator's frequency map in Fourier space. Upon transforming the wavefield back to real space, the wavefield will be in the exit plane.

plates, that was at least 15 pixels describing the smallest zone width and  $\sim 40$  pixels when calculations involved volumetric effects and near-field phenomena. In order to reduce artefacts from the periodic boundary condition induced by the Fourier transform, the patterned areas were surrounded by a large empty border. Propagation of the wavefield between the planes were calculated by the angular spectrum method. This propagator is well-suited for finite propagation distances as it leaves the pixel size and orientation unchanged. Each propagation involves the calculation of the forward Fourier transform of the wavefield, multiplying it with a quadratic phase term as Eq. 2.45 and calculating the reverse Fourier transform of the wavefield. Even when using fast Fourier transform[106, 107], the calculation time of this step rapidly increases with increasing number of pixels, hence for large arrays the FFT takes up most of the computation time with the other steps becoming negligible.

Although the exact algorithms are well described in the literature as well as in the previous chapter, their exact implementation can vary according to the available infrastructure. At the Paul Scherrer Institute, practically there were two kinds of computing resources: a standard office desktop and a hard-to-access high performance supercomputer running a historical Linux distribution. Workstations were available upon occasional request as dedicated computing resources of particular groups. Hence in order to fill this gap and ensure both high performance and availability, the possibilities

were extended by a high performance personal computer with 32 GB of RAM for storage, an AMD FX 8320 CPU and Radeon 7950 graphics card<sup>2</sup> for compute performance. Accordingly to the available hardware, two versions of the simulation software has been developed, depending on memory demand:

Memory-intensive simulations were done on a high-end workstation at PSI with 196 GB memory and two Xenon 1450 v3 CPUs. This simulation code was written in C++ and employed the FFTW library[177] for efficient Fourier Transforming algorithm and OpenMP for parallel processing.

The majority of the simulations presented in Chapter 4, 6 and 7 were performed on the personal computer, using the GPU for intensive computing. This implementation was written in OpenCL and employed AMD's clFFT package for high-speed Fourier Transforming on GPUs. The program was prepared to handle larger datasets than the GPU's on-board memory by segmenting the task to smaller slices, thus the upper limit was the 32 GB total of memory. In order to minimize data copy, subsequent steps were fused into one single processing step. As a comparison, the calculations were 3 – 5 times faster on the commercial GPU than on the workstation.

---

<sup>2</sup>Most consumer graphics cards have their double precision performance heavily penalized due to market segmentation. AMD's Radeon 7900 series was an exception with the FP64/FP32 ratio of 1:4 in comparison to Nvidia's GTX 980's 1:32 ratio.

## Chapter 4

# The mechanical stacking of blazed zone plates

Large aperture, high efficiency zone plate lenses with restricted working distance are flexible and cost-effective focusing optics for a wide range of practical applications. However as described in Chapter 2, the diffraction efficiency of conventional binary diffractive X-ray optics is fundamentally limited to 40.5% even in the idealized non-absorbing case. Symmetric structures always diffract half of the intensity into unwanted defocusing diffraction orders. This point has been addressed with the introduction of blazed multilevel zone plates[71, 81]. Yet existing approaches face severe drawbacks due to limitations in aperture size, wavefront quality, resolution or working distance. The blazed stacking of zone plates[85] has been proposed as an alternative method to avoid the fabrication of multilevel profiles. By stacking two complementary zone plates in each-others optical near-field, the blazed stacking of zone plates can double the number of steps in the optical transmission profile without the actual fabrication of multilevel structures. Therefore, this chapter is aimed surpass the limitation of binary zone plates by the blazed stacking of zone plates as described in [178] and [179].

### 4.1 Design considerations

The goal was to collect as many photons as possible in the 5-12 keV energy range. This required to maximize focusing efficiency and aperture size and although the resolution was not an important factor, but the smallest zone width had to be constrained to keep the focal length at bay. Maximizing the focusing efficiency requires going beyond binary zone plates. The blazed stacking of zone plates stacks two complementary binary zone plates, a "coarse" zone plate with  $\pi$  phase shift, and a double density "fine" zone plate with  $\pi/2$  phase shift in each others optical near-field. The combined stack will equal a four level profile in transmission as shown in Figure 4.1, allowing up to a factor of two

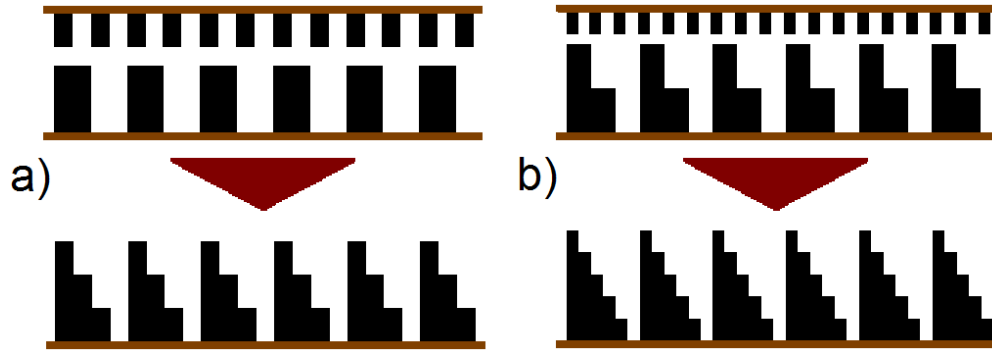


FIGURE 4.1: The blazed stacking of two zone plates offers to double the number of steps in the optical transmission profile. This allows stacking two binary zone plates into an effective four step profile (a.) as well as creating a six step profile from a pair of three level and a binary zone plate (b.). The multilevel zone plates can have greatly enhanced focusing efficiency as seen earlier in Figure 2.6.

gain focusing efficiency. Yet the number of steps can be further increased as illustrated on Figure 4.1. By stacking an  $n$ -step multilevel zone plate with an  $n$  times denser binary zone plate with  $\pi/n$  phase shift, the number of steps can be doubled in the optical transmission profile, bringing six step zone plates within reach.

In order to achieve a better coverage of the spectral range, two complementary sets of zone plates -made from gold and nickel- were planned. Considering the required structure heights shown of Figure 2.5 for gold and nickel, nickel zone plates were fabricated with 200 nm smallest zone width for the 5-8.4 keV and gold zone plates were fabricated with 150 nm smallest zone width for the 8-12 keV range. An aspect ratio of  $\sim 12$  was considered within the safe range of the process window. Maintaining a reasonable focal length was done by tuning the zone plate diameter in the 100 – 500  $\mu\text{m}$  range. The nickel zone plates were optimized to 6.5 keV where 2.3  $\mu\text{m}$  high structures provide  $\pi$  phase shift. The gold zone plates were optimized for 9 keV photon energy starting from 1.1  $\mu\text{m}$  ideal structure height. At this energy binary nickel zone plates are limited to 37% efficiency but four step profiles can provide up to 71% focusing efficiency. Due to higher absorption, binary gold zone plates are limited to 31% while a four step profile can provide up to 61% efficiency.

## 4.2 Sample fabrication and characterization

We used the fabrication method developed by Sergey Gorelick[72] for the production of high aspect-ratio metallic nanostructures with direct e-beam writing of PMMA resist mould and subsequent electroplating. A general overview of the fabrication process have been discussed earlier in Chapter 3, but additional details are summarized in the following paragraphs.



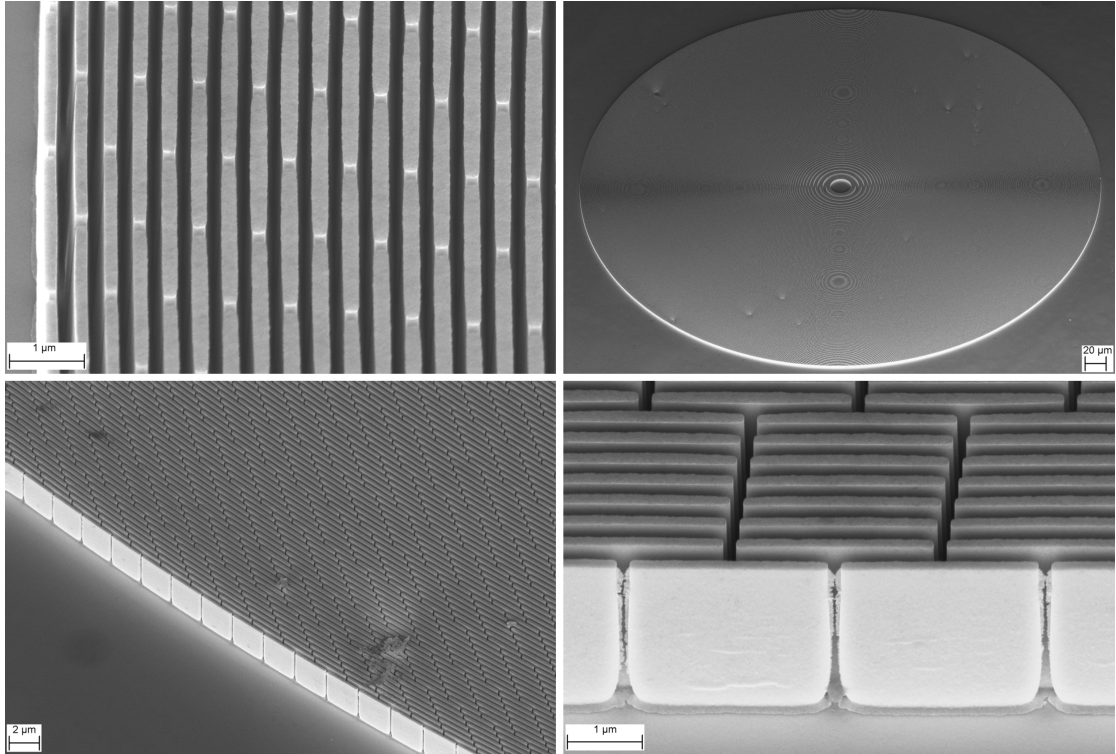


FIGURE 4.2: SEM images of a binary nickel zone plate as the "coarse" zone plate. The  $2.5 \mu\text{m}$  high and  $200 \text{ nm}$  wide structures visibly broaden towards their footing due to beam forward scattering.

The zone plates were prepared on  $1 \times 1 \text{ mm}^2$  sized,  $250 \text{ nm}$  thick  $\text{Si}_3\text{N}_4$  membranes on  $3 \times 3 \text{ mm}^2$  Si support frames with an evaporated Cr/Au/Cr plating base. The membranes were spin-coated with PMMA resist approximately  $100 \text{ nm}$  thicker than the expected structure height and the zone plate patterns were directly exposed into the resist layer by  $100 \text{ keV}$  electron beam lithography. For the three level monolithic zone plates, additional alignment markers were exposed together with the first layer of zone plate patterns. After developing and electroplating the first layer, an additional layer of PMMA was coated over the filled mould and the second exposure was precisely aligned over the first layer using the exposed alignment markers. Similarly to binary zone plates, exposed samples were developed in a mixture of isopropanol and water (7:3 by volume)[158] cooled to  $2^\circ\text{C}$  and the trenches were cleaned with oxygen plasma. The mould was subsequently filled with metallic nickel or gold using electroplating and removed via ashing in oxygen plasma.

The fabricated zone plates were pre-characterized by optical and scanning electron microscopy (SEM) in order to select the most promising candidates for X-ray analysis (Fig. 4.2). The linewidth was not optimized for fill-factor in the SEM but to show lower structure width. As described in Chapter 3, topmost SEM inspection was misleading due to non-vertical side-walls and structure broadening.

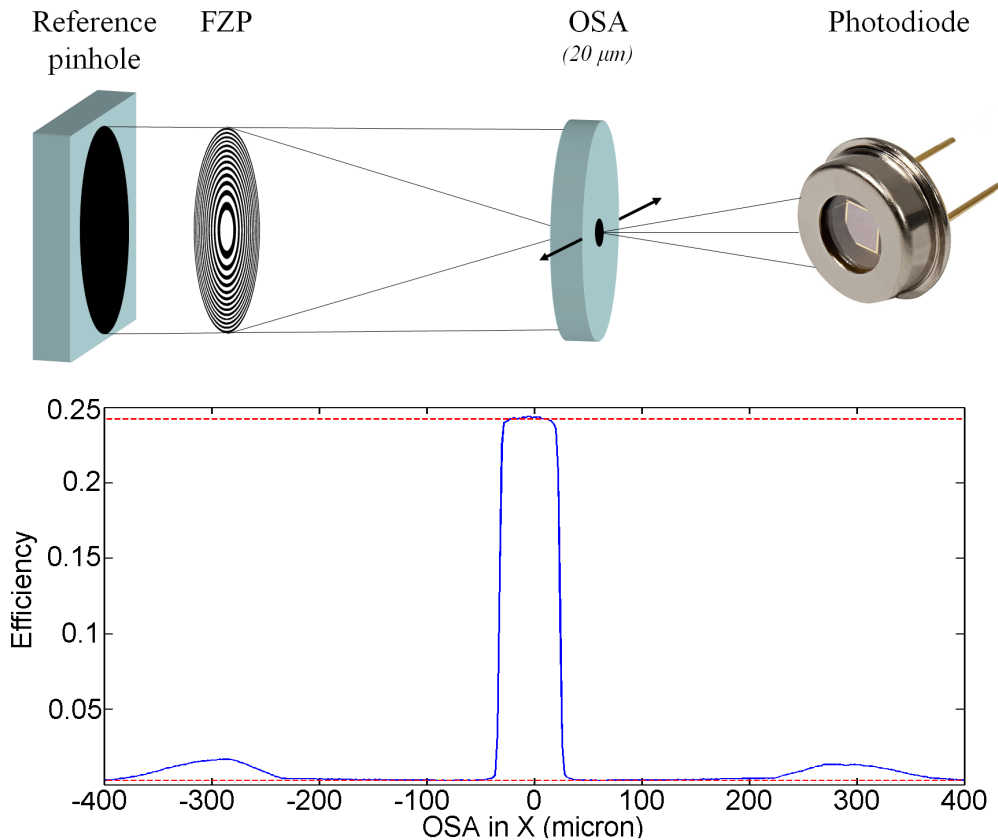


FIGURE 4.3: Up: Example of the setup for measuring the efficiency of Fresnel zone plates. The zone plate is illuminated through an equal sized reference pinhole. The first order focus is selected by a  $50 \mu\text{m}$  pinhole as order selecting aperture, that is being scanned through the focal plane. The transmitted flux is recorded as current on a photodiode and is normalized by the illuminating flux. Down: Normalized current on the photodiode during the OSA scan. A focusing efficiency of 0.239 is calculated by subtracting the background from the plateau.

### 4.3 Early measurements

Early measurements on the first set of fabricated Fresnel zone plates were performed at the cSAXS beamline of the Swiss Light Source using zone plates with 500 micron diameter and 200 nm smallest zone width and at a photon energy of 6.2 keV.

#### 4.3.1 Efficiency measurements

As blazed zone plate stacks are aimed towards increasing focusing efficiency, efficiency measurements carry the key message about the tested lenses. Hence the zone plates were illuminated through an upstream reference pinhole of equal diameter and the desired diffraction order was selected by a pinhole as order selecting aperture (OSA) in the targeted order's focal plane. While the pinhole was scanned across the focal plane, the intensity transmitted through the pinhole was recorded using a photodiode detector. The measured "background" current on the photodiode corresponds to the directly

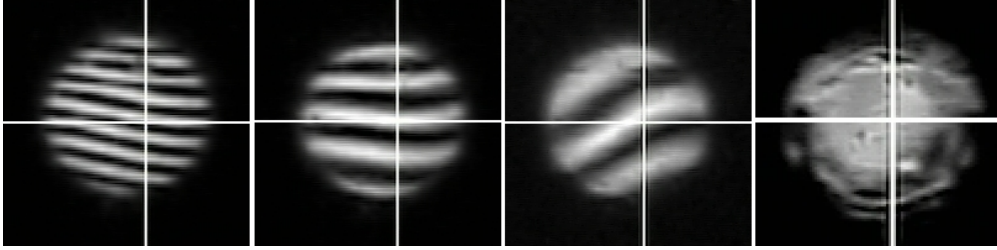


FIGURE 4.4: Aligning a stack of zone plates within an X-ray camera by eliminating Moiré fringes in the diffraction cone.

transmitted  $0^{th}$  order while the focal spot is outside of the pinhole. When the focal spot is within the OSA, the photocurrent corresponds to the focused intensity. The  $0^{th}$  order was subtracted from the focused intensity and was normalized with the reference current that was measured when the photodiode was illuminated through the reference pinhole with no zone plate or OSA in the beam.

The best zone plate with 23.9% focusing efficiency was chosen as coarse zone plate for stacking. The fine zone plate was selected by the lowest  $2^{nd}$  diffraction order implying good fill-factor. After selecting a suitable pair of coarse and fine zone plates, the pair was stacked into each others near-field, using a compact piezo actuator based mechanical stacking setup. To achieve the needed precision of  $\sim 60\text{ nm}$ , a two step alignment procedure was used. The coarse zone plate was mounted on a fixed stage on an optical rail with manual alignment, allowing a large movement range. The fine zone plate was mounted on an XYZ piezo stage with a movement range of  $100\ \mu\text{m}$ . The mechanical pre-alignment was performed offline with the aid of an optical microscope in order to bring the two zone plates within the piezo range. The lateral distance of the zone plates was adjusted by the transmitting light, while the axial distance was tuned using the narrow focal depth of the microscope. The final alignment was done in the X-ray beam, by exchanging the photodiode to an X-ray camera and inspecting the Moiré-fringes of the diffracted cone (see Figure 4.4.). When all Moiré fringes disappeared, the zone plates were assumed to be well aligned on a common optical axis.

The measured 36.7% focusing efficiency of the stack was far below expectations, prompting investigations to track down the reasons behind the loss of intensity. One can record spatially resolved maps of the diffraction efficiency by scanning a  $30\ \mu\text{m}$  pinhole upstream of the zone plate illuminating it only partially. During the scan, the focused intensity passing through the OSA can be recorded and normalized by the map of the background illumination with the same pinhole. The measurement was performed on well aligned,  $0.3\ \mu\text{m}$  (slightly) misaligned and  $3\ \mu\text{m}$  (completely) misaligned zone plate stack. As seen on Figure 4.5., the diffraction efficiency is highly inhomogeneous over the zone plate area even for the well aligned zone plate. While some areas exhibit high diffraction efficiency in the 40% range, a significant portion of the stack has poor

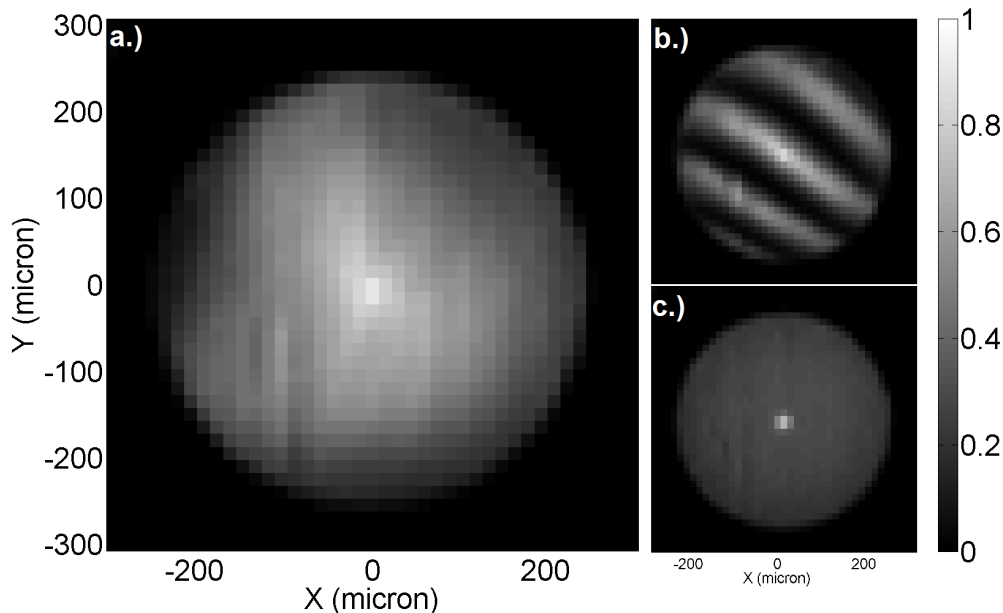


FIGURE 4.5: Spatially resolved efficiency map of stacked zone plates in a.) optimal alignment, b.)  $0.3 \mu\text{m}$  misalignment and c.)  $3 \mu\text{m}$  misalignment. Due to the "dead" areas in the well-aligned case, the mean diffraction efficiency reaches only 37.3%. By slightly misaligning the two zone plates the appearing Moiré fringes are not straight. With larger misalignment the density of fringes increases until they are unresolved.

performance. In fact, some dark areas have so disappointingly low efficiency, that it is even too low for a binary zone plate, bringing us to the question of our next section.

### 4.3.2 Spatially resolved measurements

As the dark areas have lower efficiency than the original binary zone plate, a highly plausible explanation is that in these areas the anti-blazing achieves the opposite effect than expected from blazed zone plates. If there are local deformations, the whole zone plate area can not be brought into perfect overlap. Even for the best global alignment, some areas will remain locally misaligned, as dark areas on Figure 4.5. With distortions over  $1/4$  of the local zone-width, the anti-blazing suppresses the focusing  $+1^{\text{st}}$  order while enhancing the parasitic  $-1^{\text{st}}$  order.

In order to obtain more information about the lenses, the photodiode detector was replaced by a Pilatus 2M single photon counting detector  $7.2 \text{ m}$  downstream of the OSA. The air-gap was reduced by a  $7 \text{ m}$  long, helium-flushed flight tube. An additional  $30 \mu\text{m}$  pinhole was also mounted beside the reference pinhole, to allow for a partial illumination of the zone plate.

When the full zone plate is illuminated through the reference pinhole, on the detector we record the expanded defocused cone of the zone plate. This cone is essentially a spatial map of diffraction efficiency superimposed on the beam profile. By scanning the alignment piezos while taking images of the diffracted cone, one can collect the spatial

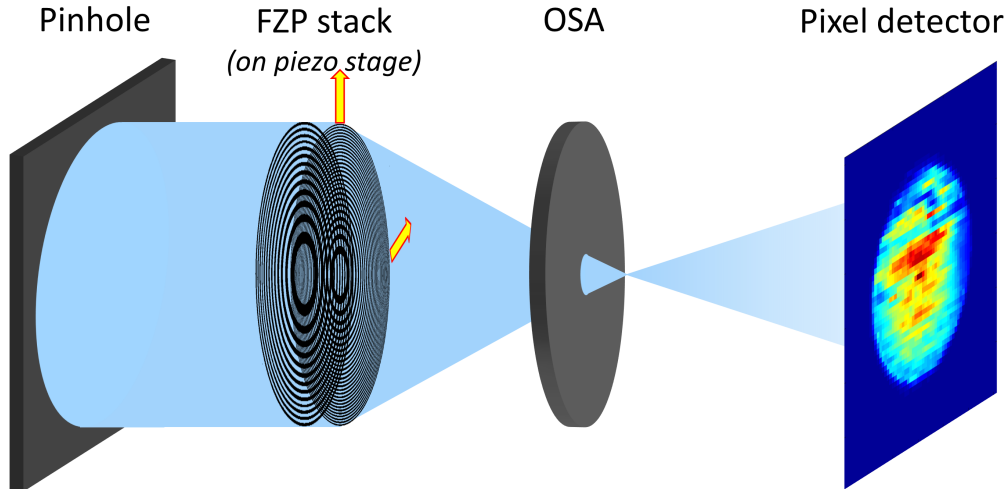


FIGURE 4.6: Experimental setup for spatially resolved measurements. The zone plate can be fully illuminated through the reference pinhole, or partially illuminated by a  $30\ \mu\text{m}$  pinhole. The order selecting aperture can be removed to allow all orders to reach the Pilatus 2M photon counting pixel detector. This is placed downstream after a  $7\ \text{m}$  long, helium flushed flight tube.

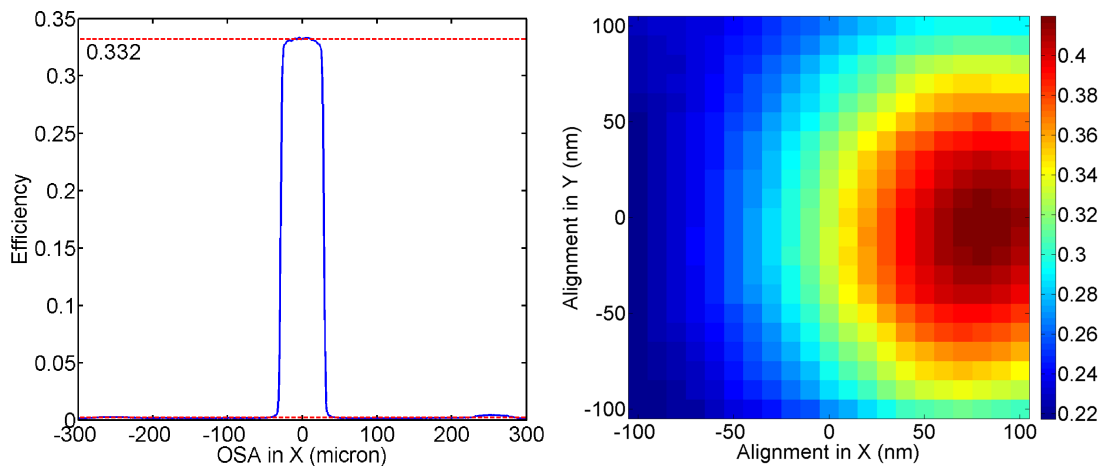


FIGURE 4.7: a.) OSA scan across the focal plane of the stacked zone plate pair right before scanning the piezo measuring 33.2% focusing efficiency. b.) Scanning the alignment piezos around the optical axis while monitoring the intensity is a more accurate alignment method than Moire fringes. It shows that the alignment could have been further refined providing up to 41.9% focusing efficiency.

map of the efficiency in all alignments. With the right shift in global alignment, the local distortions are compensated and the dark areas of the stack brighten up. The other revelation of this measurement was that the disappearance of Moire fringes does not mean the absolutely best alignment. As can be seen on Figure 4.7, it only corresponds to less misalignment than the smallest zone width. In fact by scanning the piezos in 2D, the stack gave its best performance 70 nm apart from our starting point, reaching as high as 41.9%. Hence scanning the piezos turned out to be a fail-safe method for catching the zone plates in their very best alignment.

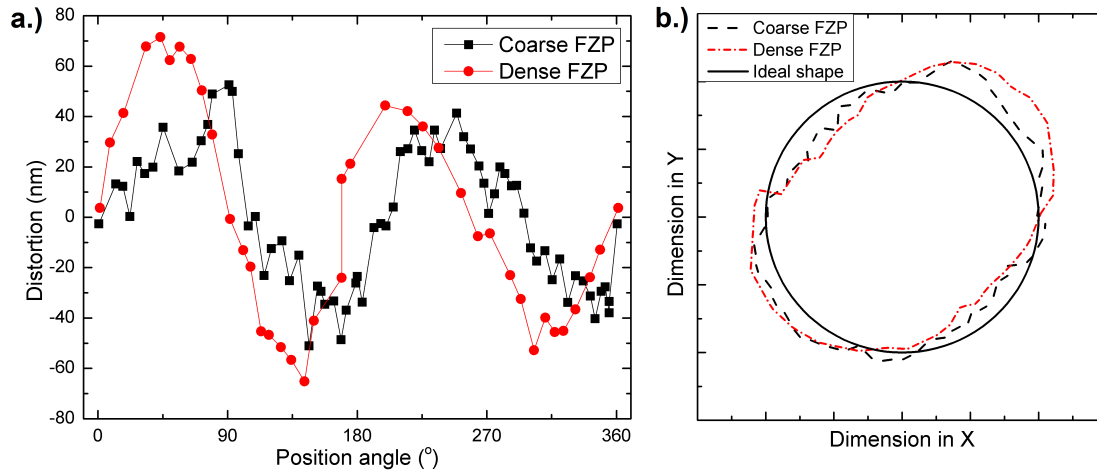


FIGURE 4.8: Zone plate distortions measured by topological SEM a.) as a function of angle and b.) as heavily exaggerated contours, showing in-phase ellipticity in both zone plates along the diagonal of the write field.

Direct mapping of deformations was performed with the interferometric stage of a Leica LION LV-1 e-beam tool in SEM mode. We tracked the position of a zone close to the zone plate edge around the circumference and compared its radius with the calculated value. The mapping seen on Figure 4.8 revealed deviations up to  $\pm 70\text{ nm}$  and showed a clear ellipsoidal main component being in-phase for both zone plates. Since the zone plates were mounted in random orientation the two ellipses did not overlap. By mounting the two zone plates in a 90 degrees angle with respect to the electron beam writers write field, the two ellipses can be brought to overlap.

#### 4.4 Final measurements

The final iterations of mechanically stacked Fresnel zone plates were performed at the Metrology beamline of Synchrotron SOLEIL. This is a bending magnet beamline with a relatively compact hutch. The complete instrumentation was mounted on three separate towers, including the photodiode and CCD detectors. Learning from previous mistakes some changes were implemented to the stacking procedure including:

- Reducing exposure dose of the zone plates to decrease line broadening towards the bottom of our structures. This was expected to increase the performance of the coarse zone plate, which was relatively low during the prior experiments.
- The zone plates were mounted in the proper rotational orientation in respect to each other. The setup also allowed the manual rotation of the coarse zone plate (although this required complete realignment).
- The efficiency of the stack was measured by scanning the alignment piezos around the optical axis while measuring the photodiode signal. This will show a peak,

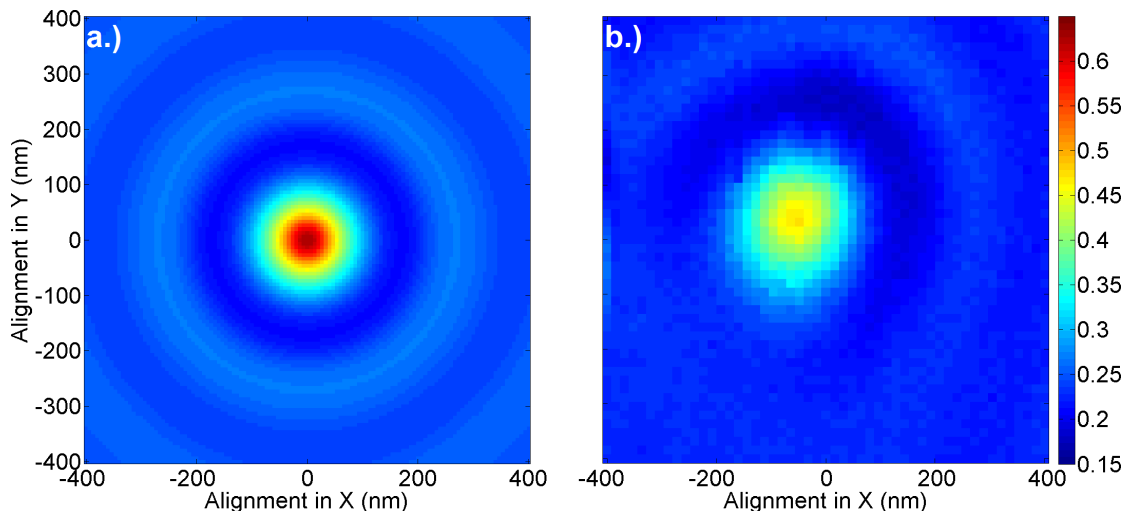


FIGURE 4.9: Efficiency of the four step zone plate stack as a function of misalignment as a.) simulated and b.) as measured. The measured decrease of efficiency is not radially symmetric due to zone placement errors.

when the two zone plates are on the common optical axis (in agreement with simulations). The diffraction efficiency was determined as the height of this peak, corresponding to the best alignment of the two zone plates.

#### 4.4.1 4-level blazed zone plate stacks

The first measurements were performed by stacking a pair of binary zone plates to produce an effective four-level profile as shown on Figure 4.1.a. These zone plates had 500 micron diameter and 200 nm smallest half-pitch. They were measured at the photon energy of 6.5 keV.

In order to use the best pair of zone plates for stacking, first the efficiency of the coarse lenses was measured individually. The best coarse zone plate was chosen as the one with the highest efficiency. With 31.0% efficiency on its own, this was clearly superior to the ones tested at the prior measurements. Due to the lack of obvious benchmark values, the fine zone plates were chosen based on prior SEM inspection.

During the optical pre-alignment procedure, excessive tilt of the zone plates was eliminated by aligning the zone plates parallel to our microscope's focal plane. The optical alignment of the zone plates was first refined in the X-ray beam by eliminating Moiré fringes. Yet this time, the focused intensity was measured by scanning the alignment piezos around the optical axis ensuring that the zone plates are caught in the best alignment. The efficiency measurements were repeated in multiple orientations, starting from the expected best overlap for two ellipsoidal zone plates, in this orientation focusing efficiencies up to 47.1% were measured as displayed on Figure 4.9.

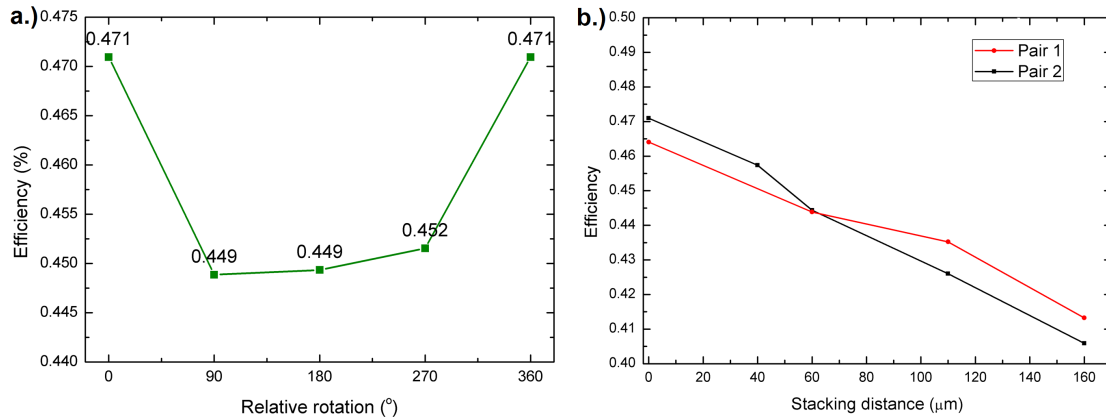


FIGURE 4.10: Measured focusing efficiency of the zone plate stack a.) in different rotational alignment and b.) at different stacking distances. Zero stacking distance corresponds to the closest contact-free distance of the chips.

One can observe that the patterns are slightly distorted from their expected circular symmetry, suggesting that the zone plates are still slightly distorted from their ideal circular shape, reducing the achievable efficiency. Figure 4.10 indicates that the effect of fine-tuning the rotational orientation and stacking distance on the focused efficiency is on the order of  $\sim 10\%$  of the total efficiency.

Altogether, the higher structure quality, the correct angular alignment and the fail-safe measurement method provided us with clearly superior zone plate performance, than achievable with a single zone plate.

#### 4.4.2 6-level blazed zone plate stacks

In order to expand the concept of the blazed stacking of zone plates, we have also tested the stacking of a three-level multilevel zone plate with a binary zone plate to create an effective six level profile as illustrated on Figure 4.1.b. The experimental setup was more compact during this experiment limiting the diameter to  $200\ \mu\text{m}$  for nickel zone plates with  $200\ \text{nm}$  smallest half-pitch. Similar to the four level zone plates, the coarse zone plate was chosen as the best performing 3-level nickel zone plate with  $40.4\%$  efficiency at  $6.5\ \text{keV}$  and a suitable dense zone plate was chosen based on SEM inspection. The original plan was to include gold zone plates with  $150\ \text{nm}$  smallest zone width and the coarse zone plate was chosen with  $33.8\%$  focusing efficiency at  $9\ \text{keV}$ . However due to the grain-size problems with the gold electroplating bath described in Chapter 3, there were no unaffected dense zone plates. As visible on Figure 4.12, grains clearly distorted the zone plate wavefront thus the idea was not pursued further. Nevertheless, both the  $200\ \text{nm}$  nickel and  $150\ \text{nm}$  gold zone plates reached  $\sim 66\%$  of their theoretical efficiency, suggesting similar optical quality.

The alignment procedure was also identical to the four step zone plates, thus after tilt elimination and pre-align the final efficiency measurements were performed by



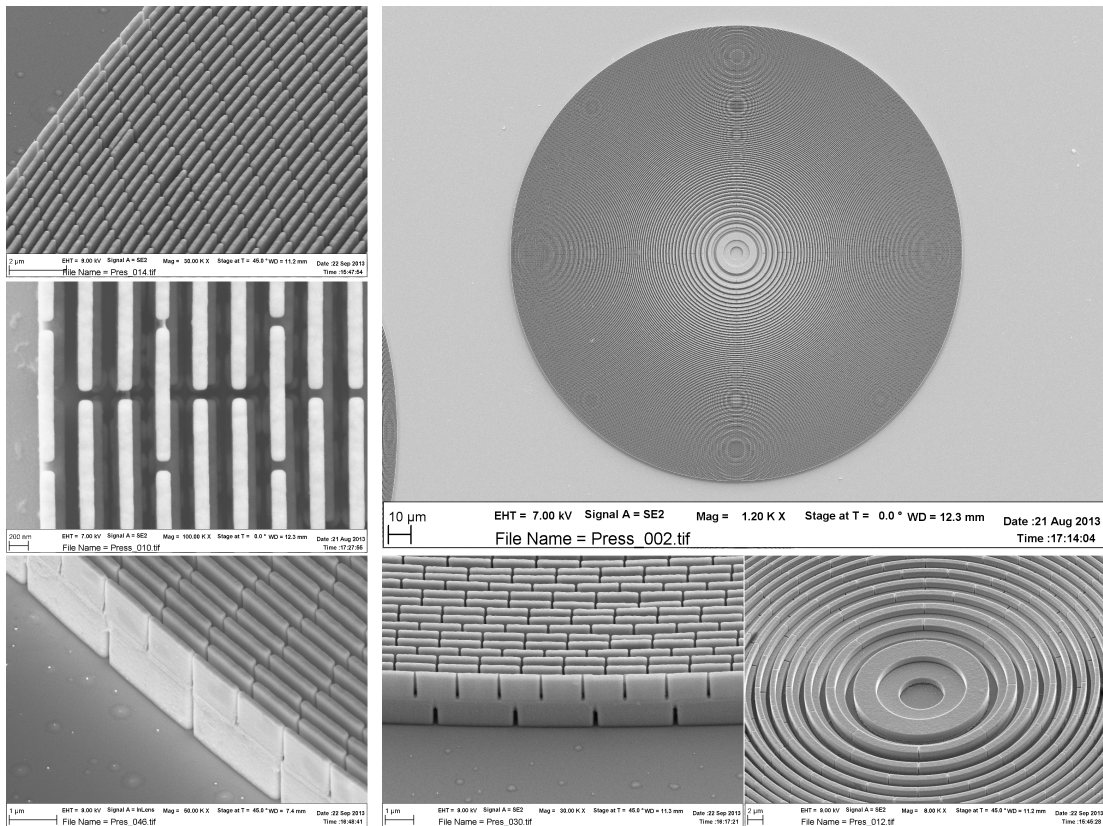


FIGURE 4.11: SEM images of the 3 level coarse nickel zone plate of the 6 level stack. The individual levels are of 1.6 and 1.8 micron height and are accurately positioned above each other.

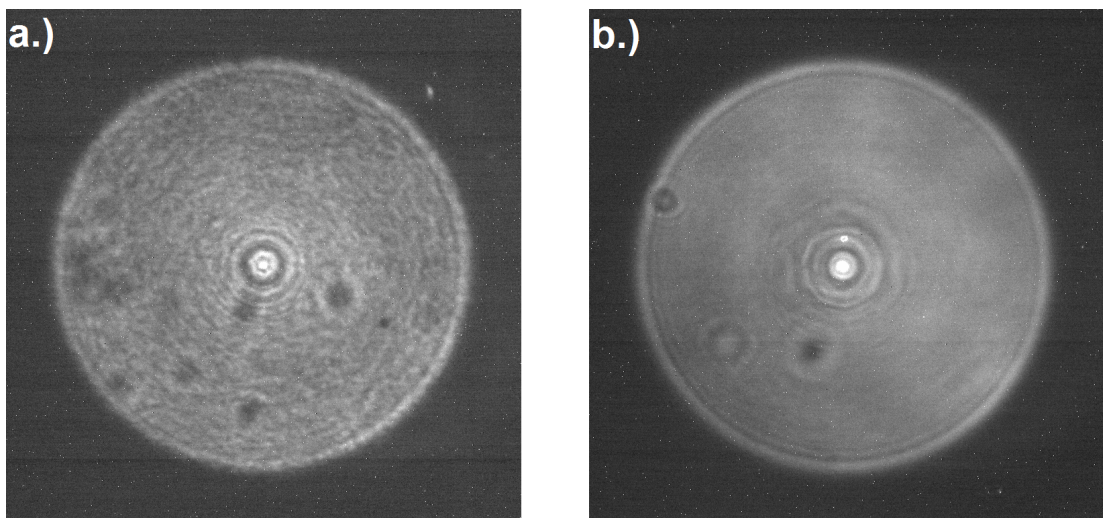


FIGURE 4.12: Diffraction cones of a.) grainy and b.) smooth gold zone plates (with some dust particles on the scintillator). The grainy gold zone plates not only had lower efficiency but also visibly different wavefront, more importantly small angle scattering around the focus.

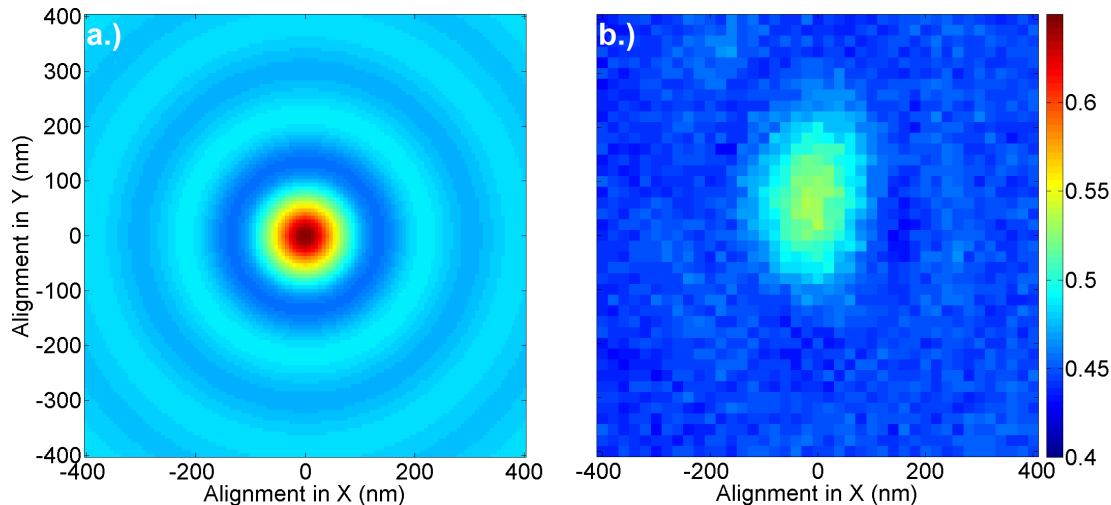


FIGURE 4.13: Efficiency of the six step zone plate stack as a function of misalignment as a.) simulated and b.) measured. The alignment peak is noticeably larger than expected which is probably caused by zone misplacements. The preferred direction of the misalignment also supports this theory. Note that misalignment leads to a considerably smaller drop in efficiency than in the four level case.

scanning the alignment piezos around the optical axis while measuring the current on the photodiode. The zone plates were mounted in the expected best orientation but this was not changed during the measurements. The measured efficiency of 53.7% stands for another clear improvement over binary and three step zone plates and clearly surpasses the previously measured four step zone plate stack. From Figure 4.13 it was also found that the stack was much more resistant to misplacement than expected from simulations, suggesting residual deformations in the zone plates.

As the aim of this experiment was to provide high efficiency focusing optics for X-rays in the 5-8.4 keV energy range, we repeated the measurements at several photon energies covering the 5.5-8.5 keV range as seen on Figure 4.14. It became confirmed, that our effectively 6-level zone plate stack provides over 40% focusing efficiency in the whole 6-8 keV range and only falls below this after the nickel edge. This proves that blazed zone plate stacks retain their advantages over a broad wavelength range.

## 4.5 Conclusions

The blazed stacking of Fresnel zone plates paves the way for high efficiency zone plates when no ultimate resolution is required. Our experiments clearly show that the blazed stacking of zone plates can surpass the limitations of binary zone plates while using the well-established high aspect-ratio patterning techniques of binary zone plates. The measured 47.1% diffraction efficiency with a 4-step zone plate stack over a 500 micron aperture and 200 nm smallest zone width offers a gain of  $10^6$  compared to the intensity of the illuminating beam. The efficiency can be even further improved with adding more

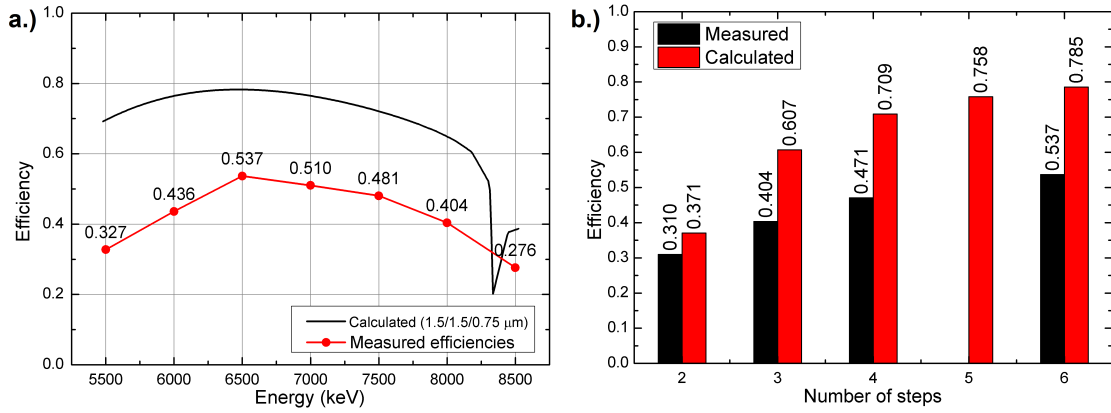


FIGURE 4.14: Focusing efficiency of the 6 step zone plates as a function of energy (a.). The Focusing efficiency stays beyond 40% between 6-8 keV. A summary of measured and theoretical zone plate efficiencies as a function of the number of steps (b.). All results were obtained at 6.5 keV for zone plates of 200 nm smallest zone width.

steps, reaching as high as 53.7% with an effectively 6-level stack. This makes blazed zone plate stacks ideal for micro-probe applications where high efficiency is preferred to push the limits of resolution and sensitivity. Potential applications include trace element analysis, microfluidics, coherent diffractive imaging and condenser optics in full field microscopy.

Besides the impressive performance of the demonstrated stacked zone plates, the use of the mechanical stacking greatly complicates the experimental setup. We encountered severe drifts with the piezo setup. Therefore day to day use of zone plates would benefit significantly from a compact, permanently fixed setup. Therefore the next chapter will describe efforts to provide the benefits of stacked zone plates in a permanently fixed geometry.



## Chapter 5

# Double-sided blazed zone plates

This chapter presents an innovative way to produce monolithic stacks of Fresnel zone plates by the aligned patterning of both the front and back side of the very same membrane. In such double-sided arrangement, the two sides will act as the two zone plates of a stack, providing the benefits of blazed zone plate stacks as a single chip solution.

### 5.1 Motivation and design consideration

The stacking of zone plates is a well-established method to ease fabrication constraints of diffractive X-ray optics. In the previous chapter it was shown that it is capable to produce very high efficiency zone plate optics with clear advantages over their binary counterparts. Yet, present day implementations of stacking suffer from major limitations regarding alignment, stability or complexity. Additionally, in order to achieve sufficient accuracy, stacks require alignment within the X-ray beam and even then, the matter of maintaining the alignment remains unanswered.

The only way to avoid any drift is to pattern them on the very same membrane. In conventional multilevel patterning[71] or on-chip stacking[92], the upcoming layers are built on the foundations of the previous layers. Any error in an underlying layer will propagate through the following layers, which puts high emphasis to process reliability. However, there is also a very straightforward way of implementing zone plate stacks on the same membrane as **the membrane has two sides**.

By patterning the two zone plates of the stack on the front and back side of a membrane –similarly to zone plate stacking– they will act as a single zone plate with combined transmission profile. While the two sides must be aligned during fabrication, they will maintain their alignment indefinitely. The actual patterning of the two sides is independent from each other, allowing to pattern the coarse and fine zone plates of the stack on the very same membrane. Similar to the blazed stacking of zone plates,

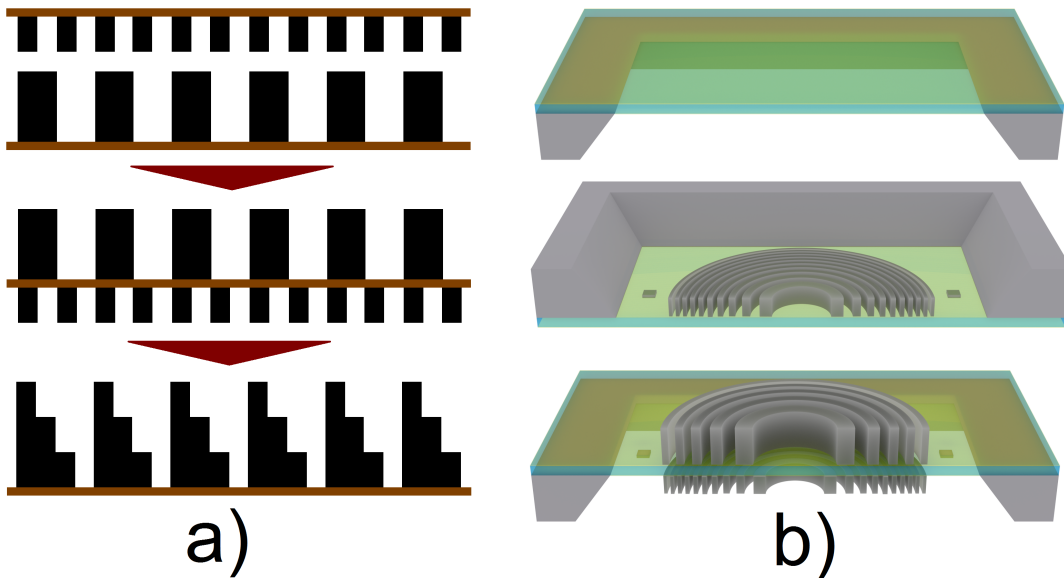


FIGURE 5.1: a.) From mechanical stacking of zone plates to double sided zone plates. b.) Key steps in the fabrication of double sided blazed zone plates. Starting from a double-side coated but otherwise empty membrane, first the dense zone plate is patterned on the back side along with a set of markers. The patterning of the coarse zone plate on the front side is then aligned on these markers through the membrane.

this can provide an effective four level profile in transmission while only producing binary structures as illustrated on 5.1.a. Hence, double-sided zone plates are inherently produced as monolithic, single chip optical elements without the possibility of later losing their alignment. In short, they offer the benefits of stacked zone plates as a monolithic device.

## 5.2 Sample fabrication

The double-sided patterning of zone plates is compatible with a number of existing, well-established fabrication methods for the production of binary zone plates. A particular example is the process described in Chapter 3 for the direct writing and subsequent electroplating of PMMA nanostructures. A slightly modified version of this process was employed to pattern the individual sides of the presented membranes.

The zone plates were prepared on 250 nm thick and  $2 \times 2 \text{ mm}^2$  sized rectangular silicon nitride membrane windows on  $6 \times 6 \text{ mm}^2$  silicon frames. The increased membrane size was crucial for the successful focusing of the e-beam writer and obtaining sufficiently flat and reproducible spin-coating on the back side of our membranes. The substrate was coated with 5 nm chromium, 25 nm gold and again 5 nm chromium layers on both sides to serve as an adhesion and conduction layer and as a plating base for electroplating. The spin-coating of the back side involved using a tape support to create a trench and raise the face-down membrane above the spin-coater's surface to avoid damaging the

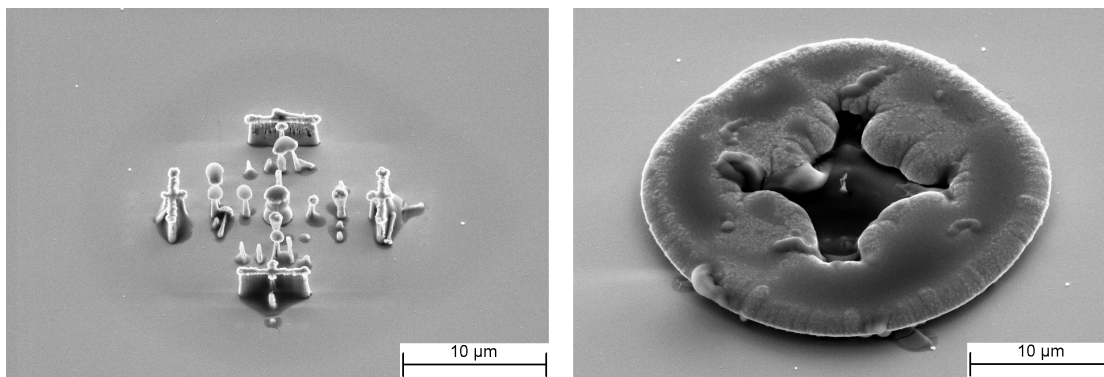


FIGURE 5.2: The marker search procedure itself exposes the resist, letting it developed and electroplated during the following steps. The search procedure is noticeable after a single search but gets overexposed during multiple searches. The electroplated structures around the marker makes the use of pre-patterned markers practically impossible.

membrane. The two sides of the membrane were patterned separately, first the back side with the fine zone plate then the front side with the coarse zone plate as shown in Figure 5.1.b.

Similar to multistep patterning, additional structures were exposed as alignment markers with the first exposure of the fine zone plate. As the markers could be clearly located through the membrane, the second exposure was aligned on these markers. Since double-sided zone plates exchange alignment in the X-ray beam to alignment during the exposure, the overlay accuracy is an important factor that eventually determines the smallest possible zone width using the double sided patterning scheme<sup>1</sup>. The exposure dose of the coarse zone plate on the second side was lowered by typically 10 – 15% in order to compensate for increased backscattering from the fine zone plate on the other side of the membrane.

Several double-sided blazed zone plates were fabricated on each membrane with 100 micron diameter and 200 nm effective half-pitch. The dense zone plates were all exposed with the same exposure settings, while both the dose and bias of the coarse zone plates were varied in order to cover the process window. Before development, the already processed side was covered by a fresh PMMA layer to protect it from the upcoming steps. As described earlier, the exposed chips were developed in a cooled mixture of isopropanol and water for increased contrast. The development times were fixed to 8 minutes for the coarse and 6 minutes for the dense side. The chromium adhesion layer was opened in the trenches by etching with chlorine and oxygen plasma. The brushed aluminium holder was smooth enough not to scratch or break the clamped membranes when mounted upside down. The PMMA mould was filled with electroplated nickel, resulting in  $\sim 2\mu\text{m}$  high coarse and  $\sim 1\mu\text{m}$  high dense structures. Upon plating the back side, membranes were likely to break during unmounting if the holder was dried with

<sup>1</sup>As the marker search procedure exposes the resist, the search pattern is also electroplated. Hence I was unable to use the procedure as described in chapter 6.

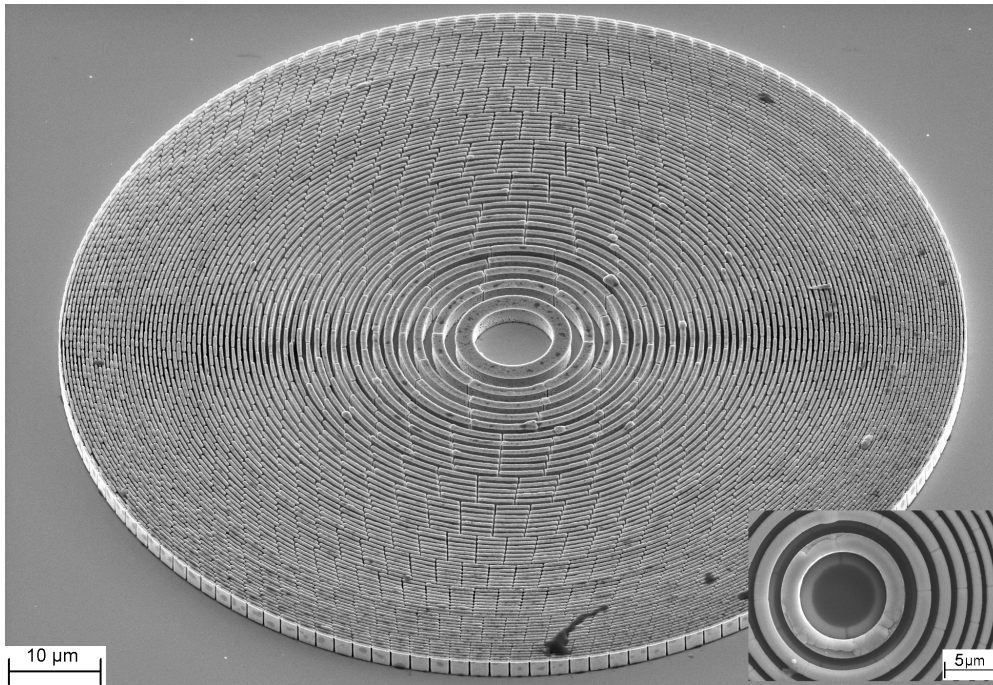


FIGURE 5.3: Scanning electron micrographs of a double sided blazed zone plate show only one side at a time, with a faint image of the other side. Electrons are unable to penetrate the high aspect ratio trenches.

nitrogen gun earlier. Detaching the chips underwater eliminated this problem. During the plating of the front side, the protective PMMA layer on the back side prevented the dissolution of the existing structures in the aggressive electrolyte. After the development and electroplating of both sides, the PMMA mould was removed from the samples using acetone or oxygen plasma. For overplated lenses, the resist removal was far from perfect, but a bit of organic residue does not affect optical properties in the hard X-ray range.

The pre-characterization of the double sided zone plates met significant challenges. As scanning electron microscopy is a surface method it is not optimal for the characterization of double-sided zone plates. Although it is evident from Figure 5.3 that with high acceleration energies the other side is detectable in backscattering mode, it provides no relevant information about smaller structures.

In order to get a better picture of the actual zone profile, an unmeasured zone plate was sliced with focused ion beam milling (FIB). The FIB cross section of Figure 5.4 clearly shows the coarse zones on the front and the dense structures on the back sides of the membrane. With  $2.2 \mu\text{m}$  high structures on the front and  $1.0 \mu\text{m}$  micron high structures on the back side, the measured structure height fits the targeted values of 2.3 and 1.15 micron height. Despite the obvious trapezoidal shape of the structures on the coarse side due to beam forward scattering, the average fill factor is close to the optimum value. The alignment accuracy of the two sides appears to be in the 30-40 nm range. One can observe, that the FIB cross-section on Figure 5.4 evidently suffers from



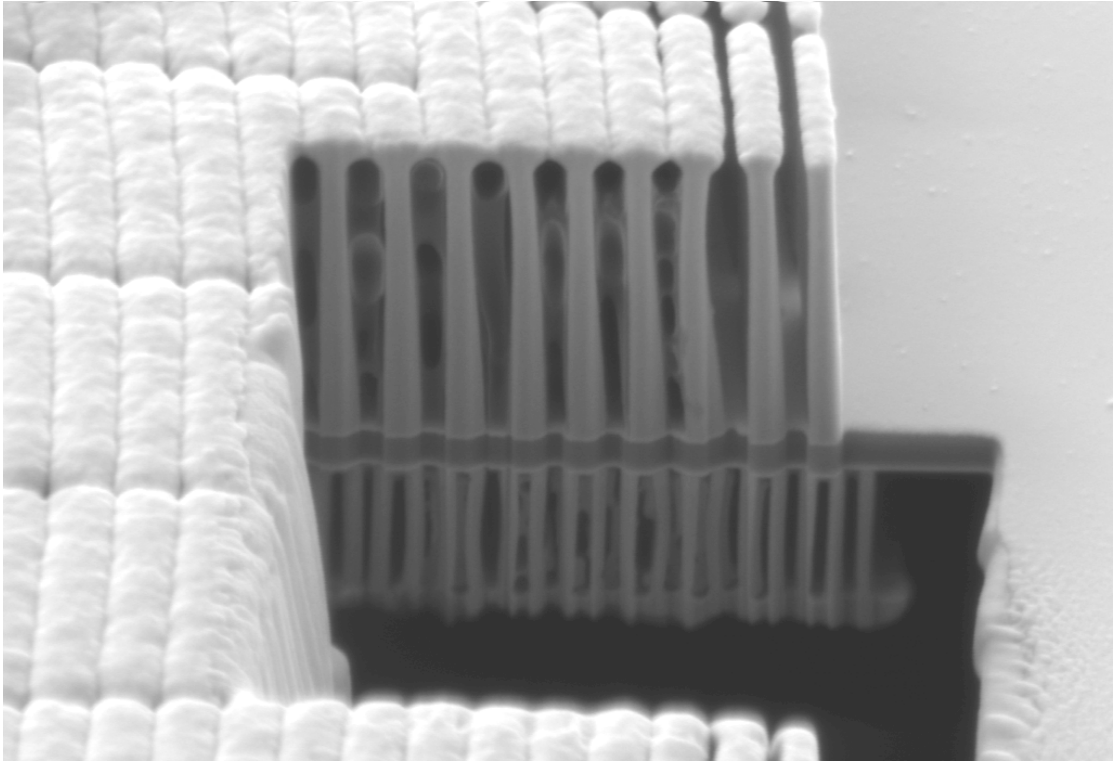


FIGURE 5.4: Focused ion beam cross section of a double-sided blazed zone plate, showing the coarse zone plate on the top and the dense zone plate on the bottom side. The coarse side structures have trapezoidal shapes due to beam forward scattering in the thick resist. Using the centre of the zones, the cross-sectioning reveals  $\sim 37\text{ nm}$  misalignment between the two sides. The FIB cross-section is plagued by curtaining artefacts –non-planar milling surface– due to the large milling rate contrasts in our samples. This complicates the determination of the optical cross-section.

non-planar milling surfaces due to the high milling rate variations within the structures. Therefore, while FIB can provide a proof of principle, it is unable to reliably determine the optical cross-section of our structures.

### 5.3 Efficiency measurements

Measurements on double-sided blazed Fresnel zone plates were performed at the cSAXS beamline of the Swiss Light Source. All measurements were carried out on zone plates with 100 micron diameter and 200 nm smallest zone width at the photon energy of 6.2 keV. The zone plates were illuminated through a pinhole with equal size as the zone plate and the first diffraction order was selected by a 10 micron pinhole in the focus. The measurements were adjusted to meet the capabilities of the beamline.

On selected zone plates of every batch, the efficiency measurements were performed as described in Chapter 4. The order sorting aperture was scanned across the focal plane while the transmitted intensity was recorded using a photodiode detector.

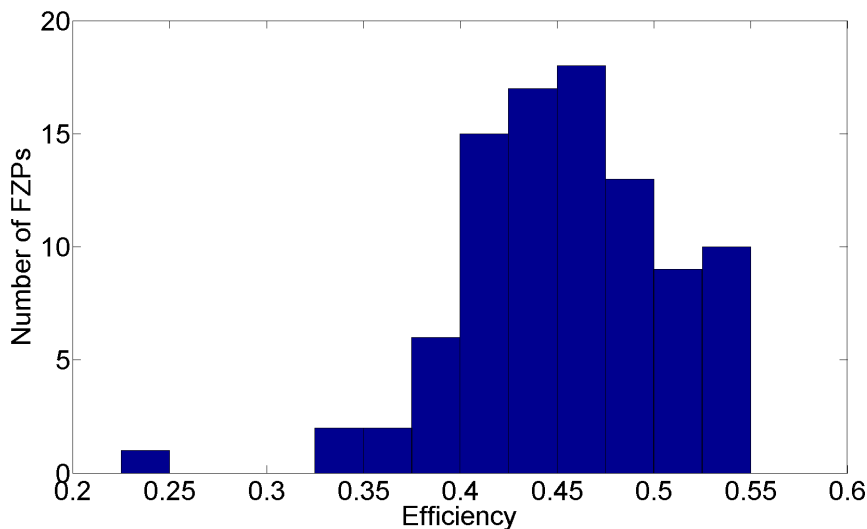


FIGURE 5.5: Histogram of the measured efficiency of 93 double sided blazed Fresnel zone plates. With an average efficiency of 45.4% and individual values up to 54.7%, double-sided blazed zone plates clearly surpass the capabilities of binary zone plates. The nearly 100 zone plates show the reliability of our process. Lenses with low efficiency either suffer from misalignment or under-development due to low exposure doses.

While the focal spot is inside of the pinhole, the current on the photodiode is proportional to the focused intensity. This was normalized with the measured photocurrent from the illuminating beam through the reference pinhole. The efficiency measurement of the rest of the zone plates was carried out by exchanging the photodiode detector to a Pilatus 2M single photon counting pixel detector placed far downstream of the focus after a 7.2 m long flight tube. This detector not only recorded the focused photon flux but also provided spatially resolved map of the diffraction efficiency. The quantitative cone images were normalized into diffraction efficiency by calibrating them on the diode based efficiency measurements. Since we did not use a central stop, the central pixels of the cone were masked during the comparison to avoid the  $0^{th}$  order as well as special care was taken to use defect free zone plates as reference.

Since the dose tables on each chip started from below the clearing dose, seven zone plates where the majority of the zones did not develop were removed from further statistical analysis. The focusing efficiency of the remaining 93 zone plates was 45.4% on average, with individual zone plates reaching up to 54.7% efficiency. These values clearly surpass the 36.8% fundamental limit of binary zone plates at this photon energy and are similar to the values demonstrated for blazed zone plates with micron-sized structures [71] or stacks that required a mechanical setup for adjustment in Chapter 4.

The high average efficiency also shows that the presented double-sided blazed zone plates were not cherry-picked results but represent a reliable fabrication process. This is also confirmed by the visual evaluation of the recorded cone patterns: only three low efficiency zone plate shows Moiré-fringes, i.e, the characteristic sign of severe

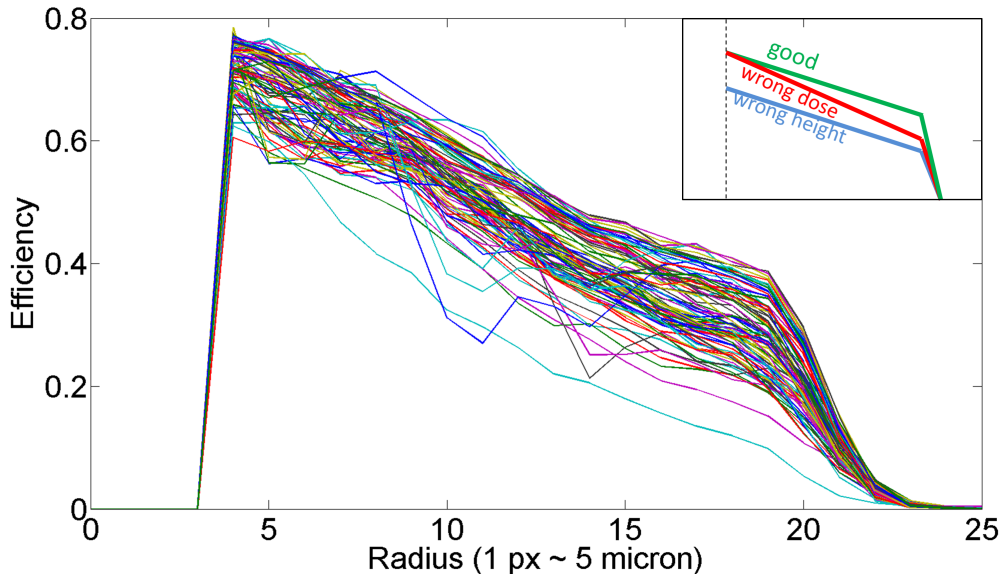


FIGURE 5.6: Radial distribution of focusing efficiency of the 93 double sided blazed zone plates. The inset provides a brief guide to distinguish height and dose related issues. Values above 0.7 are due to inhomogeneous illumination.

misalignment. As the overwhelming majority of the cones are free of misalignment, the general alignment accuracy is better than 60 nm. Beside alignment other factors including exposure dose and structure height also had significant influence over the resultant efficiency. Using the recorded diffraction cones as a spatial map of diffraction efficiency, we can connect the spread in efficiency to production properties. In the large central zones, fabrication and alignment related errors are negligible, thus the efficiency of the centre of the zone plate is influenced only by structure height, providing us with a common starting point for all zone plates on the same chip. On the other hand, the efficiency of the smaller zones is heavily influenced by fabrication parameters like exposure dose and alignment accuracy. The highest zone plate efficiencies were measured on membranes with the right height and on zone plates with the correct exposure settings.

## 5.4 Detailed characterization

Due to constraints in the experimental setup, ptychographic probe retrieval was unfeasible on these zone plates. Yet, as alignment accuracy is a critical parameter for producing double-sided zone plates with higher resolution, direct measurements were conducted to determine alignment accuracy.

By only partially illuminating the zone plate through a 10 micron pinhole, one can measure the diffraction pattern of part of the zone plate in the form of discrete diffraction peaks corresponding to the various diffraction orders of the zone plate. By scanning the zone plate in front of the pinhole, one records their spatial distribution. The

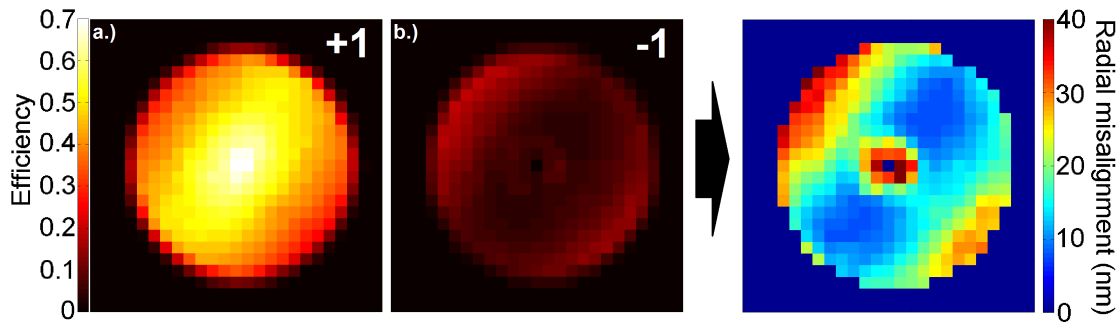


FIGURE 5.7: Distribution of the efficiency of the focusing  $+1^{st}$  a.) and the defocusing  $-1^{st}$  b.) diffraction order over the zone plate. The  $+1^{st}$  order clearly dominates, providing 48.4% efficiency. The  $-1^{st}$  order only becomes noticeable amongst the smallest zones along the diagonal of the zone plate, corresponding to the direction of misalignment. From the ratio of the  $+1^{st}$  and the  $-1^{st}$  diffraction orders, we can approximate the radial misalignment c.) which is in the 25-35 nm range.

measurement was performed by scanning an average zone plate with 45.25% focusing efficiency. The spatial distribution of the most prominent diffraction orders shows clear anti-correlation between the focusing  $+1^{st}$  and the defocusing  $-1^{st}$  diffraction orders. As seen on Figure 5.7, the  $+1^{st}$  order dominates over the zone plate area, concentrating 48.4% of the incoming radiation in the technically important  $+1^{st}$  focusing order. The  $-1^{st}$  order becomes only notable in the outermost zones along the diagonal of the zone plate containing only 10.0% of the incoming radiation. You can also see the same tendency from the efficiency distribution of the  $+1^{st}$  order, which is decreasing significantly where the  $-1^{st}$  order is increasing. The diagonal direction of the  $-1^{st}$  diffraction order marks the misplacement direction. Attributing the asymmetry of the  $+1^{st}$  and  $-1^{st}$  order to misalignment, there is an analytical expression to approximate the radial misplacement from their ratio:  $dS = \text{atan}(I_{+1^{st}}/I_{-1^{st}})/\pi$  that gives the misplacement in units of the local pitch. This suggests a  $\sim 20 - 30 \text{ nm}$  shift between the zone plates on the two sides of the sample as seen in Figure 5.7.c.

Previously the FIB cross-sectioning process provided us with the qualitative cross-section of our lenses. Yet, due to severe artefacts they still leave open questions regarding the actual transmission profile. Therefore direct at-wavelength characterization of the zone plates was performed to retrieve the optical transmission profile of the lenses using X-ray ptychography. As described in Chapter 2, ptychography is a scanning coherent diffraction imaging method, capable of simultaneously reconstructing the complex optical transmission profile of the object as well as the illuminating probe wavefront. By performing ptychography on the zone plates as a sample object, one can reconstruct their optical transmission profile the exact way as X-rays see it. Since mapping the whole zone plate was beyond the sample stage piezo's range, only a radial segment of the zone plate was scanned. A total of  $36 \times 65 \mu\text{m}^2$  area has been mapped with 300 nm step size in a round arrangement, the total area has been subdivided into overlapping sub-regions for improved stability. Each sub-scan was repeated in two detector positions

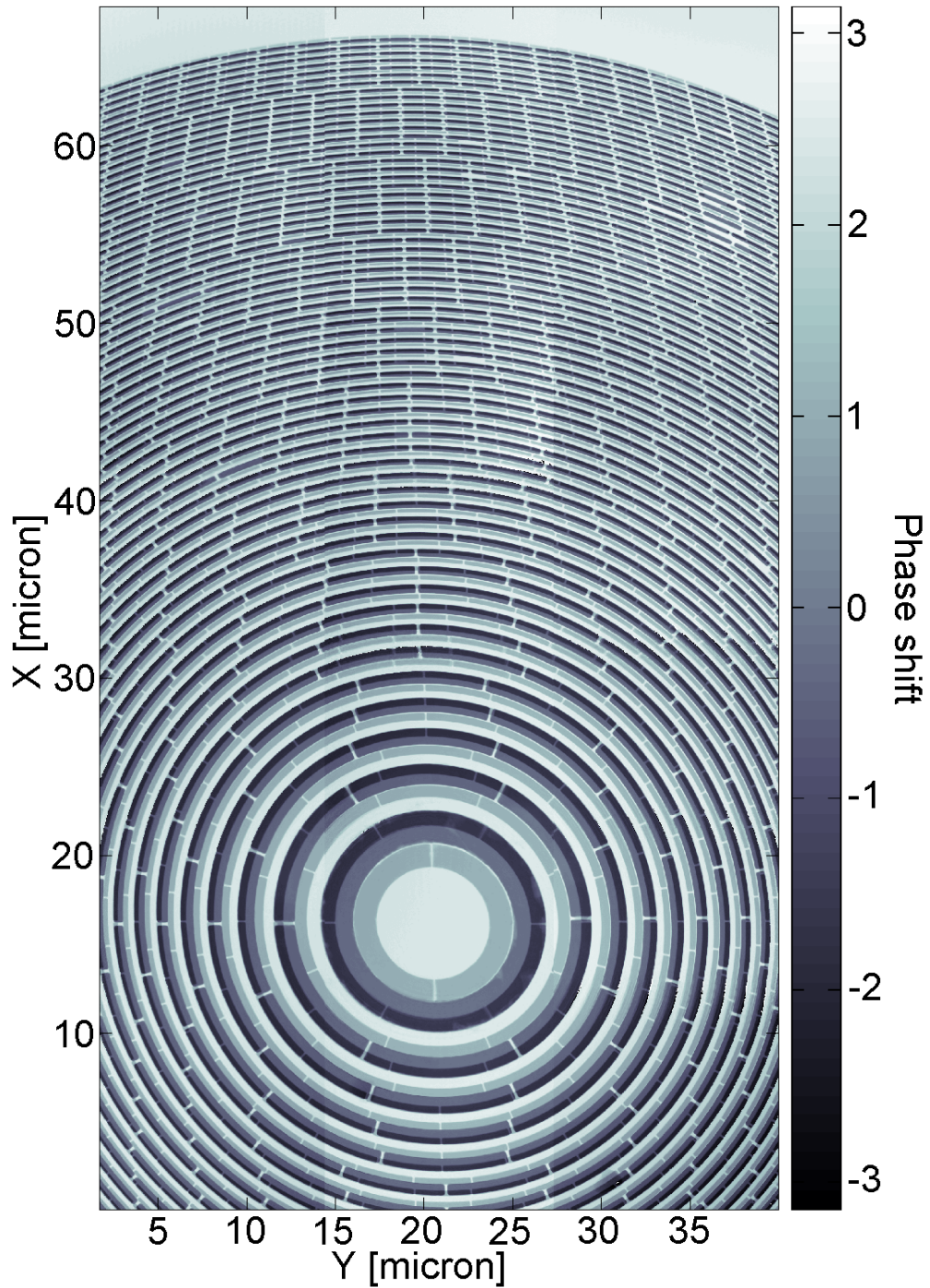


FIGURE 5.8: Phase map of a double-sided blazed zone plate using X-ray ptychography. In agreement with predictions, the two sides of the zone plate add up in transmission to provide an effective four level profile. The individual sides can be determined to be  $2.1 \mu\text{m}$  and  $0.95 \mu\text{m}$  high on the coarse and dense sides. The misalignment of the two sides can be directly seen as well as the slightly low fill factor. (The image has been stitched together from multiple reconstructions.)

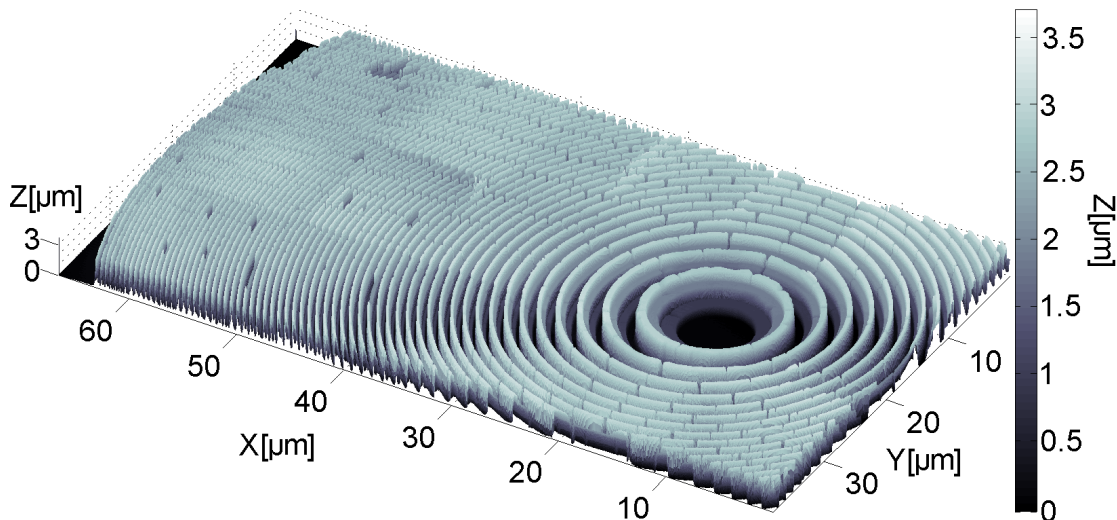


FIGURE 5.9: Rendered height map of zone plate topology from the measured phase on Figure 5.8. Occasional missing zones are clearly visible in the reconstruction. The profile of the blazed edges also provide a better understanding of the principle of phase wrapping.

to recover missing spatial frequencies due to detector gaps, resulting in a total of 32796 scan points. The reconstruction was performed using the difference map algorithm[127] for 400 iterations and averaging the object over the final 100 iterations for noise reduction. The information behind the detector gaps was accounted in the reconstruction by an implementation of a shared reconstruction between multiple scans[128]. Due to memory utilization constraints, the final object was stitched together from several reconstructions[140].

The reconstructed phase seen in Figure 5.8 clearly shows the expected four level staircase profile both amongst the central and amongst the smallest zones. Measured phase shift corresponds to  $2.1 \mu m$  coarse and  $0.95 \mu m$  dense nickel structures. The 3D rendering of the zone plate topology on Figure 5.9 also shows the discrete levels of the zone plate but provides better visualization of the occasionally missing zones. The fill factor, the misalignment and the sloped sidewalls are all clearly visible from the reconstructed transmission profile. The exact misplacement can be calculated from the phase of the coarse and dense zone plates (measured at radial supports) on Figure 5.10, implying a local misplacement of 19 nm. This corresponds to a total diagonal misalignment of 26.9 nm, which is within the range of seen earlier on Figure 5.7.

Since ptychography is a quantitative imaging method, the retrieved transmission function is equivalent to the way the X-rays see our lenses. In case of mapping the whole zone plate, the measured optical transmission profile can be propagated to the focal plane to provide us with the focal spot. Although we do not have the map of the full zone plate, Fourier transforming a zone plate segment provides the local diffraction efficiency in the different orders. By taking a segment amongst the smallest zones as seen

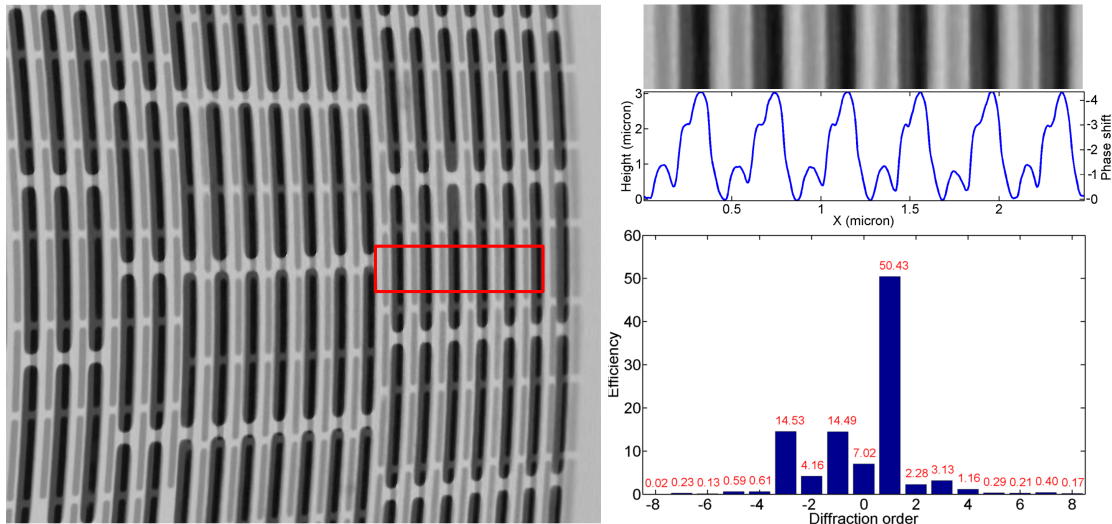


FIGURE 5.10: The magnified section shows the phase transmissivity profile induced by the smallest zones of the lens. A misalignment of 19 nm can be derived from the cross section of the marked region, corresponding to 27 nm global misalignment along the diagonal. This cross section can be Fourier transformed to obtain the local diffraction efficiency of the particular region, providing us with 50.43% diffraction efficiency of our lenses even from their smallest structures.

on Figure 5.10, its Fourier transform corresponds to 50.4% local diffraction efficiency. This is slightly higher than the directly measured value of  $\sim 42.0\%$  in the similar region. This can be partly explained by the lack of radial supports in the selection and by ptychography neglecting 5% absorption in the membrane.

## 5.5 Conclusions

The double-sided patterning of Fresnel zone plates represents a promising new technique for improving the efficiency of diffractive X-ray optics without increasing the complexity of the experimental setup. They provide all the benefits of stacked zone plates in a permanently fixed, monolithic, single chip device. The demonstrated blazed double-sided zone plates with 200 nm smallest zone width offered focusing efficiencies up to 54.7%, which is comparable to the best values achieved by mechanical stacking in the previous chapter. Moreover the demonstrated alignment procedure can routinely provide sufficient overlay accuracy for zone plates with sub-100 nm smallest half-pitch, allowing the fabrication of both binary and blazed double-sided zone plates for the multi-keV X-ray range. We believe that the high focusing efficiency, compact size, ease of use and stability provided by double-sided blazed zone plates makes them attractive alternatives to stacked zone plates.





## Chapter 6

# Line-doubled double-sided zone plates

Ever since the initial development of zone plate stacking, it has been applied for the production of high resolution Fresnel zone plates. By stacking two identical binary zone plates, the doubled structure height can provide up to a factor of four gain in efficiency that facilitates their use at higher photon energies as illustrated in Figure 2.5. As the double-sided patterning of zone plates is essentially an on-chip stacking method, whatever can be done by the stacking of two chips, can be patterned as a double-sided zone plate. Therefore the following chapter will discuss the fabrication of ultra-high aspect ratio high resolution zone plates by combining line-doubling with double-sided patterning. Extracts of this chapter can be found in the literature[180].

### 6.1 Background and motivation

Zone plate stacking was originally developed for stacking two high resolution zone plates to effectively double their height and thus increase their efficiency towards high photon energies[75, 85]. However as long-term alignment stability is critical, their practical applications remain limited due to concerns regarding the drift of the two chips. Multi-exposure on-chip stacking methods have been demonstrated in the literature[92] to provide similar benefits as an inherently fixed, single chip-solution. Yet since the upcoming layers depend upon defect-free previous layers, the described electroplating process could only produce relatively shallow nanostructures in a single step.

Double-sided patterning can provide the same benefits as stacking, but the patterning of each side is independent from each other. Thus it allows the use of line-doubling[73, 74] as a dedicated fabrication method for ultra-high aspect ratio, high resolution metallic nanostructures. By preparing a high aspect ratio HSQ resist template

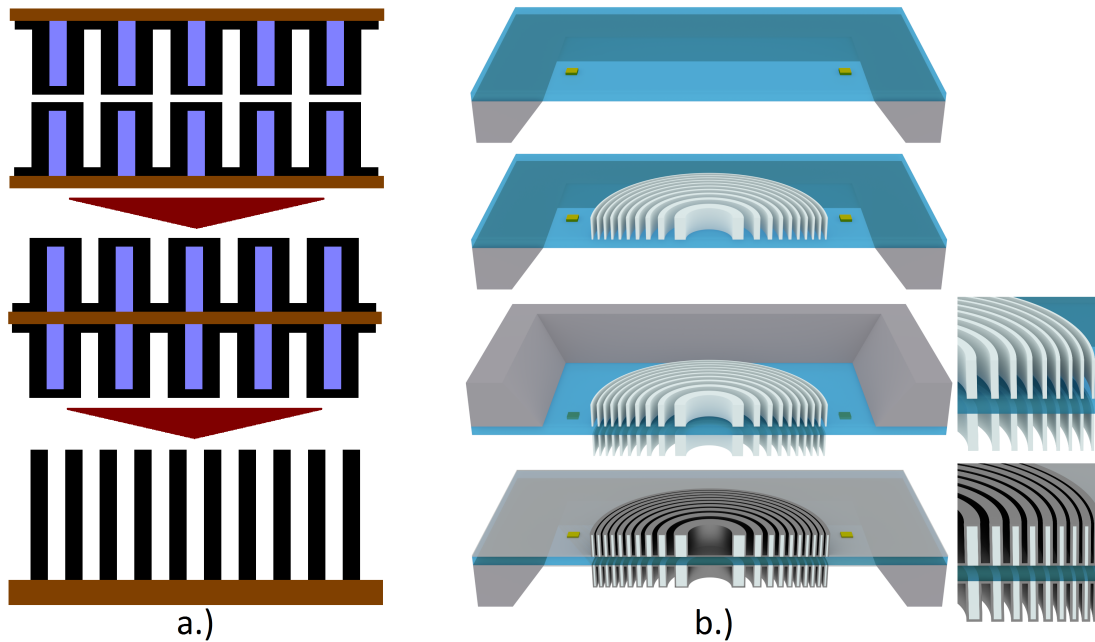


FIGURE 6.1: a.) From the stacking of line doubled zone plates towards double-sided line-doubled zone plates towards double effective structure height. b.) Key steps in the fabrication of double-sided line-doubled zone plates. Starting from a pre-patterned membrane, first we pattern front side aligned on the markers. Later the patterning of the back side is aligned on the very same markers. The complete resist template is then coated with iridium using ALD.

and coating it with heavy metals using atomic layer deposition, the effective line density can be doubled compared to the actually patterned sparse template. This can be further doubled with the use of double-sided patterning, providing even higher structures aimed for higher photon energies.

## 6.2 Sample fabrication

The fabrication of the individual zone plates was based on the line doubling scheme described in the literature[74]. Its exact adaptation is described in detail in Chapter 3, however the basic process was slightly modified to facilitate double-sided patterning.

During early developmental stage it became evident that unlike with electroplated zone plates, markers can not be patterned together with the zone plate templates, as HSQ markers had extremely low contrast. Therefore the  $2 \times 2 \text{ mm}^2$  silicon nitride membrane substrates were coated with a Cr/Au/Cr metal layer from both sides and were pre-patterned with electroplated gold alignment markers using a similar process as for electroplated zone plates[72]. The substrates were subsequently cleaned from organic contaminants and spin-coated with  $\sim 550 - 650 \text{ nm}$  thick HSQ resist. The spin-coating of the back side involved mounting the face-down membrane over a trench on the holder

to raise the membrane above the spin-coater's uneven surface. The two sides of the membrane were patterned separately, first the front then the back side.

The two electron beam exposures were aligned on the pre-patterned gold markers with the alignment of both sides performed on the very same marker set. Hence any error in marker positioning or profile inaccuracy is included in both measurements and negated. Each chip was exposed with twenty zone plate pairs of  $100\ \mu\text{m}$  diameter and  $30\ \text{nm}$  smallest zone width, with each pair having different doses and line shrinkage to control the fill factor of the resist template. As discussed earlier, the fill factor of the template not only determines the fill-factor but also the placement of the iridium zones.

The resulting zone plates have been pre-characterized with SEM, yet it can only study the individual sides of the zone plates without investigating their alignment. Therefore we used focused ion beam to cut an untested zone plate in order to obtain information about its structure quality. As seen on Figure 6.2, the two zone plates on the front and back sides of the membrane are clearly visible on the cross section image. The front side structures reach  $\sim 500\ \text{nm}$  height while the back side structures have  $700\ \text{nm}$  height. The resist template (dark) is virtually indistinguishable from the voids between the zones and is covered by the conformal iridium layer (bright) with a uniform thickness on both the front and the back side. The heights of the two sides add up in transmission, resulting in a total of  $\sim 1200\ \text{nm}$  effective structure height, corresponding to an aspect ratio of 40 for the  $30\ \text{nm}$  zones. The two sides of the zone plate appear to be in good overlay above each other as no misalignment can be observed from the recorded micrographs.

### 6.3 Efficiency measurements

Presented measurements on double-sided line-doubled Fresnel zone plates were mostly performed at the cSAXS beamline of the Swiss Light Source with additional measurements conducted at the Nanoscopium beamline of the synchrotron SOLEIL. Measurements were performed on zone plates with  $100\ \mu\text{m}$  diameter and  $30\ \text{nm}$  smallest zone width at a photon energy of  $9\ \text{keV}$ , corresponding to  $1440\ \text{nm}$  optimal height for iridium zone plates. The zone plates were illuminated through a pinhole with equal size as the zone plate and the primary focus was selected by a  $10\ \mu\text{m}$  pinhole near the focal plane. Similar to double-sided blazed zone plates, the efficiency measurements were combined with spatial efficiency mapping. On selected zone plates, the pinhole was scanned across the focal plane while the transmitted intensity was recorded using a photodiode detector. The recorded photocurrent reached a plateau when the focal spot was inside the pinhole. This was converted into efficiency by subtracting the background and normalizing it with the photocurrent of the illuminating beam. The efficiency measurement of the rest of the zone plates were carried out by exchanging the photodiode detector to a

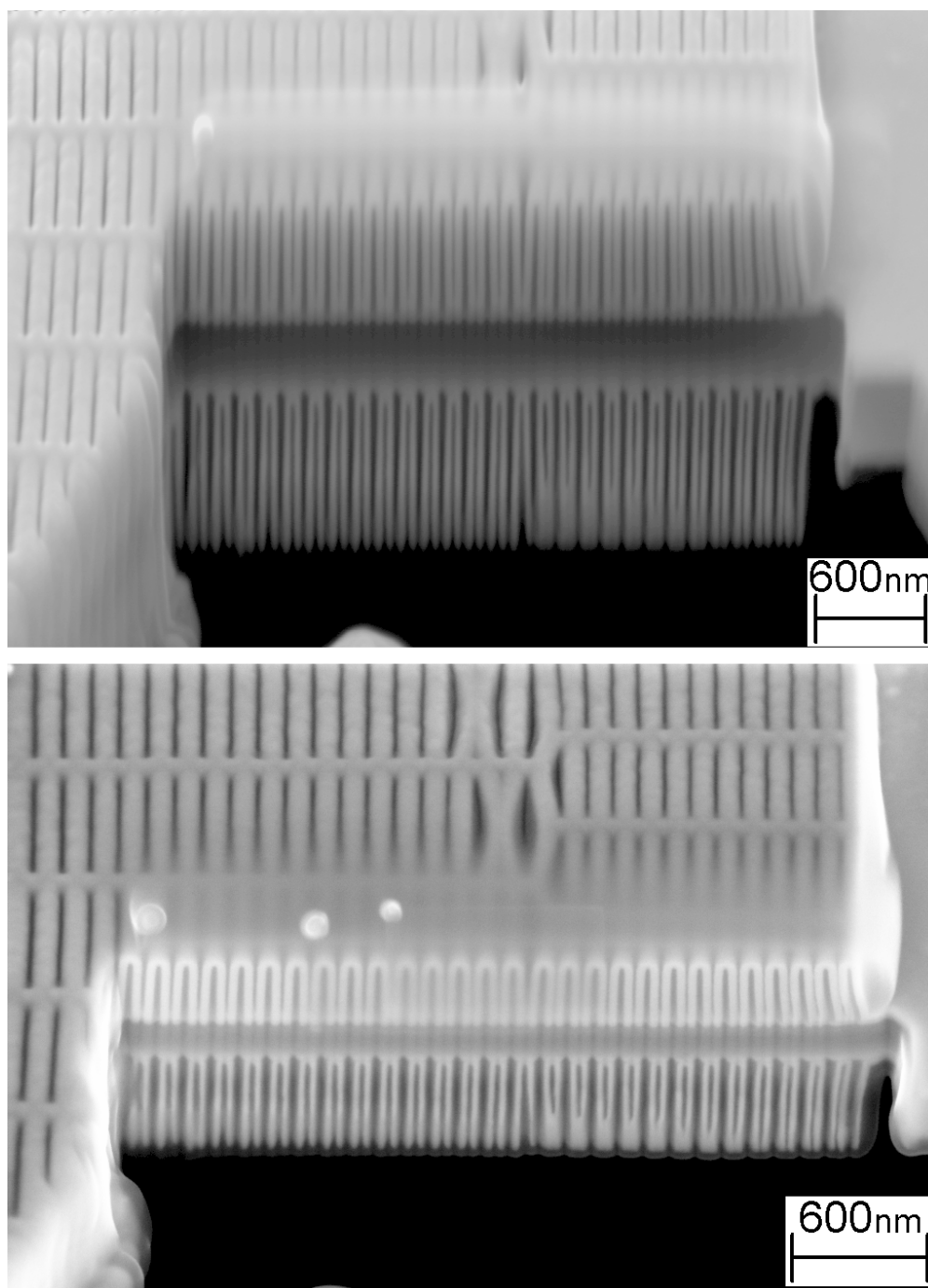


FIGURE 6.2: Focused ion beam cross section of a double sided line doubled zone plate recorded at  $54^\circ$  (up) and  $30^\circ$  (down) tilt angle. The Ir coating (bright) conformally covers the template. The lines add up in transmission, combining into a single zone plate with  $\sim 1200\text{nm}$  total iridium height. The two zone plates appear to be in excellent alignment to each other, no misalignment can be measured from the cross section.

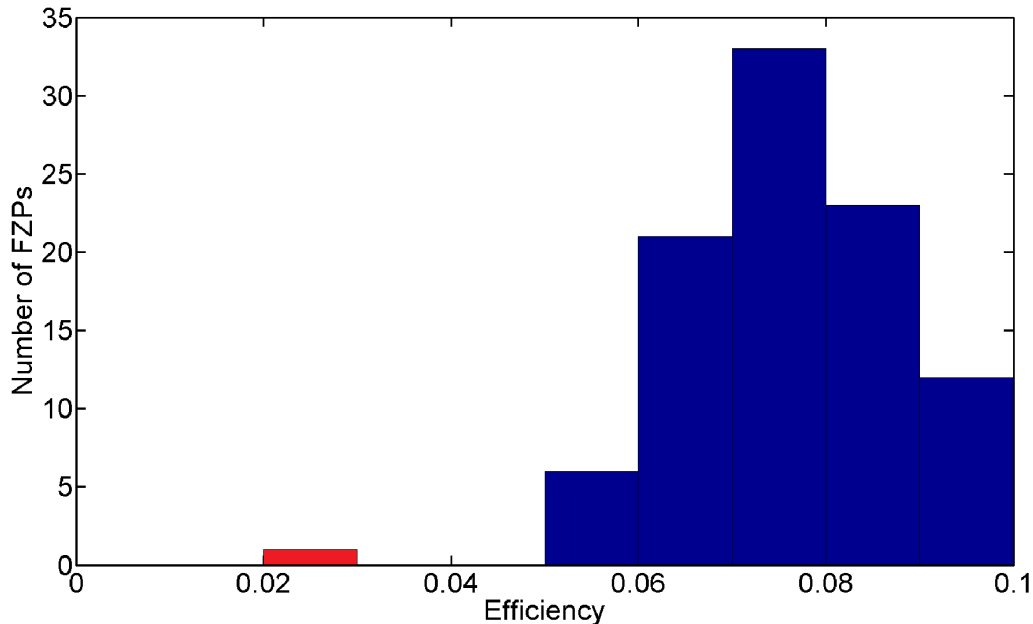


FIGURE 6.3: Efficiency histogram of the measured double-sided zone plates. The average focusing efficiency of the 95 double-sided zone plates (blue) was 7.6%. The single-sided reference zone plate had 2.8% (red), while the best double-sided zone plate had 9.9% focusing efficiency. The majority of the double-sided zone plates performed in the 7-9% range, proving that our alignment and patterning procedure can obtain reliable results.

Pilatus 2M single photon counting pixel detector, placed 7.2 m downstream of the focus after a He flushed flight tube. The expanding diffraction cone of each zone plate was recorded as a spatially resolved map of intensity. The central pixels of the cone were masked to stop the 0<sup>th</sup> order and the total intensity within the rest of the cone was calibrated with the diode based efficiency measurements. Four zone plates with visible particle contamination were excluded from further analysis, a further one was used as the single sided reference.

The average diffraction efficiency of the 95 measured double-sided zone plates was 7.6% at 9 keV with the best zone plate having 9.9% diffraction efficiency. In comparison, the highest focusing efficiency previously reported for single-sided iridium zone plates with similar zone width was 5.1%[74]. The factor of two gain in focusing efficiency shows the clear advantage of increased structure height at higher photon energies. In comparison, the single sided reference reached only 2.8 % efficiency, although it was located on the shallower front side of the membrane (see Figure 6.2). Similarly to the previous chapter, the consistently high efficiency seen on Figure 6.3 is the product of a reliable fabrication process.

Due to the short focal distance, the diffraction cone of the zone plates extended to a larger detector area, allowing detailed characterization of the radial distribution of the efficiency. The phase error induced by the radial support structures[39] produces

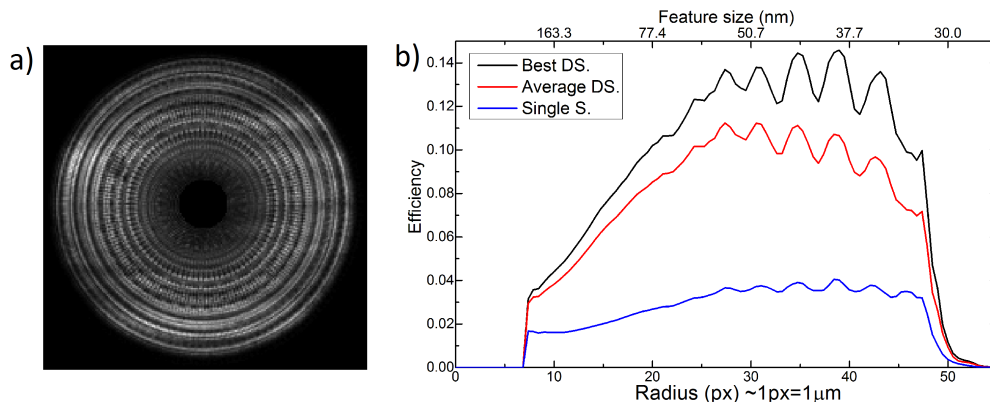


FIGURE 6.4: a) Diffraction cone of the best performing double-sided line-doubled zone plate. The changes in support structure layout are visible as quasi-periodic radial fluctuations in the efficiency[74]. b) Radially integrated efficiency distribution of the measured double-sided zone plates. The best zone plate is  $\sim 20\%$  above the average zone plate, which is possibly related to structure height. This gap is wider amongst the smaller zones as the best zone plate drops slower, probably due to better fill-factor. Nevertheless, even the average double sided zone plate stays clearly above their single-sided counterparts.

clear radial fluctuations in the diffraction efficiency as seen in Figure 6.4. In agreement with earlier assumptions in Chapter 3, the efficiency of the zone plates decrease towards the centre as well as towards the smallest zones either due to low fill factor, possible fabrication inaccuracies or small misalignment. Within the individual chips a strong dose dependence can be observed as high-dose zone plates with broader resist template tend to fall-off faster towards the edge than their low dose counterparts. As the fill-factor is negligible within the largest zones in the centre, line-doubled zone plates act as a high-pass filter. They provide excellent efficiency for high spatial frequencies but penalize low frequencies.

## 6.4 Ptychographic characterization and STXM imaging

High resolution zone plate optics have two main application fields, the first being full-field X-ray microscopy and the second being scanning probe imaging. Both fields take advantage of the high optical quality that is generally associated with e-beam patterned zone plate optics. Therefore besides efficiency, high optical quality and low aberrations are also important factors. To investigate the imaging potential of the fabricated optics, their imaging performance was tested by ptychographic probe retrieval and scanning transmission X-ray microscopy.

As described in Chapter 2, ptychography is a high resolution coherent diffraction imaging technique, that is capable to simultaneously retrieve both the studied sample object transmission profile and the illuminating wavefield. Its latter property makes it an invaluable tool for optics characterization as by using a focusing optical element its

retrieved wavefield can be reconstructed and propagated to an arbitrary plane. Ptychographic characterization of the zone plates were performed by blocking the  $0^{th}$  order with a  $40\ \mu\text{m}$  diameter central stop and mounting a strongly scattering line-doubled Siemens-star test object  $\sim 300\ \mu\text{m}$  after the focal plane. A ptychographic dataset from the central  $4 \times 4\ \mu\text{m}^2$  of the Siemens-star was recorded with each of the zone plates. Each scan had  $300\ \text{nm}$  step-size and consisted of  $2 \times 142$  diffraction patterns that were recorded in two detector positions in order to fill the detector gaps. The reconstructions were done using 400 iterations of the difference map algorithm[127] with averaging the last 100 iterations for noise-reduction. The reconstruction pixel size was  $\sim 10\ \text{nm}$ . The retrieved illumination functions were upsampled for better visibility. The probes were then propagated in the vicinity of the focal plane to find the exact focus as seen on Figure 6.5. The back-propagated probes were found to be free of commonly encountered aberrations, like astigmatism or spherical error. The retrieved focal spots met the expectations, providing a symmetric shape with minor unevenness only appearing in the first Airy ring. As a quantitative measure of spot size, the commonly used[78] full width at half maximum of the best zone plate was  $29\ \text{nm}$  which is very close to the  $28\ \text{nm}$  value expected for an annular aperture with a central stop of 40% of the radius.

While full width at half maximum is an easy to understand parameter, it is not a good indicator of optical quality. It is insensitive to the intensity contained in the sidelobes of the point spread function and thus ignores the real-world issue of contrast. Optical science has developed more sensitive benchmark values, like the Strehl criterion[181] that states that a lens can be regarded diffraction limited when the peak of its focal spot reaches at least 80% of its predicted value. Comparing the retrieved focal spot to the –intensity normalized– theoretical prediction, the Strehl ratio of our lenses could be easily determined. Retrieved spots were compared with an annular aperture with 0.4 central obstruction[182], corresponding to the central stop. Obtained Strehl ratios for high performing zone plates –with efficient smallest zones– were well beyond the criteria for diffraction limited imaging. The highest efficiency zone plate had a Strehl ratio of 0.81, other zone plates provided ratios up to 0.87, that corresponds to diffraction limited imaging.

In order to test our zone plate’s performance in real situations, scanning transmission X-ray microscopic measurements were performed on the line-doubled Siemens-star test object with  $30\ \text{nm}$  spoke distance. By recording  $151 \times 151$  scan points with  $10\ \text{nm}$  step size, a reasonable acquisition time of  $\sim 2$  hours could be maintained. Using the best zone plate as illumination, the  $30\ \text{nm}$  spokes of the Siemens star were clearly resolved as seen on Figure 6.6. This demonstrates that the lenses indeed match their expected resolution. Unfortunately large area scans were hindered by drifts during excessive scan times both at the cSAXS and at the Nanoscopium beamline.

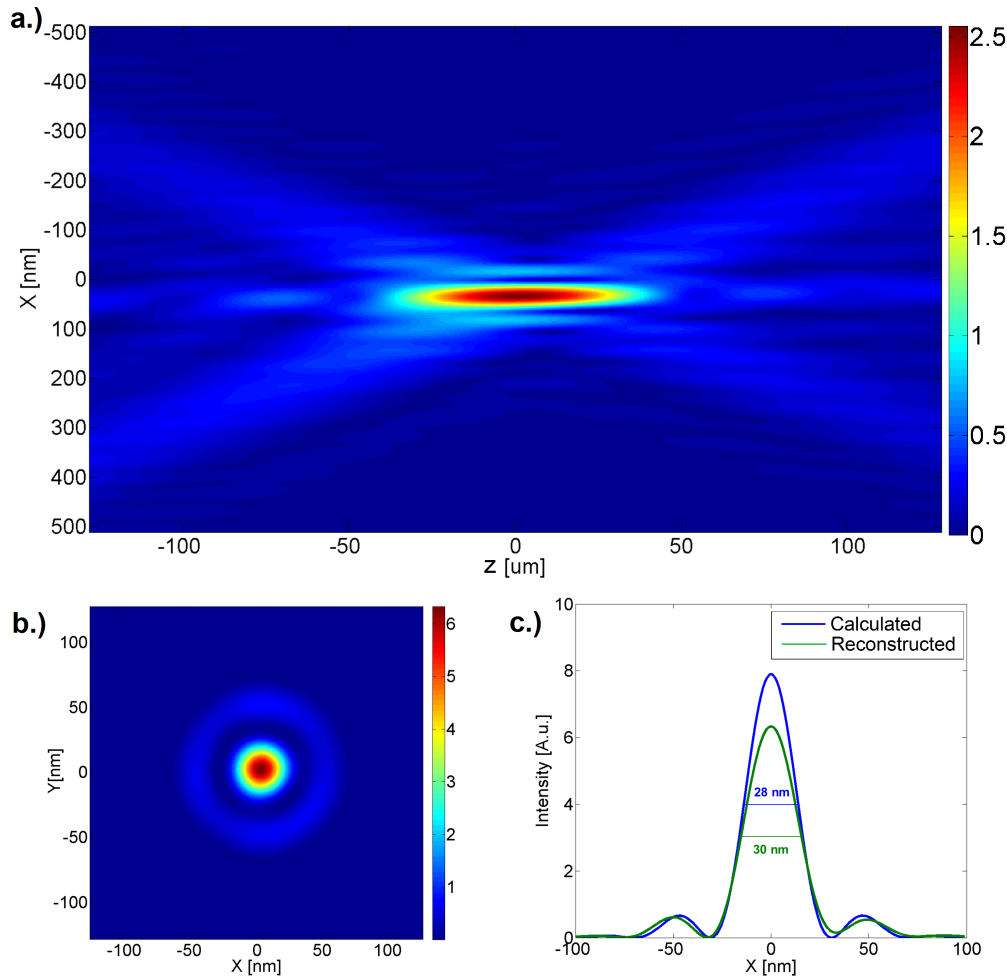


FIGURE 6.5: Reconstructed and back-propagated probe wavefield of the best zone plate. a.) The amplitude of the wavefield around the zone plate focus does not show obvious signs of aberrations. b.) Intensity in the focal plane. The focal spot has a symmetric shape, with no sign of astigmatism. c.) The reconstructed profile of the focal spot is close to the theoretical profile of a lens with central obscuration. The measured 29 nm peak FWHM is in good agreement with the predicted value of 28 nm. The side-lobes are relatively strong as a consequence of using a central obscuration.

## 6.5 Conclusions

Double-sided line-doubled zone plates show the potential of double-sided zone plates. The increased structure height provides clear benefits towards higher energies, delivering substantially increased focusing efficiency in the hard X-ray range. Presented high resolution double-sided zone plates with 30 nm smallest zone width have up to 9.9% focusing efficiency at 9 keV which is twice the value of their previously demonstrated single-sided counterparts. Besides the excellent efficiency, the lenses provide aberration-free, diffraction limited optical performance matching their nominal resolution.

As discussed earlier in Chapter 2, when applied as objective lens in full-field microscopy the improved efficiency directly translates into resolution for radiation sensitive



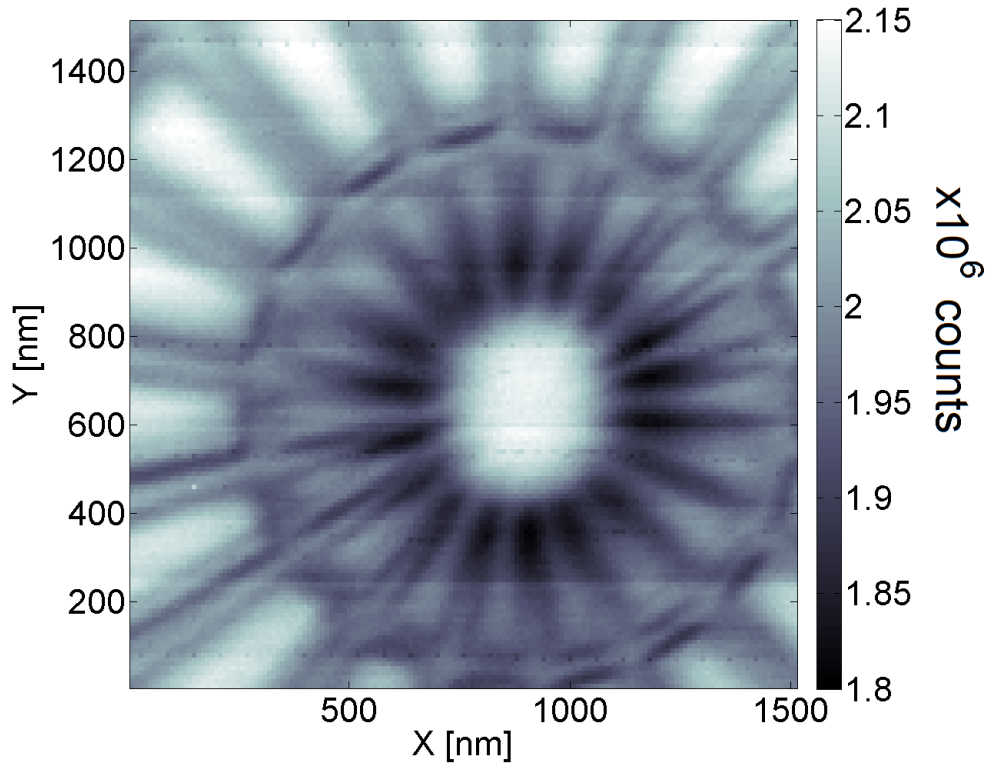


FIGURE 6.6: Scanning transmission microscopy image of a line doubled Siemens star. The 30 nm spokes are clearly resolved, proving that our zone plates indeed match their designated resolution.

biological specimens. When used as focusing lens in scanning probe experiments high efficiency increases sensitivity and measurement speed. Additionally, double-sided line-doubled zone plates have significant room for improvement both in resolution and in efficiency: 2 nm overlay accuracy have been demonstrated[92] as well as there is room for improvement for structure quality.



## Chapter 7

# The interlaced stacking of zone plates

The previous chapters have shown that double-sided zone plates can exchange conventionally stacked zone plates with a single-chip, monolithic solution. In those schemes the stacking of zone plates was used for increasing the focusing efficiency of existing Fresnel zone plates. Instead, this chapter covers a novel experimental scheme to employ zone plate stacking to increase their resolution.

### 7.1 Motivation

The recent years have shown a number of papers reporting on the emerging generation of "single digit zone plates"[78]. Due to their very short working distance, they have questionable practical use, yet as an easy to understand record, they attained large media attention, posing a challenge for the producers of zone plate optics with practically useful aperture size. Conventional, directly e-beam written processes break down in the sub-10 nm feature range and although higher order zone plates have been tried for ultra high resolution imaging[183], their spread was limited by low efficiencies.

The recently published patent application of Xradia Inc. describes a new stacking scheme[87, 88], aimed at multiplying the line density and thus the resolution of Fresnel zone plates rather than increasing their efficiency. As illustrated on Figure 7.1, by patterning every even zone on one chip and every odd zone on the other, the two partial but complementary zone plates can be stacked together. The combined zone plate will have twice the line density and thus double the resolution as the actually fabricated partial zone plates using a similar scheme as interlacing in cathode ray tube TVs and monitors. Since the fabrication of sparse patterns is easier this already relaxes fabrication constraints. Moreover by fabricating both partial zone plates using the zone doubling

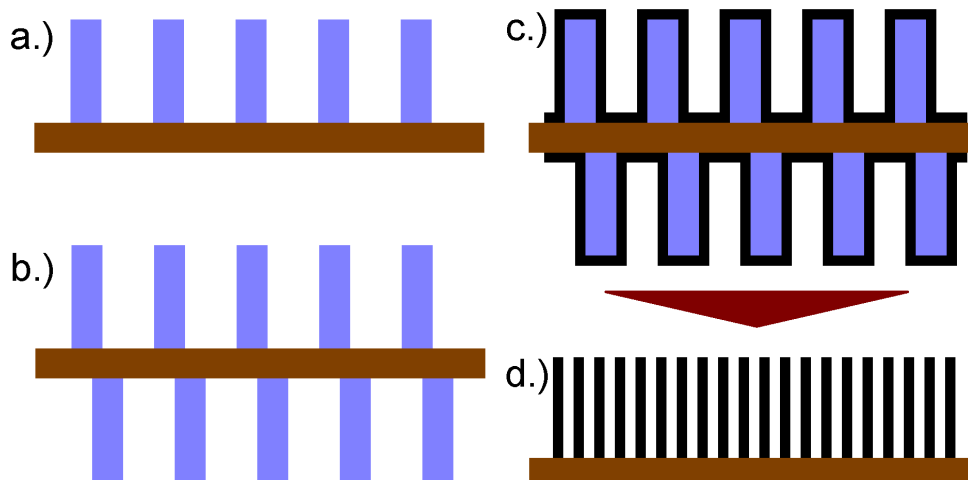


FIGURE 7.1: Fabrication and working scheme of double-sided interlaced zone plates made by the line-doubling method. Each side is patterned with complementary, deliberately shifted three zone wide resist template with a fill factor of  $3/8$  (a-b.) and the chip is then coated with iridium (c.). In transmission the sidewalls on the two sides are projected with twice the line density as the individual sides and four times of the resist template(d.). While the demands on fabricated line width is greatly reduced, alignment accuracy becomes a considerable challenge.

technique, patterning every second zone requires three zone wide resist structures in between. Hence the actually patterned structures can be 3 times wider than the eventual zone width and the fabricated pitch is eventually quadrupled after the stacking. The required fill factor of the resist template is also only  $3/8$ , which helps opening the high aspect ratio trenches.

## 7.2 Sample fabrication

The fabrication scheme employed for the interlaced zone plates bears close resemblance to the fabrication of double-sided line-doubled zone plates described in Chapters 3 and 6. The zone plates were prepared on 100 nm thick and  $2 \times 2 \text{ mm}^2$  sized silicon nitride membrane substrates on  $6 \times 6 \text{ mm}^2$  Si frames. The substrates were coated with a Cr/Au/Cr conduction layer on both sides and were pre-patterned with either electroplated or evaporated gold alignment markers. The front side of the membrane was patterned first, followed by patterning the complementary resist template on the back side.

Due to the smaller resist structures than in Chapter 6 and the demand of steeper sidewalls, the HSQ thickness has been reduced to  $\sim 300 \text{ nm}$ . Again, spin-coating of the back side was performed by supporting face-down membrane above the spin-coater's surface to prevent any roughness scratching the membrane. The front and back sides of the membranes were patterned by two complementary patterns for resist template. Due

to the narrow structures, the e-beam writer was set to 200  $\mu\text{m}$  final aperture and 1 nA beam current to increase its resolution and depth of field. Both the front and the back exposures were aligned on the same set of pre-patterned gold markers. The samples were developed in a salty developer and dried by supercritical drying after the patterning of each side.

### 7.2.1 Alignment issues

The uncoated samples were pre-characterized by scanning transmission electron microscopy. Without the iridium coating, energetic electrons could penetrate the resist template, revealing the alignment of the larger zones as seen on Figure 7.2.

This early characterization revealed evident alignment errors on the samples, reaching up to several hundreds of nanometres. Attempts to deal with the issue included reducing the number of marker searches, the beam current, changing marker fabrication process from electroplating to lift-off, changing the placement and search parameters of the markers. However, none of the mentioned methods improved the situation, proving that it was not caused by insufficient marker quality or charging. A careful study of the exposure log files revealed that regardless of the front or back side, the marker positions changed over time as seen on Figure 7.2. Besides the slow continuous thermal drift, on each membrane for some zone plates in the middle of the chip the markers were found up to 100 nm apart from the positions for the rest of the zone plates. This pattern persisted reproducibly over several chips exposed with a wide range of parameters. It later turned out that these few lenses in the centre of the membrane were well aligned, while all the rest were severely misaligned. In principle, the measured positions of the markers should be independent from the position of the patterns. Therefore a possible explanation involves a software glitch in the alignment procedure, that effectively cancels out when the markers surround the pattern nearly symmetrically in the centre of the membrane. The fabrication of the interlaced zone plates was done 1.5 years and several software updates after the previous double-sided zone plates, where the problem was clearly not present. Therefore tracking down the cause of the phenomenon is of high importance for the fabrication of double-sided zone plates in the future.

## 7.3 Efficiency measurements and pre-selection

All zone plates were tested at the cSAXS beamline of the Swiss Light Source. Although the structure height of our lenses were matched for  $\sim 4 - 5 \text{ keV}$  photon energy, for space constraints the characterization was performed at 9 keV, thus sacrificing a considerable amount of efficiency. Similarly to the double-sided zone plates in Chapter 5 and 6, the efficiency measurements were combined with an evaluation of the spatial distribution of

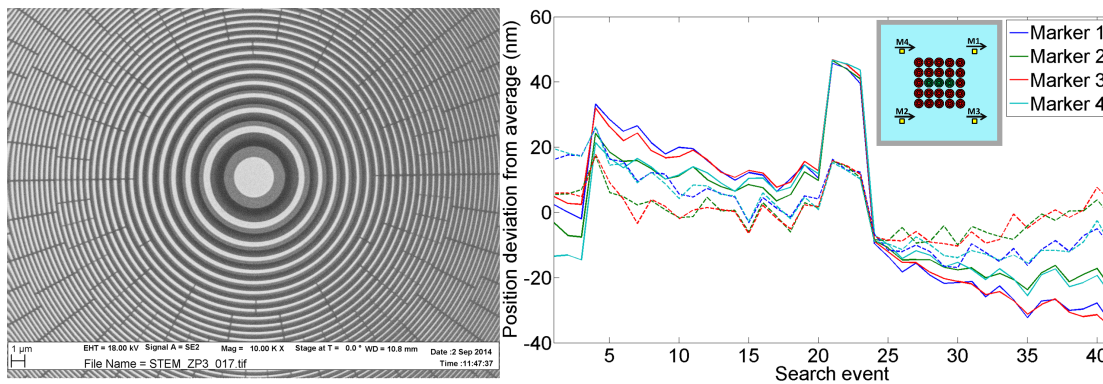


FIGURE 7.2: Left: STEM micrograph of the double-sided interlaced resist template. The left side looks brighter than the right side, which is a sign of imperfect alignment. Right: Recorded marker positions from one of the exposure log files in X (solid line) and Y (dashed line). The placement of the markers can be seen on the inset. The alignment was correct only between search events 21-23 corresponding to the middle zone plates on the membrane. All other zone plates were severely misaligned.

diffraction efficiency. Therefore the focusing efficiency of some reference zone plates were measured using a photodiode detector. These values were used to normalize the total number of counts recorded in their far-field diffraction cones. During the measurements, a total of 16 chips of zone plates with 15 nm and two chips with 7 nm outermost zone width were characterized. The diffraction cones were used as a high speed pre-selection procedure concerning the alignment of the zone plates.

### 7.3.1 15 nm outermost zone FZPs

A total of 16 zone plates with 15 nm smallest zone width were found to show no Moiré fringes, providing reasonable chance of sufficiently low misalignment. Amongst the 15 nm zone plates, the best zone plate had 0.92% focusing efficiency, which is similar to literature values for single sided line-doubled zone plates of similar zone width at much lower photon energy[74].

### 7.3.2 7 nm outermost zone FZPs

After the characterization of the 15 nm zone plates, the setup was rearranged for zone plates with 7 nm smallest zone width. During the pre-selection procedure of the first two chips of 25 zone plates, the central zone plate seen on Figure 7.3 stood out as being one without Moiré fringes. Since focusing efforts took a considerable amount of time, no further chips were tested. The tested zone plate was measured to have 0.52 % efficiency in the 7 nm diffraction order.

While the low efficiency can be partially attributed to the low structure height, another issue have been brought to our attention[88] after the experiments. Numerical

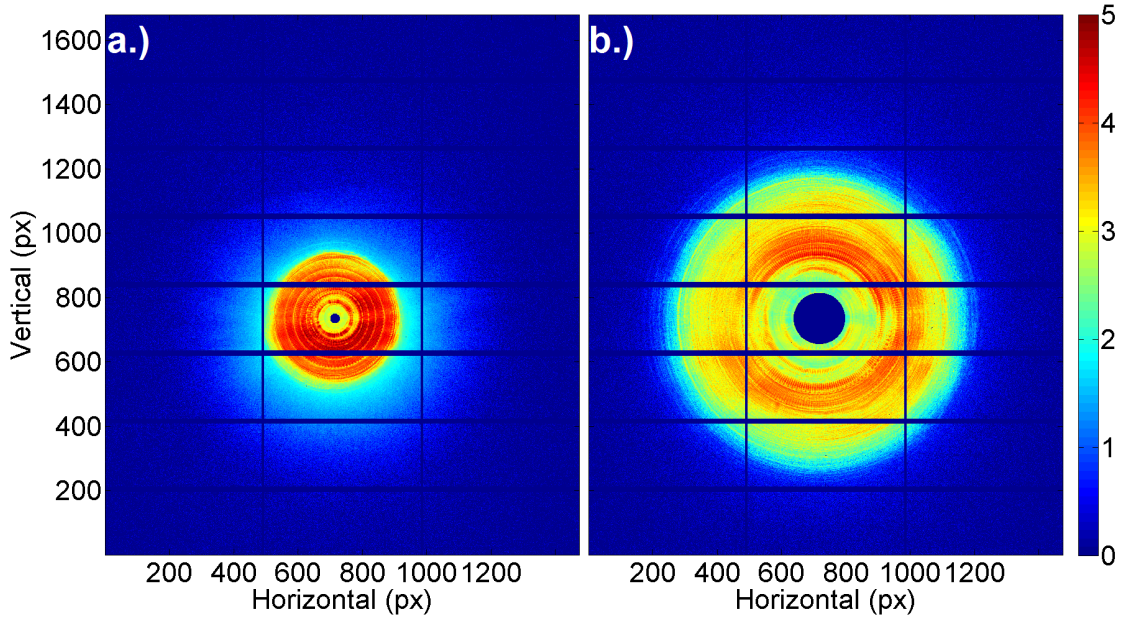


FIGURE 7.3: Diffraction cones of double sided interlaced zone plates with 15 nm (a.) and 7 nm (b.) smallest zone width on the Pilatus 2M detector on logarithmic scale.

simulations of high resolution interlaced zone plate stacks predict severely decreased focusing efficiency, due to the structure height being close to the  $d_F = dr^2/\lambda$  Fraunhofer-distance. When this happens, volumetric effects become dominant, favouring a tilted zone geometry even for single zone plates[65, 91, 92] and the adjustment of the zone plate diameters for zone plate stacks[84, 184]. Due to the unadjusted diameters as well as fabrication errors, the parasitic diffraction orders of the measured lens could be comparable with the primary focusing order.

## 7.4 Ptychography with interlaced zone plates

As it was observed in Chapter 4, the lack of Moiré fringes does not automatically mean perfect alignment. Hence each viable candidate had its wavefront characterized using ptychographic probe retrieval. The ptychographic characterization was performed on a line-doubled Siemens-star test object, mounted slightly after the focus, to obtain a 1.5 micron illumination cone.

Since the very high NA Fresnel zone plates covered a significant portion of the detector with their diffraction cone, the illuminating flux was spread over a large detector area, resulting in low counts in the individual pixels. In order to boost the illuminating coherent photon flux on the lenses, the horizontal slit of the beamline was closed down to improve horizontal coherence, while leaving the vertical coherence untouched. This resulted in an astigmatic illumination of our zone plates with 22 metre horizontal and 34 metre vertical source distance. In order to better deal with the low counts, the

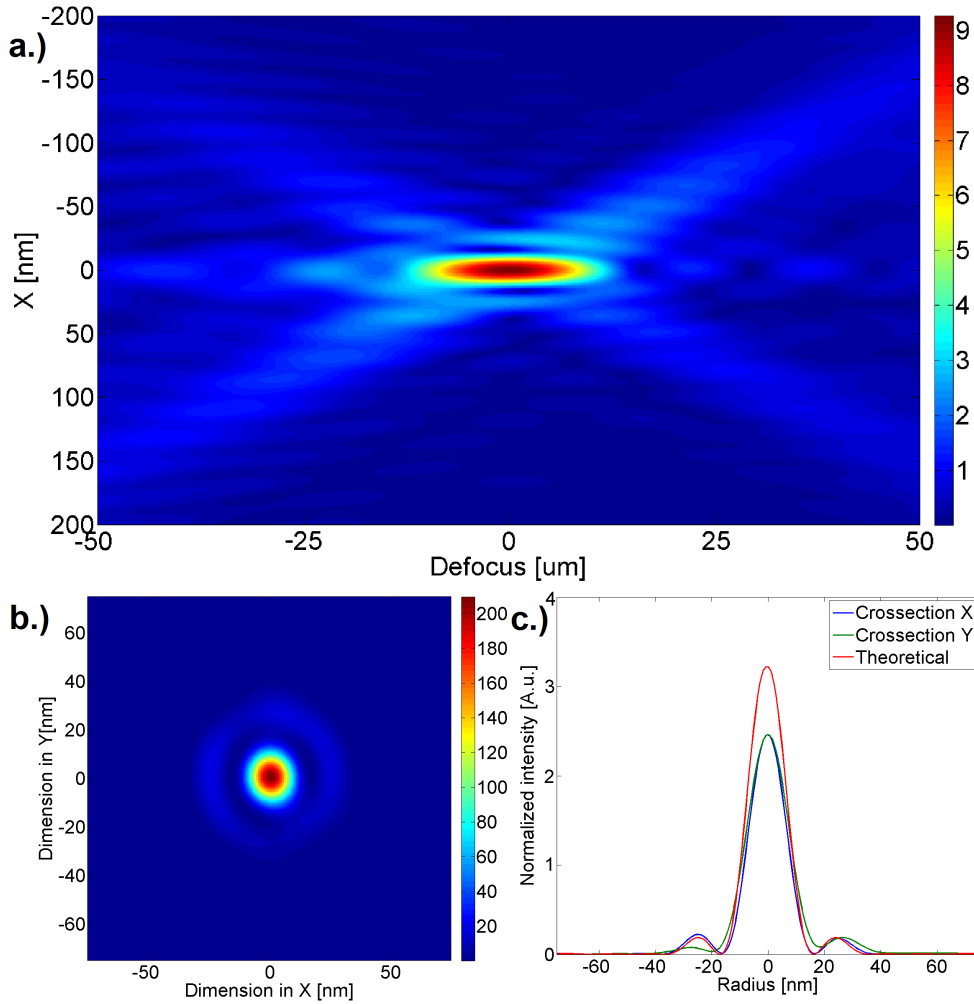


FIGURE 7.4: Ptychographic characterization of the 15 nm interlaced zone plate with the second highest Strehl ratio of 0.77 (see next section). The propagated wavefront a.) is free of major aberrations, albeit providing strong sidelobes. The retrieved focal spot b.) is slightly ellipsoidal, with 14.9 nm horizontal and 16.5 nm vertical full width at half maximum c.).

reconstructions were performed by the Maximum likelihood method[139] to account for Poisson-noise in the individual pixels. For each reconstruction a  $5 \times 5 \mu m^2$  area was sampled in 200 nm steps using a total of 2x400 views in the Fermat spiral arrangement. Please note that since each view includes the measurement of the full probe, the better sampling leads to higher quality probe reconstruction than the corresponding object reconstruction. As a single value benchmark, the Strehl ratio provides us with the relative peak intensity of the focal spot compared to the intensity normalized theoretical prediction of an aperture with a  $35 \mu m$  central stop. This value is a good indicator of the relative intensity of the peak versus the surrounding sidelobes.

Of the 16 tested 15 nm zone plates, the retrieved probes revealed that the efficiency not necessarily equalled perfect alignment or optical quality. The sidelobes were



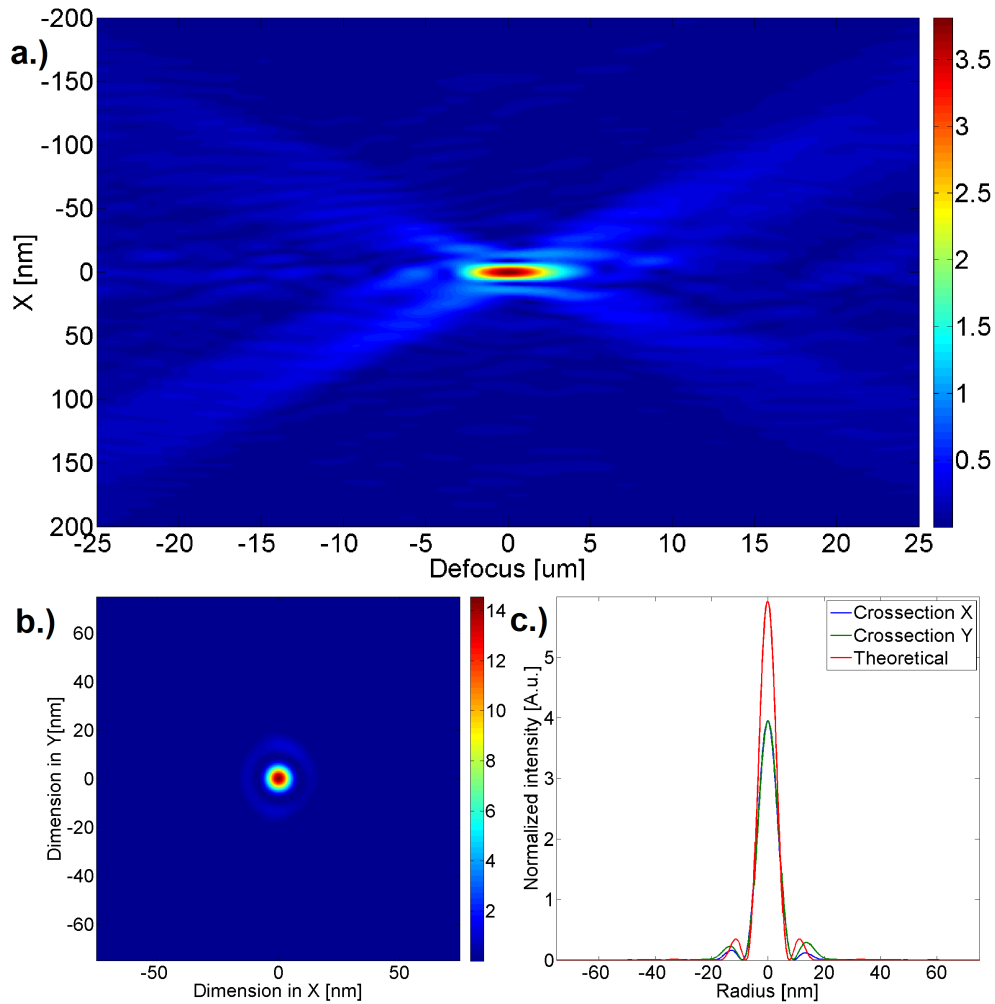


FIGURE 7.5: Ptychographic characterization of the 7 nm interlaced zone plate showing a.) the propagated amplitude and the b-c.) intensity in the focal plane. The zone plate has a single, circular focal spot with 7.8 nm full width at half maximum. A slight directionality of the sidelobes suggests only a minor shift between the two zone plates, within fraction of the smallest zone width.

slightly higher than the zone plates described in the previous chapter, which is in agreement with the measured Strehl ratios. The highest quality zone plate reached a Strehl ratio of 0.78 that is close to diffraction limited imaging. Most focal spots had a slightly ellipsoidal shape as seen on Figure 7.4 from their X and Y cross section. At total of 3 zone plates no elongation can be observed, they show a regular circular focal spot with only small unevenness in the first diffraction ring.

The retrieved focal spot of the 7 nm zone plate seen on Figure 7.5 shows a single focal spot, corresponding to the accurate alignment of the two sides. The spot is perfectly circular with a full width at half-maximum of 7.8 nm in the horizontal and 7.9 nm in the vertical direction. These values are clearly impressive, especially combined with the lack of severe aberrations. The sidelobes of the spot seen on Figure 7.5 are noticeably stronger than during the previous measurements, which is also represented by the Strehl

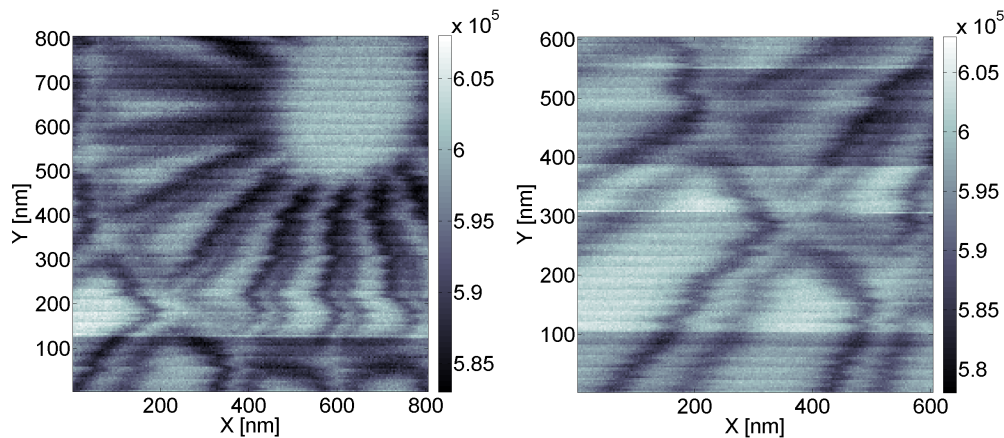


FIGURE 7.6: STXM images of a line-doubled Siemens star test pattern with 30 nm spoke size and 10 nm structures inside the tip of the spokes. The inside of the spokes is not fully resolved, the recorded scans show 12-15 nm resolution that is limited by positioning accuracy.

ratio of 0.66. Nevertheless the zone plate provides more than sufficient contrast for sub-10 nm imaging and clearly falls below the earlier predicted 13 nm limit of Fresnel zone plates[185]. The slight directionality of the sidelobes are discussed in more detail in Appendix B.

## 7.5 Imaging experiments

In order to demonstrate the imaging performance of the ultra-high resolution zone plates, some of the selected zone plates were tested in either scanning probe microscopy or full-field transmission microscopy measurements.

### 7.5.1 STXM with sub-10 nm zone plate

In particular, the 7 nm zone plate was tested as an objective for scanning transmission X-ray microscopy at the cSAXS beamline. The measurement was performed on a continuously moving sample in "flyscan mode" measuring 7 points per second in 2.5-3 nm steps. The scanning speed was limited by the detector speed and the available coherent flux, resulting in  $\sim 5 \times 10^5$  counts per point on the PILATUS 2M detector. The obtained resolution was clearly different in the horizontal and vertical direction. While the fast-scanning horizontal axis could clearly resolve 12-15 nm features, the slow-scanning vertical axis provided noticeably lower resolution in the range of 15-18 nm despite the better vertical coherence. This implied motor stability problems in the sub-10 nm range, which is not surprising, as the experimental setup was clearly not designed as a dedicated high resolution STXM setup.

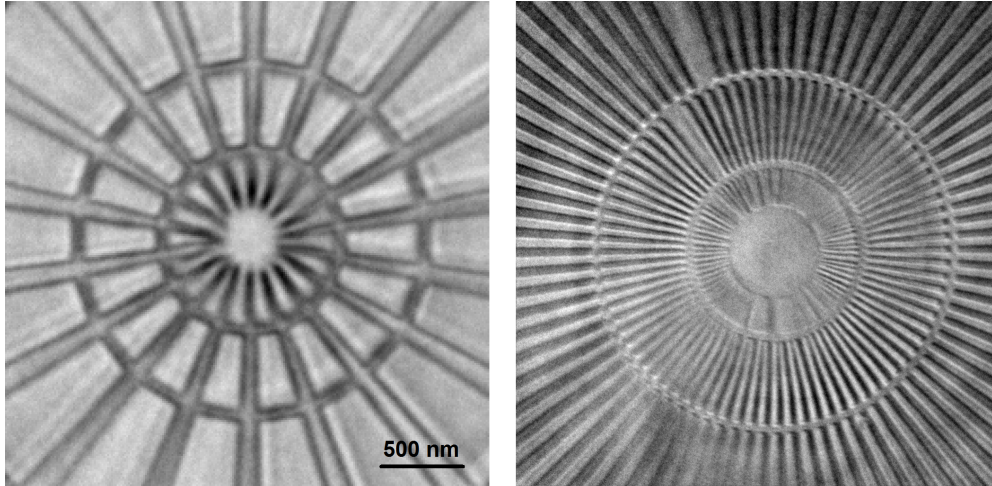


FIGURE 7.7: Preliminary full field microscopic images of Siemens star test patterns using the 15 nm zone plate as objective for focusing. The internal structure of the spokes of the line-doubled zone plate corresponds to  $\sim 15\text{-}18$  nm resolution.

### 7.5.2 Full-field X-ray microscopy with 15 nm zone plates

Some zone plates from the highest efficiency 15 nm zone plate chip were tested as an objective for full-field transmission X-ray microscopy at the 26-ID beamline of the Advanced Photon Source (APS, United States) at 9 keV.

Similarly to the scanning probe experiments, a line-doubled and an electroplated Siemens star was used as a test object down to 10 nm feature sizes with 30 nm spokes. Using the beamline's standard setup, a capillary condenser[109] with  $\sim 25$  mrad was employed as illuminating optics, that is roughly equivalent to a zone plate illumination with 25 nm smallest zone width. The condenser was mechanically shaken to destroy coherence fringes. While the results are still under evaluation at the time of writing, the high resolution zone plates had no trouble in resolving the 24 nm spokes of the electroplated Siemens star. They even revealed the internal structures of the line-doubled test object, putting their estimated resolution in the sub-20 nm range.

Unfortunately the 7 nm focus of the highest resolution zone plate could not be tested, due to the lack of matching illumination. As described earlier in Chapter 3 and illustrated on Figure 7.8, line-doubled zone plate objectives are more sensitive to the numerical aperture of the illumination than their electroplated counterparts. Using a much lower NA condenser means that low spatial frequencies pass through the centre of the zone plate, where the insufficient fill factor results in practically dead zones. This acts as a high-pass spatial filter resulting in a dark-field image, which is extremely dose inefficient[150]. The spatial filtering disappears with better matched illumination, when the frequencies are spread more evenly across the objective zone plate. However at the time of the measurements, condensers were far from reaching 7 nm smallest zone width.

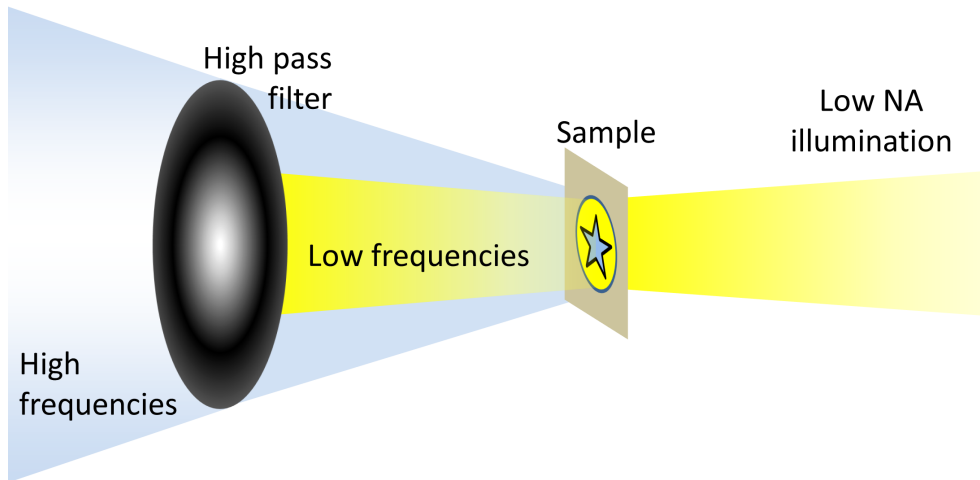


FIGURE 7.8: The problem of unmatched illumination with line-doubled zone plates. Using a low-NA condenser, the inefficient central part of the zone plate can not collect the low spatial frequencies. The high spatial frequencies are more effectively collected by the outer zones of the objective resulting in a dark-field image of the object. By a better matched illumination, the spatial frequencies can be distributed evenly over the efficient region of the zone plate.

## 7.6 Conclusion

The interlaced stacking of zone plates bears great potential to provide X-ray optics with extreme resolutions while maintaining a large aperture size and convenient working distance. During our proof-of concept measurements with double-sided interlaced zone plates, we were successful in achieving focal spots down to 7.8 nm full width at half maximum, breaking earlier predictions regarding the ultimate resolution of Fresnel zone plate optics[185]. Successful imaging experiments have shown that the tested 15 nm zone plates provided aberration free high resolution images in full-field microscopy as well as the 7 nm zone plate approached 10 nm resolution in STXM measurements. However utilizing the full potential of the presented lenses requires further development from other optical elements as well as from the beamlines themselves. While there is still room for improvements to solve issues regarding alignment, line profile and adjusted zone placement, the presented optics represent state of the art resolution combined with practical functionality.

## Chapter 8

# Summary and conclusion

The efforts presented in this thesis were driven by the needs of the Nanoscopium beamline of synchrotron SOLEIL. Therefore, the past chapters of this thesis described an innovative method for the fabrication of state of the art, easy to use zone plate optics for the hard X-ray range.

Starting with the established method of stacking two separate zone plates, Chapter 4 described the successful demonstration of very high efficiency zone plate optics using the concept of blazed stacking. The demonstrated zone plates with 47.1% and 53.7% efficiency over diameters up to 500  $\mu\text{m}$  and 200 nm smallest zone width offers gains up to  $10^6$  compared to the incident flux density. Moreover doing so while they maintain a convenient working distance and a considerable beam divergence for lensless imaging techniques. The achieved efficiencies were similar to multilevel zone plates produced with considerably larger zone width[71] or to multilayer zone plates with considerably larger spot size[81–83]. However encountered problems with stability during these early stacking experiments directed the author to an alternative solution.

The highlight of this thesis is clearly the fabrication of double-sided zone plates. While double-sided patterning has been around for a while, using pattern replication via self-aligned X-ray lithography[186] or direct patterning[100], the concept was not pursued beyond early proof-of-concept experiments. Yet the introduction of the presented through-membrane marker search procedure opened new possibilities in double-sided patterning, bringing its capabilities equal to zone plate stacking. Therefore, within this thesis double-sided zone plates are proposed to replace the conventional stacking of Fresnel zone plates.

Following the target of Chapter 4 for the production of very high efficiency zone plates, Chapter 5 reports the fabrication of the first double-sided blazed zone plates based on the blazed stacking of zone plates. The presented lenses deliver efficiencies up to 54.7% with 200 nm smallest zone width, making them appealing substitutes of

the earlier characterized mechanically stacked zone plates. They provide all of their advantages regarding efficiency and resolution while avoiding concerns regarding long term stability. Double-sided blazed zone plates are an excellent choice for the coherent diffraction imaging end-station of the Nanoscopium beamline of synchrotron SOLEIL.

Since the focusing optics for the nanoprobe end-station required completely different feature dimensions, Chapter 6 details the fabrication and characterization of high resolution line-doubled zone plate optics in double-sided stacking. With 30 nm smallest zone width, the presented double-sided line-doubled zone plates reach up to 9.9 % focusing efficiency at 9 keV, resulting in a factor of two improvement over previous values in the literature[74]. Moreover, the high efficiency comes in combination with diffraction limited optical quality, making the presented double-sided line-doubled zone plates an excellent choice for the nanoprobe end-station of the Nanoscopium beamline of synchrotron SOLEIL.

Pushing the limitations of a process always bears challenges, as demonstrated in Chapter 7 of this thesis with the production of ultra-high resolution zone plate optics following the interlaced stacking scheme[88]. Despite systematic manufacturing issues, large aperture, high resolution zone plate optics with 15 nm and 7 nm smallest zone width have been presented. Moreover, the zone plate with 7 nm smallest zone width achieved a focal spot with 7.8 nm full width at half-maximum while maintaining a considerable diameter of 100  $\mu\text{m}$  and the corresponding convenient working distance. Imaging experiments with the 15 nm zone plates have shown that the resolution of these lenses meet expectations. However, the successful use of the 7 nm zone plates need further development from other parts in instrumentation. Sub-10 nm scanning probe resolution would require a dedicated scanning setup using high accuracy, thermally stabilized stages with interferometric encoding and would also benefit considerably from more coherent flux. Full-field microscopy measurements would need a condenser with sufficiently high numerical aperture. Possibilities include the fabrication of a beamshaping condenser in higher diffraction order and matched field of view. Nevertheless presented interlaced line-doubled zone plates bear a great potential towards increasing resolution in future experimental setups in both scanning probe and full-field arrangement. This requires solving alignment related yield issues and improving focusing efficiency by adjusting zone plate diameters and improving line-profile control.

The above summarized accomplishments clearly fulfil the project goals of the Nanoscopium beamline and shall provide it with state-of-the-art X-ray optics with both excellent efficiency and optical quality. Furthermore the large diameter, high efficiency and high optical quality is accompanied with reasonable working distances and a permanently fixed, single-chip setup.

Yet, the above progress should be compared with other achievements on the

field. The past years have been a vibrant scene in the development of diffractive X-ray optics aiming to improve the resolution or the efficiency of existing optical setups. Newly developed fabrication methods like metal assisted chemical etching[79] or on-chip stacking schemes[92] –including the presented double-sided stacking[180]– fit well in the progress of providing a more efficient use of the available photon flux. Hence presented double-sided optics allow not only for improved sensitivity and measurement speed in scanning probe microscopy but also for higher resolution in full-field X-ray microscopy. Besides the developments in X-ray optics, one must not forget to mention the impressive achievements of coherent diffractive imaging methods in X-ray microscopy, that led to the redefinition of high resolution imaging for radiation hard specimens. However for low-contrast radiation sensitive specimens the resolution is ultimately limited by the exposure dose. Therefore the demonstrated increments in collection efficiency are not expected to further improve resolution, but to speed up measurements to facilitate high throughput ptychographic tomography[40, 187].

Despite all the development of the past century, X-ray science still continues to evolve. The emerging next generation of synchrotrons will offer improved coherence, improving the throughput of both coherent imaging methods and scanning probe experiments. Meanwhile advances in "big data" processing will keep pace with the ever increasing demands and throughput of tomographic full-field imaging methods. Besides developments in large scale facilities and methodology, instrumentation and computing power also became much more affordable. This opens the way for moving analytical techniques from the synchrotron to the laboratory and prompts the commercialization of X-ray microscopy in a similar fashion as with electron microscopy. For this particular field, advances in X-ray optics can provide a decisive advantage as —not only literally— every photon counts for the measurement.





## Appendix A

# Generalized update procedure in ptychographic reconstructions

While numerous algorithms have been developed over the past decade for ptychographic reconstruction, this appendix aims to extend the scope of the existing update procedures. The two most important algorithms for ptychographic reconstruction are the difference map method[127] and the ptychographic iterative engine[134, 135], which have been described in detail in Chapter 2 of this thesis. Both of these methods rely on generating a  $\Psi(r)$  exit wavefront of every  $j$  measurement at  $r_j$  position from the previous guess of the complex  $O(R)$  object and  $P(r)$  probe functions as  $\Psi_{n,j}(r) = O_n(r - r_j)P_n(r)$  in the ePIE or as  $\Psi_{n,j}(r) = 2O_n(r - r_j)P_n(r) - \Psi_{n-1,j}(r)$  in the difference map algorithm. When the algorithm converges towards a solution, in both algorithms the  $\Psi_{n,j}(r)$  converges towards:

$$\lim_{n \rightarrow \infty} \Psi_{n,j}(r) = O_n(r - r_j) \times P_n(r) \quad (\text{A.1})$$

Subsequently, each view is updated through the update procedure of coherent diffractive imaging[124]. The next step contains the key idea behind ptychography, as it aims to couple the individual  $\Psi_{n,j}(r)$  views to update a set of common object  $O(R)$  and probe  $P(r)$  functions. Since the exact update procedure is very similar in both algorithms, the further discussion will use the difference map formalism as:

$$O_{n+1} = \frac{\sum_j P_n^*(r) \Psi_j(r)}{\sum_j |P_n(r)|^2} \quad P_{n+1} = \frac{\sum_j O_n^*(r - r_j) \Psi_j(r)}{\sum_j |O_n(r - r_j)|^2} \quad (\text{A.2})$$

Yet, when substituting the assumption of Equation A.1 to the above update procedures, the above equations will take the form of:

$$O_{n+1} = \frac{\sum_j P_n^*(r) P_n(r) O_n(r - r_j)}{\sum_j |P_n(r)|^2} = \frac{\sum_j |P_n(r)|^2 O_n(r - r_j)}{\sum_j |P_n(r)|^2} \quad (\text{A.3})$$

$$P_{n+1} = \frac{\sum_j O_n^*(r - r_j) O_n(r - r_j) P_n(r)}{\sum_j |O_n(r - r_j)|^2} = \frac{\sum_j |O_n(r - r_j)|^2 P_n(r)}{\sum_j |O_n(r - r_j)|^2} \quad (\text{A.4})$$

The update procedures of Equation A.2 comes from the minimization of the  $ERR = \sum_j (|O(r - r_j) \times P(r) - \Psi(r)|^2$  error metric through complex mathematics. However, the equations in their forms of A.3 and A.4 themselves represent the rather simple mathematical context of weighted average, where the applied weight functions take the form of  $|O_n(r - r_j)|^2$  and  $|P_n(r)|^2$  i. e. the object transmissivity and the probe intensity. By putting this to a more general context, the weighted averaging can be performed with a alternative, real-valued (or constant-phased) weight function  $w(\vec{X})$  as well. Since during the object and probe update procedure the object and probe are assumed to be multiplied in the retrieved exit wavefront  $\Psi_j(r) = O^n(r - r_j) \times P^n(r)$ , the non-updated function must first be deconvolved from the exit wavefront. This modifies the weight function in the nominator into  $W_p(\vec{X}) = w_p(\vec{X})/O^n(r - r_j)$  for the probe and  $W_o(\vec{X}) = w_o(\vec{X})/P^n(r)$  for the object update. Hence the update procedure for the object and probe will become:

$$O_{n+1} = \frac{\sum_j \left( \frac{w(\vec{X})_o}{P_n(r)} \right) \Psi_j(r)}{\sum_j w(\vec{X})_o} = \frac{\sum_j W_o(\vec{X}) \Psi_j(r)}{\sum_j w(\vec{X})_o} \quad (\text{A.5})$$

$$P_{n+1} = \frac{\sum_j \left( \frac{w(\vec{X})_p}{O_n(r - r_j)} \right) \Psi_j(r)}{\sum_j w(\vec{X})_p} = \frac{\sum_j W_p(\vec{X}) \Psi_j(r)}{\sum_j w(\vec{X})_p} \quad (\text{A.6})$$

Please note the separate  $w(\vec{X})_o$  and  $w(\vec{X})_p$  weight functions of the object and probe. As the updates are performed separately, different weights can be applied based on the demands of the experiment. The most relevant question is the choice of the weight functions. Using the choice of  $w_o(r) = |P_n(r)|^2$  and  $w_p(r - r_j) = |O_n(r - r_j)|^2$ , one receives the original difference map algorithm. However the choice of weight can be chosen alternatively to increase or decrease the sensitivity of the reconstruction to other parameters.

An obvious choice of adjustment is the update procedure of the object, where the weight factor is conventionally determined as the probe intensity ( $I(r) = |P_n(r)|^2$ ), but the use of a general weighting function can cover more than polynomial dependence on the illuminating intensity. With the right scaling, the intensity dependence can be changed from a quadratic dependence to an arbitrary function, including non-linear functions like trigonometric, logarithmic, logistic, exponential or error function and their combination. Moreover there is the possibility of explicitly using distribution functions like Gaussian, logistic, or Poisson to describe probe significance. Using a customized weight function can be used to increase or decrease the significance of low- and high-intensity regions of the probe. In these terms, weighting with the intensity corresponds to using the Poisson distribution to correct for the lower statistical relevance of the

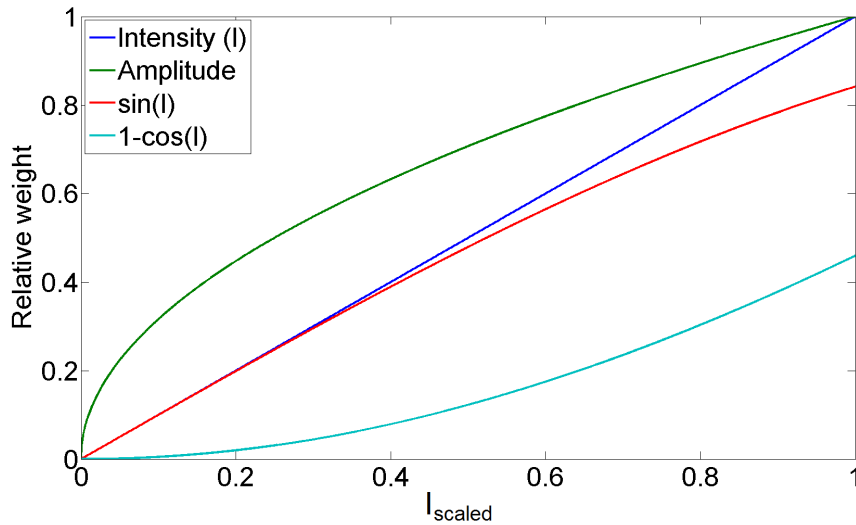


FIGURE A.1: Examples of the suggested non-linear weighting methods besides the conventional weighting with intensity.

low-intensity probe sidelobes due to discrete sampling. Another possible choice can be to increase significance of the sidelobes for high-flux ptychographic measurements (for example in the optical range) or for in-focus ptychography with sidelobe-assured overlap. Therefore, using a customized weight function can deliver an experiment specific solution, to extract the maximum amount of information from the acquired dataset. Moreover the coordinate  $\vec{X}$  was generalized for a reason as it is not limited to be a function of the illuminating intensity, since the probe can just as well be replaced by the actually measured wavefield intensity ( $w(\vec{X})_j = |\Psi_j(r)|^2$ ). One of the most important use of the weighted averaging can be the implementation of a window function. Window functions or boundary conditions are widely employed in CDI to aid the reconstruction of the exit wavefront and given ptychography's roots in CDI it have been shown to improve ptychographic reconstructions as well. Another suggested use is the implementation of coupling between multiple modes or slices in the reconstruction of optically thick objects, i.e. to focus the algorithm to regions with sufficient overall intensity or transmission.

The similarly to the object update procedure, the weight factor for the reconstruction of the probe can be also adjusted over a wide parameter range using similar functions as described for the object update procedure. A priori knowledge about the nature of the sample can provide valuable simplifications to change the contribution of unexpectedly dark or bright regions. In case of sufficiently transmitting objects, even a uniform weight can be applied or highly diverse objects can have a non-linear dependence on the transmission acting as thresholds for sufficient transmittance. Note that the Poisson statistics that is employed in the original algorithm has no physical meaning when employing it for the object transmittance, a more general approach would

employ the measured wavefield intensities instead ( $w(\vec{X})_j = |\Psi_j(r)|^2$ ). Moreover a window function can be employed to reduce the weight of under-sampled regions of the object for example on the reconstruction border. View specific weighting also allows for filtering out strong scattering centres that could hinder the initial convergence of the probe, for example based on the dark-field signal. It can also be employed to implement dependency between individual modes and planes of the reconstruction.

The weight can also be calibrated with external sensors like an external intensity monitor (photodiode, ring current, shutter status) that correct for variable statistics due to shot noise, optical or mechanical instabilities or synchronization issues even by adding view specific intensity normalization terms like  $W_o(\vec{X}) = w_o(I_{meas}, r_{sup}) \frac{I_{avg}}{I_{shot}} / P(r)$  and similar probe terms, where the weight of the statistical relevance can be separated from the normalized intensity. Note that the weighting function can be changed with every iteration.

Regarding the practical implementation of weighted averaging: While a complex window function may require considerable efforts to calculate on-the-fly, most terms of the weights will not change during one iteration. Thus the intensity dependent part of the weight functions do not have to be calculated on-the-fly but can be pre-evaluated into object and probe sized arrays, that can be calculated only once per iteration instead of being calculated at every overlap. Mixing different dependencies can be effectively calculated on a per element basis by assuming a multiplicative relationship between the terms:

$$w_o(\vec{X}) = w_o(I(r))w_{win,o}(r)w_{mode,o}(r)w_j \dots \quad W_o(\vec{X}) = \frac{w_o(\vec{X})I_{norm,o}(j)}{P_n(r)} \quad (\text{A.7})$$

$$w_p(\vec{X}) = w_p(I(r))w_{win,p}(r)w_{mode,p}(r)w_j, \dots \quad W_p(\vec{X}) = \frac{w_p(\vec{X})I_{norm,p}(j)}{O_n(R)} \quad (\text{A.8})$$

Initial tests performed on a range of parameter settings provided mixed results. High contrast test objects with coherent illumination and well defined probes seem to be largely tolerant for the nature of the update function. However datasets recorded under less-than ideal conditions, i.e. illumination instabilities, partial coherence or weakly scattering objects showed a stronger dependence. Changing the weight function lead to both positive and negative outcomes depending on the employed parameters.

In case of occasionally weak convergence, the convergence could be significantly improved by providing an accurate initial guess. This can be acquired by averaging all the measured intensity patterns, filtering it to the spatial frequency range of the well-defined illumination (like a Fresnel zone plate) and using CDI to retrieve the average exit wavefront. This way, the scattering from the sample can be averaged out, retaining only the constant component of the illuminating probe. Moreover, the presented weighted average can be also used to deconvolve the average illumination from coherent diffractive

imaging, both from overlapping and completely separated areas. As a general note, in the previous paragraphs we have shown that additional components can also be entered into the ptychographic reconstruction algorithms, this can be generalized by adding more components to the exit wavefront as well:  $\Psi = O \times P \times A \times B \times \text{etc.}$  that can be reconstructed together with the object and probe.

While the systematic studies on the matter have been put to halt during the writing of this thesis, the general concept of weighted averaging in the ptychographic update procedure is hereby described, published and opened for future progress under the Creative Commons licence.



## Appendix B

# Alignment tolerance of stacked zone plates

Using the simulation software described in Chapters 2 and 3, numerical simulations have been performed to investigate the alignment tolerance of stacked Fresnel zone plate optics. Following the concept of conventional zone plate stacking to increase effective structure height. The presented simulations have been performed on  $100\ \mu\text{m}$  diameter iridium zone plate optics with  $100\ \text{nm}$  smallest zone width at  $9\ \text{keV}$  photon energy. At this energy, the optimal structure height is  $\sim 1450\ \text{nm}$  according to Figure 2.5 and this is well below the Fraunhofer distance, so volume effects within the structures are negligible. The simulations were performed using the GPU accelerated code with  $5\ \text{nm}$  resolution. The wavefield was stored as a  $40960 \times 40960$  pixel array, with only the central  $20000 \times 20000$  pixels describing the zone plate pattern and the rest is being used as a buffer for the higher orders. The first order was summed up in the focal plane over a  $5\ \mu\text{m}$  diameter circular area corresponding to an order selecting aperture.

The simulated efficiencies are presented on Figure B.1 on two examples. In the first simulated stack each zone plate had  $725\ \text{nm}$  high iridium zones on each chip, adding up to  $1450\ \text{nm}$  which is the optimal height at this energy. In the second simulated stack each zone plate had  $300\ \text{nm}$  high iridium zones, adding up to a total of  $600\ \text{nm}$  structure height which is still far below the optimal value.

The simulations on Figure B.1 show that in case of very shallow structures, even for rather large misplacements comparable to the smallest zone width, the stacking provides a considerable increase in overall efficiency compared to the efficiency of a single zone plate. Since the misalignment is directional, there will be always well aligned regions called Moiré fringes perpendicular to the misalignment direction that quadratically benefit from the increased structure height. Hence the overall efficiency is not a good measure of alignment accuracy for very shallow zone plates.

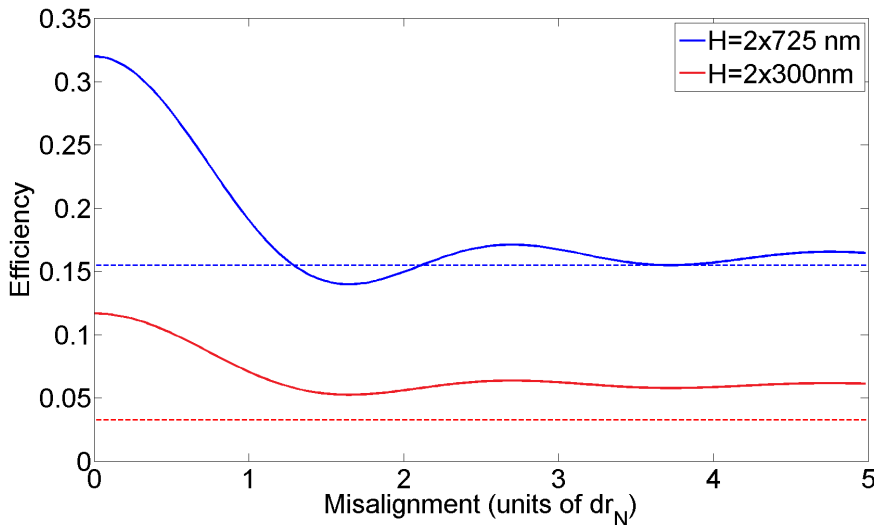


FIGURE B.1: Focusing efficiency of a zone plate stack as a function of misalignment for 1450 nm and 600 nm total structure height. Shallow structures benefit from the increased structure height even for severe misalignment.

For higher zones, misaligned stacks do not provide considerable benefits over the overall efficiency of a single zone plate. Hence the integral efficiency can be used as an indicator of the alignment accuracy as is the case in Chapter 6 for line-doubled double-sided zone plates.

The presence of Moiré fringes in the diffraction cone is a general indicator of large misalignment. However small displacements of the stack can be hard to distinguish from other fabrication inaccuracies, especially when they only affect the inefficient zone plate edge (due to fabrication inaccuracies).

The distortion of the focal spot is also relatively tolerant to the misalignment. Up to 1.5 times the smallest zone width only one, deformed focal spot is present as seen on Figure B.2. The deformations are mostly confined in the first Airy ring, while the main peak is only affected by a slight directional broadening. This can be explained by the fact that misalignment lowers the efficiency of certain spatial frequencies, resulting in an effectively lower NA illumination in that particular direction. Unfortunately inhomogeneous illumination of the zone plate also has the very same effect. For larger misplacements, the focal spot splits in two. These dual-spot Fresnel zone plates inherently provide differential interference contrast.

The interpretation of the above demonstrated simulated results can be questionable regarding the required alignment accuracy. While the literature suggests a required alignment accuracy of  $1/3$  of the smallest zone width, this does not represent a sharp barrier for imaging. Efficiency benefits can be claimed even from heavier misplacement while the imaging quality and even the imaging mechanism fundamentally changes with



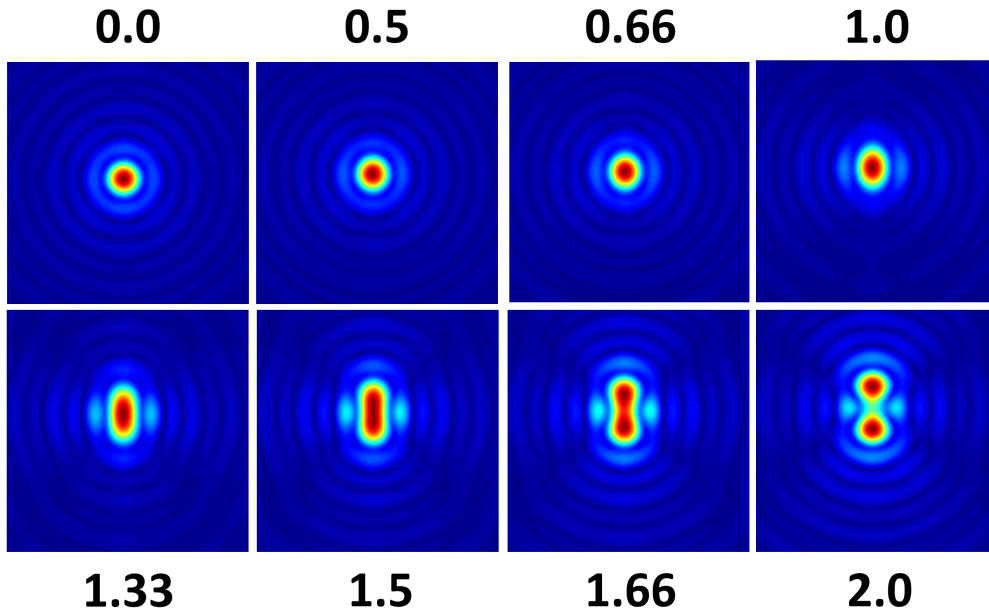


FIGURE B.2: Simulated amplitude of the focal spot under different degrees of misalignment (units are in smallest zone width). The elongation of the focal spot is barely noticeable below a misalignment of  $0.5\times$  of the smallest zone width just small deformations appear in the first ring. For further misalignment the elongation of the focal spot becomes larger, with finally splitting in two distinct spots at  $1.5\times$  the smallest zone width.

increasing misalignment. When one can expect other manufacturing issues, like distortions, rounding errors or zone placement inaccuracies affecting optical quality, this does not mean a hard limit of alignment accuracy and probably a slightly larger misalignment up to  $1/2 - 2/3$  can be still tolerated without drastic decrease in imaging performance.



# Bibliography

- [1] A. Somogyi, K. Medjoubi, C. M. Kewish, V. Le Roux, M. Ribbens, G. Baranton, F. Polack, and J. P. Samama. Status of the nanoscopium scanning nanoprobe beamline of synchrotron soleil. *Proc. SPIE*, 8851:885104, 2013.
- [2] J. Kirz and C. Jacobsen. The history and future of x-ray microscopy. *Journal of Physics: Conference Series*, 186:012001, 2009.
- [3] A. G. Michette and S. Pfauntsch. *X-rays: the first hundred years*. John Wiley and Sons, 1996.
- [4] Wikipedia: X-ray, . URL <http://en.wikipedia.org/wiki/X-ray>.
- [5] J. C. Maxwell. On physical lines of force. *Philosophical Magazine and Journal of Science*, 22-23, 1861.
- [6] E. Goldstein. Untersuchungen über die elektrische Entladung in verdünnten Gasen. *Würzburg, Physikal. Institut der Universität.*, 1886.
- [7] S. Nahorniak and M. Medyukh. *Physical-technical ideas of Ivan Pulyj*. Dschura, Ternopil, 1999.
- [8] W. C. Röntgen. Über eine neue Art von Strahlen (vorläufige mittheilung). *Würzburg, Physikal. Institut der Universität.*, 1895.
- [9] Wikipedia: Marie Curie, . URL [http://en.wikipedia.org/wiki/Marie\\_Curie](http://en.wikipedia.org/wiki/Marie_Curie).
- [10] M. von Laue. X-radiation interferences. *Particle Accelerators*, 4:211–227, 1913.
- [11] W. H. Bragg and W. L. Bragg. The reflection of x-rays by crystals. *Proceedings of the Royal Society London A*, 88:428–438, 1913.
- [12] P. Goby. New application of the x-rays: Micro-radiography. *Journal of the Royal Microscopical Society*, 33:373–375, 1913.
- [13] W. D. Coolidge. Vacuum-tube. *US patent 1203495*, 1916.
- [14] W. D. Coolidge. X-ray apparatus. *US patent 1215116*, 1917.

- [15] D. McMullan. Scanning electron microscopy 1928-1965. *51st Annual Meeting of the Microscopy Society of America*, 1993.
- [16] E. Ruska. Die elektronenmikroskopische Abbildung elektronenbestrahlter oberflächen. *Zeitschrift für Physik*, 83:492–497, 1933.
- [17] M. Knoll. Aufladepotential und Sekundäremission elektronenbestrahlter Körper. *Zeitschrift für Technische Physik*, 16:467–475, 1935.
- [18] M. von Ardenne. Das Elektronen-Rastermikroskop. *Zeitschrift für Physik*, 109:553–572, 1937.
- [19] P. Kirkpatrick and V. A. Baez. Formation of optical images by x-rays. *Journal of the Optical Society of America*, 38:766–774, 1948.
- [20] H. Mahl. Die übermikroskopische Oberflächendarstellung mit dem Abdruckverfahren. *Kolloid Zeitschrift*, 100:219–228, 1942.
- [21] M. von Ardenne. Ergebnisse einer neuen Elektronen-übermikroskop-Anlage. *Die Naturwissenschaften*, 28:113–127, 1940.
- [22] J. Larmor. On a dynamical theory of the electric and luminiferous medium. *Philosophical Transactions of the Royal Society*, 190:205300, 1897.
- [23] G. A. Schott. *Electromagnetic Radiation*. Cambridge Univ. Press, New York, 1912.
- [24] F. R. Elder, A. M. Gurewitsch, R. V. Langmuir, and H. C. Pollock. Radiation from electrons in a synchrotron. *Physical Review*, 71:829–830, 1947.
- [25] E. M. Rowe and F. E. Mills. Tantalus I: A dedicated storage ring synchrotron radiation source. *Particle Accelerators*, 4:211–227, 1973.
- [26] R. W. Gerchberg and W. O. Saxton. A practical algorithm for the determination of the phase from image and diffraction plane pictures. *Optik*, 35:237, 1972.
- [27] J. R. Fienup. Reconstruction of an object from the modulus of its Fourier transform. *Optics Letters*, 3:27, 1978.
- [28] A. V. Baez. Fresnel zone plate for optical image formation using extreme ultraviolet and soft x radiation. *Journal of the Optical Society of America*, 51(4):405, 1961.
- [29] J. Kirz. Phase zone plates for x-rays and the extreme UV. *Journal of the Optical Society of America*, 64(3):301–309, 1974.
- [30] B. Niemann, D. Rudolph, and G. Schmahl. X-ray microscopy with synchrotron radiation. *Applied Optics*, 15:1883–1884, 1976.
- [31] J. Kirz, R. Burg, and H. Rarback. Plans for a scanning transmission x-ray microscope. *Annals of the New York Academy of Sciences*, 342:135–147, 1980.

- [32] J. M. Kenney, J. Kirz, H. Rarback, R. Feder, D. Sayre, and M. Howells. Scanning soft x-ray microscopy with a Fresnel zoneplate at the National Synchrotron Light Source. *SPIE Proc.*, 447:158, 1984.
- [33] J. Ingwersen. Investigations on the Ag<sub>2</sub>S/GeS<sub>2</sub>-inorganic photoresist system for the fabrication of high resolution zone plates. *X-Ray Microscopy III.*, 67:98–100, 1990.
- [34] G. Schmahl, D. Rudolph, P. Guttman, and O. Christ. Zone plates for x-ray microscopy. *X-Ray Microscopy*, 43:63–74, 1984.
- [35] D. Kern, P. Coane, R. Acosta, T. H. P. Chang, R. Feder, P. Houzego, W. Molzen, J. Powers, A. Speth, R. Viswanathan, J. Kirz, H. Rarback, and J. Kenney. Electron beam fabrication and characterization of Fresnel zone plates for soft x-ray microscopes. *SPIE Proc.*, 447:204–213, 1984.
- [36] C. David, R. Medenwaldt, J. Thieme, P. Guttman, D. Rudolph, and G. Schmahl. Electron beam generated phase zone plates with 30 nm zonewidth for high resolution x-ray microscopy. *Journal of Optics*, 23:255–258, 1992.
- [37] Werner Meyer-Ilse. Soft x-ray imaging using CCD sensors. *SPIE Proc.*, 733:515, 1986.
- [38] H. N. Chapman and K. A. Nugent. Coherent lensless x-ray imaging. *Nature Photonics*, 4:833839, 2010.
- [39] J. Vila-Comamala, A. Diaz, M. Guizar-Sicairos, A. Manton, C. M. Kewish, A. Menzel, O. Bunk, and C. David. Characterization of high-resolution diffractive x-ray optics by ptychographic coherent diffractive imaging. *Optics Express*, 19: 21333–21344, 2011.
- [40] M. Holler, A. Diaz, M. Guizar-Sicairos, P. Karvinen, E. Färm, E. Harkonen, M. Ritala, A. Menzel, J. Raabe, and O. Bunk. X-ray ptychographic computed tomography at 16 nm isotropic 3D resolution. *Scientific Reports*, 4:3857, 2014.
- [41] D. Einfeld. Multi-bend achromat lattices for storage ring light sources. *Synchrotron Radiation News*, 27(6):4–7, 2014.
- [42] A. Streun, M. Aiba, M. Böge, M. Ehrlichman, and Á. Saá Hernández. Design studies for an upgrade of the SLS storage ring. *IPAC 2015 Proc.*, 2015.
- [43] J. Spence. Ultrafast diffract-and-destroy movies. *Nature Photonics*, 2:390–391, 2008.
- [44] O. Hemberg, M. Otendal, and H. M. Hertz. Liquid-metal-jet anode electron-impact x-ray source. *Applied Physics Letters*, 83:1483, 2003.

- [45] G. Schmahl, B. Niemann, D. Rudolph, M. Diehl, J. Thieme, W. Neff, R. Holz, R. Lebert, F. Richter, and G. Herziger. A laboratory x-ray microscope with a plasma x-ray source. *X-ray Microscopy III*, 67:66–69, 1990.
- [46] P. A. Sprangle, A. Ting, E. H. Esarey, A. Fisher, G. Mourou, and R. Sudan. Laser synchrotron source (LSS). *US patent 5353291*, 1993.
- [47] K. Yamauchi, H. Mimura, T. Kimura, H. Yumoto, S. Handa, S. Matsuyama, K. Arima, Y. Sano, K. Yamamura, K. Inagaki, H. Nakamori, J. Kim, K. Tamasaku, Y. Nishino, M. Yabashi, and T. Ishikawa. Single-nanometer focusing of hard x-rays by KirkpatrickBaez mirrors. *Journal of Physics: Condensed Matter*, 23:394206, 2011.
- [48] C. G. Schroer, F. E. Brack, R. Brendler, S. Hönig, R. Hoppe, J. Patommel, S. Ritter, M. Scholz, A. Schropp, F. Seiboth, D. Nilsson, J. Rahomäki, F. Uhlén, U. Vogt, J. Reinhardt, and G. Falkenberg. Hard x-ray nanofocusing with refractive x-ray optics: Full beam characterization by ptychographic imaging. *SPIE Proc.*, 8848:884807–1, 2013.
- [49] B. Lengeler, C. G. Schroer, M. Kuhlmann, B. Benner, T. F. Günzler, O. Kurapova, F. Zontone, A. Snigirev, and I. Snigireva. Refractive x-ray lenses. *Journal of Physics D: Applied Physics*, 38:218–222, 2005.
- [50] A. Snigirev, V. Kohn, I. Snigireva, and B. Lengeler. A compound refractive lens for focusing high-energy x-rays. *Nature*, 384:49–51, 1996.
- [51] C. G. Schroer, M. Kuhlmann, U. T. Hunger, T. F. Günzler, O. Kurapova, S. Feste, F. Frehse, B. Lengeler, M. Drakopoulos, A. Somogyi, A. S. Simionovici, A. Snigirev, I. Snigireva, C. Schug, and W. H. Schröder. Nanofocusing parabolic refractive x-ray lenses. *Applied Physics Letters*, 82:1485, 2003.
- [52] C. G. Schroer, O. Kurapova, J. Patommel, P. Boye, J. Feldkamp, B. Lengeler, M. Burghammer, C. Riekel, L. Vincze, A. van der Hart, and M. Küchler. Hard x-ray nanoprobe based on refractive x-ray lenses. *Applied Physics Letters*, 87:124103, 2005.
- [53] B. Nöhammer, J. Hozzowska, A. Freund, and C. David. Diamond planar refractive lenses for third- and fourth-generation x-ray sources. *Journal of Synchrotron Radiation*, 10:168–171, 2003.
- [54] B. Nöhammer, C. David, J. Hozzowska, A. Freund, A. Somogyi, and A. Simionovici. Focusing of hard x-rays using diamond and silicon refractive lenses. *Journal de Physique IV*, 104:223–226, 2003.

- [55] F. Seiboth, J. Patommel M. Scholz and, R. Hoppe, F. Wittwer, J. Reinhardt, J. Seidel, M. Knaut, A. Jahn, K. Richter, J. W. Bartha, G. Falkenberg, and C. G. Schroer. Hard x-ray nanofocusing by refractive lenses of constant thickness. *Applied Physics Letters*, 105:131110, 2014.
- [56] M. Polikarpov, I. Snigireva, J. Morse, V. Yunkin, S. Kuznetsov, and A. Snigirev. Large-acceptance diamond planar refractive lenses manufactured by laser cutting. *Journal of Synchrotron Radiation*, 22:23–28, 2015.
- [57] A. Andrejczuk, M. Nagamine, Y. Sakurai, and M. Itou. A planar parabolic refractive nickel lens for high-energy x-rays. *Journal of Synchrotron Radiation*, 21: 57–60, 2013.
- [58] A. Snigirev, I. Snigireva, M. Grigoriev, V. Yunkin, M. DiMichiel, G. Vaughan, V. Kohn, and S. Kuznetsov. High energy x-ray nanofocusing by silicon planar lenses. *Journal of Physics: Conference Series*, 186:012072, 2009.
- [59] J. L. Soret. Über die von Kreisgittern erzeugten Diffraktionsphaenomene. *Archives des Sciences Physiques et Naturelles*, 52:320, 1875.
- [60] C. Liu, R. Conley, A. T. Macrander, J. Maser, H. C. Kang, M. A. Zurbuchen, and G. B. Stephenson. Depth-graded multilayers for application in transmission geometry as linear zone plates. *Journal of Applied Physics*, 98:113519, 2005.
- [61] X. Huang, H. Yan, E. Nazaretski, R. Conley, N. Bouet, J. Zhou, K. Lauer, L. Li, D. Eom, D. Legnini, R. Harder, I. K. Robinson, and Y. S. Chu. 11 nm hard x-ray focus from a large-aperture multilayer Laue lens. *Scientific Reports*, 3:3562, 2014.
- [62] H. C. Kang, H. Yan, R. P. Winarski, M. V. Holt, J. Maser, C. Liu, R. Conley, S. Vogt, A. T. Macrander, and G. B. Stephenson. Focusing of hard x-rays to 16 nanometers with a multilayer Laue lens. *Applied Physics Letters*, 92:221114, 2008.
- [63] S. Caticha-Ellis. *Anomalous Dispersion of X-rays in Crystallography*. University College Cardiff Press, Cardiff, Wales, 1981.
- [64] R. G. Driggers. *Encyclopedia of optical engineering*. CRC press, 2003.
- [65] G. Schneider. Zone plates with high efficiency in high orders of diffraction described by dynamical theory. *Applied Physics Letters*, 71:2242–2244, 1997.
- [66] B. Nöhammer, C. David, J. Gobrecht, and H. P. Herzig. Optimized staircase profiles for diffractive optical devices made from absorbing materials. *Optics Letters*, 28(13):1087–1089, 2003.
- [67] D. C. Shaver, D. C. Flanders, N. M. Ceglio, and H. I. Smith. X-ray zone plates fabricated using electron-beam and x-ray lithography. *Journal of Vacuum Science and Technology*, 16:1626, 1979.

- [68] E. H. Anderson and D. Kern. Nanofabrication of zone plates for x-ray microscopy. *X-ray Microscopy III.*, 67:7578, 1990.
- [69] J. Vila-Comamala, S. Gorelick, V. A. Guzenko, E. Färm, M. Ritala, and C. David. Dense high aspect ratio hydrogen silsesquioxane nanostructures by 100 keV electron beam lithography. *Nanotechnology*, 21:285305, 2010.
- [70] W. Chao, B. D. Harteneck, J. A. Liddle, E. H. Anderson, and D. T. Attwood. Soft x-ray microscopy at a spatial resolution better than 15 nm. *Nature*, 435:1210–1213, 2005.
- [71] E. DiFabrizio, F. Romanato, M. Gentili, S. Cabrini, B. Kaulich, J. Susini, and R. Barrett. High-efficiency multilevel zone plates for keV x-rays. *Nature*, 401:895–898, 1999.
- [72] J. Vila-Comamala S. Gorelick, V. A. Guzenko and C. David. Direct e-beam writing of dense and high aspect ratio nanostructures in thick layers of PMMA for electroplating. *Nanotechnology*, 21:295303, 2010.
- [73] K. Jefimovs, J. Vila-Comamala, T. Pilvi, J. Raabe, M. Ritala, and C. David. Zone-doubling technique to produce ultrahigh-resolution x-ray optics. *Physical Review Letters*, 99:264801, 2007.
- [74] J. Vila-Comamala, S. Gorelick, E. Färm, C. M. Kewish, A. Diaz, R. Barrett, V. A. Guzenko, M. Ritala, and C. David. Ultra-high resolution zone-doubled diffractive x-ray optics for the multi-keV regime. *Optics Express*, 19:175–184, 2011.
- [75] Y. Feng, M. Feser, A. Lyon, S. Rishton, X. Zeng, S. Chen, S. Sassolini, and W. Yun. Nanofabrication of high aspect ratio 24 nm x-ray zone plates for x-ray imaging applications. *Journal of Vacuum Science and Technology B*, 25:2004, 2007.
- [76] F. Uhlén, D. Nilsson J. Rahomaki, L. Belova, C. G. Schroer, F. Seiboth, A. Holmberg, H. M. Hertz, and U. Vogt. Nanofabrication of tungsten zone plates with integrated platinum central stop for hard x-ray applications. *Microelectronic Engineering*, 116:40–43, 2014.
- [77] C. David, B. Kaulich, R. Medenwaldt, M. Hettwer, N. Fay, M. Diehl, J. Thieme, and G. Schmahl. Low-distortion electron-beam lithography for fabrication of high-resolution germanium and tantalum zone plates. *Journal of Vacuum Science and Technology B*, 13:2762, 1995.
- [78] F. Döring, A. L. Robisch, C. Eberl, M. Osterhoff, A. Ruhlandt, T. Liese, F. Schlenkrich, S. Hoffmann, M. Bartels, T. Salditt, and H. U. Krebs. Sub-5 nm hard x-ray point focusing by a combined Kirkpatrick-Baez mirror and multilayer zone plate. *Optics Express*, 21:19311–19323, 2013.



- [79] C. Chang and A. Sakdinawat. Ultra-high aspect ratio high-resolution nanofabrication for hard x-ray diffractive optics. *Nature Communications*, 5:4243, 2014.
- [80] B. Nöhammer, J. Hoszowska, H. P. Herzig, and C. David. Blazed silicon zone plates for hard x-rays with ultra-high diffraction efficiencies. *Journal de Physique IV*, 104:193–196, 2003.
- [81] S. Tamura, M. Yasumoto, N. Kamijo, Y. Suzuki, M. Awaji, A. Takeuchi, K. Uesugi, Y. Terada, and H. Takano. New approaches to fabrication of multilayer Fresnel zone plate for high-energy synchrotron radiation x-rays. *Vacuum*, 80:823827, 2006.
- [82] S. Tamura, M. Yasumoto, N. Kamijo, A. Takeuchi, K. Uesugi, and Y. Suzuki. Multilevel-type multilayer x-ray lens (Fresnel zone plate) by sputter deposition. *Vacuum*, 8:691694, 2009.
- [83] S. Tamura, M. Yasumoto, N. Kamijo, A. Takeuchi, K. Uesugi, Y. Terada, and Y. Suzuki. Quasi-blazed type multilayer zone plate for x-rays. *Vacuum*, 84:691694, 2010.
- [84] J. Vila-Comamala, M. Wojcik, A. Diaz, M. Guizar-Sicairos, C. M. Kewish, S. Wang, and C. David. Angular spectrum simulation of x-ray focusing by Fresnel zone plates. *Journal of synchrotron radiation*, 20(3):397–404, 2013.
- [85] J. Maser, B. Lai, W. Yun, S. D. Shastri, Z. Cai, W. Rodrigues, S. Xua, and E. Trackhtenberg. Near-field stacking of zone plates in the x-ray range. *Proc. SPIE*, 4783:74, 2002.
- [86] S. Chen, A. Lyon, J. Kirz, S. Seshadri, Y. Feng, M. Feser, S. Sassolini, F. Duewer, X. Zeng, and C. Huang. Absolute efficiency measurement of high-performance zone plates. *Proc. SPIE*, 7448:74480D, 2009.
- [87] M. Feser and A. F. Lyon. Stacked zone plates for pitch frequency multiplication. *US patent 20140126703*, 2014.
- [88] S. Rehbein, A. Lyon, R. Leung, M. Feser, and G. Schneider. Near field stacking of x-ray zone plates for frequency multiplication of their effective zone period. *Optics Express*, 23(9):11063–11072, 2015.
- [89] A. G. Michette. *Optical Systems for Soft X Rays*. Plenum Press, New York, 1986.
- [90] I. Snigireva, A. Snigirev, V. Kohn, V. Yunkin, M. Grigoriev, S. Kuznetsov, G. Vaughan, and M. DiMichiel. Focusing high energy x-rays with stacked Fresnel zone plates. *physica status solidi (a)*, 204:2817–2823, 2007.
- [91] J. Maser and G. Schmahl. Coupled wave description of the diffraction by zone plates with high aspect ratios. *Optics Communications*, 89:355–362, 1992.

- [92] S. Werner, S. Rehbein, P. Guttman, and G. Schneider. Three-dimensional structured on-chip stacked zone plates for nanoscale x-ray imaging with high efficiency. *Nano Research*, 7:1–8, 2014.
- [93] F. Pfeiffer, C. David, J. F. van der Veen, and C. Bergemann. Nanometer focusing properties of Fresnel zone plates described by dynamical diffraction theory. *Physical Review B*, 73:245331, 2006.
- [94] K. Jefimovs, J. Vila-Comamala, M. Stampanoni, B. Kaulich, and C. David. Beamshaping condenser lenses for full-field transmission x-ray microscopy. *Journal of Synchrotron Radiation*, 15:106–108, 2008.
- [95] P. Karvinen, D. Grolimund, M. Willmann, B. Meyer, M. Birri, C. Borca, J. Patommel, G. Wellenreuther, G. Falkenberg, M. Guizar-Sicairos, A. Menzel, and C. David. Kinoform diffractive lenses for efficient nano-focusing of hard x-rays. *Optics Express*, 22(14):16676–16685, 2014.
- [96] E. R. Dowski and W. T. Cathey. Extended depth of field through wave-front coding. *Applied Optics*, 34(11):1859–1866, 1995.
- [97] B. Kaulich, T. Wilhein, E. DiFabrizio, F. Romanato, M. Altissimo, S. Cabrini, B. Fayard, and J. Susini. Differential interference contrast x-ray microscopy with twin zone plates. *Journal of the Optical Society of America*, 19(4):797–806, 2002.
- [98] M. Lindblom, T. Tuohimaa, A. Holmberg, T. Wilhein, H. M. Hertz, and U. Vogt. High-resolution differential interference contrast x-ray zone plates: Design and fabrication. *Spectrochimica Acta B*, 62(6):539–543, 2007.
- [99] A. Sakdinawat and Y. Liu. Soft-x-ray microscopy using spiral zone plates. *Optics Letters*, 32(18):2635–2637, 2007.
- [100] E. DiFabrizio, B. Kaulich, T. Wilhein, and J. Susini. Differential interference contrast for x-ray microscopy: Fabrication and characterization of twin zone plate optics. *Surface Review and Letters*, 9(1):243–248, 2002.
- [101] G. Schneider. Influence of roughness and interdiffusion in zone plate structures on the diffraction efficiency described by coupled wave theory. *Applied Physics Letters*, 73:599–601, 1998.
- [102] Y. V. Kopylov, A. V. Popov, and A. V. Vinogradov. Application of the parabolic wave equation to x-ray diffraction optics. *Optics Communications*, 118:619–636, 1995.
- [103] A. N. Kurokhtin and A. V. Popov. Simulation of high-resolution x-ray zone plates. *Journal of the Optical Society of America A*, 19(2):315–324, 2002.

- [104] J. Goodman. *Introduction to Fourier Optics*. Roberts and Co. Publishers, 2005.
- [105] O. K. Ersoy. *Diffraction, Fourier Optics and Imaging*. John Wiley and Sons, 2006.
- [106] C. F. Gauss. Theoria interpolationis methodo nova tractata. *Göttingen: Königliche Gesellschaft der Wissenschaften*, 3:265327, 1866.
- [107] J. W. Cooley and J. W. Tukey. An algorithm for the machine calculation of complex Fourier series. *Mathematics of Computation*, 19(90):297–301, 1965.
- [108] Zeiss basic concepts in microscopy. URL <http://zeiss-campus.magnet.fsu.edu/articles/basics>.
- [109] W. Yun, F. W. Duerwer, and Y. Wang. X-ray microscope capillary condenser system. *US patent 7170969*, 2007.
- [110] H. H. Hopkins and P. M. Barham. Influence of the condenser on microscopic resolution. *The proceedings of the physical society*, 63:370, 1950.
- [111] S. Bradbury. *An Introduction to the Optical Microscope*. Oxford Science Publishers, New York, 1989.
- [112] G. Schmahl, D. Rudolph, P. Guttman, G. Schneider, J. Thieme, and B. Niemann. Phase contrast studies of biological specimens with the x-ray microscope at BESSY. *Review of Scientific Instruments*, 66:1282, 1995.
- [113] Y. Kagoshima, Y. Yokoyama, T. Ibuki, T. Niimi, Y. Tsusaka, K. Takai, and J. Matsui. High-resolution hard x-ray phase-contrast microscopy with a large-diameter and high-numerical-aperture zone plate. *Journal of Synchrotron Radiation*, 9(3):132–135, 2002.
- [114] I. Vartiainen, R. Mokso, M. Stampanoni, and C. David. Halo suppression in full-field x-ray Zernike phase contrast microscopy. *Optics Letters*, 39(6):1601–1604, 2014.
- [115] D. Weiss, G. Schneider, B. Niemann, P. Guttman, D. Rudolph, and G. Schmahl. Computed tomography of cryogenic biological specimens based on x-ray microscopic images. *Ultramicroscopy*, 84:185–197, 2000.
- [116] M. Feser, T. Beetz, M. Carlucci-Dayton, and C. Jacobsen. Instrumentation advances and detector development with the stony brook scanning transmission x-ray microscope. *AIP Conference Proceedings*, 507:367, 2000.
- [117] M. Feser, T. Beetz, M. Carlucci-Dayton, and C. Jacobsen. Integrating silicon detector with segmentation for scanning transmission x-ray microscopy. *Nuclear Instruments and Methods in Physics Research Section A*, 565(2):841–854, 2006.

- [118] M. L. Rivers, S. R. Sutton, and K. W. Jones. X-ray fluorescence microscopy. *X-ray Microscopy III*, 67:212–216, 1990.
- [119] A. Guimer and G. Fournet. *Small angle scattering of X-rays*. J. Wiley and Sons, New York, 1955.
- [120] P. Fratzl, H. F. Jakob, S. Rinnerthaler, P. Roschger, and K. Klaushofer. Position-resolved small-angle x-ray scattering of complex biological materials. *Journal of Applied Crystallography*, 30:765–769, 1997.
- [121] G. Kirchhoff. Zur Theorie der Lichtstrahlen. *Annalen der Physik*, 254(4), 1883.
- [122] M. R. Howells. Possibilities for x-ray holography using synchrotron radiation. *X-ray microscopy*, pages 318–335, 1984.
- [123] I. McNulty, J. Kirz, C. Jacobsen, E. H. Anderson, M. R. Howells, and D. P. Kern. High-resolution imaging by Fourier transform x-ray holography. *Science*, 256:1009–1012, 1992.
- [124] J. Miao, P. Charalambous, J. Kirz, and D. Sayre. Extending the methodology of x-ray crystallography to allow imaging of micrometre-sized non-crystalline specimens. *Nature*, 400:342–344, 1999.
- [125] Gy. Faigel and M. Tegze. X-ray holography. *Reports on Progress in Physics*, 62:355, 1999.
- [126] J. M. Rodenburg, A. C. Hurst, A. G. Cullis, B. R. Dobson, F. Pfeiffer, O. Bunk, C. David, K. Jefimovs, and I. Johnson. Hard-x-ray lensless imaging of extended objects. *Physical Review Letters*, 98, 2007.
- [127] P. Thibault, M. Dierolf, A. Menzel, O. Bunk, C. David, and F. Pfeiffer. High-resolution scanning x-ray diffraction microscopy. *Science*, 321, 2008.
- [128] P. Thibault, M. Dierolf, O. Bunk, A. Menzel, and F. Pfeiffer. Probe retrieval in ptychographic coherent diffractive imaging. *Ultramicroscopy*, 109:338–343, 2009.
- [129] C. M. Kewish, M. Guizar-Sicairos, C. Liu, J. Qian, B. Shi, C. Benson, A. M. Khounsary, J. Vila-Comamala, O. Bunk, J. R. Fienup, A. T. Macrander, and L. Assoufid. Reconstruction of an astigmatic hard x-ray beam and alignment of K-B mirrors from ptychographic coherent diffraction data. *Optics Express*, 18:23420–23427, 2010.
- [130] M. Guizar-Sicairos, S. Narayanan, A. Stein, M. Metzler, A. R. Sandy, J. R. Fienup, and K. Evans-Lutterodt. Measurement of hard x-ray lens wavefront aberrations using phase retrieval. *Applied Physics Letters*, 98:111108, 2011.

- [131] W. Hoppe. Beugung im inhomogenen Primärstrahlwellenfeld. I. Prinzip einer Phasenmessung von Elektronenbeugungsinterferenzen. *Acta Crystallographica A*, 25:495–501, 1969.
- [132] J. M. Rodenburg and R. H. T. Bates. The theory of superresolution electron-microscopy via Wigner-distribution deconvolution. *Philosophical transactions of the royal society of London*, 339:521–553, 1992.
- [133] B. C. McCallum and J. M. Rodenburg. Simultaneous reconstruction of object and aperture functions from multiple far-field intensity measurements. *Journal of the Optical Society of America*, 10:231–239, 1993.
- [134] H. M. L. Faulkner and J. M. Rodenburg. Movable aperture lensless transmission microscopy: A novel phase retrieval algorithm. *Physical Review Letters*, 93:023903, 2004.
- [135] A. M. Maiden and J. M. Rodenburg. An improved ptychographical phase retrieval algorithm for diffractive imaging. *Ultramicroscopy*, 109:1256–1262, 2009.
- [136] P. Thibault and A. Menzel. Reconstructing state mixtures from diffraction measurements. *Nature*, 494:68–71, 2013.
- [137] A. M. Maiden, M. J. Humphry, and J. M. Rodenburg. Ptychographic transmission microscopy in three dimensions using a multi-slice approach. *Journal of the Optical Society of America*, 29(8):1606–1614, 2012.
- [138] Y. S. G. Nashed, D. J. Vine, T. Peterka, J. Deng, R. Ross, and C. Jacobsen. Parallel ptychographic reconstruction. *Optics Express*, 22(26):32082–32097, 2014.
- [139] P. Thibault and M. Guizar-Sicairos. Maximum-likelihood refinement for coherent diffractive imaging. *New Journal of Physics*, 14:063004, 2012.
- [140] M. Guizar-Sicairos, I. Johnson, A. Diaz, M. Holler, P. Karvinen, H.-C. Stadler, R. Dinapoli, O. Bunk, and A. Menzel. High-throughput ptychography using eiger: scanning x-ray nano-imaging of extended regions. *Optics Express*, 22(12):14859–14870, 2014.
- [141] B. Henrich, A. Bergamaschi, C. Broennimann, R. Dinapoli, E. F. Eikenberry, I. Johnson, M. Kobas, P. Kraft, A. Mozzanica, and B. Schmitt. PILATUS: A single photon counting pixel detector for x-ray applications. *Nuclear Instruments and Methods in Physics Research Section A*, 607:247–249, 2009.
- [142] I. Johnson, A. Bergamaschi, H. Billich, S. Cartier, R. Dinapoli, D. Greiffenberg, M. Guizar-Sicairos, B. Henrich, J. Jungmann, D. Mezza, A. Mozzanica, B. Schmitt, X. Shi, and G. Tinti. Eiger: a single-photon counting x-ray detector. *Journal of Instrumentation*, 9:C05032, 2014.

- [143] X. Zhang, C. Jacobsen, and S. Williams. Image enhancement through deconvolution. *Proc. SPIE*, 1741:251, 1992.
- [144] D. J. Vine, D. Pelliccia, C. Holzner, S. B. Baines, A. Berry, I. McNulty, S. Vogt, A. G. Peele, and K. A. Nugent. Simultaneous x-ray fluorescence and ptychographic microscopy of cyclotella meneghiniana. *Optics Express*, 20:18287–18296, 2012.
- [145] C. E. Shannon. A mathematical theory of communication. *Bell System Technical Journal*, 27:349–423 and 623–656, 1948.
- [146] S. D. Poisson. *Probabilité des jugements en matière criminelle et en matière civile, précédées des règles générales du calcul des probabilités*. Bachelier, France, 1838.
- [147] L. Bortkiewicz. *Das Gesetz der kleinen Zahlen*. B.G. Teubner, Germany, 1898.
- [148] M. R. Howells, T. Beetz, H. N. Chapman, C. Cui, J. M. Holton, C. J. Jacobsen, J. Kirz, E. Lima, S. Marchesini, H. Miao, D. Sayre, D. A. Shapiro, J. C. H. Spence, and D. Starodub. An assessment of the resolution limitation due to radiation-damage in x-ray diffraction microscopy. *Journal of Electron Spectroscopy and Related Phenomena*, 170:4 – 12, 2009.
- [149] X. Huang, H. Miao, J. Steinbrener, J. Nelson, D. Shapiro, A. Stewart, J. Turner, and C. Jacobsen. Signal-to-noise and radiation exposure considerations in conventional and diffraction x-ray microscopy. *Optics Letters*, 17:13541–13553, 2009.
- [150] J. Kirz, C. Jacobsen, and M. Howells. Soft x-ray microscopes and their biological applications. *Quarterly Reviews of Biophysics*, 28:33–130, 1995.
- [151] A. Rose. *Vision - Human and Electronic*. Plenum Press, 1973.
- [152] R. Hegerl and W. Hoppe. Influence of electron noise on three-dimensional image reconstruction. *Zeitschrift für Naturforschung*, 31:17171721, 1976.
- [153] A. Schropp, R. Hoppe, V. Meier, J. Patommel, F. Seiboth, H. J. Lee, B. Nagler, E. C. Galtier, B. Arnold, U. Zastra, J. B. Hastings, D. Nilsson, F. Uhlén, U. Vogt, H. M. Hertz, and C. G. Schroer. Full spatial characterization of a nanofocused x-ray free-electron laser beam by ptychographic imaging. *Scientific Reports*, 3: 1633, 2013.
- [154] S. K. Dew and M. Stepanova. *Nanofabrication*. Springer Verlag, New York, 2012.
- [155] H. Demers, N. Poirier-Demers, A. R. Couture, D. Joly, M. Guilmain, N. de Jonge, and D. Drouin. Three-dimensional electron microscopy simulation with the CASINO Monte Carlo software. *Scanning*, 33:135–146, 2011.
- [156] Wikipedia: Silsesquioxane, . URL <http://en.wikipedia.org/wiki/Silsesquioxane>.

- [157] Wikipedia: Poly(methyl methacrylate), . URL [http://en.wikipedia.org/wiki/Poly\(methyl\\_methacrylate\)](http://en.wikipedia.org/wiki/Poly(methyl_methacrylate)).
- [158] Y. Shazia, D. G. Hasko, and H. Ahmed. Comparison of MIBK/IPA and water/IPA as PMMA developers for electron beam nanolithography. *Microelectronic Engineering*, 61-62:745–753, 2002.
- [159] H. Watanabe, Y. Todokoro, and M. Inoue. A novel silicon containing chemical amplification resist for electron beam lithography. *Microelectronic Engineering*, 13:6972, 1991.
- [160] H. Namatsu, T. Yamaguchi, M. Nagase, K. Yamazaki, and K. Kurihara. Nanopatterning of a hydrogen silsesquioxane resist with reduced linewidth fluctuations. *Microelectronic Engineering*, 41-42:331334, 1998.
- [161] J. K. W. Yang and K. K. Berggren. Using high-contrast salty development of hydrogen silsesquioxane for sub-10-nm half-pitch lithography. *Journal of Vacuum Science and Technology*, 25:2025, 2007.
- [162] J. K. W. Yang, B. Cord, H. Duan, K. K. Berggren, J. Klingfus, S.-W. Nam, K.-B. Kim, and M. J. Rooks. Understanding of hydrogen silsesquioxane electron resist for sub-5-nm-half-pitch lithography. *Journal of Vacuum Science and Technology*, 27:2622, 2009.
- [163] C. S. Yoo, editor. *Semiconductor Manufacturing Technology*. World Scientific, 2008.
- [164] M. Lindblom, H. M. Hertz, and A. Holmberg. Pulse reverse plating for uniform nickel height in zone plates. *J. Vac. Sci. Technol.*, B 24:2848, 2006.
- [165] V. B. Aleskovskii. Matrix hypothesis and way of synthesis of some active solid compounds, 1952.
- [166] V. B. Aleskovskii and S. I. Koltsov. Some characteristics of molecular layering reactions. *Abstract of Scientific and Technical Conference, Goskhimizdat*, page 65, 1965.
- [167] S. I. Koltsov. Synthesis of solids by the molecular layering method, 1974.
- [168] T. Suntola and J. Hyviriinen. Atomic layer epitaxy. *Annual Reviews of Materials Science*, 15:177–195, 1985.
- [169] S. M. George. Atomic layer deposition: An overview. *Chemical Review*, 110:111–131, 2010.

- [170] H. B. Profijt, S. E. Potts, M. C. M. van de Sanden, and W. M. M. Kessels. Plasma-assisted atomic layer deposition: Basics, opportunities, and challenges. *Journal of Vacuum Science and Technology A*, 29(5):050801, 2011.
- [171] T. Aaltonen, M. Ritala, V. Sammelselg, and M. Leskela. Atomic layer deposition of iridium thin films. *Journal of The Electrochemical Society*, 151:489–492, 2004.
- [172] K. Knapas and M. Ritala. In situ reaction mechanism studies on atomic layer deposition of Ir and IrO<sub>2</sub> from Ir(acac)<sub>3</sub>. *Chemistry of Materials*, 23:27662771, 2011.
- [173] Wikipedia: Supercritical drying, . URL [http://en.wikipedia.org/wiki/Supercritical\\_drying](http://en.wikipedia.org/wiki/Supercritical_drying).
- [174] S. Gorelick, J. Vila-Comamala, V. A. Guzenko, and C. David. High aspect ratio nanostructuring by high energy electrons and electroplating. *Microelectronic Engineering*, 88:22592262, 2011.
- [175] V. A. Guzenko, J. Romijn, J. Vila-Comamala, S. Gorelick, and C. David. Efficient e-beam lithography exposure strategies for diffractive x-ray optics. *AIP Conf. Proc.*, 1365:92, 2010.
- [176] M. Stepanova, T. Fito, Zs. Szabo, K. Alti, A. P. Adeyenuwo, K. Koshelev, M. Aktyary, and S. K. Dew. Simulation of electron beam lithography of nanostructures. *Journal of Vacuum Science and Technology*, 28:C6C49, 2010.
- [177] M. Frigo and S. G. Johnson. The design and implementation of FFTW3. *Proceedings of the IEEE*, 93:216–231, 2005.
- [178] I. Mohacsi, P. Karvinen, I. Vartiainen, A. Diaz, A. Somogyi, C. M. Kewish, P. Mercère, and C. David. High efficiency x-ray nanofocusing by the blazed stacking of binary zone plates. *Proc. SPIE*, 8851:88510Z, 2013.
- [179] I. Mohacsi, P. Karvinen, I. Vartiainen, V. A. Guzenko, A. Somogyi, C. M. Kewish, P. Mercère, and C. David. High-efficiency zone-plate optics for multi-keV x-ray focusing. *Journal of Synchrotron Radiation*, 21(3):497–501, 2014.
- [180] I. Mohacsi, I. Vartiainen, M. Guizar-Sicairos, P. Karvinen, V. A. Guzenko, E. Müller, E. Färm, M. Ritala, C. M. Kewish, A. Somogyi, and C. David. High resolution double-sided diffractive optics for hard x-ray microscopy. *Optics Express*, 23(2):776–786, 2015.
- [181] K. Strehl. Aplanatische und fehlerhafte Abbildung im Fernrohr. *Zeitschrift für Instrumentenkunde*, 15:362–370, 1895.
- [182] E. Wolf and M. Born. *Principles of Optics (1st edition)*. Pergamon Press Ltd., London, 1959.



- 
- [183] S. Rehbein, S. Heim, P. Guttman, S. Werner, and G. Schneider. Ultrahigh-resolution soft-x-ray microscopy with zone plates in high orders of diffraction. *Physical Review Letters*, 103:110801, 2009.
- [184] S. C. Gleber, M. Wojcik, J. Liu, C. Röhrig, M. Cummings, J. Vila-Comamala, K. Li, B. Lai, D. Shu, and S. Vogt. Fresnel zone plate stacking in the intermediate field for high efficiency focusing in the hard x-ray regime. *Optics Express*, 22(23):28142–28153, 2014.
- [185] C. Bergemann, H. Keymeulen, and J. F. van der Veen. Focusing x-ray beams to nanometer dimensions. *Physical Review Letters*, 91:204801, 2003.
- [186] A. A. Krasnoperova, Z. G. Chen, F. Cerrina, E. DiFabrizio, M. Gentili, W. L. Yun, P. G. Barry, and S. Efim. Microfocusing optics for hard x-rays fabricated by x-ray lithography. *SPIE Proc.*, 2516:15–26, 1995.
- [187] M. Dierolf, A. Menzel, P. Thibault, P. Schneider, C. M. Kewish, R. Wepf, O. Bunk, and F. Pfeiffer. Ptychographic x-ray computed tomography at the nanoscale. *Nature*, 467:436–439, 2010.

# MOHÁCSI ISTVÁN

Date of birth: 13.04.1988 Budapest (Hungary)

Phone: (079) 869-1273

E-mail: [istvan.mohacsi@psi.ch](mailto:istvan.mohacsi@psi.ch)

Mailing Address:

5200 Brugg, Seidenstrasse 13A



**NATIONALITY** Hungary (EU member)

**EDUCATION** **2011-2015: PhD in experimental physics**  
University of Basel / Paul Scherrer Institute (Switzerland)  
Advisor: Prof. Dr. Frithjof Nolting

**2009-2011: Master degree in physics**  
Eotvos Lorand University, Budapest (Hungary)  
Advisor: Dr. Peter Petrik

**2006-2009: Bachelor degree in physics**  
Eotvos Lorand University, Budapest (Hungary)  
Advisor: Dr. Geza Tichy

**COURSES TAKEN**

- *PSI Summer School on Condensed Matter Research, Imaging Life and Matter* (2012 Zugeberg, Switzerland)
- *Engineering and characterization of nanostructures by photon, ion beam, and nuclear methods ERASMUS IP* (2010 Leuven, Belgium)
- *Short course on physical characterization of nanostructures* (2011 Leuven, Belgium)

**TECHNICAL SKILLS**

**Experience with the following methods:**

- Electron beam lithography
- Scanning electron microscopy
- Experience with synchrotron radiation
- Hard X-ray microscopy and imaging
- Ptychography and coherent diffraction imaging
- Experience with XFELs
- Spectroscopic ellipsometry

**General skills:**

- Cleanroom experience
- Nanofabrication

**Research experience:**

- 2011-2015: PhD student at the Paul Scherrer Institute
- 2009-2011: Master student at HAS Institute for Technical Physics and Materials Science (Budapest, Hungary)

**COMPUTER  
SKILLS**

**Operating systems:**

Microsoft Windows 7, Arch Linux

**Programming, scripting and markup languages:**

C (advanced), C++, CUDA, OpenCL, Python, MatLab, LaTeX

**LANGUAGE  
SKILLS**

**Hungarian:** Native Language

**English:** Fluent level.

**German:** Basic level.

**REFERENCES**

**Prof. Dr. Nolting Frithjof,**

Laboratory Condensed Matter Physics  
Paul Scherrer Institute & University of Basel  
CH-5232, Villigen PSI  
Phone: (056)-310-5111  
Email: [frithjof.nolting@psi.ch](mailto:frithjof.nolting@psi.ch)

**Dr. David Christian,**

Laboratory of Micro- and Nanotechnology  
Paul Scherrer Institut  
CH-5232, Villigen PSI  
Phone: (056)-310-3753  
Email: [christian.david@psi.ch](mailto:christian.david@psi.ch)

**Dr. Alke Meents,**

Deutsches Elektronen-Synchrotron  
Notkestraße 85, 22607 Hamburg, Germany  
Phone: +49 (0)40 8998 5468  
Email: [alke.meents@desy.de](mailto:alke.meents@desy.de)

**LIST OF  
PUBLICATIONS**

I. Vartiainen, C. Holzner, I. Mohacsi, P. Karvinen, A. Diaz, G. Pigino and C. David, "Artifact characterization and reduction in scanning X-ray Zernike phase contrast microscopy", Optics Express (accepted) (2015)

I. Mohacsi, I. Vartiainen, M. Guizar-Sicairos, P. Karvinen, V. A. Guzenko, E. Müller, E. Färm, M. Ritala, C. M. Kewish, A. Somogyi and C. David, High resolution double-sided diffractive optics for hard X-ray microscopy, Optics Express, 23(2), 776-786 (2015)

C. David, P. Karvinen, M. Sikorski, S. Song, I. Vartiainen, C. J. Milne, A. Mozzanica, Y. Kayser, A. Diaz, I. Mohacsi, G. A. Carini, S. Herrmann, E. Färm, M. Ritala, D. M. Fritz and A. Robert, "Following the dynamics of matter with femtosecond precision using the X-ray streaking method", Scientific Reports, 5, 7644 (2015)

I. Mohacsi, P. Karvinen, I. Vartiainen, V. A. Guzenko, A. Somogyi, C. M. Kewish, P. Mercere and C. David, High-efficiency zone-plate optics for multi-keV X-ray focusing, Journal of Synchrotron Radiation, 21(3), 497-501 (2014)

G. Lovric, P. Oberta, I. Mohacsi, M. Stampanoni and R. Mokso, "A robust tool for photon source geometry measurements using the fractional Talbot effect", Optics Express, 22(3), 2745-2760 (2014)

I. Mohacsi, P. Karvinen, I. Vartiainen, A. Diaz, A. Somogyi, C. M. Kewish, P. Mercere and C. David, High efficiency x-ray nanofocusing by the blazed stacking of binary zone plates, Proc. SPIE, 88510Z (2013)

I. Mohacsi, P. Petrik, M. Fried, T. Lohner, J.A. van den Berg, M. A. Reading, D. Giubertoni, M. Barozzi, A. Parisini, Characterization of ultra-shallow disorder profiles and dielectric functions in ion implanted Si, Thin Solid Films, 519(9), 2847-2851 (2011)

**ORAL  
CONFERENCE  
CONTRIBUTIONS**

I. Mohacsi, I. Vartiainen, M. Guizar-Sicairos, P. Karvinen, V. A. Guzenko, E. Müller, E. Färm, M. Ritala, C. M. Kewish, A. Somogyi and C. David, "Double-sided Fresnel zone plates", XRM 2014 ( Oct 2014, Australia)

I. Mohacsi, P. Karvinen, I. Vartiainen, A. Diaz, A. Somogyi, C. M. Kewish, P. Mercere and C. David, "High efficiency x-ray nanofocusing by the blazed stacking of binary zone plates", SPIE Optics + Photonics 2013 (August 2013, USA)

**POSTER  
CONFERENCE  
CONTRIBUTIONS**

I. Mohacsi, I. Vartiainen, M. Guizar-Sicairos, P. Karvinen, V. A. Guzenko, E. Müller, E. Färm, M. Ritala, C. M. Kewish, A. Somogyi and C. David, "Double-sided X-ray optics for the hard X-ray range", MNE 2014 (Sept 2014, Switzerland)

I. Mohacsi, C. David, P. Karvinen, I. Vartiainen, A. Somogyi, C. M. Kewish, "High efficiency X-ray nanofocusing by stacked binary zone plates", SRI 2012 (July 2012, France)

I. Mohacsi, P. Petrik, M. Fried, T. Lohner, J.A. van den Berg, M.A. Reading, D. Giubertoni, M. Barozzi, "Parametrization of ultra-shallow disorder profiles and dielectric functions in ion implanted Si", EuroNanoForum 2011 (May 2011, Hungary)